Imperial College
London

Experimental study of combustion and scalar mixing in swirling jet flows

Viacheslav Stetsyuk
Dipl.Eng.

Multiscale Flow Dynamics Group
Thermofluids Division
Mechanical Engineering Department
Imperial College London
London SW7 2BX

December 2013

Submitted in partial fulfilment of the requirements for the degree of Doctor of Philosophy of the Imperial College London.

Declaration of Originality

This work, unless where the reference is mentioned, is the result of the study carried out by Viacheslav Stetsyuk.

Viacheslav Stetsyuk, *Dipl.-Ing, MSc.*, London, UK, 2013.

Copyright Declaration

Abstract

Turbulent mixing of passive scalar field and combustion of gaseous fuel were studied in the context of a non−premixed isothermal and reacting swirling jets discharged from a swirl−stabilised burner, as a function of swirl number. The rate of molecular mixing, which was quantified by the scalar dissipation rate was computed from measured scalar fields that were recorded by using Planar Laser Induced Fluorescence (PLIF) of acetone. The influence of the swirl number on the scalar mixing, unconditional and conditional scalar dissipation rate statistics was investigated. Scalar fields were measured with an average error of ±3%. Scalar dissipation rate was measured with an average error of 12% after de-nosing.

The influence of swirl number on combustion characteristics was examined by using Rayleigh scattering with accuracy of 90%. The flow fields in non−reacting and reacting swirling jets were investigated by using Particle Image Velocimetry (PIV). The effect of swirl number on a recirculation zone was shown and discussed. The flow structures were evaluated by using Proper Orthogonal Decomposition.

Experimental assessment of presumed filtered density function and subgrid scale (SGS) scalar variance models that are being developed in the context of Large Eddy Simulation (LES) was performed by using the data obtained from measured scalar fields.

Measurements were performed in a flow formed by discharging a central jet in the annular stream of swirling air. This is a typical geometry used in swirl−stabilised burners where the central jet is the flow. The measurements were performed at a constant Reynolds number of 28662, based on the area−averaged velocity of 8.46 (m/s) at the exit of the swirl−stabilised burner and the diameter of the annular swirling stream of 50.8(mm). Three swirl numbers $S = \{0.3, 0.58, 1.07\}$ of the annular swirling stream were considered.

Acknowledgement

First of all I wish to thank my supervisors Prof. Yannis Hardalupas and Prof. Alex Taylor for sharing their understanding of combustion and fluid dynamics. Their support throughout my thesis was invaluable. I am thankful for having Dr. Nikolaos Soulopoulos as my informal supervisor and for helping me with all technical and non−technical issues during my time at Imperial. I thank them sincerely.

My special thanks also goes to Dr. Frank Beyrau , Dr. Georgios Charalampous, Dr. Srikrishna Sahu, Mr. Ian Wright, Mr. Asanka Munasinghe, Mr. Alan Bayley, Mr. Panagiotis Sphicas, Mr. Johannes Kerl, Mr. Benoit Fond for their help and support. The assistance received from Ian, Guljar and Eddy for building up the experimental setup is acknowledged with deep regards.

I would also like to mention some of my colleagues who helped me with different aspects of my life in London: Mr. Kyriakoulis Resvanis, Mr. Constantinos Hadjiyiannis, Ms. Huan Lian, Mr. Dimitrios Katsikadakos, Mr. Christopher Hong, Mr. Thomas Sponfeldner, Mr. Henkel Sebastian, Mr. Richard Neve, Mr. Edward Smith, Mr. Michalis Hadjipanayis and all the rest in the Department of Mechanical Engineering. Administrative assistance from Ms. Serena Dalrymple and Ms. Victoria Harding is also deeply acknowledged.

I am also grateful to my former supervisor at the Technion-Israel Institute of Technology, Prof. Yeshayahou Levy for his encouragement for this research.

This work was sponsored by the Alan Howard Scholarship for Energy Futures and needs, obviously, to be gratefully acknowledged.

My mother, stepfather and my grandmother receive my deepest gratitude for their dedication, love and support, which go beyond words. I always have them in my heart and, even if I spent most of my time away, I missed them greatly. Even to think of thanking them is to trivialise all that they have done for me. I dedicate this thesis to them.

An investment in knowledge pays the best interest.

Benjamin Franklin

To my family Natalie, Alexander and Peter

Contents

List of Figures

List of Tables

Nomenclature

Symbol	*Description*	*Units*
A_{ij}	Einstein A coefficient for spontaneous emission	$1/s$
B_{ij}	Einstein B coefficient for single-photon laser stimulated process	$-$
$B_z\left(\bar{z}, \bar{z}''^2\right)$	Presumed $\beta-$ FDF	$-$
C_{ij}	Cross-stress tensor	m^2/s^2
D	Diffusion coefficient, burner diameter	cm^2/s, m
D_0	Laser beam diameter	m
D_f	Fuel nozzle diameter	m
Da	Damkohler number	$-$
d_0	Laser beam focal spot size	nm
E_v	The spectral fluence of the laser	W/m^3
$F_m(k)$	Fast Fourier transform of an original raw image	$1/mm$
$f_\phi(\hat{\phi}; x, t)$	Filtered mass density function	$-$
f_l	Focal length of a lens	m
$f_1(T)$	Fractional population of lower laser-coupled state in the absence of the laser field	$-$
$f\#$	F-number (f-ratio, f-stop, or relative aperture)	$-$
$f_z\left(x, t\right)$	Measured FMDF	$-$
$G(x)$	Convolution kernel	$-$
$G(k)$	Fast Fourier transform of the Wiener function	$1/mm$
G_Θ	Axial flux of angular momentum	$-$
G_z	Axial flux of axial momentum	$-$
$H(k)$	Fast Fourier transform of a point spread function	$1/mm$
I	Incident laser intensity	W/m^2
k	Turbulent kinetic energy	m^2/s^2
L	Integral scale of turbulence	m
L_{ij}	Leonard tensor	m^2/s^2
M	Laser beam quality factor	$-$
N_R	Number density of scatters	$1/m^3$
$N_{samples}$	Total number of samples	$-$
N_L	Number of laser shots (number of images)	$-$
n	The total gas number density	$-$
n_i	Number of samples in a histogram bin	$-$
p	Pressure	Pa
Q_{ij}	The collision transfer coefficient from level i to level j	
R	Burner radius	m
Re	Reynolds number	$-$

Continued on the next page.....

Nomenclature: Continued

Symbol	*Description*	*Units*
R_L	Turbulent Reynolds number	$-$
R_{ij}	Reynolds subgrid tensor	m^2/s^2
R_λ	Reynolds number based on Taylor's length scale	$-$
S	Swirl number	$-$
sf	Scale factor	$mm/pixel$
Sc	Schmidt number	$-$
$S_s(k)$	Spectrum of a blurred image	$1/mm$
$S_F(x,y)$	Measured acetone fluorescence signal	counts
$S_{R_{ref}}(x,y)$	Reference acetone fluorescence signal	counts
$S_R(x,y)$	Rayleigh scattering intensity at each pixel	counts
S_{tk} Stokes number	$-$	
T	Temperature	K
T_C	Temperature from the flamelet solution	K
T_A	Temperature from the polynomial$-$cubic approximation	K
$\overline{T}_{f_z}$	Resolved temperature computed from measured FMDF	K
$\overline{T}_\beta$	Resolved temperature computed from presumed $\beta - FDF$	K
$\overline{T}_{\Pi_l}$	Resolved temperature computed from presumed top-hat FDF	K
t	Time	s
U_0	Bulk velocity	m/s
u	Velocity	m/s
u_i	Velocity components in Cartesian system	m/s
u_η	Kolmogorov's velocity scale	m/s
V	Volumetric air or fuel flow rate	l/min
V_p	Particle ensemble velocity	m/s
V_c	Collection volume imaged onto photodetector element	m^3
W_0	Laser beam waist,	μm
$W(k)$	Fast Fourier transform of the Wiener filter	$1/mm$
x, y, z	Spatial coordinates	m
x_1, x_2, x_3	Spatial coordinates	m
z	Instantaneous mixture fraction	$-$
$\tilde{z}$	Spatially filtered mixture fraction	$-$
$\tilde{z}''^2$	Resolved 'subgrid' scale variance	$-$

Continued on the next page.....

Nomenclature: Greek letters

Symbol	*Description*	*Units*
α	Thermal diffusivity	m^2/s
τ_{ij}	Subgrid tensor	m^2/s^2
ρ	Density	kg/m^3
$\bar{\rho}$	Spatially filtered density	kg/m^3
$\overline{\dot{\omega}_k}$	Filtered reaction rate	$m^3/mol \cdot s$
δ	LES filter width	mm
$\Delta\tau$	Time delay between the two laser pulses	s
Δx	Distance travelled by a particle in two frames	$pixels$
Δ_{bin}	Histogram bin width	$-$
$\tilde{\phi}$	Favre filtered value	$-$
$\hat{\phi}$	Sample space variable	$-$
χ_z	Scalar dissipation rate	$1/s$
χ_T	Thermal dissipation rate	$1/s$
η	Kolmogorov's length scale	mm
λ_B	Batchelor length scale	mm
λ_D	Scalar dissipative layer thickness	μm
λ	Taylor length scale, Wavelength of light	mm, nm
ε	Turbulent energy dissipation rate	m^2/s^3
ν	Kinematic viscosity	m^2/s
$\Pi_l\left(\bar{z}, \bar{z}''^2\right)$	Top-hat FDF	$-$
χ_m	The mole fraction of the absorbing species	$-$
Ω	Solid angle collected by imaging optics	rad
η_{ef}	Transmission efficiency of collection optics	$V/photon$
σ	Standard deviation	$-$
$\partial\sigma/\partial\Omega$	Differential scattering cross section of the gas mixture	$-$
δ_i	Rayleigh scattering cross section of i-th species	cm^2
$\Im$	Fast Fourier Transform	$-$

Abbreviations

Abbreviation	*Description*
APS	Advanced photo system
CCD	Charged−couple device
CFD	Computational fluid dynamics
CDF	Cumulative distribution function
CMOS	Complementary metal−oxide−semiconductor
CMC	Conditional moment closure
DLN	Dry low−NOx
DNS	Direct numerical simulation
EGR	Exhaust gas recirculation
EOS	Electro−optical system
FWHM	Full width at half maximum
FDF	Filtered density function
FMDF	Filtered mass density function
FOV	Field of view
FGR	Flue gas recirculation
FLOX	Flameless oxidation combustion
LIF	Laser−induced fluoresce
LES	Large eddy simulation
LSF	Line spread function
LP/LPP	Lean premixed/prevaporized
MTF	Modulation transfer function
m.s.e.	Mean−square−error
OTF	Optical transfer function
p.d.f.	Probability density function
p.m.d.f	Probability mass density function
ppm	Particles per million
ppmv	Particles per million by volume
PLIF	Planar laser−induced fluoresce
PSF	Point spread function
PSR	Perfect stirred reactor
RANS	Reynolds averaged Navier−Stokes equations
RQQL	Rich burn, quick quench, lean combustion
RIO	Region of interest
SGS	'Subgrid' scale
SNR	Signal to noise ratio
SRF	Step response function
SFR	Spatial frequency response
STP	Standard temperature and pressure
SPRFC	Stagnation point reverse flow combustor
UHC	Unburned hydrocarbons
UV	Ultra−violet light

Subscripts

Symbol	*Description*
a	Air
f	Fuel
mix	Mixture

1 Introduction

> Nothing is too wonderful to be true if it be consistent with the laws of nature.
>
> Michael Faraday

In this chapter the introduction to the field of combustion and a brief literature review are given to facilitate understanding of the motivation, requirements and state of the art in low−emission combustion as well as to define the research needs. The process of combustion in gas turbine and jet engines and various factors that contribute to pollutants formation will be briefly explained. Turbulent combustion modelling with the emphasis on Large Eddy Simulation (LES) and its relationship to experimental methods is also briefly discussed.

1.1 Combustion and pollutant formation

A gas turbine engine, or simply a gas turbine (GT), is a type of internal combustion engine that converts chemical energy stored in the fuel into a useful type of work (thrust or torque). A typical gas turbine engine consists of a compressor, a combustor, a turbine and a nozzle. The compressor is used to compress the air and deliver the air flow to the combustion chamber. Energy is added to the gas stream in the form of gaseous or liquid atomized fuel. In the high pressure environment the fuel quickly evaporates (if liquid) and is mixed with the preheated air, which was delivered by the compressor. A total air mass flow rate that is pumped through the compressor split into two parts. The first part, which is called a primary air or combustion air consists of only 30% of the total air mass flow rate. The first part is used in the primary combustion zone where the flame temperature is close to the adiabatic flame temperature, which is about 2200K. The temperature of burnt products is therefore far beyond the limit that any turbine can withstand. The remaining 70% of the total air mass flow rate is therefore used to cool combustion products down to the required temperature. The products of combustion accelerate towards the turbine, where a part of energy is converted into mechanical energy. The turbine is used to drive the compressor and in some cases is used to drive a shaft (like in helicopters) or a propeller (like in turboprops). The remaining energy, stored in the gas stream, is used in propelling nozzle thus creating thrust. Energy can be extracted in the form of shaft or propeller power, compressed air, thrust or a combination of these. Gas turbine engines can also be used to generate electricity. In these systems, a GT is simply connected to an electrical power generator.

It is typically considered that a primary anthropogenic source of important pollutants is the combustion of fossil fuel in combustion devices. Main pollutants emitted from virtually

all types of transportation, electric power generation stations and gas−fired cooking stoves are nitrogen oxides, carbon monoxide, unburned hydrocarbons and soot.

1.1.1 Nitrogen oxides

Nitrogen oxides (NO_x) consist of nitric oxide (NO) and nitrogen dioxide (NO_2), which are both produced during high temperature combustion. The main component of nitrogen oxides consists primarily of NO, which is formed through so called Zeldovich's mechanism. This mechanism was named after Zeldovich[1] who first discovered it. This mechanism is commonly known as thermal NO (Baulch *et al.*, 1994). The thermal NO is usually converted into NO_2 in the atmosphere when it leaves a combustion chamber. The detailed review of NO formation process and the methods of calculation of NO quantities can be found in the sources of Rokke *et al.*, (1993), Lipfert (1972), Lefebvre (1984), Odgers & Kretchmer (1985), Warnatz, (1990) and Lewis, (1991). Fenimore (1971, 1972) proposed an additional mechanism of NO formation that was named prompt. This mechanism consists of a set of chemical reactions that take place at low temperature and contribute to the overall rate of NO formation (De Soete 1975). Improved mixing of fuel and air before reaction can reduce NO_x emissions, in particular during reaction under lean conditions.

1.1.2 Carbon monoxide

Carbon monoxide is an intermediate product of energy conversion. It is generally found that only 10% energy is released during hydrocarbon conversion to CO and 90% during conversion from CO to CO_2. It is generally believed that carbon monoxide is responsible for the formation of photochemical smog. From the engineering points of view the presence of CO in burnt products has negative effects in terms of energy loss due to incomplete fuel oxidation. In an ideal combustor the formation of CO should be minimized to literally zero levels. The basic principle of CO formation is an incomplete oxidation of carbon monoxide, due to the lack of oxygen in zones of rich combustion, and the dissociation of CO_2 back to CO at high temperatures. In general, mechanism of CO formation is typically associated with slow oxidation rate due to low residence time or low combustion temperature, incomplete mixing that could result in local fuel rich zones and the quenching of burnt products on combustor walls. The CO emissions are therefore strongly dependent on an equivalence ratio. Rink & Lefebvre (1989) found that the minimum of CO was observed during slightly lean combustion, which corresponded to 0.8 equivalence ratio.

1.1.3 Unburned hydrocarbons and soot

Unburned hydrocarbons (UHC) are normally associated with the term product of incomplete combustion. UHC are the hydrocarbons emitted after fuel is burnt in an engine. The term UHC is used to describe species, such as formaldehyde and alkenes that are formed in the regions of low temperature. The UHCs consist of products of fuel thermal decomposition into species of lower molecular weight, such as for example methane and

[1] Yakov Borisovich Zeldovich (1914−1987) was a prolific Soviet physicist born in Belarus. He played an important role in the development of Soviet nuclear and thermonuclear weapons, and made important contributions to the fields of adsorption and catalysis, shock waves, nuclear physics, particle physics, astrophysics, physical cosmology, and general relativity (http://en.wikipedia.org).

acetylene. The composition and quantity of UHC in burnt products depend on the nature of fuel and on the process that limits oxidation. The factors, which affect the formation of CO, in the same manner influence UHC (Lefebvre, 1995), so that the CO and UHC can be controlled by increasing the air temperature or by increasing the combustion pressure. In addition, the formation of UHC can be directly related to liquid fuel atomization. Pure atomization with large fuel droplets will induce fuel pyrolysis and increase UHC. Soot is caused by incomplete combustion in a fuel rich zone or by significant lack of oxygen under high temperature. Soot primarily consists of carbon 95−98%, hydrogen, oxygen and other atoms. Carbonaceous particles are formed during combustion process and can be identified in the flames as yellow luminescence. Experiments confirm that soot particles are mostly found as agglomerates, typically no larger than 500(A) with the hydrogen to carbon ratio between 1:8 to 1:10. Physically, the process of soot formation can be related to imperfect atomization and imperfect mixing. Lefebvre (1982, 1995) found a relationship between soot formation, pressure, temperature, equivalence ratio, atomization quality and regime of the fuel injection. Some specific models for soot formation can be found in the work of Glassman (1988).

In gas turbine and jet engines, the process of pollutant formation is directly related to specific combustor design and operating conditions. At low working load significant concentrations of UHC and CO should be expected. Significant CO concentrations can also be expected at high load due to the highest flame temperature and dissociation of CO_2 back to CO. In contrast, the nitrogen oxides and smoke attain their maximum values at high operational load where temperature is at its maximum. It should be noted that there is always conflict of interests between clean combustion and engine efficiency or fuel consumption. In order to minimize pollutant emissions from combustion chambers different technologies can be used, which are briefly discussed below. Since the most important pollutants are nitrogen oxides, only low-NO_x techniques will be mentioned.

1.2 Introduction to low NOx techniques

All low−NO_x technologies can be basically split into two large groups. The first group consists of so called wet low−NO_x technologies, which is the most traditional approach to decrease amount of nitrogen oxides from gas turbine and internal combustion engines. In this technology, humidifying fuel gas, combustion air or the flame is used to decrease the flame temperature. The second group consists of so called dry low−NO_x technologies in which a combustor is modified (lean−premixed, rich−quench−lean etc.) and no additional additive (e.g. water/steam) is used to decrease the flame temperature.

1.2.1 Steam/water injection technology

Steam/water injection technology could be the first example of different concepts for reducing thermal NO_x by decreasing the flame temperature in a combustion chamber. Steam/water injection is the method for cooling the combustion products in the combustion chambers by adding water to incoming fuel−air mixture or directly into the combustion zone. Even though, steam/water injection was primarily used with piston−powered

internal combustion engines (mainly during WW2 to increase power of piston−propelled aircraft), it can also be applied to gas turbine engines.

1.2.2 Exhaust gas recirculation

Exhaust gas recirculation (EGR) is another method for reducing NO_x formation in combustion chambers. Exhaust gases consist basically of CO_2, water vapour and N_2 and when the exhaust gases are recirculated into the combustion area they act as diluter in the combusting mixture, thus reducing oxygen concentration in the fresh mixture. Negative aspect of the EGR is that the use of the EGR also promotes soot formation. As a result, the soot particles come into contact with high velocity components of the engine, such as the turbine in the gas turbine engines, or the cylinder in internal combustion engines. This can cause mechanical failure in these components and as a result premature breakdown. During the past 20 years significant research has been done on EGR and its effects on the engine performance in terms of NO_x formation, reduction of fuel consumption, reliability and durability of the engine itself and its components.

1.2.3 Air and fuel staging combustion

Air and fuel staging combustion is another example of low$-NO_x$ technique. In this technique combustion air or the fuel stream is separated into primary and secondary flow streams to achieve complete burnout, and to prevent the formation of NO_x. In the air staging combustion, the primary air (10−30%) is mixed with fuel producing a relatively low temperature oxygen deficient fuel−rich zone, and therefore moderate amounts of NO_x. The secondary portion (70−90%) of the combustion air is injected into the combustion zone diluting burnt products and decreasing the flame temperature. The location of the injection ports and mixers of secondary air is critical to maintain efficient combustion and is subject to individual design issues. During the past 10 years, many different practical forms of staged gas turbine combustors have been designed. Nevertheless, some drawbacks of these systems, such as complex control mechanisms and heavy weight, restricted this technology from being widely used. The disadvantages of fuel and air staging have motivated the development of different forms of staged combustors. For instance, instead of one combustion zone, two or more combustion zones were used (Bahr, 1982). Staged combustors were designed especially to provide a stable combustion under lean premixed operating regimes (Lefebvre 1974, Mosier & Roberts 1973). The design and manufacture of staged combustion gas systems are more complicated and expensive than traditional ones. Many of the components, such as channels, flame holders, ignition systems and combustion chambers might have to be redesigned. This will also increase the manufacturing cost of the combustion system.

1.2.4 Selective catalytic reduction

Selective catalytic reduction is a method of combustion with ammonia on the surface of a catalyst. This process occurs typically at elevated temperatures of 600−800(K). The selective catalytic reduction is a very expensive method due to high capital expenditures and high operating cost. Other serious problems include safe transportation and storing of the

significant amounts of ammonia. In addition, pollution of ammonia into the atmosphere could have severe consequences.

1.2.5 Catalytic combustion

Catalytic combustion is an another method for reducing NO_x emissions. This method is based on a Pt catalyst $+K_2CO_3$. The catalyst is regenerated in the combustion process and this technology is applicable to gas turbine engines, which operate with natural gas only. It is highly questionable that this technology can be applied to aircraft propulsion or transportation that is based on the GT engines.

1.2.6 Rich burn, quick quench

Rich burn, quick quench, lean combustion (RQQL) is the technology in which the combustion process is formed within three different zones. In the beginning, the combustion process takes place in the first zone with a relatively high equivalence ratio ($\Phi > 1.4$) and hence significant lack of oxygen. After initial combustion the burnt products are mixed with relatively cold air. Hot products from the first reaction zone pass onto the second reaction zone with a low equivalence ratio ($\Phi < 0.4$). In the last stage of combustion chamber further conversion from CO to CO_2 takes place.

1.2.7 Lean premixed prevaporized

Lean premixed/prevaporized (LP/LPP) technology is the most promising one and is the main object of intensive research studies. Nevertheless, some drawbacks also restrict this method from being widely used. If fuel is premixed and vaporised before combustion, the combustion temperature becomes a function of equivalence ratio only. For example, mixing fuel and air before combustion with equivalence ratio $\Phi = 0.6$ restricts rise in temperature to below 1800(K) where NO_x formation drastically drops. The LPP concepts for liquid fuels have been widely investigated, e.g. by Anderson (1981), Lyons (1981) and Semerjian & Vranos (1994). The main advantage of LPP systems over conventional combustion devices is that the amount of NO_x formed does not increase significantly with increasing residence time (Anderson, 1975). At present, this technology is expected to be an economical and efficiency method to achieve low$-NO_x$ emissions. Currently low$-NO_x$ combustors operate with emissions around $20-25$ (ppmv) using natural gas as fuel. For liquid fuel, these values will be higher, ranging typically from 70 to 90 (ppmv), and many problems still remain unresolved. Among them is the problem of flashback in premixed systems, as it was noted in the work by Plee & Millor (1978).

1.2.8 Flameless oxidation combustion

Flameless oxidation combustion is a relatively new type of combustion that is based on flue gas recirculation (FGR). Wunning (1991) was the first researcher who discovered the flameless combustion under specific operating conditions. Wunning found that, under highly preheated combustion air and high exhaust recirculation ratios, a stable combustion would be sustained. This principle was named FLOX^{TM}, or flameless oxidation combustion. This regime is characterized by low noise, invisible flame, distributed reaction zone,

low temperature and little pollutant emission. This regime of combustion was studied in many countries. In Japan and the USA, the process was called Excess Enthalpy Combustion (EEC) and then renamed to Colourless Combustion (or High Temperature Air Combustion).

Wunning and Wunning (1997) have investigated a burner under flameless regime and proposed several flameless combustor schemes. Several attempts have been also taken to design a flameless combustor for a gas turbine engine (Levy, 1998). Luckerath *(*et al.) (2008) observed the flameless combustion in a through−flow cylindrical combustor at high pressure of 30(bar). The temperature distribution was found to be uniform and low, which was the main criterion of flameless combustion. Another type of flameless technology was mentioned in the works by Ben T. Zinn and by Suresh Menon *et al.* (Ohio State University, School of Aerospace Engineering) and was called stagnation point reverse flow combustor (SPRFC). This combustor operated in premixed and non−premixed regime produced little amounts of nitrogen oxides, which were less than 5(ppm).

The introduction of the gaseous or liquid fuels inside a combustor is quite often performed separately for the supply of air (due to safety reasons). This means that reaction of fuel with an oxidizer will lead to diffusion−type flames, which lead to stoichiometric combustion and high NO_x emissions. However, is mixing is fast enough, then some of the reaction can occur in premixed mode. Therefore, it is worth summarising the expected behaviour of nominally diffusion flames.

In typical diffusion flames the combustion process is governed by the mixing time, because the chemical reaction time is very short, of the order of 2−5(ms). The mixing time is directly proportional to the turbulence kinetic energy and the energy dissipation rate. The process of mixing and combustion takes place simultaneously at small scales of flow that are typically of the order of 80−150(μm), which are denoted by the so called Kolmogorov[2] length scale. At present, modern turbulence theory states that large eddies (vortex like structures) are unstable and break into smaller and smaller eddies until they reach Kolmogorov scale when finally the smallest eddies are dissipated by viscous forces into heat. The large eddies are dependent on the flow geometry while the Kolmogorov scale is the universal scale, which is independent of the large eddies. At small scales, fuel and oxidizer are brought in contact and react forming a thin reaction zone, which is known as a flame front. In order to be able to initiate and maintain the chemical reaction, the reactants must co−exist in the same volume for a certain period of time and must be supplied to the reaction zone at right rates to prevent extinction. Since a combustion phenomenon is governed by chemical reaction and flow time scale, it is necessary to emphasize the meaning of these time scales. Non−premixed flames are primarily governed by turbulent mixing, because chemistry is usually faster than mixing times. It is true for conventional diffusion flames but may not be true for example for low−NO_x flameless combustion regime. During flameless combustion regime mixing time is approximately equal to the reaction time due to suppressed fuel oxidation rate.

In order to characterize different combustion regime it is convenient to define a dimen-

[2]Andrey Nikolaevich Kolmogorov (1903−1987) was a Soviet mathematician, preeminent in the 20th century, who advanced various scientific fields, among them probability theory, topology, intuitionistic logic, turbulence, classical mechanics and computational complexity (http://en.wikipedia.org/).

sionless parameter, which is called the Damkohler[3] number as follows.

$$Da \equiv \tau_t/\tau_c \tag{1.1}$$

The turbulent time scale can be seen as a rate at which reactants are supplied to a reaction zone. The chemical time scale is a rate at which reactants are consumed by chemical reaction. It is therefore possible to classify the combustion process according to the Damkohler number as follows.

- Da $\ll 1$. This regime corresponds to a perfect stirred reactor (PSR) model, in which reactants are rapidly mixed. This is an ideal situation and is typically not found in reality.
- Da $= 1$. This regime corresponds to so called distributed combustion regime in which reactants are rapidly mixed and fuel oxidation rate is suppressed, so the chemical time increases. In the distributed combustion regime chemical time scale is larger than for conventional combustion under equivalent operating conditions. This is in fact due to, for example, large exhaust recirculation ratios and suppressed chemical reaction rates.
- Da $\gg 1$. This regime is found in conventional non−premixed diffusion flames. The combustion process is controlled and governed by the turbulent mixing. This is a common situation in gas turbine and jet engines.

1.3 Turbulent combustion modelling

In a typical GT engine, the combustion process is controlled by mixing between a fuel and an oxidiser, because the fuel and the oxidiser are supplied separately into a combustor. The mixing process is controlled by turbulence levels that are related to degrees of swirl, in swirling flows. This means that, for example, high enough turbulence levels may affect combustion process and can lead to the so−called 'delayed' combustion in which the temperature is a function of local air/fuel mixture composition. In addition, these high turbulence levels may also lead to flame local extinction as well as to flame local reignition. The turbulent mixing process is therefore considered to be one of the most important issues in the design of gas turbine combustors and jet engines. It is worth summarising how the turbulent combustion is modelled, before discussing experimental techniques and associated issues in details.

At present, different computational techniques can be used to model combustion processes. The oldest computational approach relies on the so called Reynolds Averaged Navier[4]−Stokes[5] (RANS) equations. The RANS technique was developed to solve ensemble-averaged equation of fluid motions and was the traditional approach to model combustion over decades. In the RANS modelling, the direct closure of the mean chemical source

[3] Gerhard Damkohler (1908−1944) was a German chemist.

[4] Claude-Louis Navier (1785−1836) born Claude Louis Marie Henri Navier was a French engineer and physicist who specialized in mechanics (http://en.wikipedia.org/).

[5] Sir George Gabriel Stokes, 1st Baronet FRS (1819−1903), was a mathematician and physicist, who, at Cambridge, made important contributions to fluid dynamics, optics, and mathematical physics (http://en.wikipedia.org/).

term in the averaged species transport equation can hardly be accomplished and hence conserved scalar methods have been used in many applications. The most popular models were based on non−reactive scalars and became standard tool in modelling non−premixed combustion.

The rate of mixing between fuel and oxidizer can be described by a non−reactive scalar, which in most cases of non−premixed combustion, is the mixture fraction. Different definitions of mixture fraction were formulated (Bilger 1976, Pitch & Peters 1998). The mixture fraction is in fact a measure of the local equivalence ratio and is a conserved scalar that is independent of the chemistry. Methods that are based on the mixture fraction concepts were named conserved scalar methods, which were the basis for many computational codes. The RANS equations also require turbulence models to model Reynolds[6] stress as well as turbulent combustion models to describe chemical species conversion. By solving the RANS equations, coupled with turbulence and combustion models, it is possible to obtain ensemble−averaged stationary flow field. The flame temperature, mixture fraction, species mass fractions etc. predicted by RANS model correspond therefore to the corresponding ensemble−averaged quantities. Hence, the most significant advantage of the RANS technique is in its applicability to model almost any flow configurations and operating conditions. On the other hand, this approach suffers from many drawbacks, such as for example, inability to predict instantaneous flow structures.

An alternative approach that has been underdevelopment for several years is named Large Eddy Simulation (LES). LES is believed to be a useful tool in modelling combustion phenomena, combustion instabilities as well as pollutant formation in existing and future combustion chambers. In LES technique, the turbulent reacting and non−reacting flows filtered versions of the equations describing motion, chemical reaction and mixing are solved on a grid which is 'coarse' relative to the smallest scales of fluid motion. The LES model can predict the instantaneous positions of large eddies or the instantaneous positions of large−scale flow structures. Roughly speaking, the LES model captures low−frequency variation of temperature, mixture fraction, velocity etc. and is based on spatially−filtered instantaneous Navier−Stokes equations. On the other hand, several closure models need to be employed in order to model the effects of the smallest or so called subgird scales that are not resolved by a numerical grid. The combustion process takes place at the smallest scales of turbulence, and the so−called subgrid scales have a large influence on the resulting flow field. Typically, the subgrid scalar variance and the conditional subgrid scalar dissipation rate need modelling to perform closure of the LES equations. Some of the mathematical models that are used to represent combustion in the context of LES are based on the subgrid scale probability density function of mixture fraction (as in flamelet models) and/or chemical species (as in PDF transport equation models). The PDF transport model can simulate realistic finite−rate chemistry in turbulent flame, can handle arbitrary chemical mechanism and has the important advantage of closed chemical source term. The laminar flamelet model has the advantage of strong coupling between chemical reaction and molecular transport, which is important in non−premixed turbulent combustion. The weakest link in the LES approach however, is the subgrid scale models

[6]Osborne Reynolds (1842−1912) was a prominent innovator in the understanding of fluid dynamics (http://en.wikipedia.org/).

that must accurately describe the subgrid local state. In order to illustrate the principle of the LES technique, an example of the LES equation is given.

In the physical space the velocity field, expressed in a Cartesian coordinate system is defined by time dependent Navier−Stokes equation as follows. By applying spatial filter (any instantaneous variable can be split into spatially averaged value $\bar{u}$ and subgrid contribution $u^{'}$) to the initial Navier−Stokes equation, the filtered Navier−Stokes equation is obtained as follows:

$$\rho\left[\frac{\partial u_i}{\partial t}+\frac{\partial}{\partial x_j}\left(u_i u_j\right)\right]=-\frac{\partial P}{\partial x_j}+\mu\left(\frac{\partial u_i}{\partial x_j}+\frac{\partial u_j}{\partial x_i}\right) \tag{1.2}$$

$$\frac{\partial \overline{u}}{\partial t}+\frac{\partial}{\partial x_j}\left(\overline{u}_i\overline{u}_j\right)=-\frac{\partial \overline{P}}{\partial x_j}+\mu\frac{\partial}{\partial x_j}\left(\frac{\partial \overline{u}_i}{\partial x_j}+\frac{\partial \overline{u}_j}{\partial x_i}\right)-\frac{\partial \tau_{ij}}{\partial x_j} \tag{1.3}$$

$$\tau_{ij}=L_{ij}+C_{ij}+R_{ij} \tag{1.4}$$

The last term $\partial\tau_{ij}/\partial x_j$ in the equation above is called subgrid stress tensor and must be modelled. The subgrid tensor is usually split in Leonard tensor L_{ij}, cross−stress tensor C_{ij} and Reynolds subgrid tensor R_{ij}. The subgrid tensor represents all possible interactions between larger and smaller scales. The Leonard tensor represents the interactions between larger scales, the cross−stress tensor represents the interactions between larger and smaller scales and finally the Reynolds stress represents small scale interactions. The detailed information on the LES modelling can be found, e.g. in Sagaut (1998)[7]. Since the concept of spatial filtering plays an important role it is important to explain the meaning of the filtering procedure in the LES context. The filtered quantity ϕ (velocity field, mixture fraction etc.) in physical space is simply defined as a convolution of non−filtered field with a function or a convolution kernel as; where $G(x-x^{'})$ is a convolution kernel (LES filter).

$$\bar{\phi}(x)=\int \phi(x^{'})G(x-x^{'})dx^{'}. \tag{1.5}$$

The LES equations are derived for constant filter width, which is usually a box filter in physical space. The box filter in 2D/3D is written as, where (x_1, x_2, x_3) are the spatial coordinates of the location x.

$$|x_i|\leq\Delta/2\rightarrow G(x)=G(x_1,x_2)=1/\Delta^2; i=1,2. \tag{1.6}$$

$$|x_i|\leq\Delta/2\rightarrow G(x)=G(x_1,x_2,x_3)=1/\Delta^3; i=1,2,3. \tag{1.7}$$

The box filter corresponds to an averaging over squared area (2D) or a cubic box (3D). Another type of LES filter can be for example a Gaussian filter in 2D physical space. All filters are normalized i.e.

$$\int_{-\infty}^{\infty}\int_{-\infty}^{\infty}\int_{-\infty}^{\infty}G(x_1,x_2,x_3)dx_1dx_2dx_3=1 \tag{1.8}$$

[7] P. Sagaut (Large Eddy simulation of incompressible flows: An Introduction, Second edition, Springer Berlin Heidelberg, 1998)

Regardless of the flow modelling a statement of the conservation of mass is generally required in virtually all computational simulations. Since mass, energy, electric charge etc. are conserved quantities their behaviour can be described by an equation, known as a continuity equation that is generally written as follows:

$$\frac{\partial \rho}{\partial t} + \frac{\partial}{\partial x_i}\left(u_i \rho\right) = 0 \tag{1.9}$$

The continuity equation is then filtered similar to the filtering procedure, outlined earlier, which gives the next expression.

$$\frac{\partial \bar{\rho}}{\partial t} + \frac{\partial}{\partial x_i}\left(\overline{u_i \rho}\right) = 0 \tag{1.10}$$

The term $\overline{u_i \rho}$ requires additional subgrid closure model, because no information on non−filtered density and velocity fields is available. Favre (1983) proposed a density−weighted filtering operation, which was called Favre filtering. For any arbitrary variable the Favre filtering operation would be as follows: $\tilde{\phi} = \overline{\rho \phi}/\bar{\rho}$, which in case of the continuity equation becomes as follows: $\tilde{u}_i = \overline{\rho u_i}/\bar{\rho}$ and hence the filtered continuity equation is written as follows:

$$\frac{\partial \bar{\rho}}{\partial t} + \frac{\partial}{\partial x_i}\left(\tilde{u}_i \bar{\rho}\right) = 0 \tag{1.11}$$

The Favre filtering can also be written in terms of convolution of non−resolved field of both density and any arbitrary variable as follows:

$$\bar{\rho}\tilde{f}(x) = \int \rho f(x^{'}) G(x - x) dx^{'} \tag{1.12}$$

A set of the LES equations in Favre $\tilde{\phi}$ notation can then be written as follows:

$$\frac{\partial \bar{\rho}}{\partial t} + \frac{\partial}{\partial x_i}(\bar{\rho}\tilde{u}_i) = 0 \tag{1.13}$$

$$\frac{\partial \bar{\rho}\tilde{u}_i}{\partial t} + \frac{\partial}{\partial x_i}(\bar{\rho}\tilde{u}_i\tilde{u}_j) + \frac{\partial \bar{p}}{\partial x_j} = \frac{\partial}{\partial x_i}\left[\bar{\tau}_{ij} - \bar{\rho}(\widetilde{u_i u_j} - \tilde{u}_i\tilde{u}_j)\right] \tag{1.14}$$

$$\frac{\partial(\bar{\rho}\tilde{Y}_k)}{\partial t} + \frac{\partial}{\partial x_i}\left(\bar{\rho}\tilde{u}_i\tilde{Y}_k\right) = \frac{\partial}{\partial x_i}\left[\overline{V_{k,i}Y_k} - \bar{\rho}(\widetilde{u_i Y_k} - \tilde{u}_i\tilde{Y}_k)\right] + \overline{\dot{\omega}_k}, k = 1, N \tag{1.15}$$

$$\frac{\partial(\bar{\rho}\tilde{h}_s)}{\partial t} + \frac{\partial}{\partial x_i}\left(\bar{\rho}\tilde{u}_i\tilde{h}_s\right) = \frac{\overline{Dp}}{Dt} + \frac{\partial}{\partial x_i}\left[\lambda\frac{\partial T}{\partial x_i} - \bar{\rho}(\widetilde{u_i h_s} - \tilde{u}_i\tilde{h}_s)\right] + \overline{\tau_{ij}\frac{\partial u_i}{\partial x_j}} \tag{1.16}$$

$$\frac{\overline{Dp}}{Dt} = \frac{\partial \bar{\rho}}{\partial t} + \overline{u_i \frac{\partial p}{\partial x_i}} \tag{1.17}$$

In this set of equations the following unclosed term must be modelled.

- Unresolved Reynolds stresses $\widetilde{u_i u_j} - \tilde{u}_i\tilde{u}_j$
- Unresolved species fluxes $\widetilde{u_i Y_k} - \tilde{u}_i\tilde{Y}_k$

- Enthalpy fluxes $\widetilde{u_i h_s} - \tilde{u}_i \tilde{h}_s$
- Filtered laminar diffusion fluxes $\overline{V_{k,i} Y_k}$
- Filtered chemical reaction rate $\overline{\dot{\omega}_k}$

The equation for species can be eliminated if, for example, a laminar flamelet approach is used, in which species mass fractions are precomputed and stored in look−up tables for later integration with an assistance of probability density function (filtered density functions in the LES context). A description of a laminar flamelet concept will be briefly described later. The LES filter removes smaller scales, which can be easily seen in a Fourier space (Figure 1.1). If the LES filter is assumed to be equal to the computational grid size then the effect of the LES filtering can be observed in the next Figure 1.1. If the filter size is chosen to be exactly the same as the numerical grid size, then it yields to sharp cut−off in the Fourier domain Sagaut (1998). A more detailed information on the LES approach can be found, e.g. in Sagaut[8] (2006) and Pope[9] (2000). A detailed information on subgrid closure models can be found in e.g Germano *et al.* (1991), Kim *et al.* (1995), Nicoud *et al.* (1999) and You *et al.* (2007). An example of an effect of box filter size on a resolved mixture fraction field, obtained from planar laser−induced fluorescence measurements and a principle of resolved field and subgrid scale scalar variance computation from the experimental data is shown in Figure 1.2. Smoothing effect of the box filter on the resolved field is clearly visible. The detailed description of resolved field computation from the experimental data as well as a principle of subgrid scale scalar variance computation will be given in a corresponding chapter.

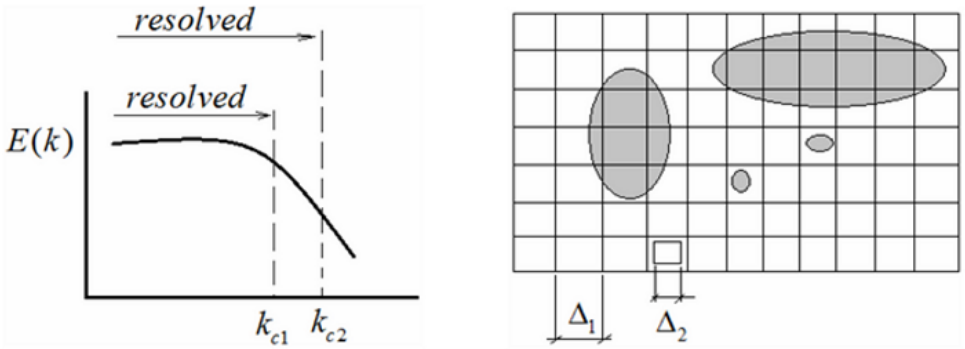

Figure 1.1: A schematic representation of the effect of two different LES filters on the scale separation in the Fourier domain (left) and spatial domain (right). Filters are assumed to be equal to the numerical grid size

In a non−premixed flame fuel and oxidizer diffuse into reaction zone where they undergo chemical reaction and are converted into combustion products. In flames that are near equilibrium, the reaction rate is much faster than the diffusion rate, which is governed by the mixture fraction gradients. In turbulent flow the flame is stretched and wrinkled due to turbulent motions so that the flame temperature, mixture fraction and species gradients increase. This gradient increases the diffusion out of the flame, while the local

[8] P.Sagaut. Large eddy simulation for incompressible flows. Third edition, Springer, 2006.
[9] S.B.Pope. Turbulent flows. Cambridge university press, 2000.

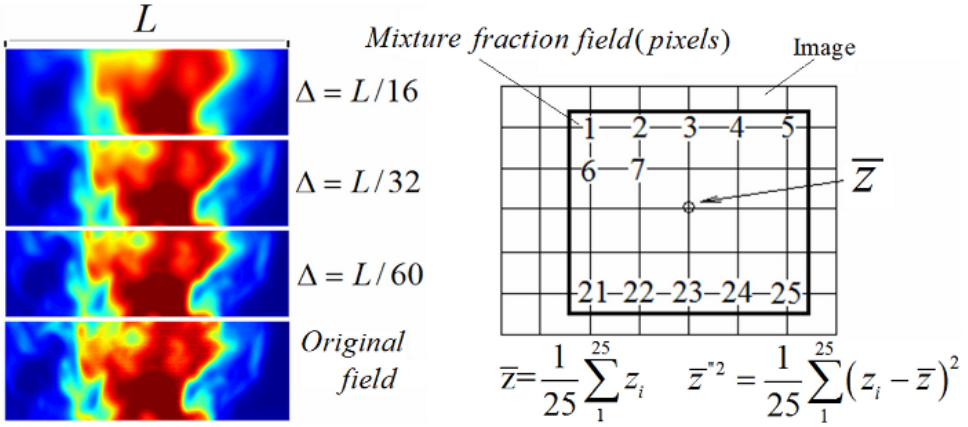

Figure 1.2: An effect of box filter size on a resolved mixture fraction field, obtained from planar laser−induced fluorescence measurements (left) and a principle of resolved field $\bar{z}$ and subgrid scale scalar variance $\bar{z}''^2$ computation from the experimental data (right). This is equivalent to the moving average, which is well−known in signal processing.

chemical non−equilibrium[10] also increases. If this assumption is valid, then a laminar flamelet model can be used to model such regime (detailed description is given in Chapter 5). However this could not be the case in slow reacting flows e.g. flameless oxidation, lean or rich combustion etc. The laminar flamelet approach relies on a principle of infinitely fast chemistry compared to mixing times. To extend this assumption to finite rate chemistry, the scalar dissipation rate was introduced as a parameter to describe the degree of departure from the equilibrium state. However, even when the scalar dissipation rate is introduced, the flamelet approach still relies on the assumption that chemical reaction time is much faster than the time scale of convection and diffusion. Therefore, a turbulent flame is modelled as an ensemble of discrete laminar flamelets embedded into turbulent flow. In adiabatic systems, the flame temperature and the species mass fractions can be parameters of the mixture fraction and the scalar dissipation rate only. It is possible to pre−build so called look−up tables with values of the temperature and species mass fractions as a function of scalar dissipation rate and the mixture fraction. Since in LES only filtered values of the flow field are known it is impossible to integrate the look−up tables in order to obtain the filtered temperature and the filtered species mass fractions, because no subgrid distribution is known.

A general approach to integrate the look−up flamelet tables is based on the solution of a transport equation for the Filtered Density Function (FDF) of the mixture fraction, which is similar to the transport equation for the RANS−PDF. However, the most simplified approach is based on presumed filtered density functions (FDFs) of the mixture fraction, which are usually approximated to be β−FDF or top−hat FDF that are parametrized by the first two statistical moments of the mixture fraction, namely the filtered mixture fraction and its subgrid scale variance.

The success of transported PDF methods (Pope, 1985) in the RANS context promoted the development of the transported FDF concept in the LES context. Transported FDF

[10] Chemical equilibrium is the state in which both reactants and products are present at concentrations which do not change with time.

methods have been developed for instance by Gao & O'Brien (1993), Colucci *et al.* (1998), Sheikhi *et al.* (2003), Raman *et al.* (2006).

The validity and applicability of the $\beta-$function approximation were investigated by several authors using DNS data of non−premixed reacting flows (Cook & Riley 1994, Jimenez *et al.* 2000, Floyd , Kempf *et al.* 2009). The results confirmed that the $\beta-$function provided a good estimate for the FDF of the mixture fraction. However, Tong (2001) and Tong *et al.* (2005) showed that the FDF can substantially deviate from the $\beta-$function.

If an assumption of linearity within the LES cells is made, the FDF can be approximated by so called a top−hat function Borghi & Moreau (1977). The top−hat function, spanning from minimum value z_a to maximum value z_b and the $\beta-$function are defined as follows:

$$\begin{aligned} &\Pi_l(\bar{z},\bar{z}''^2) = \tfrac{1}{z_b - z_a} \\ &z_a = \bar{z} - \tfrac{l}{2} \\ &z_b = \bar{z} + \tfrac{l}{2} \\ &l = \sqrt{12\bar{z}''^2} \end{aligned} \tag{1.18}$$

$$\begin{aligned} &B_Z(\bar{z},\bar{z}''^2) = \frac{z^{a-1}(1-z)^{b-1}}{\int_0^1 z^{a-1}(1-z)^{b-1}dz} \\ &a = \bar{z}\left(\tfrac{\bar{z}(1-\bar{z})}{\bar{z}''^2} - 1\right) \\ &b = (1-\bar{z})\left(\tfrac{\bar{z}(1-\bar{z})}{\bar{z}''^2} - 1\right) \end{aligned} \tag{1.19}$$

The filtered mixture fraction is determined by the solution of the transport equations and its subgrid scale variance is usually modelled by algebraic models. If the FDF is known then all dependant variables can be computed; for instance, if chemistry is assumed to be infinitely fast then local equilibrium is reached and species mass fractions, reaction rate or temperature are functions of mixture fraction only. In this case, all the dependant variables (e.g. temperature) can be computed by employing, for instance the $\beta-$FDF or the top−hat FDF as follows:

$$\bar{T}(x,t) = \int_0^1 T(z) B_Z(\bar{z},\bar{z}''^2)dz \tag{1.20}$$

$$\bar{T}(x,t) = \int_0^1 T(z) \Pi_l(\bar{z},\bar{z}''^2)dz \tag{1.21}$$

The concept of the FDF can be extended to finite−rate chemistry as well. In this case the FDF is a joint FDF of mixture fraction and its scalar dissipation rate. It is a common practice to write the joint FDF as a product of individual FDFs (assuming statistical independence). More detailed information on scalar dissipation rate modelling will be given in the corresponding chapter (Chapter 4).

Since the FDF concept plays an important role in LES context it is necessary to emphasize the meaning of the FDF in this context. Mixture fraction concept used in the LES allows computation of all the dependant variables, such as for example density, viscosity etc. only if the FDF of mixture fraction field z is known. Generally, the FDF can be computed from any subfilter scalar variable that is obtained, e.g. from experiments as

follows. At given spatial location the box filter of known size is applied and the scalar values, e.g. of mixture fraction are extracted and distributed into 10−15 bins, which then can easily be converted into the FDF, by counting frequencies and dividing them by a corresponding bin width multiplied with the total number of samples. The filtered density function of a scalar f and the SGS scalar variance are given according to the following formulas (Tong, 2001), where $\hat{\phi}$ is the sample space variable for ϕ.

$$f_{\phi}(\hat{\phi}; x, t) = \int \delta \left[\phi\left(x,t\right) - \hat{\phi}\right] G\left(x - x^{'}\right) dx \tag{1.22}$$

$$\bar{\phi}^{''2} = \int \left\{\phi(x) - \langle\phi\rangle_{L}\left(x\right)\right\}^{2} G(x - x^{'}) dx^{'} \tag{1.23}$$

The last and the most expensive approach in modelling both reacting and non−reacting flows is Direct Numerical Simulation (DNS). This approach does not require any modelling and explicitly resolves all turbulence scales and hence is the most accurate. Full instantaneous Navier−Stokes equations are solved on a very fine grid in order to capture the effect of the smallest flow structures. Potentially, the DNS can predict all variations of the temperature and the mixture fraction but this will require very powerful and high performance computers often embedded into a cluster. Therefore, this approach is still limited to simple flows, often to non−reacting flows with low Reynolds numbers. The grid requirements for DNS lay in the range of 50 to 100(μm), LES in the range of 0.5−1.5(mm), while RANS can be computed on 3−7(mm) grid. On the other hand the grid requirements are highly dependent on many factors, such as for example a type of simulation, modelling of reacting or non−reacting flows etc.

1.4 Experiment of evaluation of LES dynamics

Experimental investigation of the LES dynamics started relatively recently (Liu *et al.* 1994). Most of the experimental work was carried out to validate the so−called LES subgrid scale models, while filtered density functions and subgrid models for scalar variance have not yet received attention in swirling flows. It is especially important to emphasize that the FDF dynamics as well as SGS models for mixture fraction variance are important in swirling flows for two reasons. The first reason is the validation of computational codes, which are used to design GT combustors. The second reason is the fundamental understanding of the flow behaviour in swirling jets, which can be described with relation to LES computational technique, thus providing both, the physical basis and the experimental data.

Liu *et al.* (1994) used two−dimensional particle image velocimetry (PIV) to obtain two velocity components in a water jet. The fundamental properties of subgrid scale stresses were also studied experimentally using two−dimensional particle displacement velocity (PDV) techniques by Liu, Meneveau & Katz (1994) as well as by Bastiaans, Rindt & van Steenhoven (1998). The studies of resolvable and SGS dynamics Domaradzki *et al.* (1993) suggested that LES was relatively insensitive to the details of its SGS closure if the energy and flux containing eddies are well resolved. Subgrid scale dynamics was also extensively studied e.g Tong *et al.* (1998) with applications to atmospheric turbulence. The effects of

LES grid resolution on passive scalar mixing dynamics were studied both experimentally and theoretically by Frank *et al.*, (2010). Frank *et al.* (2010) used a set of LES simulations to investigate how LES filter size affected the LES scalar mixing as well as high−resolution laser Rayleigh scattering imaging to measure temperature. Temperature measurements were performed by using DLR−A fuel, which was a mixture of $CH_4/N_2/H_2$ that had the same Rayleigh scattering cross section (with the error of $\pm 3\%$) as the air.

Experimental investigation of the SGS mixing in non−reacting turbulent jets was done by e.g. Danhong (2005). Measurements were made in the fully developed region of an axisymmetric turbulent jet with a jet Reynolds number of 40000. Measurements were carried out by a set of three X−wires along with a resistance wire. The study revealed two limiting SGS mixing regimes. The first regime corresponded to the well−mixed regime with small SGS variance and small SGS kinetic energy. The second regime corresponded to non−equilibrium regime with large values of the SGS variance and the SGS kinetic energy. The observed SGS mixing process was quite different in those two regimes. In addition, reacting flow was also investigated in the work of Danhong (2005) in which the filtered mass density functions were experimentally investigated in the turbulent partially premixed methane/air flames. The SGS scalar variance showed similar trends to the non−reacting case. The conditionally filtered temperature near the stoichiometric mixture fraction decreased progressively with increasing SGS scalar variance. In addition, local extinction events appeared in the regions where SGS scalar variance was large. The results suggested that the mixture fraction field and the mixing regimes could potentially have strong influences on the combustion regime and extinction/reignition in turbulent non−premixed combustion Danhong (2005).

Investigation of SGS mixing of mixture fraction and temperature in turbulent partially premixed flames was done by Cai, Wang, *et al.* (2009). Experimental data was obtained in the piloted turbulent partially premixed methane flames. The measurements were performed by using combined line−imaging of Raman scattering, Rayleigh scattering and laser−induced CO fluorescence. Major chemical species were also measured along with temperature and radial component of the scalar dissipation rate. A one−dimensional filtering was employed contrary to LES filtering in three dimensions. It was pointed out that scalar filtered density function obtained with one−dimensional filters was similar to that obtained with two dimensional filters with a good approximation of three−dimensional filtering and with the errors of approximately 5% for the r.m.s. of the resolvable fluctuations and the SGS scalar variance Cai *et al.* (2009).

A highly sophisticated phenomenon, which involves chemical reactions, unsteady fluid motion at different time scales and the stochastic nature of turbulence, makes computational methods extremely complicated. Therefore, new experimental data should be gathered in order to fulfil a gap between computational modelling and real processes that occur in real systems. A study of the subgrid scale scalar mixing is therefore of paramount importance for developing new improved models for computational combustion as well as for providing new fundamental understanding of turbulent mixing, especially in swirling flows.

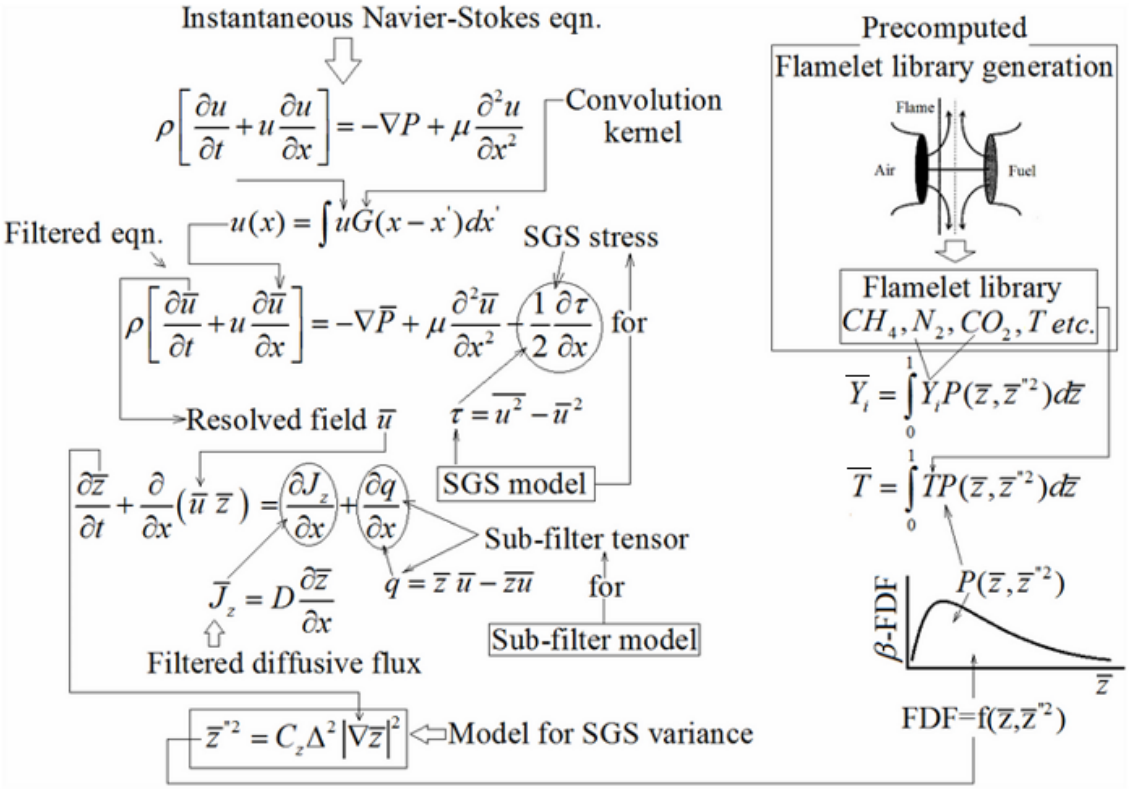

Figure 1.3: A schematic representation of Large Eddy Simulation computational procedure coupled with laminar flamelet model of reacting turbulent flows. The main principle behind flamelet approach is to separate the CFD solver and the detailed chemical calculations. Subgrid scale closure and sub−filter models are also shown.

1.5 Mixture fraction concept

The mixture fraction concept plays a central role in all non−premixed turbulent combustion models (Bilger, 1980). According to Bilger (1980), the fast−chemistry assumption states that the temperature and e.g. the species mass fraction are functions of a conserved scalar only. This assumption can simplify the solution to the reacting flow problems in the limit of fast chemistry. It should be noted that the fast chemistry assumption leads to over-prediction or underprediction of pollutant formation and other phenomena, such as for example extinction and reignition. This is the main reason why other concepts have been introduced in the field of combustion, e.g. conditional moment closure (CMC), flamelet PDF methods etc. Among them, the concept of scalar dissipation rate was used to couple non−equilibrium chemistry and turbulence. However, the concept of a conserved scalar or the mixture fraction is still a very useful method to simplify the solution of reacting problems. The mixture fraction definition is given according to Bilger (1976), as the ratio of mass of fluid having its origin in the fuel stream to the total mass of fluid, in two stream problems. The mixture fraction represents the mass fraction of the fuel stream in the mixture and measures the fuel/oxidizer ratio. The mixture fraction varies between zero and one, meaning that there is no fuel (0) and pure fuel (1). Therefore, the mixture fraction can be written as follows, where β is the oxidizer−fuel coupling function.

$$
\begin{aligned}
z &= \frac{\beta-\beta_{ox,0}}{\beta_{fuel,0}-\beta_{ox,0}} \\
\beta &= Y_{fuel} - Y_{ox}/S \\
S &= vMW_{ox}/MW_{fuel} \\
z &= \left\{ \begin{array}{l} 1.0 \text{ if } \beta = \beta_{fuel,0} \\ 0.0 \text{ if } \beta = \beta_{ox,0} \end{array} \right\}
\end{aligned}
\tag{1.24}
$$

1.6 Scalar dissipation rate

The dissipation rate requires modelling in essentially all computations of non−premixed combustion. The scalar dissipation rate can be used for instance in a PDF−flamelet approach in which species mass fraction and mean reaction rate are pre−computed and stored in a library as a function of two variables, namely mixture fraction and scalar dissipation rate. Peters (1983) identified the scalar dissipation rate as a characteristic diffusion time scale imposed by the mixing field. The scalar dissipation rate provides a measure of the maximum possible chemical reaction rates and hence is one of the main parameters that need to be computed. Therefore, the accurate measurements or modelling of the scalar dissipation rate is paramount in a wide range of turbulent flow applications. Experimental measurements of the scalar dissipation rate are challenging, because it involves measurements of either mixture fraction or temperature gradients or both, at smaller turbulent scales. Such measurements require small spatial resolution and high precision, which is not easily achieved in practice, due to different optical aberrations, imperfections and laser beam limitations. The key milestones in experimental investigation of the scalar dissipation rate is briefly introduced here for convenience in reverse chronological order.

Soulopoulos (2009) investigated a scalar mixing in starting turbulent jets experimentally by using planar laser−induced fluorescence of acetone. The signal−to−noise ratio was reported as 100 for the mixture fraction measurements and of the order of 10 for the scalar dissipation measurements. The jet Reynolds number was measured up to 11 nozzle diameters as was equal to 4500. A Wiener filter was applied to the raw mixture fraction data after which a computation of the scalar dissipation rate was performed within 30% accuracy. It was also pointed out that the profiles of the mean scalar dissipation conditional on mixture fraction had a complex shape that was also dependent on the position in the flow field. It was postulated that the assumption of statistical independence between the scalar and its dissipation rate had not held. Later statement was proven by the fact that the product of the individual probabilities of mixture fraction and its dissipation rate were different in shape from the joint probability of mixture fraction and the dissipation rate.

Markides & Mastorakos (2006) employed a planar laser−induced fluorescence of acetone in order to measure the scalar dissipation rate in a turbulent plume. A silica tube with an inner diameter of 33.96(mm) was used in the scalar dissipation measurements. Turbulence was generated by a grid with 3.0(mm) diameter holes. A mixture of diluted nitrogen with acetylene or hydrogen was used as the fuel. The coflow and the fuel bulk injection velocities were in the range of 3−7 and 3−27(m/s). The acetone seeder was immersed in a stirred, isothermal bath of hot water to ensure that the fuel stream was saturated with a steady concentration of acetone. A Nd:YAG solid state laser at the 266(nm) with measured power of 80(mJ/pulse) was used in the work. A laser beam was expanded into

a sheet of height 60(mm) by using cylindrical and spherical lenses. The laser beam waist was found to be 0.10±0.03(mm) at 1/e2 intensity. A LaVision© intensified CCD camera equipped with 13(mm) extension tube and a Nikkor AF lens f2.8 was used. The image area after cropping was defined to be 1280×480 pixels with spatial nominal resolution of 0.050−0.055(mm/pixel). It was found that the mean and variance of the normalized conserved scalar were not strongly dependent on the level of denoising techniques, while the scalar dissipation rate was affected by different methods of denoising. It was also suggested that in order to be able to represent the scalar dissipation rate accurately, a careful data processing method should be chosen. It was also pointed out that the mean three−dimensional scalar dissipation rate, measured along the centreline, was related to the mixture fraction variance and the local turbulent kinetic energy.

Bilger (2004) stated that the scalar dissipation rate was linked to the instantaneous rate of chemical reaction per unit volume and under the assumption of fast chemistry, via the following relationship, where the function $a_i(z)$ is determined by the chemistry and hence is different for different fuels.

$$\begin{aligned} \omega_i &= \rho a_i(z)\chi \\ \chi &\equiv D\nabla z \nabla z \end{aligned} \tag{1.25}$$

Bilger (2004) also mentioned briefly that significant research had been carried out, especially in flows with mixing scalars that were passive (the scalar has no effect on turbulence dynamic). It was also pointed out that the conditional average scalar dissipation was not a simple function of the mixture fraction but was also a function of the nature of the flow field. An experimental data that was obtained, following the simplest relationship between the measured mixture fraction field and the computed scalar dissipation rate, possesses little value if the dissipation rate measurements were not validated according to conservation laws. Therefore, it is quite apparent that different denoising techniques can contribute to the uncertainties of scalar dissipation measurements. Direct measurements of scalar dissipation rate are difficult as all three components of the scalar dissipation must be measured accurately. Bilger (2004) stated that 'Many of the measurements in the literature are of doubtful quality, as they have questionable spatial resolution and have not been validated by reference to the constrains arising from the conservation laws.' According to Bilger, a conservation equation of the mixture fraction that can be used to validate the accuracy of the measurements can be written as follows:

$$\rho\frac{\partial z}{\partial t} + \rho U \cdot \nabla z - \nabla \cdot (\rho D \nabla z) = 0 \tag{1.26}$$

Using decomposition to mean (time averaged) and fluctuating components for the velocity and mixture fraction $z \equiv \bar{z} + z^{'}; U \equiv \bar{U} + u$ and after some manipulations the equation yields to.

$$\frac{\partial \rho\left(\bar{z}^2 + z'^2\right)}{\partial t} + \nabla \cdot \left(\bar{\rho}\bar{U}\left(\bar{z}^2 + \overline{z^2}\right) + 2\bar{\rho}\bar{z}\overline{uz'} + \bar{\rho}\overline{uz'^2}\right) + 2\bar{\rho}\bar{\chi} - \nabla\left(\bar{\rho}\overline{D\nabla z^2}\right) = 0 \tag{1.27}$$

For stationary flows and with the use of the flux divergence theorem it yields to the

following equation, where x is the coordinate in the streamwise direction, U and u are the mean and fluctuating velocity component in the same direction and A is the area normal to this direction.

$$\frac{d}{dx}\int_A \left(\bar{\rho}\bar{U}\left(\bar{z}^2+\overline{z'^2}\right)+2\bar{\rho}\bar{z}\overline{uz'}+\bar{\rho}\overline{uz'^2}-\bar{\rho}D\nabla z^2\right)dA+2\int_A \bar{\rho}\bar{\chi}dA=0 \tag{1.28}$$

The above−mentioned equation is exact and does not rely on any assumptions about the turbulence modelling and therefore can be used to evaluate scalar dissipation measurements. On the other hand in order to employ this equation velocity fields must be known, which in some cases are unavailable.

Wyngaard (1971) pointed out that the spatial resolution requirements for flows with Schmidt[11] number greater than one should be at least smaller than about twice the Batchelor[12] scale. The Batchelor scale is proportional to the Kolmogorov length scale and defined according to the following relationship.

$$\lambda_B = \eta Sc^{-1/2} \tag{1.29}$$

If, for example, the Kolmogorov scale is 150(μm) and taking the Schmidt number as 1.22 the Batchelor scale is computed as 136(μm) and hence the minimum resolution should not be less than 0.272(mm). This resolution is not easily achievable and could be a problem if the laser sheet thickness is larger than 0.272 (mm). In addition, the nominal resolution of an optical system may be, e.g. 40(μm), which is not the actual resolution. The actual resolution depends on the modulation transfer function (detailed description is given in Chapter 6.6.2) and in some cases could be larger than minimum requirements for the scalar dissipation measurements. In swirling flows, the Batchelor scale might be smaller than 0.272(mm) due to the fact that Kolmogorov scale decreases as swirl number (Eq. 1.32) increases. In fact, swirling flows that are in the range of turbulent Reynolds number of 20000−50000, the laser sheet thickens should not be greater than 0.15(mm).

Wang *et al.* (2005) used Rayleigh thermometry to study the temperature fluctuations, power spectra and thermal dissipation rates of a non−premixed turbulent jet flame at a Reynolds number of 15200. The experimental investigation was carried out in a weakly coflowing jet flame. The coflow velocity was 0.45(m/s) and the flow was filtered in order to remove particles larger than 0.2(μm). The fuel, a mixture of 22.1% CH_4, 33.2% H_2 and 44.7% N_2 (by volume), was injected via a long tube with inside diameter of 7.75(mm). The Rayleigh scattering cross section of this fuel has been shown to vary by ±3% across the whole flame. The light source was a Nd:YAG solid state laser operated at 71(W) average power, 532(nm) wavelength and 10(Hz) repetition rate. The laser beam was focused into the test section by a 300(mm) focal length lens and was corrected to the variations in laser pulse energy on a shot−to−shot basis. The measured beam waist was 0.3(mm). An optical system used in this experiment was designed with ZEMAX© and produced an

[11] Ernst Heinrich Wilhelm Schmidt (1892−1975) was German engineer. Sc =ν/D, where ν is kinematic viscosity and D is mass diffusivity (m2/s).

[12] George Keith Batchelor FRS (1920−2000) was an Australian applied mathematician and fluid dynamicist. He was for many years the Professor of Applied Mathematics in the University of Cambridge (http://en.wikipedia.org).

aberration limited blur−spot of less than 34(μm). The working f−number was 2.4 with magnification of 0.685. The turbulent Reynolds numbers were computed to be in the range of 2090−2350, depending on a position in the flow. The Batchelor scale was computed to be in the range of 0.32−0.58(mm) The temperature power spectrum along the jet centreline, computed from experimental data, showed a small inertial sub−range, which was explained by the low local Reynolds number. However larger inertial sub−range was found at off−centreline positions. Bilger (2004) mentioned that the probability density function of the fluctuations of the scalar dissipation rate was close to log normal, while Wang *et al.* (2005) pointed out that the p.d.fs. of the thermal dissipation rate were found to deviate from log−normality in the low−dissipation portion of the distribution when only one component of the gradient was used.

Kyritsis *et al.* (2002) reported quantitative scalar dissipation rate measurements in vortex perturbed counterflow diffusion flames, using Raman line imaging technique. A horizontal, gaseous counterflow diffusion flame was established between two vertical nozzles. The diameter of the nozzles and the distance between nozzles were 12.7 and 13.5(mm) correspondently. The bulk velocities were in the range 0.63−0.80(m/s) in the oxidizer and 0.62−0.90(m/s) in the fuel nozzles. The source of fuel was methanol (CH_3OH). The flame was perturbed at a frequency of 10(Hz) by loudspeakers. A Nd:YAG solid state laser at 532(nm) with energy of 100(mJ/pulse) was used. The laser waist was claimed to be 0.2(mm). It was generally found that for given composition of the counterflow streams extinction occurred at a definite stoichiometric value, irrespective of the mode of perturbations. It was also observed that vortex−perturbed flames can sustain an almost double strain rate at extinction than steadily strained flames. The maximum error in the measurements of scalar dissipation rate was reported as 15%.

Mason *et al.* (2002) investigated the effects of unsteady scalar dissipation rate on ignition of non−premixed hydrogen/air mixtures in counterflow numerically. It was observed that ignition limits were sensitive to the changes in scalar dissipation rate. A new ignition criterion based on the instantaneous Damkohler number was also proposed. Mastorakos *et al.* (1992) analysed governing equations for an axisymetric turbulent isothermal opposed jet with the purpose of facilitating estimates of the scalar dissipation rate in turbulent counterflow non−premixed flames. The main motivation for this work was the lack of experimental data for the mixture fraction fluctuations in the turbulent counterflow geometries. The governing equations were formulated for the mean mixture fraction, its fluctuations and a constant density along the centreline of the stagnation flow geometry. Results showed that the maximum values of the scalar dissipation rate were found to be across the mixing layer. The estimated scalar dissipation rate at extinction was found to be constant to within about 7% and was reported as 2.3, 6.8 and 17.4(1/s) for different premixing ratios (0, 0.5 and 0.8 air volume fractions in fuel stream). This numerical work confirmed the theory initially proposed by Peters & Williams (1983) that extinction occurred at a critical value of the mean scalar dissipation rate. It was pointed out that partial premixing of the fuel stream with air and at the same time partial premixing of the air stream with fuel, in order to keep the stoichiometric mixture fraction and the flame axial position constant, is different from the partial premixing of only fuel or air streams.

Sutton &Driscoll (2002) proposed a new method to image the scalar dissipation rate

by using nitric oxide (NO) as a tracer, instead more traditional tracer, which had been acetone for many years. Sutton &Driscoll combined planar laser−induced fluorescence of NO with temperature imaging by a Rayleigh scattering and reported greatly improved signal−to−noise ratios and spatial resolution. It was pointed out that this method had three advantages over traditional method with acetone as a tracer. Since the diffusivity of nitric oxide is equivalent to that of the methane/nitrogen fuel mixture, the differential diffusion problems could be avoided. Nitric oxide can be added in large amounts to achieve higher values of the signal−to−noise ratio. It was also mentioned that NO was an excellent marker of the fuel, because it would properly disappear from the centreline to the flame boundaries due to rapid reactions with free radicals. A laminar and a turbulent jet flames, produced by a pipe of 4.55(mm) diameter, surrounded by 33×33(cm) coflow of low speed air, were studied. The laminar and the turbulent flames had the Reynolds numbers of 1800 and 7700 correspondently. The jet fuel consisted of 40% CH_4, 45% N_2 and 5% H_2 for the laminar flame, while for the turbulent flame the fuel mixture was 40%N_2, 5%H_2 and 10% NO. A light source was a 226(nm) UV laser beam created by frequency doubling the 452(nm) output from an Nd:YAG−pumped dye laser. The fluorescence light was collected by an intensified CCD camera coupled with a Nikon UV f4.5 lens and a 3(mm) Schottglass UG−5 filter. The Rayleigh scattering temperature measurements were made with a 355(nm) laser operated at 300(mJ/pulse) and both the 266(nm) and 355(nm) beams were monitored with a photodiode to account for variations in laser sheet energy. Sutton & Driscoll reported measurements of the maximum scalar dissipation rates in the laminar flame. A maximum scalar dissipation rate of 15.5(1/s) was measured in the laminar flame and was located on the rich side of the stoichiometric contour. The maximum measured scalar dissipation rate in the turbulent flame was not given.

Effelsberg *et al.* (1988) employed laser Rayleigh scattering and laser Doppler measurement techniques to investigate the scalar dissipation rate in the stabilization region of a lifted propane air diffusion flame (Re=7500, 10000). The laser Doppler technique was used to obtain the mean flow field while the Rayleigh scattering techniques was employed to obtain the mixture fraction and its spatial gradients. The experiments were performed in turbulent jets and jet flames of propane (Re=7500) with an internal diameter of 3(mm). The coflow of air was set at 0.1(m/s) axial velocity and both the air and the fuel were filtered for the Rayleigh scattering measurements. A 5(W) Argon−Ion laser at 488(nm) wavelength was used. The laser beam waist was estimated to be less than 0.3(mm). The velocity measurements were performed with a two−colour LDV system so that the mean velocity and fluctuating components were measured. The error introduced by the use of Taylor's hypothesis was estimated to be of the order of 10%. Statistical independence between mixture fraction and scalar dissipation rate was also used for the sake of simplicity. It was found that an assumption of log−normality distribution of the scalar dissipation rate seemed to be an acceptable approximation. It was shown that the parameter, describing the variance of the log−normal distribution could be assumed to be a constant and close to unity.

Diblle *et al.* (1984) presented the first laser−based measurements of scalar dissipation in turbulent non−premixed, non−reacting jets and the first laser−based or otherwise in reacting jet flames by using an optical multichannel analyser. Two jets were investigated;

a non−reacting propane jet and a reacting jet mixture of hydrogen and argon (22% argon in hydrogen by volume). A forced−draft vertical wind tunnel with an axisymetric fuel jet (inside diameter of 0.526cm), located at the upstream end of a 30−cm−square test section was used. A constant coflow of air at 8.5(m/s) velocity was used in both cases. The jet bulk velocity was 108(m/s) (Re=134000) for propane and was 71(m/s, Re = 9100) for the argon in hydrogen mixture. A dye laser rated at a 500(mJ/pulse), repetition rate of 1(Hz), wavelength of 514.5(nm) and a pulswidth of 21(μs) was focused to a 500(μm) diameter line. The Rayleigh scattered light was collected at an angle of 90 degrees to the incident beam and imaged onto a 500−channel optical multichannel analyser. The effective resolution along the laser beam was defined as 0.34(mm). A local isotropy was assumed that is each component of the scalar dissipation was equal. The experimental data was compared with a second−order closure numerical model, the effects of density fluctuations on the scalar dissipation were analysed and also compared with experimental results.

In modelling turbulent reacting flows the conditional statistics are also required, which in turn requires measurements of conditional probability density functions with higher precision than the unconditional statistics Bilger (1993). The scalar and thermal dissipation rate, like other variables in turbulent flows, fluctuate in time and space and the formal definition is given by the following formulas. In some cases, the formula is occasionally multiplied by a coefficient of 2.

$$\chi_z = D\left[\left(\frac{\partial z}{\partial x}\right)^2 + \left(\frac{\partial z}{\partial y}\right)^2 + \left(\frac{\partial z}{\partial z}\right)^2\right] \tag{1.30}$$

$$\chi_T = D\left[\left(\frac{\partial T}{\partial x}\right)^2 + \left(\frac{\partial T}{\partial y}\right)^2 + \left(\frac{\partial T}{\partial z}\right)^2\right] \tag{1.31}$$

1.7 Overview of swirling flows

Flows with swirling velocity components are common in nature and in industrial applications. In industrial applications the swirling flows are typically found in the combustion chambers, heat exchangers, internal combustion engines, separators etc. This type of flow is generally well understood and many research papers have been published in this field. Higher level of turbulence may be achieved in swirling flows, which in turn enhances mixing. Besides, the swirling flows are used to stabilize and anchor the flame in the combustion systems and hence the combustion process can be controlled. Axial, radial and tangential velocity components create corresponding pressure gradients and a region of low pressure is generated within the central core of the swirling jet. At a certain degree of swirl the momentum of rotating fluid cannot longer overcome the pressure gradient, created by the swirling components, leading to flow reversal and vortex breakdown. This flow reversal zone, which is called a recirculation zone, is the primary source of the flame stabilization, due to recirculation of hot gases (burnt products), mixing with the fresh reactants and subsequent ignition. The central flow zone experiencing solid body rotation is typically defined as the vortex core. According to Gupta *et al.* (1984), the swirling flow can be seen as a combination of a free vortex, in which the tangential velocity W is

inversely proportional to the radius and a forced vortex in which the tangential velocity is proportional to the radius. A commonly used parameter that describes the swirling flows is the swirl number, which is defined as the ratio of the axial flux of angular momentum to the axial flux of axial momentum multiplied with the equivalent exit radius (Gupta *et al.* 1984).

$$S = \frac{2G_\Theta}{G_Z D} \tag{1.32}$$

This definition in some cases is not straightforward, because the velocity profiles are not constant and are dependent on downstream axial locations. The axial fluxes can be determined as (Milosavljevic 1993).

$$G_\Theta = 2\pi\rho \int_{r=r_i}^{R} UW_r r dr \tag{1.33}$$

$$G_z = 2\pi \int_{r=r_i}^{R} \left(\rho U^2 + p\right) r dr => G_z = 2\pi\rho \int_{r=r_i}^{R} UU r dr \tag{1.34}$$

An alternative definition of the swirl number can be used if the geometry of the swirling device is known. The swirl number in this case is named the theoretical or geometric swirl number S_g and is defined as follows (Gupta *et al.* 1984):

$$S_g = \frac{2}{3} \frac{\left[-\left(D_i - D_o\right)^3\right]}{\left[-\left(D_i - D_o\right)^2\right]} \tan\gamma \tag{1.35}$$

The equations that describe the flow motion are usually written in polar coordinates as follows. The velocity vector is decomposed into its three cylindrical components (u, v, w), namely axial, radial, and azimuthal components (swirling component). The continuity equation and a set of Navier−Stokes equations become as.

$$\frac{1}{r}\frac{\partial}{\partial r}(rw) + \frac{1}{r}\frac{\partial v}{\partial \phi} + \frac{\partial u}{\partial x} = 0 \tag{1.36}$$

$$\frac{\partial w}{\partial t} + w\frac{\partial w}{\partial r} + \frac{v}{r}\frac{\partial w}{\partial \phi} + u\frac{\partial w}{\partial x} - \frac{v^2}{r} = -\frac{1}{\rho}\frac{\partial p}{\partial r} + \upsilon\left(\nabla^2 w - \frac{w}{r^2} - \frac{2}{r^2}\frac{\partial v}{\partial \phi}\right) \tag{1.37}$$

$$\frac{\partial v}{\partial t} + w\frac{\partial v}{\partial r} + \frac{v}{r}\frac{\partial v}{\partial \phi} + u\frac{\partial v}{\partial x} + \frac{wv}{r} = -\frac{1}{\rho r}\frac{\partial p}{\partial \phi} + \upsilon\left(\nabla^2 v - \frac{v}{r^2} - \frac{2}{r^2}\frac{\partial w}{\partial \phi}\right) \tag{1.38}$$

$$\frac{\partial u}{\partial t} + w\frac{\partial u}{\partial r} + \frac{v}{r}\frac{\partial u}{\partial \phi} + u\frac{\partial u}{\partial x} = -\frac{1}{\rho}\frac{\partial p}{\partial x} + \upsilon\nabla^2 u \tag{1.39}$$

$$\nabla^2 = \frac{1}{r}\frac{\partial}{\partial r}\left(r\frac{\partial}{\partial r}\right) + \frac{1}{r^2}\frac{\partial^2}{\partial \phi^2} + \frac{\partial^2}{\partial x^2} \tag{1.40}$$

The equation above describes instantaneous flow field and typically cannot be solved. If the Reynolds decomposition (mean or time independent and fluctuating parts or time dependent) is introduced then the following equations, assuming a steady and axisymmetric mean flow, will describe the time−averaged flow field in polar coordinates.

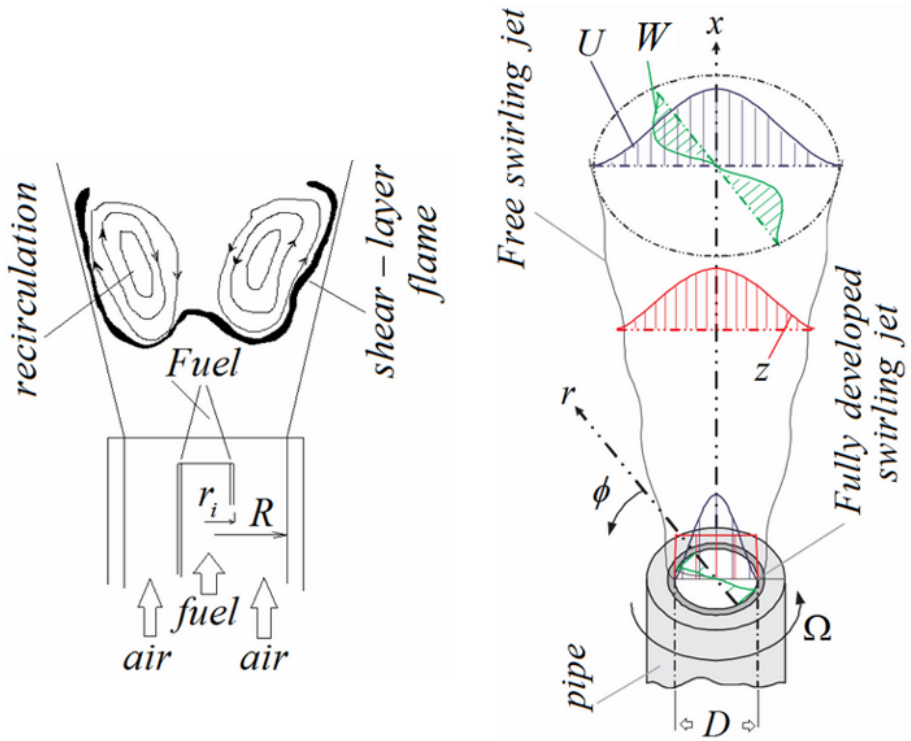

Figure 1.4: Schematic of the flame provided by swirling flow (left) and the cylindrical coordinate system of the free developing swirling jet (right). Profile of passive scalar is denoted as z (adapted from Orlu, 2006).

$$\begin{aligned} u &= U + u' \\ v &= V + v' \\ w &= W + w' \\ p &= P + p' \end{aligned} \tag{1.41}$$

$$\frac{\partial}{\partial t} = 0, \frac{\partial}{\partial \phi} = 0 \tag{1.42}$$

$$W\frac{\partial W}{\partial r} + U\frac{\partial W}{\partial x} + \frac{\partial \overline{w'^2}}{\partial r} + \frac{\partial \overline{u'w'}}{\partial x} - \frac{1}{r}\left(V^2 + \overline{v'^2} - \overline{w'^2}\right) = -\frac{1}{\rho}\frac{\partial P}{\partial r} + \upsilon\left(\nabla^2 W - \frac{W}{r^2}\right) \tag{1.43}$$

$$W\frac{\partial V}{\partial r} + U\frac{\partial V}{\partial x} + \frac{VW}{r} + \frac{\partial \overline{u'w'}}{\partial x} + \frac{1}{r^2}\frac{\partial}{\partial r}\left(r^2\overline{v'w'}\right) = \upsilon\left(\nabla^2 V - \frac{V}{r^2}\right) \tag{1.44}$$

$$W\frac{\partial U}{\partial r} + U\frac{\partial U}{\partial x} + \frac{\partial \overline{u'^2}}{\partial x} + \frac{1}{r}\frac{\partial\left(r\overline{u'w'}\right)}{\partial r} = -\frac{1}{\rho}\frac{\partial P}{\partial x} + \upsilon\nabla^2 U \tag{1.45}$$

The transport equation for the passive scalar, e.g. mixture fraction (z), can be written as follows:

$$\frac{\partial z}{\partial t} + w\frac{\partial z}{\partial r} + \frac{v}{r}\frac{\partial z}{\partial \phi} + u\frac{\partial z}{\partial x} = D\nabla^2 z \tag{1.46}$$

By applying the Reynolds decomposition, the transport equation (time-averaged) for

the passive scalar is written as follows:

$$W\frac{\partial \bar{z}}{\partial r} + U\frac{\partial \bar{z}}{\partial x} + \frac{\partial \overline{uz}}{\partial x} + \frac{1}{r}\frac{\partial \left(r\overline{wz}\right)}{\partial r} = D\nabla^2 \bar{z} \tag{1.47}$$

If the passive scalar is chosen to be the temperature, then the diffusivity D in the equation above is replaced with the thermal diffusivity α. It should be noted that the equations above are written for constant density flows, which means that the temperature fluctuations must be small enough so that the flow field is not affected and the density is indeed constant. The equation for the mixture fraction is valid for any other passive scalars, e.g. pollutants, small particles, smoke, ink etc. The mixture fraction or temperature is replaced with concentration (mixture fraction is in fact normalised concentration) and appropriate mass diffusivity is used. The form of the equation is similar regardless the nature of the passive scalar.

All swirling flows can generally be split into two groups i.e. weak ($S < 0.6$) and strong ($S > 0.6$) swirling flows. From the survey of experimental studies of swirling flows a qualitative picture can be drawn. For low swirl numbers $S < 0.5$, the flow patterns demonstrate so−called a 'solid body' rotation, which is initially observed at S≈0.1. For high swirl number S>0.5, flow develops a structure with rapidly rotating core, which is surrounded by annulus of low vorticity. A flow reversal is observed in the central region of the swirling flow Steenbergen (1995). In this work, both weak and strong swirling flows are studied with the maximum swirl number of 1.07. Even though, weak swirling flows have limited industrial applicability it is necessary to investigate such regimes and compare with highly swirled flows, especially when statistics of the scalar dissipation is considered. In addition to 'scalar dissipation−related' issues, the effect of the vortex breakdown is still not well understood and requires careful attention. Unfortunately, it is impossible to describe all the characteristics of the swirling flows in this work. Fortunately, the detailed description of the characteristics of the swirling flows and associated effects, such as vortex breakdown phenomenon and flame stabilization can be found in e.g. Bulat[13] (2012), Orlu[14] (2006), Huang[15] (2008), Moene[16] (2003). A list of selected experiments in swirling flows is summarised and presented in Table 1.1.

1.8 Motivation and objectives

The motivation of the present work originates from combustion in gas turbine and jet engines with emphasis on the reduction of nitrogen oxides from current and prospective combustion systems. The present work also aims to provide experimental data, which can be used in validation of existing and prospective combustion models. Despite considerable research, the scalar dissipation statistics are virtually not available in both reacting and non−reacting swirling flows. Understanding of scalar mixing in non−reacting flows and

[13] G. Bulat. Large Eddy Simulations of Reacting Swirling Flows in an Industrial Burner (PhD thesis). Department of Mechanical Engineering Imperial College London, UK, 2012.

[14] R. Orlu. Experimental study of passive scalar mixing in swirling jet flows. Technical Reports from Royal Institute of Technology KTH Mechanics, Stockholm, Sweden, 2006.

[15] Y. Huang. Combustion dynamics of swirl-stabilized lean premixed flames in an acoustically-driven environment (PhD thesis). University of Iowa, 2008.

[16] A.F. Moene. Swirling pipe flow with axial strain Experiment and Large Eddy Simulation (PhD thesis). Technische Universiteit Eindhoven, 2003.

temperature measurements (both mean and fluctuations) in non−reacting and reacting flows is considered to be one of many problems that need to be addressed. This work presents experimental studies of the scalar mixing and combustion in non−reacting and reacting swirling flows with a variable degree of swirl at a constant Reynolds number of 29,000 based on the area−averaged velocity of 8.46(m/s) at the exit and the diameter of 50.8(mm).

Therefore, the intention of this work is to capture sufficient experimental details in both non−reacting and reacting flows in order to understand the interaction between turbulence and, to some extent, chemistry. This work presents benchmark for the numerical study and numerical evaluation of present combustion models that are based on statistical approach. The data gathered in this work can also assist the evaluation of the laminar flamelet concept coupled with presumed filtered density functions scalar dissipation rate models and provides further insight into combustion processes in swirling flows. An important contribution is the evaluation of the SGS models for mixture fraction variance as well as presumed FDFs models for LES the experimental study.

1.9 Description of the thesis

A swirling unconfined coaxial jet at constant and uniform temperature (non−reacting case) and a swirl−stabilized flame (reacting case) at a Reynolds number of 29,000 are examined. The idea behind this experiment is to conceptually imitate the mixing and combustion process in swirl−stabilized gas turbine engine−like burners. The large scale mixing and the small scale mixing (scalar and thermal dissipation) will be analysed as a function of spatial locations in the flow and degree of mixing, which is quantified by the swirl number. Both large, $S > 0.6$, and weak, $S < 0.6$, swirl numbers will be studied. It should be mentioned that apart from conceptual similarities, extrapolations to practical swirl−stabilized combustors should not be made. The thesis is split into several chapters and structured as follows:

Chapter 2 provides the detailed description of the flow arrangement and the experimental conditions. Description and characteristics of the optical setup are given. The length scales of the flow are presented and discussed. The experimental techniques, used in this work are also discussed in details.

Chapter 3 outlines a procedure for de-noising the experimental data obtained from non−reacting jets, which is based on a Wiener−Kolmogorov filtering theory. A detailed description of the image processing including measurements of the Modulation Transfer Function and its effects on the results are presented. This chapter also describes a procedure for denoising the experimental data obtained from reacting measurements. The procedure for denoising thermal dissipation images was based on a Wiener wavelet−based filter.

Chapter 4 describes the mixture fraction fields obtained from PLIF experiments. Instantaneous and mean contours of the mixture fraction are presented.The scalar dissipation rate is also presented, both in terms of two−dimensional fields (instantaneous and mean) and in terms of probability density functions. Statistical assumption between the scalar and its dissipation is also assessed and discussed.

Chapter 5 focuses on turbulence−chemistry interaction relevant to the LES method, as the most promising approach for computing reacting flows. Presumed Filtered Density Functions (FDF) are studied both experimentally and theoretically by using experimental data from isothermal non−reacting swirling flows with different degree of swirl. The filtered density functions are measured at different locations in the flow and are reported as a function of subgrid scale variance (SGS) and the 'LES'[17] filter size. The SGS variance was also measured and investigated numerically by using two common models; a gradient assumption and a scale similarity model.

Chapter 6 presents temperature and thermal dissipation measurements in a non−premixed turbulent swirling jet flame. Rayleigh thermometry was used to study the temperature fluctuations, power spectra and the thermal dissipation rate.

Chapter 7 reviews the occurrence of an internal recirculation zone (IRZ) and completes a set of measurements on the swirl−stabilized burner. This chapter presents velocity measurements in swirl−stabilized combustor by using a particle image velocimetry (PIV).

Chapter 8 ends with the summary of the main conclusions.

[17] This is referred to spatial filtering of acquired images with a box filter of size Δ.

Table 1.1: Selected experiments in swirling flows.

Author	Swirl generator	Exp. technique	Re $*10^3$	S	x/D	Reported
Present work	tang. injection with split streams for varying S	2D−PLIF, 2D−RS	28.6	0.3;0.5;1.07	Up to 3	images of scalar mixing, scalar dissipation, conditional and unconditional statistics
Facciolo (2006)	rotating pipe	XW, 2D−LDV, 2D−PIV	12−33.5	0−0.5	0−8	U, V, W, statistics
Orlu (2006)	rotating pipe	XW−CW	24	0−0.5	0−6	U, V, W, statistics
Toh *et al.* (2005)	tang. injection	PIV, PLIF	3.9	0.06−0.15	0−5.8	images
Gilchrist and Naughton (2005)	tang. injection	IP	100	0−0.23	0−20	U, V
Oljaca *et al.* (1998)	rotating paddle	XW, US	10	0−0.24	0.25−3	U, V
Feyedelem and Sarpkaya (1998)	tang. injection	3D−LDV	18	0−0.52	0.14−32	U, V, W, statistics
Park and Shin (1993)	Swirl burner	SV	13−20.5	0−1.87	0−5	images
Milosavljevic (1993)	tang. injection swirl burner (coal, gas and kerosene fired)	LDA, PP	29	0.3;0.5;1.07	Up to 1.9	U, V, major species concentration, blow-out limits
Mehta *et al.* (1991)	rotating honeycomb	XW	n/a	0−0.2	0−2.31	U, V, blow-out limits
Farokhi *et al.* (1989)	tang. nozzles	IP, SW	375	0.48	0−6	U, V, W, P
Elsner and Kurzak (1989)	passive vanes	XW, CW, SW	80	0−0.42	1−15	U, V, W, statistics, fluxes
Samet and Einav (1988)	tang. injection	IP	n/a	0−0.49	2−20	U, V

CW−Cold−wire, XW−Hot−wire, SW−Single hot−wire,IP−Impact probe, PIV−Particle image velocimetry, PLIF−Planar laser induced fluorescence, LDV−Laser Doppler velocimetry, PP−Pitot probe, US−Ultrasound scattering, SV−Schlieren visualization, RS−Rayleigh scattering

2 Experimental setup

> A theory is something nobody believes, except the person who made it. An experiment is something everybody believes, except the person who made it.
>
> Albert Einstein

In gas turbine combustion chambers flame is anchored and stabilized by a region of flow recirculation, which acts as an ignition source to the fresh reactants. The recirculation zone is often initiated by the introduction of swirling motion to the inlet air stream. This can be done for instance by using a swirler, i.e. a device that creates circular motion of air passing through it. The swirling motion is highly likely to influence the temperature patterns and the formation of pollutants within a combustion chamber. There is much current interest in the development and the design procedure for practical combustion devices, especially low$-NO_x$ systems, which are typically based on swirl-stabilized combustors. As pointed out earlier, a possible approach to low$-NO_x$ combustion was the flameless combustion that is based on flue gas recirculation. Flue gas recirculation within a combustor can be created, e.g. by using a strong swirling flow, and hence understanding of mixing process, especially at small scales is vitally important, because the combustion takes place after molecular mixing, i.e. at the small scales. Despite the importance of aerodynamics and mixing processes at small scales on practical aspects such as for instance emission levels, there is still no sufficient information on mixing processes at small scales in swirl$-$stabilized burners, to the best of my knowledge. This chapter is aimed to give an overview of an experimental setup that was based on a swirl$-$stabilised atmospheric burner.

2.1 Flow configuration

The experimental setup consisted of an atmospheric burner operated with a mixture of $CH_4/H_2/N_2$ (sometimes known as the DLR[1] fuel) during experiments in reacting flows and with air seeded with acetone vapour during non$-$reacting measurements. A built$-$in swirl generator was used to obtain swirling flow with different degree of mixing, i.e. with different swirl numbers. The axial direction, parallel to the flow propagation was denoted as y and the radial direction, perpendicular to the jet propagation, as x (Fig. 2.3). Note that y and x correspond to x and r in polar coordinate system.

[1] Deutsches Zentrum fur Luft$-$und Raumfahrt is the German Aerospace Centre, abbreviated DLR and is the national centre for aerospace, energy and transportation research of the Federal Republic of Germany.

Table 2.1: Operating conditions (reacting).

S	V_a l/min	V_s l/min	V_f l/min	V_{CH_4} l/min	V_{H_2} l/min	V_{N_2} l/min	u_f m/s	u_a m/s	Re_a	Re_f
1.07	150	750	65.63	14.50	21.79	29.34	6.19	8.46	28662	2134
0.58	350	550	65.63	14.50	21.79	29.34	6.19	8.46	28662	2134
0.30	500	400	65.63	14.50	21.79	29.34	6.19	8.46	28662	2134

Note: Mixture of 22.1%CH_4, 33.2%H_2, and 44.7% N_2 is denoted as the DLR fuel.

Table 2.2: Operating conditions (non−reacting).

S	V_a l/min	V_s l/min	V_f l/min	u_f m/s	u_a m/s	Re_a	Re_f
1.07	150	750	40	3.77	8.46	28662	3770
0.58	350	550	40	3.77	8.46	28662	3770
0.30	500	400	40	3.77	8.46	28662	3770

Note: V_f, u_f, Re_f correspond to air flow through the acetone seeder.

2.2 Atmospheric burner

The burner used in this study (Figs. 2.1, 2.2 and item 15 in Fig. 2.13) was designed in such a manner that it was able to produce flow with different characteristics, was based on the design of Dixon *et al.* (1983) and replicated in the work of Milosavljevic (1993). This burner was capable of burning a mixture of pure gaseous fuel and produce flows with different degrees of swirl. The burner consisted of two cylindrical bodies for the swirl and axial air flow with a central fuel pipe. The flow of a mixture of $CH_4/N_2/H_2$ in Rayleigh thermometry or acetone vapour in PLIF was injected through an axial nozzle (Fig. 2.2), consisted of a pipe of 15(mm) internal diameter D_f, 0.75(m) long and centred within the surrounding circular duct by three locking screws at 25(mm) upstream end of the burner tube. The combustion air was passed through the outer 50.8(mm) internal diameter pipe D, concentric with the fuel nozzle and the airflow developed within this annulus for 264(mm). The swirl number varied by dividing the air supply into two streams namely axial and swirl. The swirling stream, referred to as 'swirl air', was introduced tangentially from four entries located symmetrically around the upper drum. The unswerled stream, referred to as 'axial air', was introduced from four entries located also symmetrically and below the tangential entries. The tangential components were generated by a swirl generator, which consisted of six tangential slots milled into the wall of the pipe (Fig. 2.2). The swirl numbers covered the range investigated by Hagiwara *et al.* (1984) and reported by Dixon (1983) namely 0 to 1.07. The swirl number of the secondary air was calculated in the work of Milosavljevic (1993) from the LDV data and the flow conditions are summarized in Tables 2.1 and 2.2. Measurements were obtained at the near burner region and at the locations indicated in Figure 2.3.

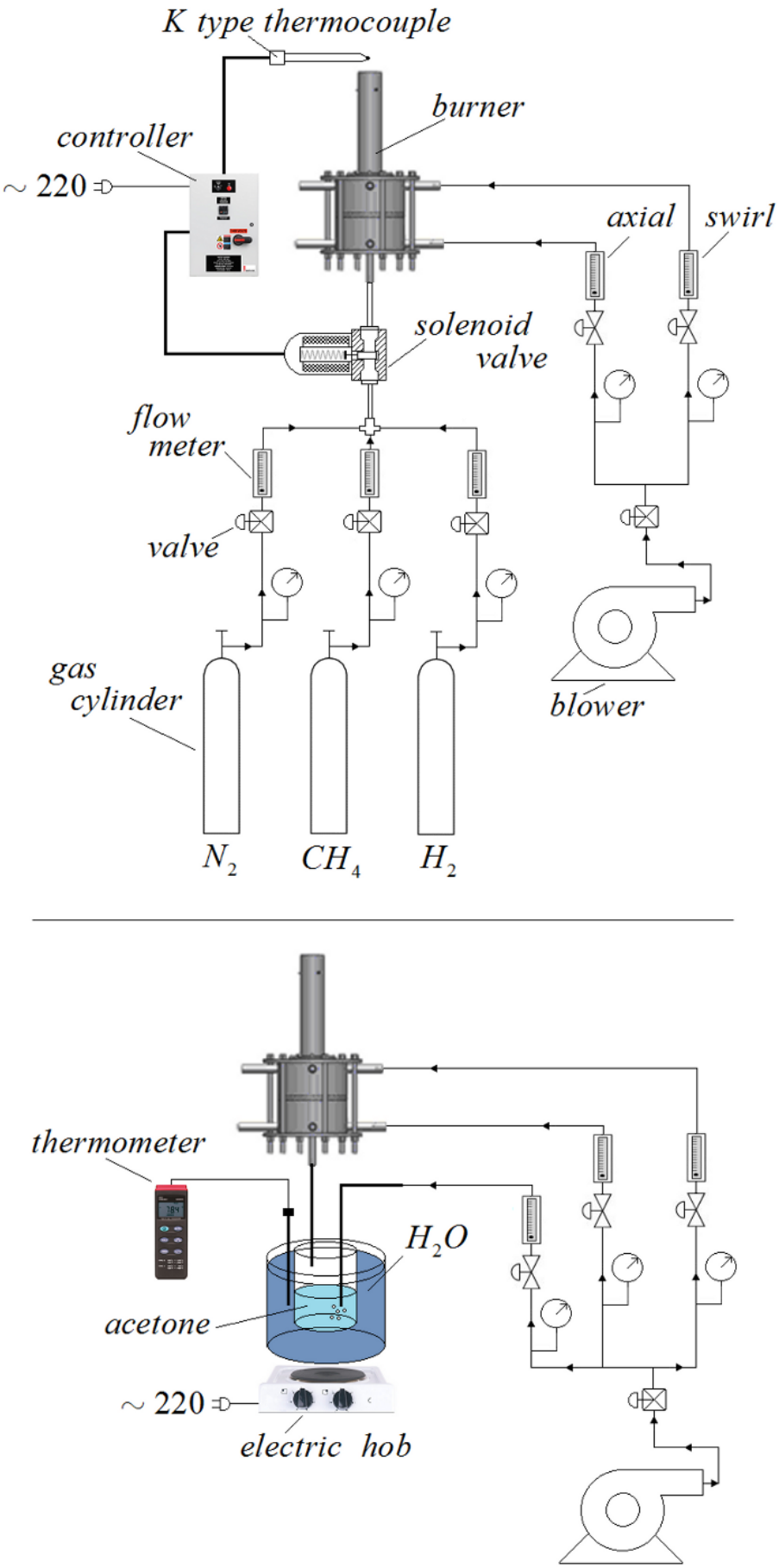

Figure 2.1: Schematic representation of rotameter feeds, reacting case (upper figure) and isothermal case (lower figure). A controller, which is seen in upper picture was used as a safety device during burner operation with combustible fuel jet.

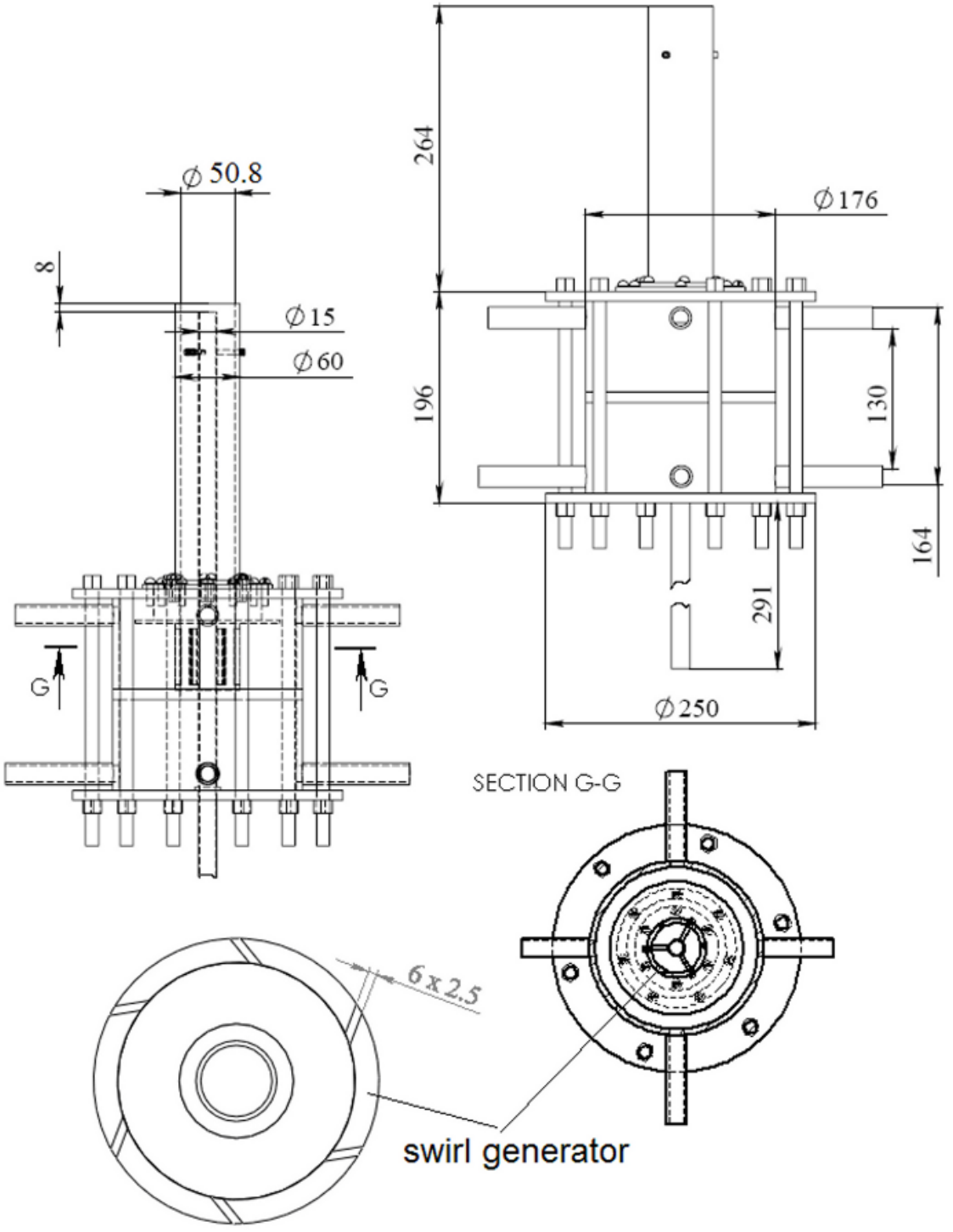

Figure 2.2: Cut view of atmospheric burner used in this work. The burner consists of two cylindrical bodies for the swirl and axial air flow with a central fuel pipe. The fuel flow or acetone vapour is injected through an axial nozzle, consisted of a pipe of 15(mm) internal diameter D_f, 0.75(m) long and centred within the surrounding circular duct by three screws at 25(mm) upstream end of the burner tube. The combustion air passes through the outer 50.8(mm) internal diameter pipe D. The swirl number varied by dividing the air supply into two streams namely axial and swirl.

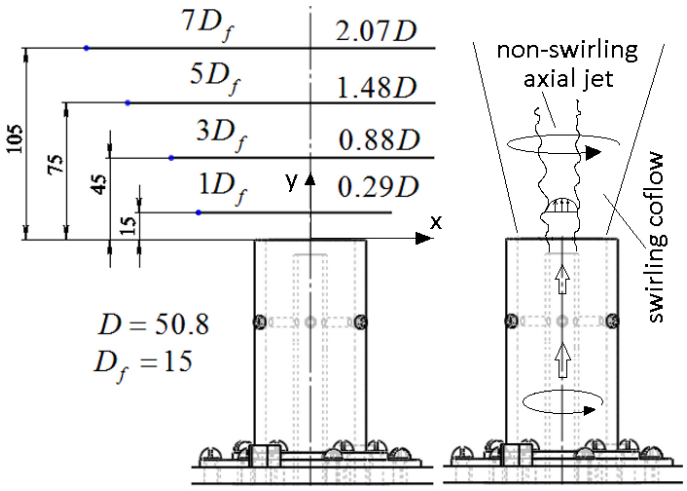

Figure 2.3: A schematic view of laser sheet positions during PLIF measurements (left picture) and flow arrangement (right). Laser sheet positions are shown in absolute values (mm), normalized by the fuel pipe internal diameter D_f and by the burner internal diameter D. During Rayleigh thermometry measurements the laser sheet positions were the same, up to $y/D_f = 10$ (not shown here).

2.3 Flow length scales

Fully developed turbulent flow at high Reynolds number is generally considered to consist of turbulent eddies of different sizes. It can be thought of as a turbulent motion, which is localized over a certain region of size l. Different eddies have different sizes l and characteristic velocity $u(l)$ associated with their characteristic time $\tau(l) = l/u(l)$. The largest eddies are considered to be in the range L of flow scales. Their length scales and characteristic velocity are defined as l_0 and u_0 correspondently. The large eddies are unstable and eventually break up, thus transferring their energy to smaller eddies[2]. These smaller eddies undergo a similar break−up process and transfer their energy to the smallest eddies where they are dissipated by viscosity into heat.

The turbulent kinetic energy is commonly defined as follows:

$$k = \frac{1}{2} < u_i u_i > = \frac{1}{2}(\overline{u'^2} + \overline{v'^2} + \overline{w'^2}) \tag{2.1}$$

The Reynolds number associated with the largest eddies is referred to as the turbulence Reynolds number Re_L, which is defined (where l_0 in the following formula is usually referred to as the integral scale of turbulence) as follows:

[2]

Big whirls have little whirls
Which feed on their velocity
And little whirls have lesser whirls
And so on to viscosity
in the molecular sense.
L.F. Richardson. *Weather Prediction by Numerical Process.* Cambridge Univ. Press, 1922.

Lewis Fry Richardson, FRS (1881 1953) was an English mathematician, physicist, meteorologist and psychologist.

$$\mathrm{Re}_L = \frac{k^{1/2} l_0}{\nu} = \frac{k^2}{\varepsilon \nu} \tag{2.2}$$

In 1941 Kolmogorov introduced the idea that the smallest scales of turbulence were similar for every turbulent flow and were dependent on kinematic viscosity of the fluid and average energy dissipation rate only. Kolmogorov's theory assumes that energy is transferred along one way, i.e from large eddies to the smallest eddies and the turbulence is completely random. Experimental studies demonstrated that energy could also be transferred from smaller scales to large scale and this process was named backscatter. The backscatter process takes place at a much lower rate and the dominant process is indeed from large eddies to small eddies. The Kolmogorov length, time and velocity scales of a flow are commonly defined as follows:

$$\begin{aligned} &\textit{length scale}: \quad \eta = (\nu^3/\varepsilon)^{1/4} \\ &\textit{velocity scale}: \quad u_\eta = (\varepsilon \nu)^{1/4} \\ &\textit{time scale}: \quad \tau_\eta = (\nu/\varepsilon)^{1/2} \end{aligned} \tag{2.3}$$

The ratios between the smallest scale and the largest scale eddies can be calculated using the following relations.

$$\eta/l_0 = \mathrm{Re}_L^{-3/4} \tag{2.4}$$

$$u_\eta/u_0 = \mathrm{Re}_L^{-1/4} \tag{2.5}$$

$$\tau_\eta/\tau_0 = \mathrm{Re}_L^{-1/2} \tag{2.6}$$

$$R_\lambda = (20 Re_L/3)^{1/2} \tag{2.7}$$

$$\lambda = \sqrt{10}\, \eta^{2/3}\, l_0^{1/3} \tag{2.8}$$

$$\lambda_B = \eta Sc^{-1/2} \tag{2.9}$$

The higher the Reynolds numbers, the higher the scale separation is so that for high Re numbers, Kolmogorov scale becomes increasingly smaller. Since η/l_0 decreases with increasing Reynolds number, at high Reynolds number there will be a range of intermediate scales l which are smaller compared to l_0 and larger compared to η. This range is referred to as the universal equilibrium range and is similar for all turbulent flows if they are properly scaled by the Kolmogorov length scale. The Reynolds number of the intermediate scales l is relatively large, so that they are not generally affected by the viscosity ν. Based on that, Kolmogorov proposed the second similarity hypothesis stated that in every turbulent flow at sufficiently high Reynolds number, the statistics of the motions of scale l in the range $l_0 >> l >> \eta$ (from the largest eddies to the smallest ones) had a universal form that was uniquely determined by the dissipation energy ϵ independent of kinematic viscosity ν.

A length scale, defined as l_{DI}, is typically introduced (Fig. 2.4) so that the inertial

subrange can be written as $l_{EI} > l > l_{DI}$, where motions determined by inertial effects and viscous effects are negligible. Most of the dissipation (approximately 90%) occurs within this dissipation range. This means that most of the dissipation takes place at scales that are large than Kolmogorov scale. The Kolmogorov scale can simply be seen as a measure of the smallest eddies that are present in the turbulent flows. This inertial subrange $l_{EI} > l > l_{DI}$ also contains the so called Taylor[3] microscale, which represents the largest scale at which viscous forces can affect the dynamics of turbulent eddies.

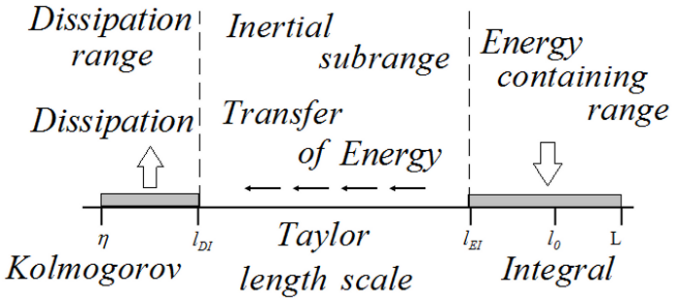

Figure 2.4: A schematic representation of eddy sizes, turbulent scales and the process of energy transfer. The largest scale is the integral scale L, the smallest scale is the Kolmogorov scale η.

Figures 2.5 and 2.6 show radial profiles of axial U, swirl W velocity components, axial and swirl r.m.s. of velocity fluctuations components near burner exit plane at $y/D = 0.08$ (4(mm) above the burner exit). The values of the LDA measurements were reprinted from the work of Milosavljevic[4] (1993) in which axial, swirl velocity components and the r.m.s. of the corresponding fluctuations were measured by using a laser−Doppler velocimeter, operated in dual beam forward−scatter mode. The detailed description of the measurement technique and associated issues can be found in before−mentioned work. The r.m.s. of velocity fluctuations components can be used to compute the turbulence kinetic energy. Assuming that the integral length scale of turbulence is the size of domain, i.e. the burner diameter D, and by using the kinematic viscosity for air of ν =15.11e−6 (m2/s) at 293(K), it is possible to compute the turbulent Reynolds number and hence all the dependant scales. However, the assumption on the integral scale is in many cases not plausible, because the integral scale is usually not the size of domain and by using the integral scale of order of the size of domain leads to overprediction of Batchelor/Kolmogorov scale.

The r.m.s. of velocity fluctuations were in order of 0.1, 0.12 and 0.18(m/s) for three swirl numbers of 0.3, 0.58 and 1.07. In addition, two components of the velocity fluctuations (axial and swirl) were quite similar. If the axial and the swirl r.m.s. of velocity fluctuations are quite similar, then the turbulence isotropy can roughly be assumed. In real flows, however, the assumption of isotropy is usually not valid. In order to be able to conclude whether turbulence is isotropic or not, one must know all three components of velocity fluctuations (generally the r.m.s. components cannot provide information whether the

[3]Sir Geoffrey Ingram Taylor (1886 - 1975) was a British physicist, mathematician and expert on fluid dynamics and wave theory. He was an academic advisor to George Keith Batchelor (http://en.wikipedia.org/).

[4]The values of the LDA measurements were reprinted from Milosavljevic (Figure 2.25, pp.54−55, University of London, 1993).

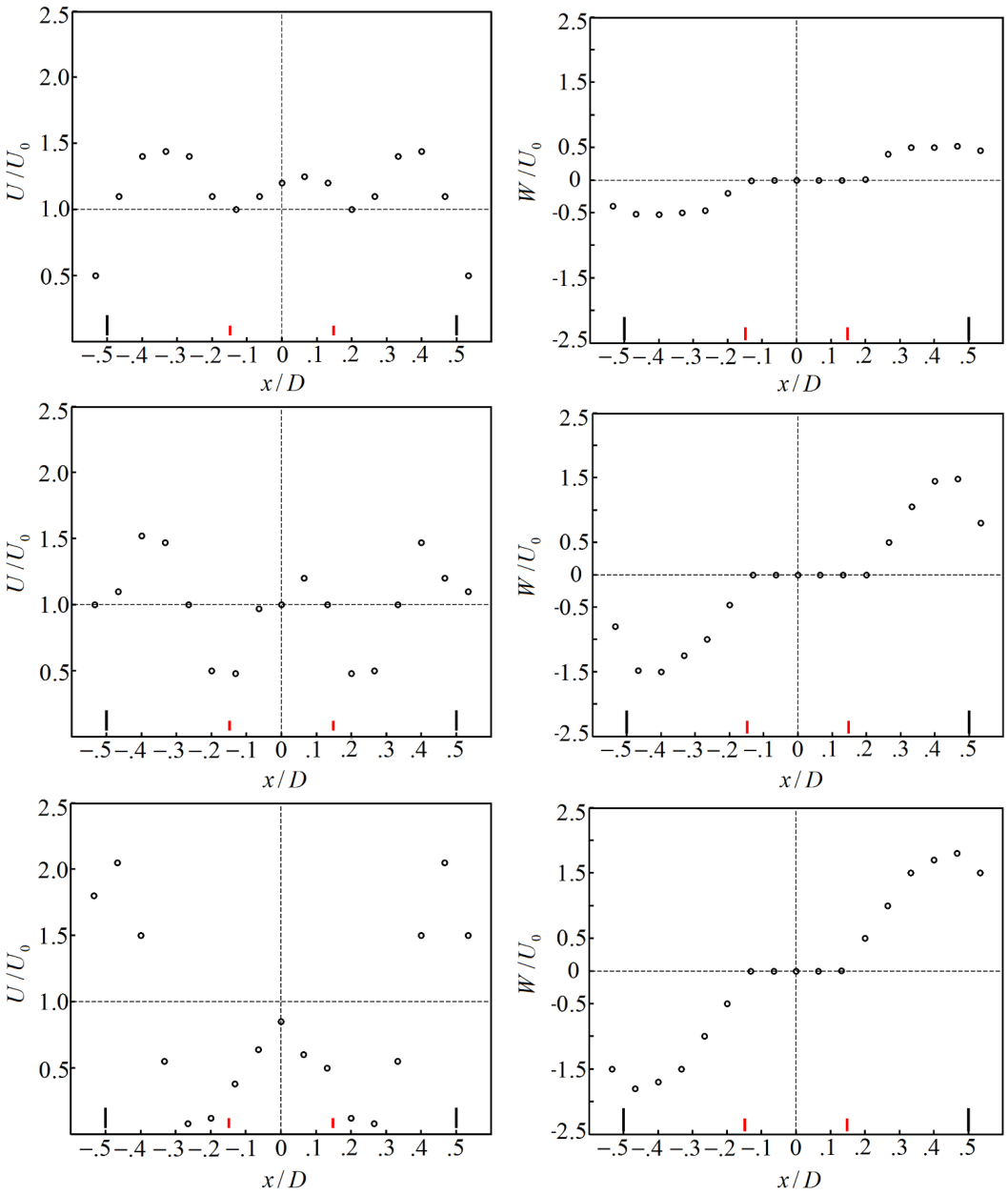

Figure 2.5: Radial profiles of axial U (left) and swirl W (right) velocity components near burner exit plane at $y/D = 0.08$. The values of the LDA measurements were directly reprinted from Milosavljevic (1993). Velocity components were normalized by the bulk velocity $U_0 = 8.46$(m/s) and radial distance was normalized by the burner diameter D. From top to bottom $S = 0.3$, 0.58 and 1.07.

turbulence is isotropic or not and the p.d.f. of the velocity fluctuations is usually required). It should be noted that in the past the concept of turbulence isotropy in swirling flows has generally been assumed Lilley[5] (1976).

However, numerous papers have been published during recent years that dispute isotropy assumptions for turbulent swirling flows. As demonstrated in this section, the presence of swirl increases turbulence intensity (r.m.s. components of velocity fluctuations are higher for higher swirl number) and so smaller Kolmogorov length scale would be expected. This

[5]D. G. Lilley. Non−isotropic turbulence in swirling flows, Acta Astronautwa Vol. 3, pp.919−933, 1976.

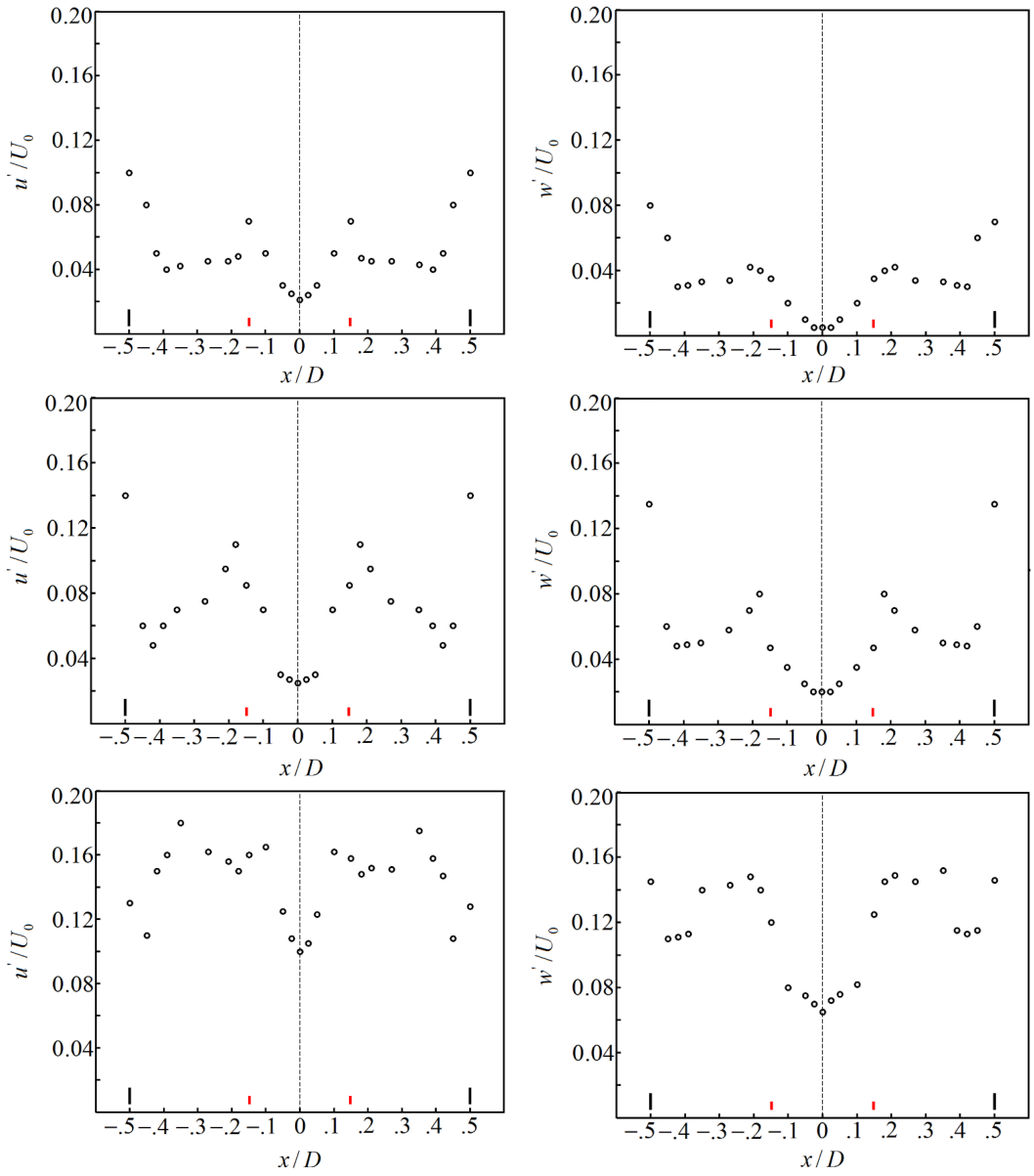

Figure 2.6: Radial profiles of axial u' (left) and swirl w' (right) r.m.s. velocity components near burner exit plane at $y/D = 0.08$. The values of the LDA measurements were directly reprinted from Milosavljevic (1993). Velocity components were normalized by the bulk velocity $U_0 = 8.46$ (m/s) and radial distance was normalized by the burner diameter D. From top to bottom $S = 0.3$, 0.58 and 1.07.

means that the inertial range increases, because eddies contain more kinetic energy that has to be dissipated by the viscosity. The higher the turbulence kinetic energy the smaller the Kolmogorov scale is. It can be seen from the point that if the smallest turbulent eddy increases its kinetic energy, which is done by increasing the swirl number, the molecular force cannot longer dissipate the smallest eddies into heat until smaller eddy sizes are reached. Assuming that the integral length scale of turbulence is the size of domain, i.e. the burner diameter, and by using the kinematic viscosity for air of 15.11e-6 (m^2/s) at 293(K) it is possible to calculate the turbulent Reynolds number and hence all dependant variables. Table 2.3 and 2.4 summarize all relevant turbulent scales computed from LDA

Table 2.3: Turbulent scales computed from the LDA data (two r.m.s. components only).

S	Re_L	Re_λ	$\eta, \mu m$	$u_\eta, m/s$	τ_η, s	$\lambda_\beta, \mu m$	λ, mm	$k, m^2/s^2$
0.3	1223	90	246	0.0615	0.0040	223	4.59	0.132
0.58	1799	109	184	0.0822	0.0022	167	3.79	0.286
1.07	3698	157	107	0.1411	7.59e-4	97	2.64	1.210

Table 2.4: Turbulent scales computed from the LDA data (turbulence isotropy $u^{'}=v^{'}=w^{'}$)

S	Re_L	Re_λ	$\eta, \mu m$	$u_\eta, m/s$	τ_η, s	$\lambda_\beta, \mu m$	λ, mm	$k, m^2/s^2$
0.3	1770	108	186	0.0812	0.0023	169	3.82	0.277
0.58	2459	128	145	0.1039	0.0014	132	3.24	0.535
1.07	4976	182	86	0.1762	4.87e-4	78	2.28	2.190

data (Sc number was computed to be 1.22).

The turbulent microscales can also be estimated by using an analysis proposed by Wang *et al.* (2006) and Pope (2000). Wang *et al.* (2006) estimated that the spatial frequency corresponding to 2% of the peak power spectral density was a cut−off frequency above which there would be less than 1% contribution to the mean dissipation. In order to estimate the Batchelor scale the dissipation spectra must be computed first. Spectrum of the mixture fraction fluctuation can be written as, where $\Im$ denotes Fourier transform.

$$D_x(k) = \left| \Im \left(\frac{\partial z}{\partial x} - \overline{\frac{\partial z}{\partial x}} \right) \right|^2 \tag{2.10}$$

$$D_y(k) = \left| \Im \left(\frac{\partial z}{\partial y} - \overline{\frac{\partial z}{\partial y}} \right) \right|^2 \tag{2.11}$$

The dissipation spectra were computed from an entire region of the instantaneous mixture fraction image as the ensemble average of the squared Fourier transform of the fluctuations of the axial and radial gradients of the mixture fraction. The mean mixture fraction gradient in the axial (same for radial) direction was subtracted from instantaneous values of the gradient of the mixture fraction in the axial direction. The final dissipation spectra that were computed from 1500 instantaneous images were finally spatially averaged across the image so as to obtain ensemble−averaged spectra in the axial direction. The same procedure was used to compute the scalar dissipation spectra in the radial direction.

Figure 2.7 shows an example of dissipation spectra for the fluctuations of the axial and radial mixture fraction gradients computed at $y/D_f = 1$ for axial acetone vapour jet only without swirling coflow of air. The figure also presents the dissipation spectra for $S = 0.3$ and shows the wavenumber corresponding to 2% of the peak value of the dissipation spectrum (spectrum was normalised by its corresponding maximum value). For the radial−derivative spectra for axial acetone vapour jet without coflow of air the wavenumber was ~ 3.264 that corresponded to an estimated Batchelor scale of $\sim 306(\mu m)$, for the axial−derivative spectra the wavenumber was ~ 1.855 that corresponded to $\sim 539(\mu m)$. For higher swirl number, the estimated Batchelor scale increased perhaps due to the presence of slow recirculation zone in which velocity and turbulence intensity are reduced. Since, in swirling flows, the Batchelor scale computed from the radial−derivative is smaller than that computed from the axial−derivative, the Batchelor scale from the radial−derivative

is presented. The Batchelor scales for $S = 0.3$, 0.58 and 1.07 are ∼473, ∼483 and ∼457 (μm) correspondingly. The smallest Batchelor scale should be taken as an estimate of the requirements for the spatial resolution, i.e. η_β ∼300(μm). The detailed description of the optical system with relation to resolution requirements can be found in subsequent section.

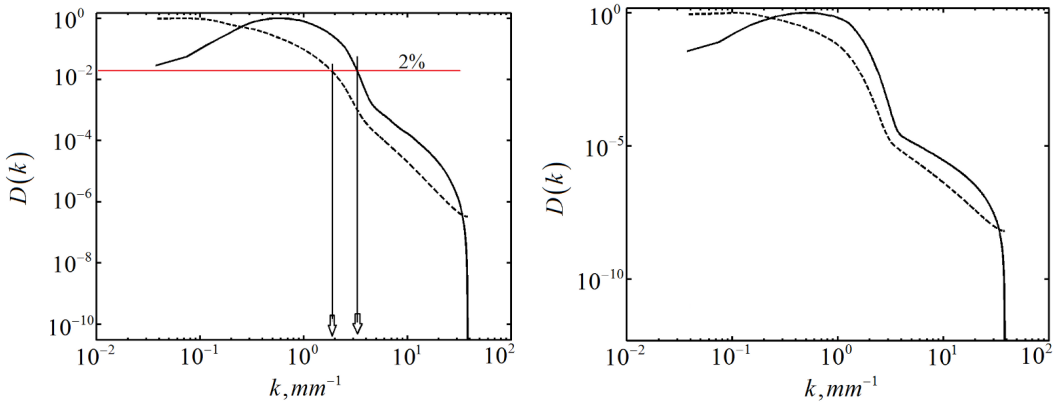

Figure 2.7: Determination of the Batchelor scale from the measured dissipation power spectra at $y/D_f = 1$ for acetone vapour jet (left) and $S = 0.3$ (right). Vertical lines denote the position of the wavenumber corresponding to 2% of the spectrum peak value. The dissipation spectrum was normalized with its maximum value for clear presentation. Solid line − denotes the dissipation spectrum computed from radial−derivative, dashed line −− denotes the dissipation spectrum computed from axial−derivative.

In this work a spatial low−pass filter was also used to perform spatial filtering of instantaneous mixture fraction fields that were obtained from PLIF experiments. In addition, the filter was required to study the turbulence−chemistry interactions and a concept of presumed filtered density functions as well as the SGS scalar variance models. The filter sizes employed in this work were 0.3(mm) and 1.0(mm), respectively. Tong *et al.* (2007) pointed out that the filter sizes should be significantly larger compared to the dissipative scales to ensure that the results are relevant to LES. However, it is not yet clear what an optimal ratio of typical LES filter size to the dissipative scales is. As noted by Celic[6] (2008), a good LES is almost DNS. In general, the LES results should be in better agreement if the LES filter is chosen to be as close as possible to the Kolmogorov or Batchelor scales. The smallest filter of 0.3(mm) that was chosen in this work was used to ensure that the SGS scalar variance was small and filter contained sufficient data. It was done in order to study how the SGS scalar variance affected the presumed and measured filtered density functions of mixture fraction. The detailed description of the turbulence−chemistry interactions and the corresponding results will be given in Chapter 5.

2.4 Optical arrangement

The optical setup for the laser−based measurements consisted of a laser setup, sheet forming optics, a CCD camera and associated control devices. This section provides a summary

[6] J. Meyers *et al.* (eds). Quality and Reliability of Large-Eddy Simulations, Springer©Science+Business Media B.V, p.93, 2008.

of each component used in the present work during experiments in both non−reacting (PLIF) and reacting flows (Rayleigh thermometry).

2.4.1 Optical setup of planar laser-induce fluorescence (PLIF)

A class−IV high power Q−switched Nd:YAG frequency−quadrupled 266(nm) laser (item 3 in Fig. 2.13) from Continuum© Inc.[7] was used to excite the acetone fluorescence (specifications are in Table 2.6). The laser beam was produced at the fundamental wavelength of 1064(nm) rated at 1050(mJ) and passed through frequency doubler to produce green light at wavelength of 532(nm) rated at 455(mJ), then passed through a fourth harmonic generator in order to produce 266(nm) rated at 120(mJ) at the exit port of the laser. The laser pulse width was in the range of 5−7(ns) at Full Width at Half Maximum (FWHM). The sheet forming optics consisted of a single dichroic mirror (item 2 in Fig. 2.13) and a cylindrical positive lens (item 1 in Fig. 2.13) with focal length of f−310(mm). A single dichroic mirror was employed in order to decrease the amount of 532(nm) light reaching the burner and to steer the laser beam from the laser exit port towards the experimental setup and the sheet forming optics. The remaining 532(nm) component of light was blocked by a beam damper (item 4 in Fig. 2.13).

Laser sheet size

The light rays passing through a lens converge on the focal plane and interfere with each other. During this process constructive and destructive superposition takes place. The light energy is distributed so that the central maximum contains 86% of the total laser power. The intensity distribution somehow resembles Gaussian profile but in reality is never found. The ratio of the laser performance, i.e. the beam waist and divergence from an ideal Gaussian beam at the same wavelength is called the beam propagation factor M^2. The waist of the laser sheet can be estimated by using an assumption of Gaussian intensity distribution in symmetrical laser beam. The point where the intensity is $1/e^2 \approx 0.135$ of the maximum intensity is defined as the beam waist radius. For a Gaussian beam propagating in free space, the spot size can be computed as follows:

$$d_0 = (M^2 4\lambda f_l)/(\pi D_0) \tag{2.12}$$

This equation shows that the focused spot size is larger than it would be for pure Gaussian beam (TEM00[8]). For example for the 266(nm) wavelength, focal length of 300(mm), laser beam diameter of 9(mm)and perfect Gaussian beam, the beam waist would be as.

$$\frac{M^2 \cdot 4 \cdot 266 \cdot 300 \cdot 10^6}{3.14 \cdot 9 \cdot 10^6} = 11295M^2[nm] \approx 11M^2[\mu m] \tag{2.13}$$

From the formula it is clear that for perfect Gaussian beam the beam waist is $11(\mu m)$. Typically for new Nd:YAG lasers the M parameter can be in order of 30-50 and hence the

[7] Continuum is a wholly owned subsidiary of the GSI Group of companies (NASDAQ:GSIG) and headquartered in Santa Clara California. 3150, Central Expressway, Santa Clara, CA 95051, USA.

[8] A transverse mode of a beam of electromagnetic radiation is a particular electromagnetic field pattern of radiation measured in a plane perpendicular (i.e., transverse) to the propagation direction of the beam.

beam waist can be in order of 0.3−0.6(mm) depending on a laser model. In practice, due to the laser and doublers deterioration the M parameter can be significantly larger, which in turn affects measurements. There is no practical procedure known that can be used to decrease the M parameter and in some cases the laser needs to be replaced if its beam quality is not satisfactory. Additional procedure that can be used to decrease the beam waist is by using a set of concave−convex lenses to expand and focus beam into thinner waist diameter. A typical optical setup would consist a concave cylindrical lens, a convex cylindrical lens and a final positive convex lens. The ratio of focal length of the concave lens and the first convex lens will determine the beam diameter reaching the last positive focusing lens. For instance, if an initial beam diameter was 9(mm), the concave lens had the focal length of -20 and the convex lens had the focal length of 110, the resulting beam diameter would be (110/20)×9 or 49.5(mm). The larger beam diameter will result in smaller beam waist after focusing onto a line by the positive lens. The distance between the first concave−lens and the second convex−lens is simply the sum of their focal lenses -20+110=90(mm). The lenses should be positioned at exact distance of 90(mm) between them, otherwise it will lead to non−collimated laser beam.

In additional, different optical components and alignment errors can influence to the quality of beam. It is generally advised that the beam quality should be checked prior to each measurement. In this work, the laser beam waist, from a Nd:YAG laser used for PLIF measurements, was measured directly by using a CCD camera technique. The CCD camera technique is the simplest and reliable technique to measure the laser sheet profile and its thickness. The positive cylindrical lens was rotated to 90° so the waist thickness could be captured directly by measuring acetone intensity in the potential core of the jet. Averaging of CCD images (50 images) was performed in order to remove image noise and laser beam intensity fluctuations. The beam waist was defined as equal to the distance between the two points on the intensity distribution that are 1/e2 (0.135 times the maximum value) and was defined to be 0.16(mm). Similar techniques were used to measure the laser beam waist for the Rayleigh thermometry experiments (Rayleigh scattering signal from the air was used to measure the laser beam waist diameter).

Image acquisition and spatial resolution

A double frame Charge−Couple Device (CCD) (Imager Intense) camera (item 12 in Fig. 2.13) from LaVision Inc[9]. was used in this work. This camera was equipped with a Nikkor lens with focal length $f_l = 50$ (mm) and f1.4 (where f1.4 is the f−number). A 13(mm) extension ring was also used after the camera lens for tighter focusing. A BG3 bandpass Schott filter (item 13 in Fig. 2.13) was used in the front of the camera lens in order to block any remaining 532(nm) light that might interfere with the acquired signal. The emitted fluorescence from acetone was in the range of the operating window of the BG3 filter. The internal transmittance of the BG3 bandpass filter allowed passing the light with wave length in the range of 300−500(nm) and 750−900(nm). On the other hand the BG3 filter tends to decrease the acetone fluorescence signal from the test volume, which in some cases should be avoided. It is advised that the thickness of any BG3 filters

[9]LaVision founded in 1989 is a spin−off from Max Planck Institute and Laser Laboratory in Goettingen, Germany. LaVision GmbH., Anna−Vandenhoeck−Ring 19, D−37081,Goettingen, Germany.

Table 2.5: Main characteristics of a CCD camera used in this work.

Description	**Value**
Resolution, (pixels)	1376×1040
Frame rate at maximum resolution, (Hz)	10
Pixel size, (μm)	6.45×6.45
Min time acquisition interval, (ns)	500
Dynamic range, (bit)	12 (4095 discrete intensity levels)

should be as thin as possible. Any scattered 266(nm) UV light that might come from the test volume was blocked by the glass material of the camera lens. The array size of the CCD camera (Table 2.5) was 1376×1040 pixels and the pixel size was 6.45(μm). The magnification was determined by using a special calibration target plate (type 7) and was found to be 0.0263(mm/pixel). The camera exposure time was set to be 1(μs) at the maximum aperture of 1.4.

The image correction procedure calibrates the image field from a unit of pixels to a unit of length and corrects for any distortions between the camera's perspective and the actual experimental plane. This can be done by using for example a plate with an array of crosses with known dimensions and spacing. The plate, which is known as a calibration target (type 7 was used in this work) was placed in the experimental plane. The calibration target was imaged and data about cross dimensions was found and processed by the software. The software was able to assign real unit of length removing any distortion to actual acquired images. The image calibration process can easily be performed by the DaVis© 7.2[10] software and the detailed explanation of calibration technique can be found in its manual.

Light intensity in each experimental image that was obtained during experiments was the sum of fluorescence light, background light that came from the surrounding and the camera's dark current. Light from surrounding was blocked by the BG3 filter while the dark current needed to be eliminated from the images. Dark current is a low amount of current that flows through the camera even though no photons are detected on a camera CMOS censor or a photocathode. In order to eliminate the dark noise, a correction procedure was used. A set of images was recorded, averaged and then simply subtracted from each image taken during experiments. No background image was taken during PLIF experiments since incident background light was blocked by the BG3 filter.

The spatial resolution and the image quality, however, are not directly related to the pixel size. The pixel size in the image plane describes rather magnification than the actual quality of the imaging system. A common metric, which is used to quantify the image quality is the modulation transfer function (MTF), which is non−negative, space dependent in general. The MTF of an optical system can be determined by evaluating the response of the system to periodic patterns. The detailed description and evaluation of the modulation transfer function will be given in Chapter 6.6.2.

[10] A software tool for intelligent (laser) imaging applications for non−reactive and reactive flows.

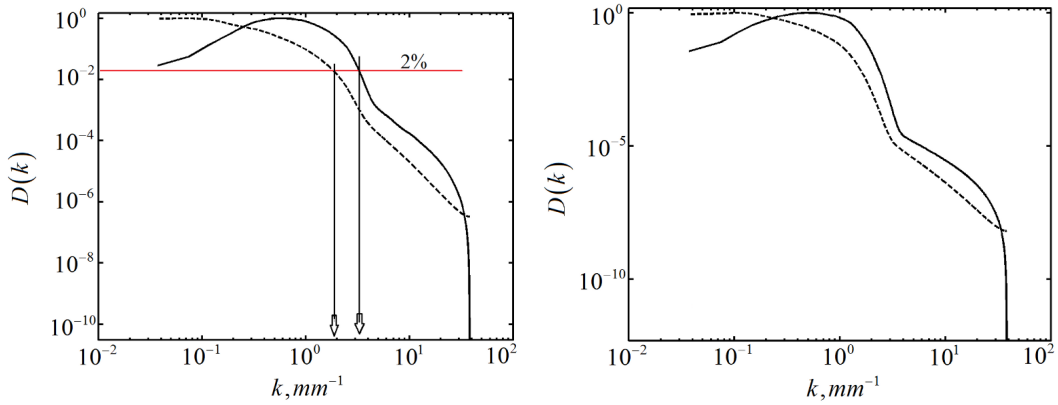

Figure 2.8: Determination of the Batchelor scale from the measured dissipation power spectra at $y/D_f = 1$ for acetone vapour jet (left) and $S = 0.3$ (right). Vertical lines denote the position of the wavenumber corresponding to 2% of the spectrum peak value. The dissipation spectrum was normalized with its maximum value for clear presentation. Solid line − denotes the dissipation spectrum computed from radial−derivative, dashed line −− denotes the dissipation spectrum computed from axial−derivative.

Triggering

The synchronization of the laser flashlamp, the laser Q−switch and the CCD camera was done by using a programmable PC−based timing unit (PTU) using TTL pulses. The laser flashlamp was fired continuously at 10(Hz). The laser Q−switch was triggered every time when an image was taken. Numerous instrument delays contributed to an uncertainty in the precise time after the Q−switch trigger and the images acquisition. The main delay occurred between the TTL pulse to the Q−switch and the actual lasing, which was of the order of 150(ns). The CCD camera was triggered at the same time as the Q−switch trigger (TTL pulse was sent to Q−switch and to the CCD camera instantly) and the camera exposure time was set to $1(\mu s)$ thus overlapped all uncertainties in the precise time (laser shot and camera opening time). The camera shutter opened before laser pulse and closed after the laser pulse. Both the laser and the CCD camera were electronically controlled from a software package DaVis©7.2, provided by LaVision© Inc. installed on a computer running Windows XP©. The computer, which ran the LaVision© software package was used for all aspects of the experiment, including tuning the system, calibration and acquiring the experimental data.

2.4.2 Optical setup of Rayleigh thermometry

A class−IV high power pulsed neodymium−doped yttrium aluminium garnet (Nd:YAG) frequency doubled Q−switched laser (Quanta−Ray PRO−Series, PRO−270−10) from Spectra−Physics® Inc.[11], USA emitted in the green visible range of 532(nm) was used in Rayleigh thermometry experiments (item 4 in Fig. 2.14). The laser beam was produced at the fundamental wavelength of 1064(nm) and passed through a frequency doubler to produce 532(nm). The laser pulse width was in the range of 8−12(ns) at Full Width at

[11] Spectra−Physics, Inc. was acquired by Newport® in 2004. Newport Corporation established in 1969 is a leading global supplier of advanced technology products and solutions for Scientific Research.

Half Maximum at 1064(nm) and 1−2(ns) at 532(nm). The laser was controlled locally by using the standard table−top controller for alignment purposes and electronically from a computer during the experiments (specifications are in Table 2.6).

The sheet forming optics consisted of a single mirror (item 3 in Fig. 2.14) $\phi = 25.4$(mm), $\lambda = 532$(nm) and a cylindrical positive lens (item 2 in Fig. 2.14) with focal length of f−310(mm). The lens was used to focus the laser beam into a thin waist, with focal point located at the axis of symmetry of the flow. The average laser energy at the exit port of the laser was circa 950(mJ/pulse). Actual laser energy fluctuations during experiments from pulse to pulse were less than 2.7%. The instantaneous corrections of the sheet profile intensity variations were not performed. The mean laser sheet profile was acquired and was used as the reference Rayleigh signal.

Laser sheet size

In the Rayleigh thermometry, the laser beam waist from the laser was also measured directly by using the CCD camera technique. The positive cylindrical lens was rotated to 90° so the waist thickness could be captured by measuring the Rayleigh scattering intensity from the air. Averaging CCD images was done in order to remove image noise, laser beam intensity fluctuations and eliminate effects of Mie scattering from dust particles. The beam waist was defined as equal to the distance between the two points on the intensity distribution that are 1/e2 (0.135 times the maximum value) and was defined to be 0.4(mm).

Image acquisition and spatial resolution

The same, as in PLIF experiments, double frame CCD camera from LaVision© Inc. was used in this work. The camera was equipped with a Nikkon lens with focal length $f_l = 50$(mm) and f1.2. A 13(mm) extension ring was also used after the camera lens for tighter focusing. A 532−3 bandpass filter was used in the front of the camera lens in order to block any incoming light that might interfere with the acquired signal thus transmitting only 532±1.5(nm). The magnification (nominal resolution) was determined by using a special calibration target plate and was found to be 0.025(mm/pixel). The camera exposure time was set to be 1(μs) at the maximum aperture of 1.2.

Triggering

The synchronization of the laser flashlamp and the CCD camera was done by using a programmable PC−based timing unit using TTL pulses. The laser flashlamp was triggered every time when an image was taken. The Q−switch delay was set by a top−table controller to its optimal values thus providing maximum power, which was controlled by a laser power meter.

Table 2.6: Laser specifications.

Description	**Isothermal**	**Reacting**
Repetition rate, Hz	10	10
Energy, (mJ/pulse) at $\lambda = 1064$, (nm)	850	1750
Energy, (mJ/pulse) at $\lambda = 532$, (nm)	425	950
Energy, (mJ/pulse) at $\lambda = 355$, (nm)	165	475
Energy, (mJ/pulse) at $\lambda = 266$, (nm)	120	160
Beam diameter, mm	9.5	< 10
Energy stability, $\pm\%$ at $\lambda = 1064$, (nm)	2.5	2.0
Energy stability, $\pm\%$ at $\lambda = 532$, (nm)	3.5	3.0
Energy stability, $\pm\%$ at $\lambda = 355$, (nm)	4.0	4.0
Energy stability, $\pm\%$ at $\lambda = 266$, (nm)	7.0	8.0
Maximum deviation from Gaussian profile $\pm\%$ at the beam centre	30	30

2.5 Acetone laser-induced fluorescence

A planar laser−induced fluorescence technique was used to obtain the scalar fields (mixture fraction fields) in the isothermal swirling flow. The PLIF is a non−invasive measurement technique that can provide qualitative as well as quantitative characterization of the flow fields. The fluorescence signal is directly related to the concentration of tracer species in the flow being investigated and the laser energy. This technique can provide a set of detailed flow field maps both resolved spatially and temporally. The PLIF technique is, therefore, an ideal method to study non−reacting flows in various combustion systems. Moreover, PLIF technique can be used under a wide range of operating conditions and, therefore, has been widely applied to study various aspects of mixing in non− reacting jets. Acetone[12] has been used as a tracer for many years. The choice of acetone is simple due to its outstanding properties and in many ways can be regarded as an ideal tracer for the PLIF technique due to its linear relationship between the fluorescent intensity, laser power and acetone concentration in the flow.

Acetone has also an accessible absorption spectrum at the UV. The fluorescent signal is emitted in the visual range of light spectrum 350−600(nm) and the corresponding peak of the fluorescent emission spectrum is between 450 to 500(nm). Fluorescent signal can be recorder onto a digital sensor of a CCD camera and after which can be post processed as required. Moreover, the signal from acetone fluorescence is relatively high and its interpretation in actual fuel concentration is in fact straightforward. Other acetone properties that can potentially attract many researchers are high vapour pressure, which allows acetone seeding at high flow rates, low cost and low toxicity level.

The LIF/PLIF method is based on molecule excitation to a higher electronic energy level by absorbing the energy of a laser beam. The molecule at this energy state is unstable and will go from upper energy level to the lower energy level emitting photon of the same energy as the original absorbed photon. The emitted photon can be detected and used to measure the light intensity, which is proportional to a number of molecules, or simply concentration of a tracer. The measured acetone fluorescent signal (the total number of

[12] Acetone (systematically named propanone) is the organic compound with the formula $(CH_3)_2CO$. It is a colourless, mobile, flammable liquid, and is the simplest ketone.

photons) at each pixel position on the CMOS sensor (x, y) can be written as follows:

$$\mathrm{S_F}(x,y) = \eta_{ef}\frac{\Omega}{4\pi}f_1(T)\chi_m n V_c B_{12} E_v \frac{A_{21}}{A_{21}+Q_{21}} \tag{2.14}$$

All the quantities in the equation above are dependent on the position in the flow via pressure, temperature and tracer's concentration. For conditions of constant temperature and pressure the ratio of acetone fluorescent signal over the fluorescent signal at a reference position of known acetone concentration can provide measurements of the mixture fraction. If the reference position is at the exit of the fuel nozzle in a potential core, where no mixing with ambient air occurs, then the above mentioned ratio is directly related to the mixture fraction.

$$z(x,y) = \frac{S_F(x,y)}{S_{F_{ref}}(x,y)} \tag{2.15}$$

In order to reduce uncertainties in the reference signal, the reference measurements were taken over a small square region within the potential core of the fuel jet without coflow of air. A set of reference measurements consisted of 2650 images was taken continuously in potential core at air flow rate of 40(l/min) passing through the seeder. The relationship between the level of reference signal and a number of acquired images was deduced. A six−degree polynomial fit was then used to approximate this relationship. This approximation was used in computation of reference signal as a function of acquired images in order to reduce uncertainties in the fluorescent signal at reference position. The time−dependent fluorescent signal at a reference position is then given by the following equation as follows:

$$S_{Fref} = p1 \cdot N_{i,img}^5 + p2 \cdot N_{i,img}^4 + p3 \cdot N_{i,img}^3 + p4 \cdot N_{i,img}^2 + p5 \cdot N_{i,img} + p6 \tag{2.16}$$

$$\begin{aligned} \mathrm{p1} &= -2.9668\mathrm{e}-014 \\ \mathrm{p2} &= 2.2016\mathrm{e}-010 \\ \mathrm{p3} &= -5.818\mathrm{e}-007 \\ \mathrm{p4} &= 0.00061902 \\ \mathrm{p5} &= -0.36668 \\ \mathrm{p6} &= 1105.4 \end{aligned} \tag{2.17}$$

The fluctuations of the acquired signal are mainly due to the fluctuations in laser power from pulse to pulse (less than 3%). The acquired signal decreases due to acetone evaporation, which decreases acetone concentration. In order to stabilize the acetone evaporation rate, the acetone seeder was placed on a heater, which maintained constant temperature of 45°. A RS−1313[13] (accuracy $\pm 0.05 + 0.5^0$) 1−channel thermometer and an N−type thermocouple of 3.0(mm) diameter and 500(mm) length were used to measure acetone temperature in the acetone seeder.

[13] RS Components is the trading brand of Electrocomponents plc., the world's leading high service distributor of electronics and maintenance products.

2.6 Rayleigh thermometry

Rayleigh thermometry is based on the Rayleigh scattering named after the British physicist Lord Rayleigh[14]. It is the elastic scattering of light or other electromagnetic radiation from atoms, molecules or particles that are smaller than the wavelength of the light. The elastic scattering of light by a molecule or a particle is proportional to their Rayleigh scattering cross section, which is an intrinsic property of a molecule. The Rayleigh scattering is commonly assumed to be temperature−independent. The process of Rayleigh scattering can be seen as the process of radiation from the molecules, which act like dipole antennas when they are forced to oscillate by an applied electromagnetic field. The wavelength of scattered light is unchanged (elastic scattering) and the scattering amplitude is proportional to the weighted sum of the number of scatters in the observation volume. The scattering intensity is proportional to λ^{-4} thus a wavelength at 450(nm) in the blue spectrum is scattered a factor ≈6 times as efficient as a wavelength of 650(nm) in the red[15].

The Mie scattering from dust particles and background scattering from polished surfaces have exactly the same wavelength as the laser beam and are regarded as unwanted scattered light. The Rayleigh scattering from molecules has the bandwidth[16] due to the Doppler effect. If a special filter with a substance is placed in the front of the CCD camera, which absorbs light with exactly the same wavelength as the laser beam it is possible to 'filter' out the Rayleigh signal from the molecules and separate the 'true' signal from unwanted scattered light. This technique was named molecular filtered Rayleigh scattering (FRS) and usually employs an iodine vapour filters with injection-seeded[17] Nd:YAG lasers. The vapour within the cell (or filter) strongly absorbs background scattering from the dust particles and surfaces. The Doppler-broadened Rayleigh signal is not absorbed by the cell and therefore can be recorded by the CCD camera and the temperature can be deduced. This technique is usually used in sooting flames. However, the description of the filtered Rayleigh scattering technique is beyond the scope of the present work. The total Rayleigh scattering signal at every pixel on a CMOS sensor of a camera can be written as follows:

$$S_R(x,y) = \eta_{ef} I N_R V_c \int_{\Omega} \left(\frac{\partial\sigma}{\partial\Omega}\right)_{mix} d\Omega \tag{2.18}$$

The differential scattering cross section of the gas mixture is defined as the mole fraction weighted sum of all the species present in the observation volume.

$$\left(\frac{\partial\sigma}{\partial\Omega}\right)_{mix} = \sum_i \frac{\partial\sigma_i}{\partial\Omega} X_i \tag{2.19}$$

In the experiments two Rayleigh scattering signals were measured. First, a reference

[14] John William Strutt, 3rd Baron Rayleigh, OM (12.11.1842−30.07.1919) was an English physicist who, with William Ramsay, discovered argon, an achievement for which he earned the Nobel Prize for Physics in 1904.

[15] That is why the sky is blue...

[16] The optical bandwidth is the width of the optical spectrum.

[17] Injection seeding is a techniques is mostly applied to pulsed laser with the main goal of achieving emission with a narrow optical bandwidth.

signal was measured in the region of flowing dry air of a known temperature T_1, giving a signal $S(T_1)$. Second, the signal from the flame region was measured at unknown flame temperature T_2, giving a signal $S(T_2)$.

$$S(T_1) = \eta_{ef} I N_R V \left(\frac{\partial\sigma}{\partial\Omega}\right)_{air} \Omega \tag{2.20}$$

$$S(T_2) = \eta_{ef} I N_R V \left(\frac{\partial\sigma}{\partial\Omega}\right)_{flame} \Omega \tag{2.21}$$

For atmospheric pressure flames the ideal gas law can be applied with negligible error as follows:

$$N_1 k T_1 = N_2 k T_2 => T_2 = \frac{N_1}{N_2} T_1 \tag{2.22}$$

Hence, the flame temperature can be estimated as follows:

$$T_2 = \delta \frac{S(T_1)}{S(T_2)} T_1 \tag{2.23}$$

Where the ratio of differential scattering cross sections of air/mixture is defined as follows:

$$\delta = \frac{(\partial\sigma/\partial\Omega)_{flame}}{(\partial\sigma/\partial\Omega)_{air}} \tag{2.24}$$

The ratio of the Rayleigh scattering signals can be measured simultaneously so that fluctuations in the laser power will not affect the measurements. It can be seen from the equations that in order to determine the flame temperature the ratio of differential cross sections of air/mixture must be calculated. In turbulent non−premixed flames, this ratio is unknown and cannot be determined without additional information from the experimental data. For example, simultaneous Rayleigh/Raman scattering technique can be used to measure mixture composition and the Rayleigh signals. On the other hand, there is also alternative approach that makes possible direct Rayleigh scattering without having additional information. The idea behind this approach is that any fuel that has the same scattering cross section during combustion, as the air, can be used, which eliminates differential cross section dependence (Table 2.7).

The fuel that was used in this work was occasionally called the DLR fuel and consisted of a mixture with volumetric composition of 22.1%CH_4, 33.2%H_2, 44.7%N_2 (stoichiometric mixture fraction is 0.167). The ratio of DLR fuel Rayleigh scattering cross section to the air Rayleigh scattering cross section as a function of mixture fraction was computed by employing a commercial software CHEMKIN©[18] and its subroutine OPPDIF[19]. Figure 2.9 presents the results from the opposed−flow simulation in terms of major species mole fractions and major species balance.

The species balance is shown here in order to justify that only major species i.e. CO_2, H_2O, O_2, CH_4, N_2, CO and H_2 were chosen to compute the mixture Rayleigh scattering

[18] CHEMKIN is a software tool for solving complex chemical kinetics problems initially developed at Sandia National Laboratories and is now being developed at Reaction Design Inc.

[19] OPPDIF is a Fortran program that computes the diffusion flame between two opposing nozzles.

cross section (sum of all species must be equal to one). As it can be seen the selection of only major species as a basis for scattering cross section computations introduces insignificant error. Figure 2.10 shows the Rayleigh scattering cross section of the DLR fuel as well as the ratio of its Rayleigh scattering cross section to the Rayleigh scattering cross section of the air. As it can be seen the relationship is non−linear and the error in temperature measurements depends on the mixture fraction reaching maximum circa 12% in worst case scenario. The mean error in temperature prediction (mean error in scattering cross section difference) was circa 0.18% (Fig. 2.10).

Table 2.7: Scattering cross section for the major combustion species, air and DLR fuel at 532(nm) for standard temperature and pressure Suton *et al.* (2006) and Namer & Schefer (1985).

Species	Cross section $\sigma_i \cdot 10^{-28}$, cm^2
N_2	6.29651
H_2	1.35887
CH_4	13.625
Air	6.1036
DLR	6.27681
$\sigma_{DLR}/\sigma_{Air}$	1.02838

N_2, H_2, Air were taken from 'Suton *et al.* A combination temperature and species standard for the calibration of laser diagnostic techniques. Combustion and flame 147, pp.39-48, 2006'.
CH_4 was taken from 'Namer and Schefer. Error estimates for Rayleigh scattering density and temperature measurements in premixed flames, Exp. Fluids, 3, pp.1-9, 1985.'

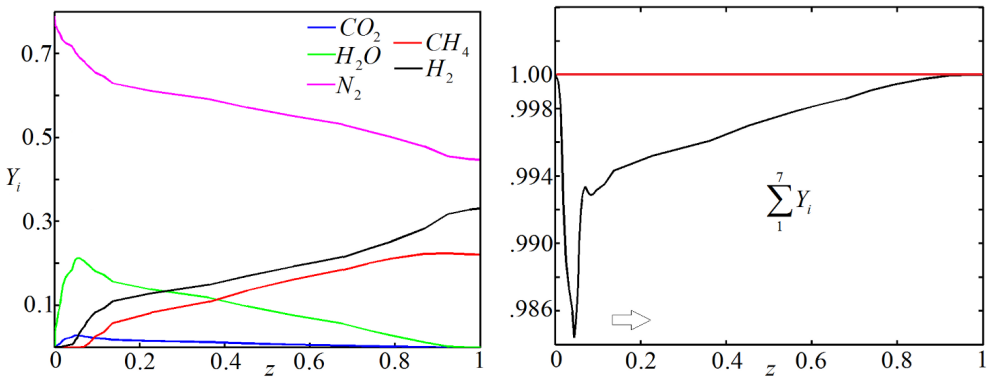

Figure 2.9: Opposed−flow combustion simulation (mole fractions of major species) for DLR fuel as a function of mixture fraction (left) and major species balance (right). O_2 and CO are not shown in the figure.

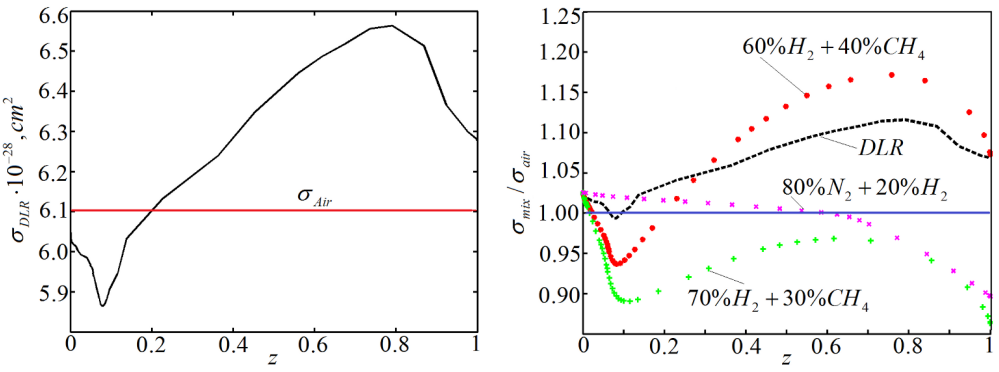

Figure 2.10: Rayleigh scattering cross section of the DLR fuel (left) and the ratio of its scattering cross section to the Rayleigh scattering cross section of the air (right). In addition, three different fuel compositions with H_2 and CH_4 only were investigated and shown in the figure.

2.7 Particle image velocimetry

Particle image velocimetry is a non−intrusive technique, which provides instantaneous velocity vector fields. Typically, two velocity components are recorded but with the aid of a stereoscopic arrangement, all three velocity components can be obtained. Stereo PIV measures three velocity components in a plane using two cameras, while Volumetric Velocimetry (Tomographic PIV) measures three velocity component in a volume using two, three or four cameras.

The principle of PIV is based on recording of two separate images with time delay $\Delta\tau$ between them. Seed particles or traces are used to seed airflow, which reflect light when illuminated by a laser pulse. The traces must be small enough in order to follow the flow. A variety of tracers can be used, consisting of small oil droplets (0.2−5 μm) or solid particles (10−100 μm). A typical PIV system consists of the following components a laser, a CCD camera, a synchronizing device and an associated software to process the data.

The flow seeded with particles is illuminated twice and two images are recorded with small time separation $\Delta\tau$ between them. In PIV, the velocity vectors are derived from sub−windows (interrogation windows) of the acquired image by measuring the movement of particles.

The interrogation windows (typically 16×16 or 32×32 pixels[20]) from each image frame are cross−correlated with each other. The cross−correlation procedure is repeated for each interrogation window over the two images captured by the camera producing a signal peak in each interrogation window. A sub−pixel interpolation is used to measure the velocity with high accuracy. The velocity computation is directly dependent on a number of particles in the flow. It is advised to have at least 10 to 20 particles per interrogation window.

The accuracy of the measurements is dependent on the ability of the particles to follow the flow and adjust their velocity to the flow fluctuations. If the flow is subjected to extreme acceleration, for example just behind the flame front, the inertia of the particles

[20]Ken Kiger. *Introduction of Particle Image Velocimetry.* Burgers Program For Fluid Dynamics Turbulence School College Park, Maryland, May 24−27, 2010.

Table 2.8: Particle response in turbulent flow Melling (1997).

Particle	ρ_p, kg/m^3	Gas at (10^5 Pa)	Density ratio ρ_p/ρ_f	S_{tk}	d_p, μm
TiO_2	3500	Air (300K)	2950	0.0295	0.45/1.44
Al_2O_3	3970	Flame (1800K)	20250	0.0113	0.78/2.46
Glass	2600	Air (300K)	2190	0.0342	0.53/1.67
Olive oil	970	Air (220K)	617	0.0645	0.98/3.09
Microballoon	100	Air (300K)	84.5	0.1742	2.69/8.50

can affect the velocity measurements. This effect can be crucial for application of PIV to combustion Picano *et al.* (2011). Table 2.8 and 2.9 show particle response in turbulent flows and seeding particles in gas flows.

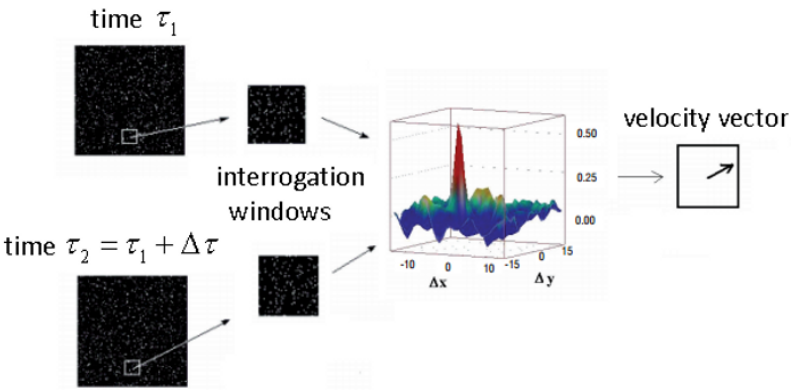

Figure 2.11: Derivation of velocity vectors by cross−correlation of a pair of interrogation windows from two exposed recordings. The cross−correlation procedure is repeated for each interrogation window over the two images captured by the camera producing a signal peak in each interrogation window. A sub−pixel interpolation is used to measure the velocity with high accuracy. Figure adapted from C. Brossard *et al.* Principles and Applications of Particle Image Velocimetry. Journal Aerospace Lab, Issue 1, December 2009.

During PIV measurements, the same downstream positions $y/D_f = 1, 3, 5, 7, 10$ were tested. The PIV system consisted of a frequency−doubled (532nm) dual−pulsed Nd:YAG laser from Litron Lasers Ltd[21]. and the same double−frame CCD camera, which was used during PLIF and Rayleigh thermometry. Laser characteristics are summarised in Table 2.10.

The camera was equipped with a Nikkon lens with focal length of $f_l = 50$(mm) and the F-number of 1.2. A 13(mm) extension ring was also used after the camera lens for tighter focusing. A 532−3 bandpass filter was used in the front of the camera lens in order to block any incoming light that might interfere with the acquired signal thus transmitting only 532±1.5(nm).

The sheet forming optic consisted of two mirrors $\phi = 25.4$(mm) a plano−concave f=-20(mm), a plano−convex f=200(mm) and a cylindrical positive lens with focal length of f−310(mm). The sheet forming optics created laser sheet of 50(mm) width and the final

[21]Litron Lasers is a manufacturer of pulsed and CW Nd:YAG and Nd:YLF lasers. All its lasers are designed and manufactured by Litron in Rugby, England.

Table 2.9: Seeding particles in gas flows; adapted from Melling (1997).

Material	d_p, μm	Laser	Pulse energy/time mJ/ns	Laser sheet thickness (mm)	Reference
TiO_2	<1	Nd:YAG	10/20	0.3	Reuss *et al.* (1989)
TiO_2,ZrO_2	0.7-1	Nd:YAG	110/12	n/a	Paone *et al.* (1996)
Al_2O_3	0.3	Nd:YAG	$400/n/a$	0.2	Muniz *et al.* (1996)
Al_2O_3	3	Nd:YAG	9/6	n/a	Anderson *et al.* (1996)
Al_2O_3	0.8	Ruby	$20/n/a$	≈ 1	Krothapalli *et al.* (1996)
Polycrystalline	30	Nd:YAG	135/6	n/a	Grant *et al.* (1994)
Glass	30	Ruby	30/30	n/a	Schmidt & Loffler (1993)
Oil smoke	1	Ruby	$5000/n/a$	n/a	Stewart et al (1996)
Corn oil	1-2	Nd:YAG	$100/n/a$	n/a	Jakobsen et al (1994)
Oil	1-2	Nd:YAG	$120/n/a$	n/a	Westerweel et al (1993)
Olive oil	1.06	Nd:YAG	70/16	0.5	Hocker & Kompenhans (1991)

Table 2.10: Main characteristics of a laser used in the PIV analysis

Description	**Value**
Laser model	NANO-T-120-15
Beam diameter	5(mm)
Optimum Q−Switch delay	≈144 (μs)
Repetition rate	Up to 15(Hz)
Output energy (mJ/pulse) @15(Hz), 532(nm)	
@100% Power settings	140
@ 95% Power settings	110
@ 90% Power settings	85
@ 80% Power settings	27
@ 70% Power settings	1

positive lens was used to focus the laser beam into a thin waist, with focal point located at the axis of symmetry of the flow. The average laser energy at the exit port of the laser was circa 20 (mJ/pulse). The thickness of the laser sheet was measured in the same manner as for the PLIF beam and found to be around 0.5(mm) at $1/e^2$. Scattered light was collected with the same camera and a lens as in Rayleigh thermometry. Perspective distortion was corrected by using a three dimensional imaging target. The separation time between the two PIV frames was 60(μs).

The swirling air coflow was seeded with Al_2O_3 particles with a diameter of 1 μm. Velocity tracing accuracy errors for particles with the Stokes number[22] $S_{tk} << 1$ are below 1% Tropea *et al.* (2007). Velocity fields were computed from particle images by using a commercial PIV software provided by LaVision Inc. (DaVis 7.2). A multi

[22]The Stokes number is a dimensionless number corresponding to the behaviour of a particle suspended in a fluid flow. Stokes number is defined as the ratio of the stopping distance of a particle to a characteristic dimension of the obstacle $S_{tk} = \frac{\tau U_0}{d_p}$, where U_0 is the fluid velocity of the flow well away from the obstacle.

step cross−correlation algorithm was used with an initial interrogation window of 64×64 pixels and resulting interrogation window of 32×32 pixels. This corresponded to a spatial resolution of 2 mm and velocity vector spacing of 1 (mm).

2.8 Measurement uncertainty

The focus of this section is to summarize the different effects of uncertainties on the experimental data and discuss various sources of error and possible steps that can be obtained in order to decrease uncertainty in the measurements. There are many types of error that can contribute to the final results, the various components of the uncertainty and their contributions have to be, therefore, determined. The components of the uncertainty can be divided in several groups e.g. reference standard uncertainty, drifts of readings, inaccuracies in calibration etc. For instance, the reference standard uncertainty can be related to the thermal and pressure influence on the measurements and system, drifts of reading can also be related to various sources. The reference standard uncertainty can usually be estimated from known information either from a manufacturer or from precalibrated measurement devices. The drifts of reading can be estimated by using a statistical analysis, usually by repeated readings. There are also many so called analysis errors that can contribute to the uncertainty in the final values, which are derived for a measured quantity. In fact, in many cases this could lead to systematic errors rather than random ones, which also can be evaluated by using statistical approaches.

2.8.1 Uncertainty in flow rate measurements

During experiments the air referred as to swirling component was measured by KDG Rotameter Series 2000 variable−area flowmeter, which was individually calibrated to accuracy of Class 1.6 (VDI/VDE3513)[23], i.e. ±1.2% of indicated flow and plus ±10.4% full scale reading. For actual flow of 750, 550 and 400(l/min) for all three swirl numbers using a flowmeter with a full scale of 2000 (l/min) yields: For S=1.07 the total tolerance is 1.2% of 750 l/min + 0.4% of 2000 l/min = ± 17(l/min). For S=0.58 the total tolerance is 1.2% of 550 (l/min) + 0.4% of 2000 (l/min) = ±14.4 (l/min) for S=0.58. For S=0.3 the total tolerance is 1.2% of 450(l/min) + 0.4% of 2000(l/min) =±13.4(l/min). The actual flow rate in a swirling component of air it was determined as 750±17 (S=1.07), 550±14.4 (S=0.58) and 450±13.4 (S=0.3), which lead to uncertainties in the measurements of the swirl component of the flow as ±2.27%, ±2.62% and ±2.98%.

Finally, assuming that there is no error in the measurements of the axial flow component the swirl number uncertainty can be written as S=1.07±0.024, S=0.58±0.015 and S=0.3±0.0089. However, there is also error accociated with the measurements of the axial flow component, which must also be taken into account. The axial component of air was measured by Fisher Control Limited flowmeter rated at a maximum flow of 1000(l/min). Given that the flow meter was calibrated to accuracy of Class 1.6, and according to the mentioned procedure the total tolerance is as follows: For S=1.07 the total tolerance is 1.2% of 150(l/min) + 0.4% of 1000(l/min) =±5.8(l/min). For S=0.58 the total tolerance

[23] Variable−area flowmeters. Maximum permissible error, G, of the system. The Association of German Engineers (http://www.vdi.eu/).

Table 2.11: Uncertainties in main variables.

S	Units of measure	Computed uncertainty
0.3	n/d	0.3±0.0152
0.58	n/d	0.58±0.0288
1.07	n/d	1.07±0.0657
Re_{air}	n/d	28662±1456 for S=0.3 28662±1422 for S=0.58 28662±1760 for S=1.07
U_{air}	m/s	8.46±0.430 for S= 0.3 8.46±0.420 for S= 0.58 8.46±0.519 for S=1.07

is 1.2% of 350 + 0.4% of 1000 =±8.2(l/min). For S=0.3 the total tolerance is 1.2% of 500(l/min) + 0.4% of 1000(l/min) =±10(l/min). This leads to uncertainties in the measurements of the axial component of the flow as ±3.87%, ±2.34% and ±2%. A combined effect of measurement uncertainty for both the axial and the radial components can be computed as the sum of modulus of the individual components, i.e. ±6.14% (S=1.07), ±4.96% (S=0.58), and ±5.08% (S=0.3).

The final uncertainty in measurement of swirl number, Reynolds number, air velocity and the velocity in the fuel pipe (acetone seeded in air velocity) can then be computed from the instrument uncertainties. The flow rate of the mixture of acetone and air was measured by flowmeter from Platon Inc. (NGXV series) with the accuracy of ±1.25%. The fluorescent intensity variations due to the temperature were accounted by measuring the temperature in the test volume by a commercial thermometer RS−1313 with accuracy of ±0.05% of measured value + 0.5° and by an N−type thermocouple (tolerance class one) 1.5%. However, it should be noted that the manufacturers want to present their products in the most favourable, but honest manner and, therefore, the accuracy quoted is likely to be as good as can be achieved by the manufacturing methods and hence should not be taken for granted. It should also be noted that the measurement uncertainty is task−specific and it is impossible to evaluate all possible error−related issues that can be found in experimental measurements. The uncertainty analysis is a broad range and could be the source of an entire chapter on its own. The various uncertainties that are related to the measurements are summarized in a Table 2.11.

2.8.2 Uncertainty in scalar measurements

The temperature variance in the control volume was found to be uniform and within 1(K). The fluorescent intensity due to temperature variations was found to be less than 0.4% based on 0.36%/K decay for 266(nm) Thurber (1999). The temperature in an immersed, stirred, isothermal bath of hot water was measured by the same equipment, which was used in temperature measurements in the control volume.

The resolution requirements may vary from case to case and are related to turbulent length scales. In high Reynolds numbers turbulence, the minimum turbulent eddies can be quite low e.g. 90-100(μm). This imposes certain requirements and in some cases cannot be achieved. The actual spatial resolution of the optical system should resolve the Kolmogorov or Batchelor scales. It should be noted that the actual spatial resolution is not

Table 2.12: Uncertainties in scalar field measurements

Variable	Units of measure	Computed uncertainty
$\left\langle z''^2 \right\rangle$	%	1.5−2.6 for S= 0.3 0.8−1.6 for S= 0.58 1−1.5 for S=1.07
$\left\langle (\nabla z)^2 \right\rangle$	%	6.1−19.2 for S= 0.3 8.4−11 for S= 0.58 6.8−7.5 for S=1.07

Note: $\left\langle z''^2 \right\rangle$ and $\left\langle (\nabla z)^2 \right\rangle$ are percentages (%) errors of the variances of the mixture fraction and of the scalar spatial derivative after using Wiener. The procedure of computing the uncertainties is given in Chapter 6.6.2.

a nominal resolution, which is quantified by a magnification. This means that if a nominal resolution was defined by the magnification e.g. 0.0263 (mm/pixel) the actual resolution would not be 0.0263 (mm/pixel). Optical aberrations lead to blurring of the acquired image, which is produced by an image−forming optical system (a CCD camera and a lens). In fact, the image can be corrected for optical aberrations if the point spread function (PSF) is known. In practice, the PSF can be measured in a straightforward manner and a number of techniques exists. Since optical systems are corrupted with different optical aberrations and imperfections a filtering procedure must be used to remove noise from the acquired data. The filtering errors that were computed in this work were in the range of 10-20% depending on the case. There are many digital filters that can be used to reduce the amount of noise that is present in the experimental data. However, it was proven that the most suitable filtering technique was based on the Wiener filter and hence was chosen in this work. The detailed description of the denoising procedure and the PSF measurements are given in Chapter 6.6.2. Uncertainties in scalar field measurements are summarised in Table 2.12

2.8.3 Uncertainty in temperature measurements

The Rayleigh thermometry used in this work utilizes the ratio of signal measured in air and in the combustion region. The first signal is the reference signal S_{mix} taken at known temperature T_{air}. The second signal S_{mix} is the Rayleigh signal taken at unknown temperature T_f. The flame temperature, which is deduced from the following equation will have an intrinsic sensitivity to a number of parameters.

$$T_f = \frac{\sigma_{mix}}{\sigma_{air}} \frac{S_{air}}{S_{mix}} T_{air} \tag{2.25}$$

It will depend on the Rayleigh scattering cross section of the mixture σ_{mix} and more precisely on the ratio $\delta(z)$ of the Rayleigh scattering cross section of the mixture to the scattering cross section of air σ_{air}. A propagation error analysis can be used to asses different uncertainness in the temperature measurements as a function of the mixture fraction z. Thus, the equation above can be written as follows; where $S_{am}(z) = S_{air}/S_{mix}$ is the ratio of the reference signal to the measured signal.

$$T_f(z) = \delta(z)\, S_{am}(z)\, T_{air} \tag{2.26}$$

If variables have errors, which are uncorrelated and random, then the following equation can be written for uncertainty in temperature measurements.

$$\Delta T_f^2(z) = \left(\frac{\partial T_f(z)}{\partial \delta(z)}\Delta\delta\right)^2 + \left(\frac{\partial T_f(z)}{\partial S_{am}(z)}\Delta S_{am}\right)^2 + \left(\frac{\partial T_f(z)}{\partial T_{air}}\Delta T_{air}\right)^2 \tag{2.27}$$

The last therm in the equation above is equal zero, because ΔT_{air}=0 (no fluctuations in reference temperature). After some manipulations and omitting the dependence on z it leads to.

$$\frac{\partial T_f}{\partial \delta} = S_{am} T_{air} \tag{2.28}$$

$$\frac{\partial T_f}{\partial S_{am}} = \delta T_{air} \tag{2.29}$$

$$\left(\frac{\Delta T_f}{T_f}\right)^2 = \frac{\Delta\delta^2 (S_{am}T_{air})^2}{\delta^2 (S_{am}T_{air})^2} + \frac{\Delta S_{am}^2 (S_{am}T_{air})^2}{S_{am}^2 (S_{am}T_{air})^2} \tag{2.30}$$

$$\frac{\Delta T_f}{T_f} = \sqrt{\left(\frac{\Delta\delta}{\delta}\right)^2 + \left(\frac{\Delta S_{am}}{S_{am}}\right)^2} \tag{2.31}$$

The relative uncertainty in temperature measurements $\Delta T_f/T_f$ depends on the uncertainty in the ratio of Rayleigh scattering cross section area $\Delta\delta/\delta$ and on the fluctuations of the laser power, which is expressed here as $\Delta S_{am}/S_{am}$. Applying the same procedure to the ratio of Rayleigh signal and the signal from combustion zone and neglecting fluctuations in the reference signal (if the mean signal is used) leads to the following expression.

$$S_{am} = \frac{S_{air}}{S_{mix}} => \Delta S_{am} = \left(\frac{\partial S_{am}}{\partial S_{air}}\Delta S_{air}\right)^2 + \left(\frac{\partial S_{am}}{\partial S_{mix}}\Delta S_{mix}\right)^2 \tag{2.32}$$

$$\Delta S_{am} = \left(-\frac{S_{air}}{S_{mix}^2}\Delta S_{mix}\right)^2 \tag{2.33}$$

$$\frac{\Delta S_{am}}{S_{am}} = \frac{\left(\frac{\Delta S_{mix}}{S_{mix}}\right)^2 \left(-\frac{S_{air}}{S_{mix}}\right)^2}{\left(\frac{S_{air}}{S_{mix}}\right)^2} = \left(\frac{\Delta S_{mix}}{S_{mix}}\right)^2 \tag{2.34}$$

$$\frac{\Delta T}{T} = \sqrt{\left(\frac{\Delta\delta}{\delta}\right)^2 + \left(\frac{\Delta S_{mix}}{S_{mix}}\right)^2} \tag{2.35}$$

Contribution from the fluctuations in laser power $\Delta S_{mix}/S_{mix}$ is minor compared to $\Delta\delta/\delta$, which can be directly computed from the laminar flamelet solution. In a broad sense the ratio $\Delta\delta/\delta$ is also dependent on the strain rate (or scalar dissipation), because the laminar flamelet solution is dependent on the strain rate. It is, therefore, suggested that the main source of error lays in the discrepancy between the ratio of Rayleigh scattering cross sections or the departure from 'ideal' cross sectional ratio, which is equal to one.

Figure 2.12 shows the temperature as a function of mixture fraction and the ratio of Rayleigh scattering cross section of the mixture to the air, obtained from opposed−jet simulation for DLR fuel as a function of strain rate The opposed−jet simulation was carried out with the GRI-3.0 detailed chemical mechanism. Temperatures of fuel and oxidizer were held constant for all strain rates and equal to 300(K). The strain rate was ranged from 100 to 250 (1/s), where the strain rate of 250 led to extinction. Nominal strain rate was directly computed from opposed−jet simulations as given by Pope[24] as $\dot{\varepsilon} = (VFUE + VOXI) / (XEND \cdot GFAC)$. Where $VFUE, VOXI$ are velocities in the air and the fuel streams in opposite−flow problem, $XEND$ is the distance between fuel and air streams and $GFAC$ is a multiplying factor used to modify all gas−phase reaction rates[25]. In all the simulations the $GFAC = 1$ and the strain rate varied only by varying the velocity in the fuel and air streams. The distance between streams was $XEND = 2.0$(sm). In all computational cases, the ratio of Rayleigh scattering cross section of the mixture (fuel) to the air laid within 12% range, while for the high temperature region ($0.15 < z < 0.2$) the error was less than 2%. This indicates that no significant variations of the ratio of Rayleigh scattering cross sections as a function of the strain rate were found.

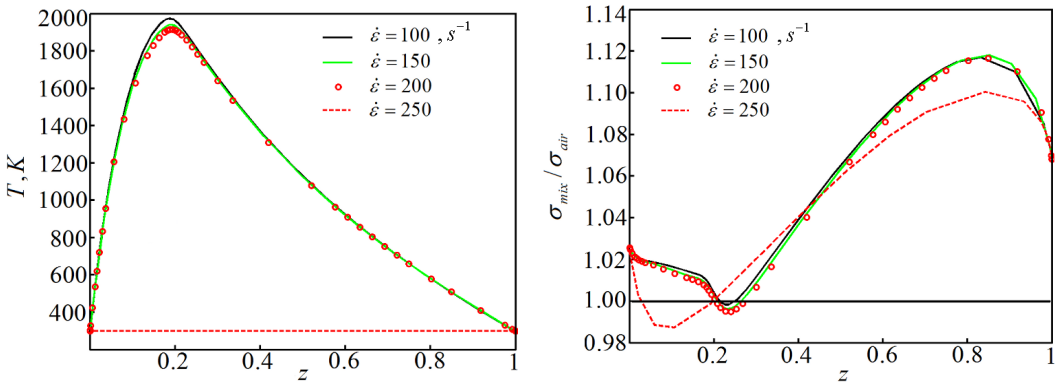

Figure 2.12: Temperature as a function of mixture fraction (left) and the ratio of Rayleigh scattering cross section of the mixture to the air (right), obtained from opposite−flow simulation for DLR fuel as a function of strain rate (1/s). Temperatures of fuel and oxidiser were 300(K) and GRI-3.0 detailed chemical mechanism was used. Strain rate varied from 100 to 250 (1/s), where for 250 (1/s) extinction was observed.

A 3D model of experimental setup for PLIF, Rayleigh and PIV experiments is given in Figure 2.13, Figure 2.14 and in Figure 2.15. The following definitions are given for Figure 2.13.

- 1. A cylindrical positive lens with focal length f−310(mm).
- 2. A dichroic mirror (transparent for 532nm).
- 3. A frequency doubled Q−switched Nd:YAG laser Quanta−Ray PRO−Series, PRO-270-10 from Spectra Physics Inc.

[24] S.B. Pope, MAE643, Spring 2006, Project 4: Non-Premixed Laminar Flames project notes; Cornell University.

[25] All gas−phase reaction rate are computed by the GAS−PHASE KINETICS preprocessors used by the CHEMKIN® software.

- 4. A beam damper (used to block laser beam and prevent reflections).
- 5. A vertical traverse handle and mechanism.
- 6. A ruler.
- 7. A commercial thermometer RS−1313 with accuracy of ±0.05% of measured value +0.5°.
- 8. An electrical hob with manual control.
- 9. A water bath with hot water inside it (+45°).
- 10. An acetone seeder (air supply was provided via standard flexible ducts).
- 11. A 3(mm) N−type thermocouple with Nicrosil sheath (tolerance class one) 1.5% for temperature control in the seeder.
- 12. A 12 bit CCD camera Imager Intense from LaVision© Inc. with maximum recording rate of 10(Hz) and maximum resolution of 1376×1040 pixels.
- 13. A band pass BG3 filter.
- 14. The swirl−stabilized burner.
- 15. Flow test section.

Definitions below are given for Figure 2.14.

- 1. A vertical traverse (milling table).
- 2. A cylindrical positive lens with focal length f−310(mm).
- 3. A laser mirror $\phi = 25.4$(mm) for $\lambda = 532$(nm).
- 4. A Q−switched Nd:YAG frequency−quadrupled (266nm) laser from Continuum Inc.
- 5. A CCD camera (the same as in PLIF experiments).
- 6. A vertical traverse for the CCD camera.
- 7. A beam damper (used to block laser beam and prevent reflections).
- 8. The swirl−stabilized burner.
- 9. Flow test section.

Definitions below are given for Figure 2.15.

- 1. A laser mirror $\phi = 25.4$(mm) for $\lambda = 532$(nm).
- 2. A plano−concave with focal length f=-20(mm) lens.
- 3. A plano−convex with focal length f=200(mm) lens.
- 4. A laser mirror $\phi = 25.4$(mm) for $\lambda = 532$(nm).
- 5. A frequency−doubled (532nm) dual−pulsed Nd:YAG laser from Litron Lasers Ltd.
- 6. A CCD camera (the same as in PLIF experiments).
- 7. Laser sheet.
- 8. The swirl−stabilized burner.
- 9. A vertical traverse (milling table).
- 10. A cylindrical positive lens with focal length f−310(mm).

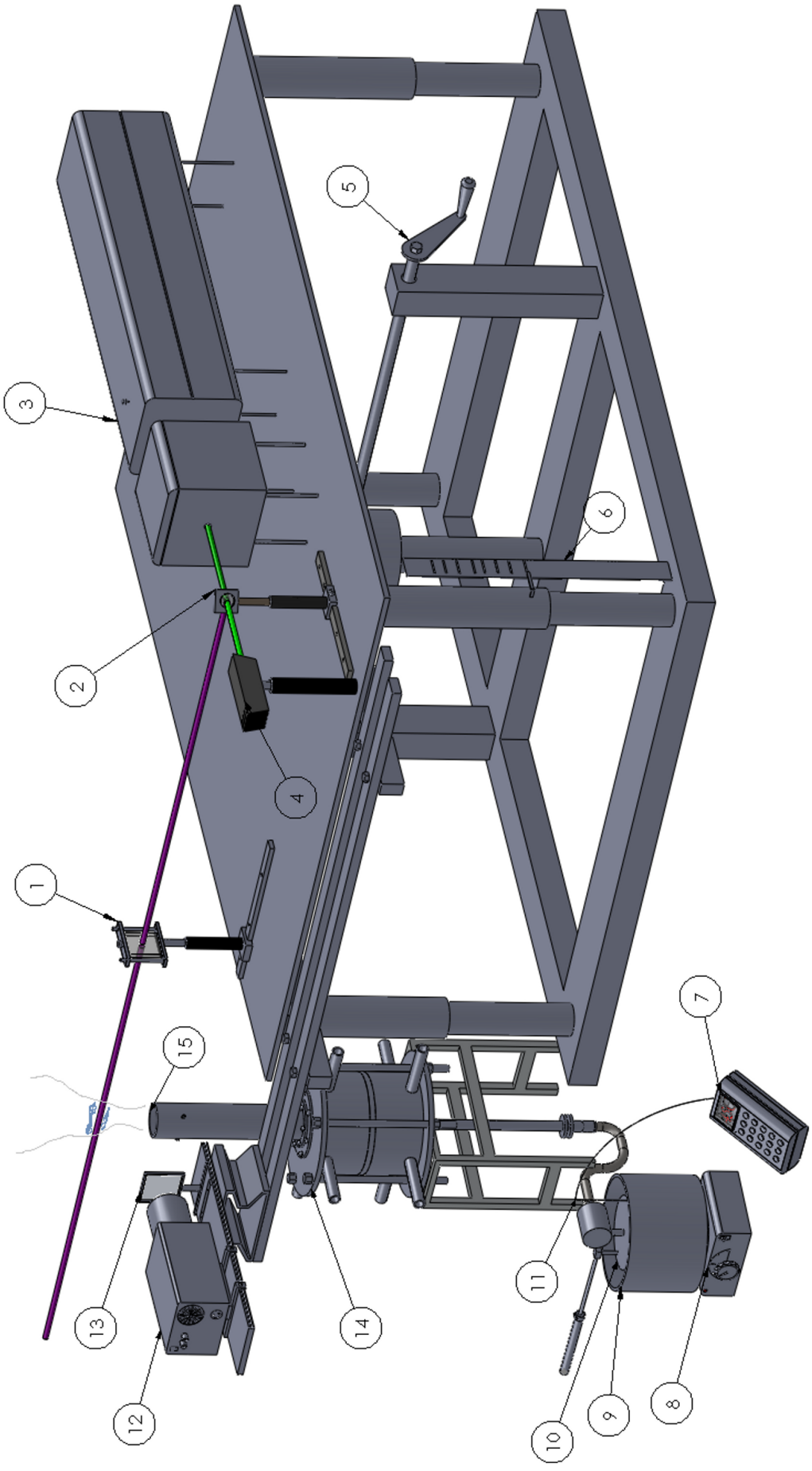

Figure 2.13: A 3D model of the experimental setup used for PLIF experiments.

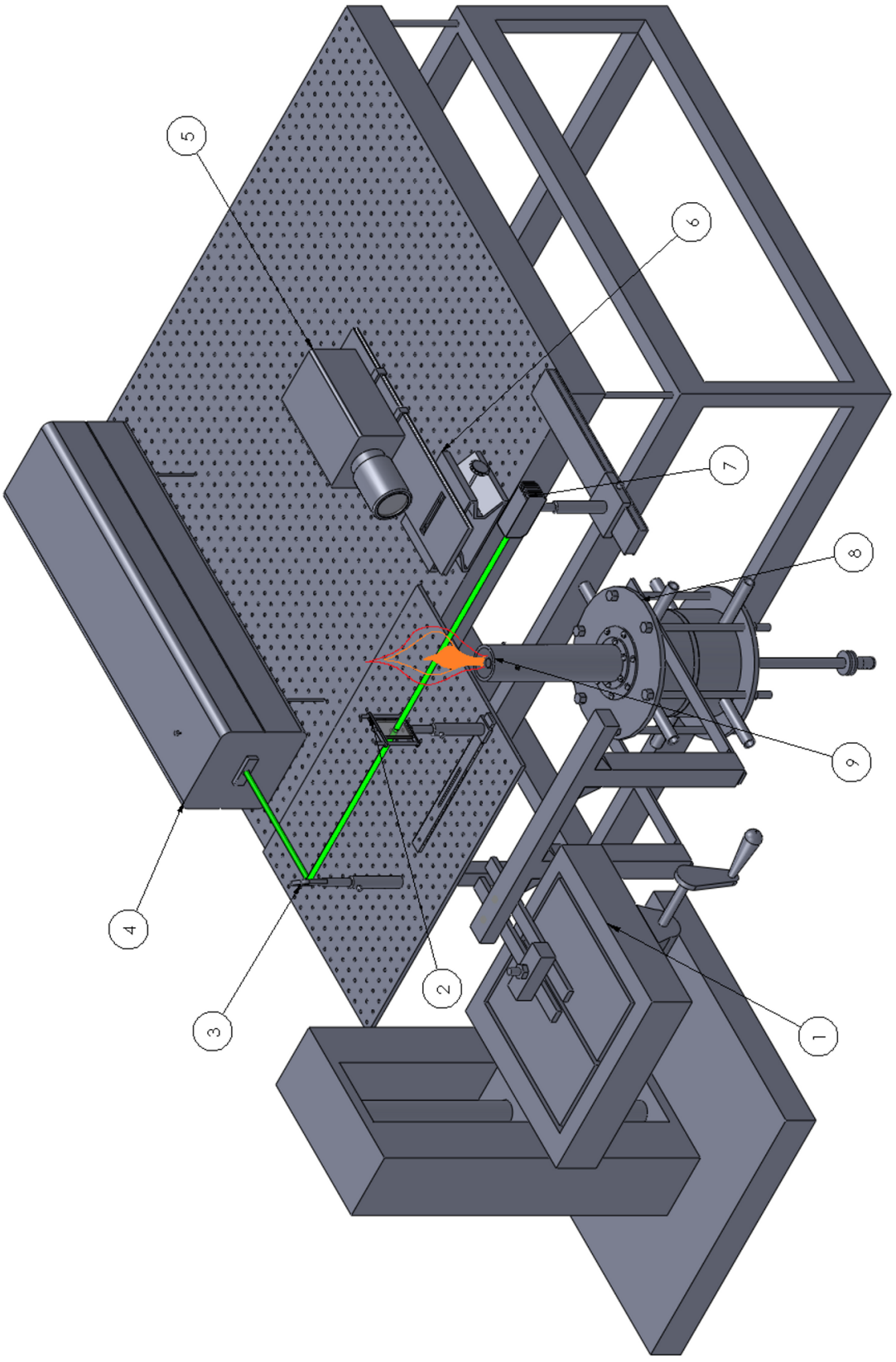

Figure 2.14: A 3D model of the experimental setup used for Rayleigh thermometry experiments.

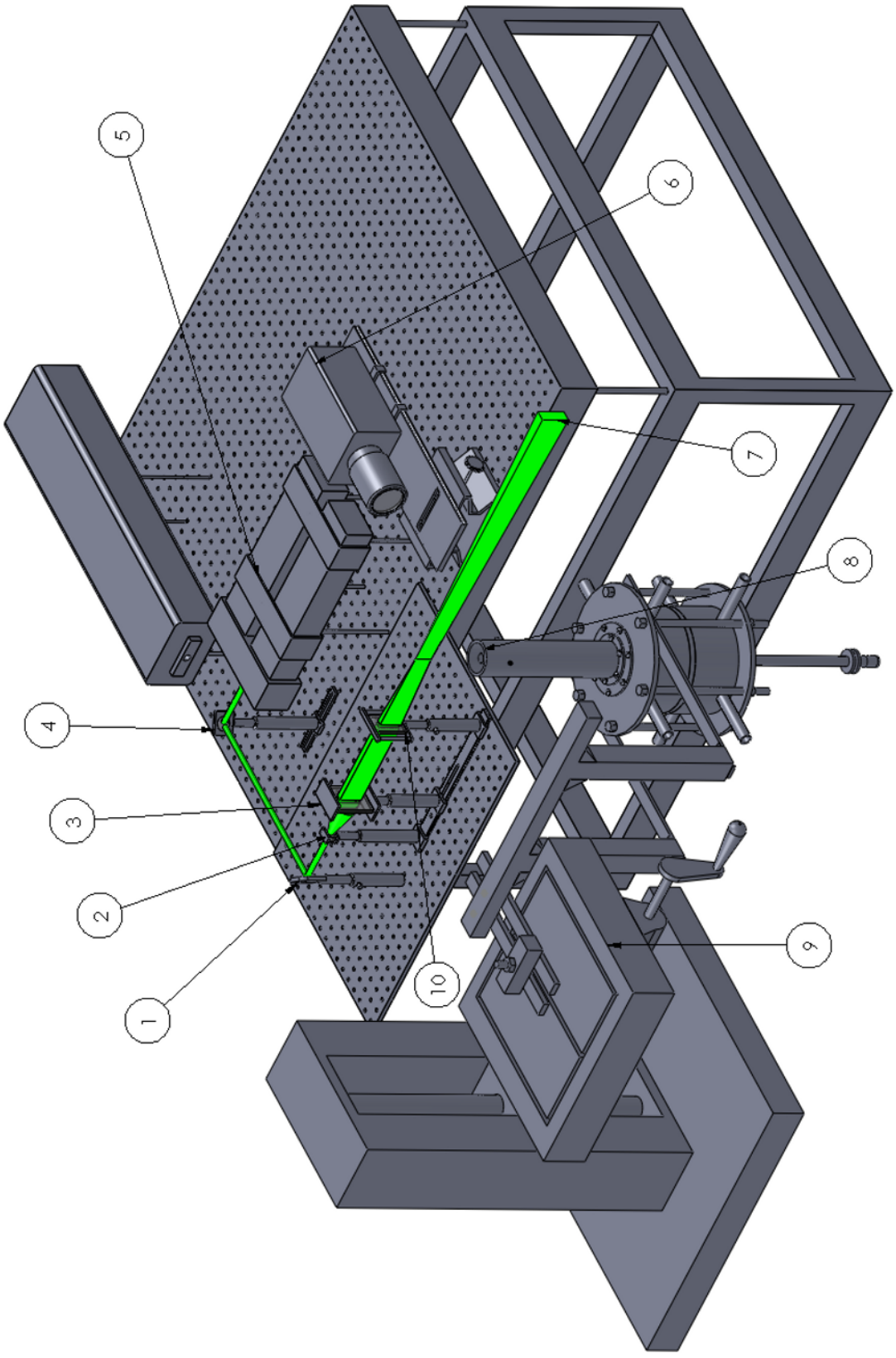

Figure 2.15: A 3D model of the experimental setup used for PIV experiments.

2.9 Summary

This chapter presented the experimental setup used in this work. The experimental setup was based on the atmospheric swirl−stabilised burner, on two different laser excitation sources and on the laser sheet optics. The reason for separate selection of two different excitation sources was that the signal−to−noise ratio during Rayleigh scattering experiments was typically less than that of PLIF experiments. As a result, a higher power laser was required for accurate and reliable Rayleigh measurements. The same CCD camera with an array of 1376×1040 pixels and with pixel dimensions of 6.45(μm) was used in both experiments. Both lasers in PLIF and Rayleigh scattering experiments were controlled electronically from the same personal computer running Windows XP©, which was provided by LaVision Inc.

3 Data processing

In scientific work, those who refuse to
go beyond fact rarely get as far as fact.

Thomas Huxley

Digital images are usually affected by various sources of noise, which results in intensity values that do not represent the true intensities of the real recording quantity. This can lead to significant errors in the measurements of mixture fraction, temperature fields etc. and hence a denoising procedure must be used to eliminate or at least to decrease the level of noise in the acquired images, which are obtained during experiments. In this chapter, a denoising procedure, which is known as the Kolmogorov−Wiener[1] filtering theory, is introduced along with a concept of deconvolution using a point spread function for the processing of raw mixture fraction images, obtained from planar laser−induced fluorescence experiments. In addition, the introduction to denoising of the temperature data obtained from Rayleigh thermometry is also outlined.

3.1 Image quality and spatial resolution

The most commonly used cameras in imaging experiments are currently based on CCD image sensors. Therefore, image quality is the most important characteristics of all imaging systems that must be taken into account. The image quality is related to the actual spatial resolution and to the ability to transmit contrast from a real object to the camera detector. The nominal resolution of any optical system is typically determined by using a calibrating target with known spatial resolution. However, in several applications, the nominal spatial resolution (or magnification) is not a limiting factor and differs from the so−called 'real' spatial resolution. For instance, in mixture fraction gradient measurements (or scalar dissipation rate measurements) there is a parameter that can represent the actual optical resolution.

This parameter is called a point spread function or simply a -PSF. The PSF is defined as intensity distribution at an image plane, produced by imaging of infinitesimally small portion of light. If there was no aberration in the optical system then the resulting intensity distribution in the image plane would be the same as in the real object. However, in most cases the measured object in the image plane will be smeared or blurred due to optical imperfections and aberrations. In diffraction limit system, i.e. an ideal system without any aberrations, imperfection and focusing errors, the blur spot diameter will be an Airy[2] disk diameter. The PSF directly affects the resolution of an image and the image can

[1] Norbert Wiener (26.11.1894−18.03.1964) was an American mathematician and a Professor of Mathematics at MIT.

[2] Sir George Biddell Airy (27.07.1801−02.01.1892) was an English mathematician and astronomer.

then be seen as a convolution of the image of the true object and the PSF. If there is no distortion in the optical system, the image plane coordinates are simply related to the object plane through magnification measured in *pixels/mm*. Figure 3.1 show a principle of image formation and an effect of PSF on the image.

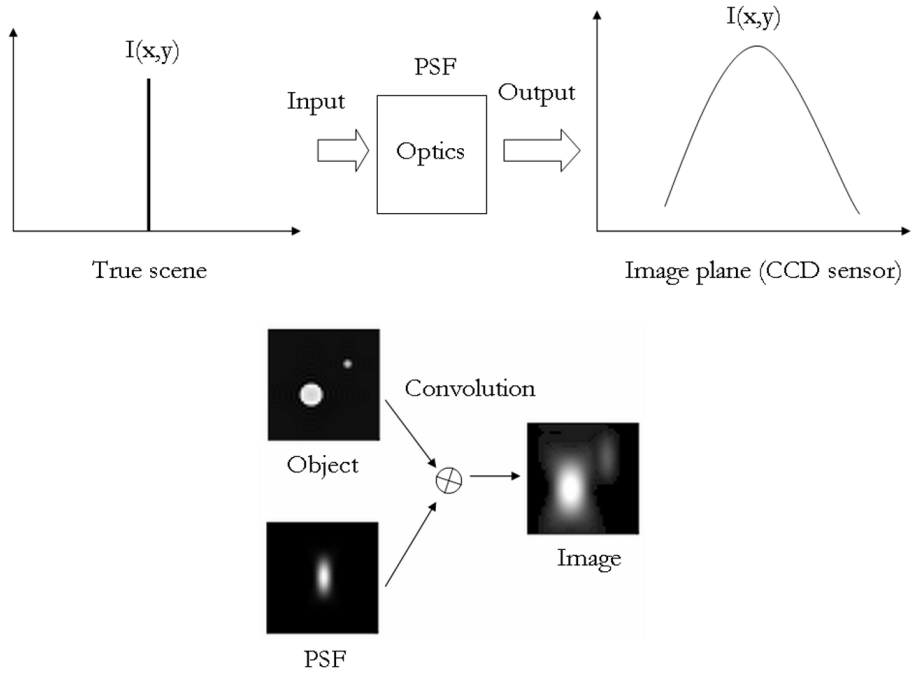

Figure 3.1: Image formation in a CCD camera. Point spread function (PSF) is described as two−dimensional distribution of light intensity in an image plane for point sources of light (delta function).

Therefore, in most real imaging systems, the image appears to be distorted and the smallest objects that can be imaged by the CCD array are directly related to the shape of the PSF. The PSF is related to another parameter, which is called an optical transfer function (OTF) via a modulation transfer function (MTF). The OTF is defined as the ability to transfer contrast from a real object to the image plane at various spatial frequencies. The OTF can be measured by using an optical target with different spatial frequencies, e.g. USAF 1951 Chart[3](Fig. 3.2). The chart consists of a series of elements having two sets of lines. Each set of lines consists of three lines separated by space equal to the line width. Elements are arranged in groups of six bars aligned vertically (3 bars) and horizontally of the same size. Resolution then can be defined as a threshold i.e. the last group of bars that can be seen and correctly counted in both horizontal and vertical directions. It should also be noted that the bars must be clearly identified in order to be able to determine the spatial resolution correctly. The modulation transfer function is generally the OTF magnitude with phase ignored. The MTF decreases with increasing spatial frequency, which automatically implies that a level of contrast reduction is inevitable. The MTF is limited by the lens aperture diffraction and hence there is an optimal aperture for any lens and image sensor size. The MTF can be measured by imaging objects that have a sine wave irradiance variation at different spatial frequencies. Image contrast is

[3]The 1951 USAF resolution test chart is a resolution test pattern conforming to MIL-STD-150A standard, set by US Air Force in 1951.

calculated for each frequency and finally the MTF is obtained.

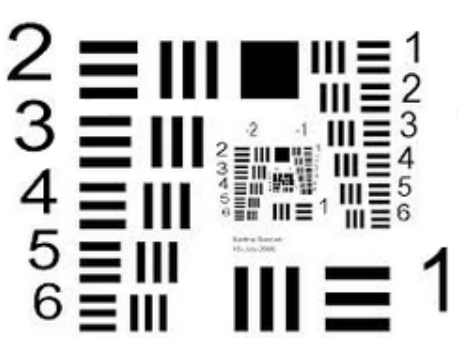

Figure 3.2: USAF 1951 Chart.

In a perfect optical system a maximum spatial resolution can be computed by using the Nyquist[4] theorem[5], which states that aliasing can be avoided if the Nyquist frequency is twice greater than the bandwidth of the signal being sampled. Taking the example of a current CCD array of 1376×1040 pixels and assuming that the pixel size is 26(μm) the Nyquist frequency is 19.23 line pairs (black and white lines) per mm. According to the Nyquist's theorem, in a perfect system it should be possible to resolve fully nearly 688 line pairs per image width. The image width 26×1376×0.001 is equal to 35.78 (mm) and hence the Nyquist's frequency is equal to 688/35.78 = 19.23 lines per mm. However, in reality due to optical aberrations, imperfections and system deterioration the MTF can significantly deviate from the ideal modulation transfer function that was specified by a manufacturer. Kychakoff *et al.* (1984) discussed the importance of the MTF for quantifying the optical system resolution. Kychakoff also introduced the cut−off frequency of the MTF. The cut−off frequency is a limiting frequency above which the system is unable to transfer contrast and is often taken as the frequency where MTF is equal to 4%.

Other methods for MTF measurements involve knife−edge scanning technique and a slant edge method. Knife−edge technique uses a sharp knife−edge aligned with the rows or columns of the detector (Fig. 3.3). The knife−edge is moved along a line perpendicular to its edge. A single pixel near the edge is monitored and the frequency is recorded as a function of discrete steps. The displacement must be small enough with respect to the pixel size in order to avoid aliasing. A function of pixel intensity versus knife−edge displacement is the Step Response Function (SRF) and its derivative is the Line Spread Function (LSF). The Fourier transform of the LSF is the MTF. The SRF and the LSF are related via the following relationship.

$$LSF(x) = \frac{dSRF(x)}{dx} \tag{3.1}$$

The LSF is the Gaussian function (if error function fit is used) that can also be approximated by the Gaussian function with known standard deviation. If standard deviation is known then it is possible to use an analytical expression for the Fourier transform of the

[4]Harry Nyquist (1889−1976, Sweeden) was an important contributor to information theory.

[5]The theorem shows that a bandlimited analog signal can be perfectly reconstructed from an infinite sequence of samples if the sampling rate exceeds 2B samples per second, where B is the highest frequency of the original signal.

Gaussian function. The LSF can then be approximated by the Gaussian function and its Fourier transform are given by:

$$LSF(x) = \frac{1}{\sigma\sqrt{2\pi}} e^{\frac{-x^2}{2\sigma^2}} \tag{3.2}$$

$$MTF(x) = e^{\frac{-\omega^2\sigma^2}{2}} \tag{3.3}$$

The scanning knife−edge technique is well−established method, which on the other hand, suffers from several disadvantages. The most important one is the longest measurement time. There is also the need for precise equipment that is used to control the knife−edge movement. An alternative method that can be used to compute the MTF is specified in the International Standard 12233:2000 (Photography. Electronic still−picture cameras. Resolution measurements). This method is based on only one image acquisition and was named as the Slant Edge Target Technique. The slant edge method uses a digital camera sensor for measuring illuminance. The same setup as for the step response function (scanning knife−edge) can be used in slant edge method as well. In this work, the slant edge target method was used and several lenses were tested. The reason for this choice was that the Slang Edge Target Technique was the fastest method for the MTF evaluation among others.

The 50% MTF computed by the slant edge method resulted in 1/3 spatial frequency i.e. ≈300(μm). The nominal resolution that was computed by calibration target was 26(μm), while in fact the actual resolution of the optical system was ten times larger. Even though, this might be seen as inadequate spatial resolution for the scalar dissipation measurements the acquired images can be corrected for blur, caused by the low MTF.

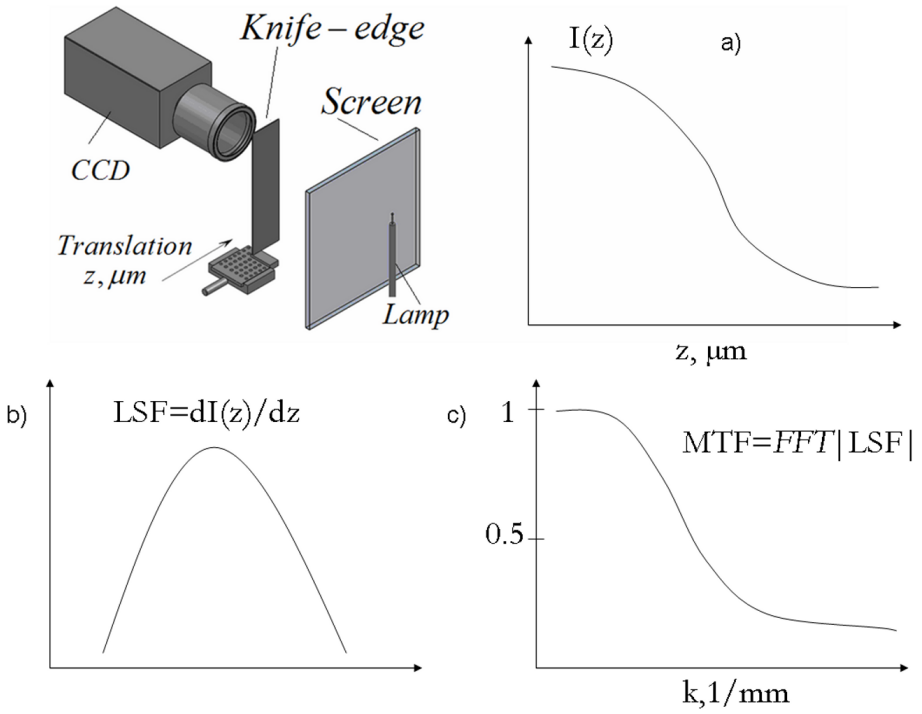

Figure 3.3: Knife−edge scanning technique and a principle of modulation transfer function (MTF) computation. Note that FFT stands for Fast Fourier Transform.

3.2 Noise reduction

Images acquired during experiments are stored in a computer memory in the form of an intensity matrix, which contains intensity values obtained from the CCD camera sensor. The values of the matrix (intensity matrix) contain integer values (ranging from 0 to 4095[6]) that represent the intensity of light coming from the measured control volume[7]. It is well−known that the intensity matrix does not represent the 'true' intensity of an object due to various sources of noise, which may be related to camera dark current, random fluctuations in power etc. It is, therefore, apparent that high quality and robust noise reduction mechanisms are needed, while retaining at the same time image sharpness and details.

3.2.1 Laser−induced fluorescence

The raw images that were recorded during PLIF experiments were corrected by using the following formula. This formula takes into account several different sources of noise.

$$I_{cor}(x,y) = \frac{I_{raw}(x,y) - I_{bgr}(x,y) - I_{dark}(x,y)}{L_{sh}(x,y)} \tag{3.4}$$

The background image $I_{bgr}(x,y)$ is usually acquired with the same camera settings and with the laser firing but without flow in the test volume. The background image that was acquired during experiments was blank, i.e. no photons were detected. This was achieved through BG3 filter that blocked ambient light. In addition, no reflections from the burner were observed. Reflections from the dust particles (due to 532(nm) light wavelength component in the laser beam) that were present in the test volume were also blocked by the BG3 filter. The dark image was acquired with a cap placed on the lens and then was simultaneously subtracted from recorded images during imaging. The average laser sheet intensity distribution was obtained by supplying acetone vapour through the axial fuel nozzle without air coflow and subsequent measuring the intensity in the jet potential core. The laser sheet profile measured in this way is negligibly different from the laser sheet profile that can be obtained from the dye cells (Soulopoulos, 2009). The variations of the profile from laser shot-−to−shot were negligible.

One of the main problems for scalar dissipation rate measurements is the noise that present in the raw mixture fraction fields. This noise may not create a problem when is mixture fraction only discussed, providing that the spatial resolution is adequate enough. However, the noise that comes from the optical aberrations can (and does) affect the scalar dissipation measurements. This can lead to an overestimation or underestimation of instantaneous scalar dissipation rate and, as a result, leads to wrong statistics if the noise is not properly accounted for. In this study, the effective resolution that was determined by the MTF and a noise filtering technique was proposed to be a proper criterion for quan-

[6] In this work, a CCD camera had bit depth of 12. Bit depth refers to the binary range of possible signal levels that are generated by the analogue-to-digital (A/D) converter. For example, 8−bit converters have range, ranging from 0 to 8^2-1 or 0−255 possible values. The bit depth of the A/D converter dictates the signal scale increment and hence, higher bit depth leads to a greater range of image information.

[7] Image files were stored in a computer in the form of LaVision format '.im7' as a set of sequences e.g. 'B00001.im7'. The image files contained all the required information including magnification, data, date and time etc. The intensity matrix was stored as integer 16-bits values (int16).

tifying the 'true' scalar dissipation measurements. In this work, the Wiener−Kolmogorov filtering procedure was used to reduce noise that was present in the measured data.

The Wiener filter is a filter that was proposed by Norbert Wiener in 1940 and published in 1949. The equivalent filter was also proposed by Kolmogorov independently and hence this procedure is sometimes called the Wiener−Kolmogorov filtering theory. This theory is based on a signal comparison between noiseless (measured) and noise corrupted signal. The input to the Wiener filter, assuming that the input signal and noise are stationary linear stochastic processes with known spectral characteristics, is given by a signal $f_M(r)$ corrupted with the noise $n(r)$ according to the following convolution, where vector $r = (x, y)$ corresponds to the vector in physical space, and $k = (u, v)$ corresponds to the vector in Fourier space (correspond to wave numbers in horizontal and vertical directions in 2D images).

$$f(r) = f_M(r) + n(r) \tag{3.5}$$

The filtering error is defined as the difference between the ideal noise−free signal $f(r)$ and the filter output $f_F(r)$ as.

$$e = f(r) - f_F(r) \tag{3.6}$$

The filter output can be written as a convolution integral as follows, where $g(r)$ is the filter, $f_M(r)$ is the measured image and $h(r)$ is the point spread function.

$$f_F(r) = \int_{-\infty}^{\infty} g(r - r^{'}) f_M(r^{'}) dr^{'} <=> F_F(k) = G(k) F_M(k) \tag{3.7}$$

$$f_M(r) = \int_{-\infty}^{\infty} h(r - r^{'}) f(r^{'}) dr^{'} + n(r) <=> H(k) F(k) + N(k) \tag{3.8}$$

$$f_S(r) = \int_{-\infty}^{\infty} h(r - r^{'}) f(r^{'}) dr <=> F_S(k) = H(k) F(k) \tag{3.9}$$

The means−square−error (m.s.e) is defined as expectation E over all possible realizations of image $f(r)$ and is written as.

$$e^2 = E\left[(f(r) - f_F(r))^2\right] \tag{3.10}$$

In other words, the Wiener filter is the function $\omega(r)$ that minimizes the m.s.e. when deconvolved with the point spread function. The detailed explanation of the minimization problem can be found e.g. in Petrou & Bosdogiani[8] (1999). Petrou & Bosdogiani proven that Fourier transform of the function $g(r)$ can be written in terms of the Fourier transform of the Wiener function and the Fourier transform of the PSF as follows, where $H(k)$ is the Fourier transform of the PSF (which is the measured MTF), $W(k)$ is the Fourier transform of the Wiener filter.

[8] Maria Petrou, Panagiota Bosdogianni. Image Processing: The Fundamentals. John Wiley & Sons Ltd., 1999.

$$G(k) = \frac{W(k)}{H(k)} \tag{3.11}$$

$$W(k) = \frac{|H(k)|^2}{|H(k)|^2 + \frac{S_n(k)}{S(k)}} \tag{3.12}$$

The spectrum of the blurred images can be written as $S_S(k) = |H(k)|^2 S(k)$ and hence the Fourier transform of the Wiener filter and the Fourier transform of the filtered and deblurred image can also be written as follows.

$$W(k) = \frac{S_S(k)}{S_S(k) + S_n(k)} \tag{3.13}$$

$$F_F(k) = \frac{F_M(k)W(k)}{H(k)} \tag{3.14}$$

In order to be able to compute the Wiener filter, the power spectral densities of both the noise−free image and the noise must be known, which are typically not available in advance. Petrou & Bosdogianni (1999), Krawczynski *et al.* (2002) suggested that a recorded set of images can be used to estimate the general trend of the true signal spectral density and the corresponding variations of the noise density. If the general trend of the true signal is known, then it will be possible to model the true signal for the wave numbers, where the noise contributes significantly.

In this work, the spectrum was computed from 1500 instantaneous images as the average of the square of the magnitude of the 2D Fast Fourier Transform of the mixture fraction fluctuations (mean mixture fraction image was subtracted from each instantaneous image). All instantaneous images were multiplied with a Hann window in order to reduce ringing effects, caused by abrupt cut−off of the image at its edges. This is a standard practice to remove possible high frequencies due to abrupt changes at the image borders. An example of a horizontal cut through the averaged 2D spectrum of the mixture fraction fluctuations, computed at $y/D_f = 3$ for $S = 0.58$ and the transfer function of the Wiener filter are shown in Figure 3.5. The model signal spectrum, which was modelled by an exponential function[9] is shown as a dashed line.

The Wiener filter is proven to be an adequate choice in removing noise that is present in the experimental data. An example of averaged 2D spectrum (logarithmic scale) of the fluctuations of the mixture fraction computed at $y/D_f = 3$ for $S = 0.58$ is shown in Figure 3.4. Single frequency component was shifted to the centre of the image and actual image (1376×1040) was zero padded to increase frequency resolution, so the resulting 2D spectrum was computed from the 2048×2048 matrix. At low wave numbers (centre of the image and outwards) the contour of the 2D spectrum is not circular, which demonstrates that the flow field is not homogeneous. As the wave number increases the 2D spectrum becomes circular, which illustrates that the flow field at smaller scales becomes homogeneous.

An example of a horizontal cut through the centre of the frequency plane along the radial direction of the averaged 2D spectrum (logarithmically scaled) of the fluctuations

[9] An exponential decay at high wave numbers is usually used to model turbulent spectrum e.g. by Pope (2000).

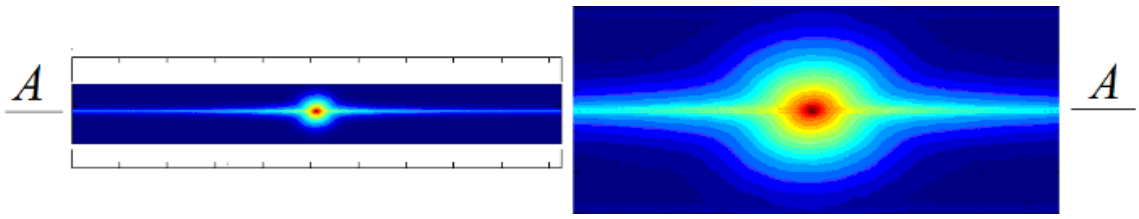

Figure 3.4: An example of averaged logarithm of 2D spectrum of the fluctuations of the mixture fraction computed at $y/D_f = 3$ for $S = 0.58$. Single frequency component was shifted to the centre of the image and original image was zero padded to increase frequency resolution. A horizontal cut through the averaged 2D spectrum is computed through the centre of the frequency plane A−A, which is shown in Figure 3.5.

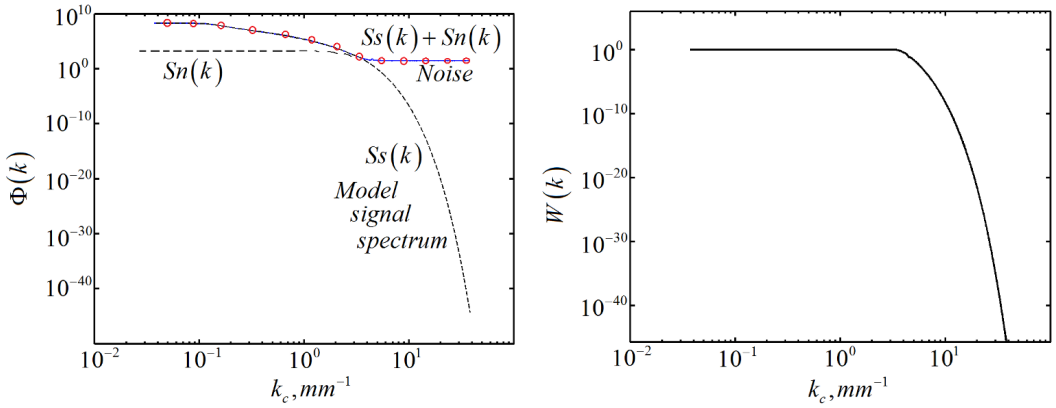

Figure 3.5: A horizontal cut (section A-A in Fig. 3.4) through the averaged 2D spectrum $\Phi(k)$ of the mixture fraction fluctuations at $y/D_f = 3$ for $S = 0.58$ shown here as $Ss(k) + Sn(k)$ (left) and the transfer function of the Wiener filter $W(k)$ (right). Modelled by an exponentiation function $Ss(k)$ and noise $Sn(k)$ spectra are also shown.

of the mixture fraction computed at $y/D_f = 1$ for $S = 0.3$ is shown in Figure 3.6. Two scales, which are Batchelor length scale computed from the dissipation spectrum and the modelling scale, are also shown in Figure 3.6. The modelling scale in the context of this work is referred to the wave number at which an exponential fit of the turbulent decay is used. In fact, the modelling scale should be as close to the Batchelor length scale as possible. If the Batchelor or Kolmogorov scales are not known then the scales can be determined from the averaged 2D scalar dissipation spectrum of the mixture fraction fluctuations as it was outlined earlier.

Using the modelled spectrum, the Wiener filter transfer function can be computed, and the 'true' scalar dissipation rate can be estimated. Figure 3.7 shows an example of centreline radial profiles of an instantaneous raw mixture fraction image and the corresponding filtered image as well as the radial derivatives of the same profile. It is clear from the figure that the small fluctuations in the mixture fraction space are due to the noise and hence a direct derivation of unfiltered mixture fraction fields leads to overestimated scalar and its dissipation statistics. Therefore, it is quite apparent that the raw mixture fraction images cannot be used to estimate the scalar dissipation rate and hence a filtering procedure must

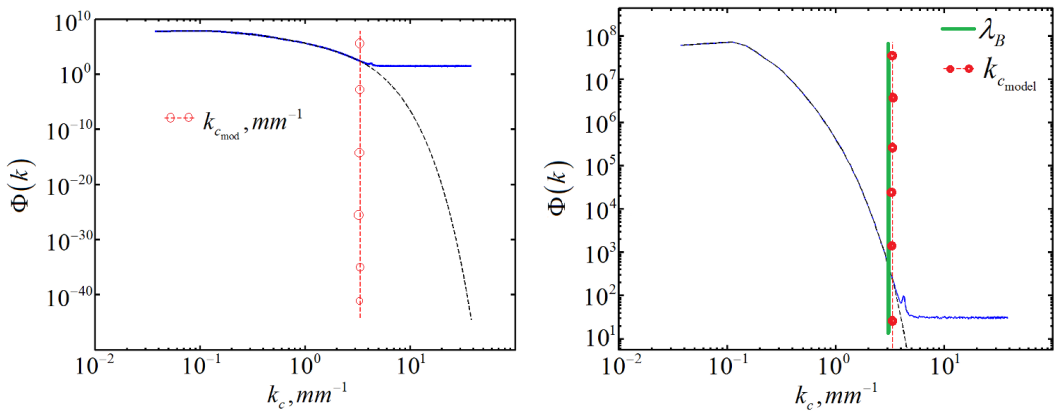

Figure 3.6: A horizontal cut (through the centre of the frequency plane, along radial direction) of the averaged 2D spectrum of the fluctuations of the mixture fraction computed at $y/D_f = 1$ for $S = 0.3$. Vertical circled dashed line shows the scale where an exponential function of the turbulent decay is used while vertical solid line is the Batchelor scale computed from the dissipation spectrum. Note that Batchelor scale and modelling scale almost coincide.

be used.

The application of the Wiener filter reduces significantly the amount of noise in the experimental data with relatively easy implementation. On top of that, the most important characteristic of the Wiener filter is the possibility of calculating the filtering errors for both the variance of the mixture fraction and the scalar dissipation fields. The mean of the square of the filtering error is given according to the following equation.

$$e^2 = \int_{-\infty}^{+\infty} |f(r) - f_F(r)|^2 dr = \int_{-\infty}^{+\infty} |F(k) - F_F(k)|^2 dk \tag{3.15}$$

Similarly, the mean of the square of the filtering error is written as follows; where dependence on the wave number is omitted for clarity. If the optimal Wiener filter is used, then the mean square error can be written as.

$$e^2 = \int_{-\infty}^{+\infty} \frac{1}{H^2} \left[F_S^2 (W-1)^2 + N^2 W^2 \right] dk \tag{3.16}$$

$$e^2 = \int_{-\infty}^{+\infty} \frac{1}{H^2} \frac{F_S^2 N^2}{F_S^2 + N^2} dk \tag{3.17}$$

The mean−square−error in the spatial derivative was computed according to the following mean−square−error form, where the total derivative error is the sum of the errors along x and y directions.

$$e_d^2 = e_{d,x}^2 + e_{d_y}^2 = \int_{-\infty}^{+\infty} \left[\left| \frac{\partial f}{\partial x} - \frac{\partial f_F}{\partial x} \right| + \left| \frac{\partial f}{\partial y} - \frac{\partial f_F}{\partial y} \right| \right] dr \tag{3.18}$$

Given the fact that the Fourier transform of a function $f(r)$ is $F(k)$ then the Fourier transform of the derivative $f(r)$ in x and y directions $f_x = \partial f(r)/\partial x$, $f_y = \partial f(r)/\partial y$ is

$iuF(k)$. Therefore, the mean−square−error in the spatial derivative along x direction $e^2_{d,x}$ can be written as follows:

$$e^2_{d,x} = \int_{-\infty}^{+\infty} \left| \frac{\partial f}{\partial x} - \frac{\partial f_F}{\partial x} \right| dr^2 = \int_{-\infty}^{+\infty} |iuF(k) - iuF_F(k)|^2 dk = \int_{-\infty}^{+\infty} u^2 \left| F(k) - F_F(k) \right|^2 dk \tag{3.19}$$

Hence the mean−square−error in the spatial derivative of the mixture fraction field is according to the following equation.

$$e^2_d = \int_{-\infty}^{+\infty} k^2 \frac{1}{H^2} \frac{F_S^2 N^2}{F_S^2 + N^2} dk \tag{3.20}$$

A final remark on the Wiener filter is on the effect of the spectral fitting (i.e. the modelled spectrum). If the Wiener transfer function was estimated from a different spectrum, i.e. the spectrum that was different from the 'real' spectrum, this would produce non−optimum Wiener function W_*, instead of the correct one W. The mean−square−error is then given by the following equation, where W_* represents non−optimal Wiener filter.

$$e^2_* = \int_{-\infty}^{+\infty} \frac{1}{H^2} \left[F_S^2 \left(W_* - 1 \right)^2 + N^2 W_*^2 \right] df \tag{3.21}$$

After some manipulations, the resulting mean−square−error in case of non−optimal Wiener filter can be written as follows:

$$e^2 = \int_{-\infty}^{+\infty} \left[\frac{1}{H^2} \left(F_S^2 + N^2 \right) \left(W_* - W \right)^2 + \frac{1}{H^2} \frac{F_S^2 N^2}{F_S^2 + N^2} \right] df \tag{3.22}$$

The mean−square filtering errors were evaluated from Eq. 3.17 and 3.20 and shown in Tables 3.1, 3.2 and 3.3 where values obtained from Eq. 3.17 were normalized with $\int_{-\infty}^{+\infty} S(k) dk$ and values from Eq. 3.20 were normalized with $\int_{-\infty}^{+\infty} k^2 S(k) dk$, i.e. the 'true' variance[10] and the 'true' dissipation rate respectively.

3.2.2 Wiener filter summary

The Wiener filter is the m.s.e. optimal stationary filter for images that were degraded by the additive noise. Calculation of the Wiener filter requires a priori knowledge of the signal and noise power spectra and its applicability may be rather limited due to the following reasons.

- Calculation of the Wiener filter requires the assumption that the signal and noise processes are second−order stationary[11].

[10] The variance is the average power of a signal, which can be found by integrating the PSD over all frequencies $k_c(mm^{-1})$.

[11] A stationary process is a process whose probability density function does not change when shifted in time or space, as a result, the mean and the variance of the process are constant.

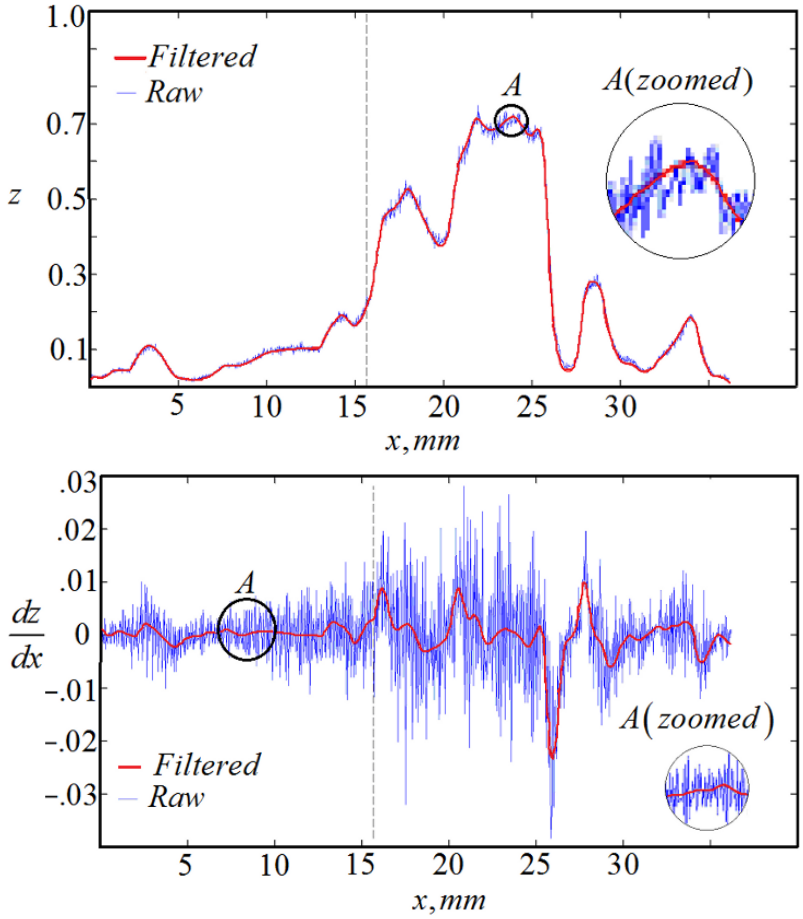

Figure 3.7: On the top are shown centreline radial profiles of an instantaneous raw mixture fraction image and of the corresponding filtered image. On the bottom are shown the radial derivatives of the same profile. Vertical dashed black line is the burner centreline. The profile was computed for $S = 0.58$ at $y/D_f = 5$. Note that the derivative dz/dx possess little experimental value due to significant noise variations if no denoising procedure is used.

- Signal and noise spectra are invariant throughout the image. The power spectra that is used for the design of the Wiener filter is computed from the whole image, whilst local variations in power spectra can be significant, especially in reacting flows. The spectrum that is computed from the constant temperature turbulent flow may be quite different from the spectrum obtained from turbulent flames. In this case, the use of the Wiener filter with no local adaptability will result in filtering that is far beyond optimal. Locally adaptive Wiener filters, e.g. wavelet−based, may be used in reacting flows.
- Wiener filter is typically applied in the frequency domain leading to slow performance (even though may not be relevant to data processing).
- If the PSF is taken into account and used for deblurring, the deconvolution can produce artefacts in the reconstructed image[12].

[12]Such ringing artefact may present in a reconstructed image due to the poor quality of the point spread function, which can be related to noisy or improperly scaled PSF. If this is a case, then, the point spread function must be measured again or the estimate of the PSF must be refined.

The applicability of the Wiener filter to a range of flow conditions can be therefore limited and requires careful attention. The results that are derived from the image processing technique should be carefully examined. Real physical events that are observed from measured data may be simply artefacts due to non−optimal image processing technique.

Percentage (%) errors of the variances of the mixture fraction and of the scalar spatial derivative after using Wiener filter during isothermal experiments for different swirl numbers and different downstream positions are summarized in Tables 3.1−3.3. The errors were normalized with the model scalar variance and the model scalar dissipation.

The Wiener filter design consists of the following steps according to Figure 3.8.

- Computation of the mean mixture fraction image (2).
- Subtraction of mean image (2) from instantaneous mixture fraction image (1) resulting in the image of mixture fraction fluctuation (3).
- Fourier transformation by Fast Fourier Transform (FFT) of the mixture fraction fluctuation image (4).
- Obtaining the modulus of the Fourier transform and shifting the zero-frequency component to centre of spectrum[13] (5).
- Squaring the modulus of the Fourier transform (5) leading to instantaneous power spectral density (6).
- Averaging instantaneous PSD (7) to obtain time-averaged power spectral density of the mixture fraction fluctuation (8).
- Horizontal cutting the time-averaged PSD to obtain 1D power spectral density (9).
- Modelling a part of the 1D PSD by an exponential function (10). Noise can be modelled by e.g. polynomials or splines and subtracted from the measured PSD (9).
- Obtaining the Wiener transfer function by division of the modelled spectrum by the 1D PSD (11).
- The Wiener filter in 2D space is obtained by 'rotating' the Wiener transfer function around zero-frequency component[14]

[13] fftshift(X) is used in MATLAB software and rearranges the outputs of Fast Fourier Transform by moving the zero-frequency component to the centre of the array. It is useful for visualizing a Fourier transform with the zero-frequency component in the middle of the spectrum.

[14] Obtaining the 2D Wiener transfer function can be done by invoking a circle equation $K = \sqrt{u^2 + v^2}$, where u and v are the wave numbers in x- and y-directions in the image, and K is the radius vector and the wave number along the 1D Wiener transfer function.

Table 3.1: Percentage (%) errors of the variances of the mixture fraction and of the scalar spatial derivative after using Wiener filter during isothermal experiments for $S = 0.3$. The errors were normalized with the model scalar variance and the model scalar dissipation.

y/D_f	$\left\langle z''^2 \right\rangle$	$\left\langle (\nabla z)^2 \right\rangle$
1	2	11
3	1.3	8.6
5	0.9	9.7
7	0.8	8.4

Table 3.2: Percentage (%) errors of the variances of the mixture fraction and of the scalar spatial derivative after using Wiener filter during isothermal experiments for $S = 0.58$. The errors were normalized with the model scalar variance and the model scalar dissipation.

y/D_f	$\left\langle z''^2 \right\rangle$	$\left\langle (\nabla z)^2 \right\rangle$
1	1.6	9
3	0.7	12.3
5	1	7.7
7	0.8	9

Table 3.3: Percentage (%) errors of the variances of the mixture fraction and of the scalar spatial derivative after using Wiener filter during isothermal experiments for $S = 1.07$. The errors were normalized with the model scalar variance and the model scalar dissipation.

y/D_f	$\left\langle z''^2 \right\rangle$	$\left\langle (\nabla z)^2 \right\rangle$
1	1	7.5
3	0.4	7.8
5	0.8	9.5
7	1.5	6.8

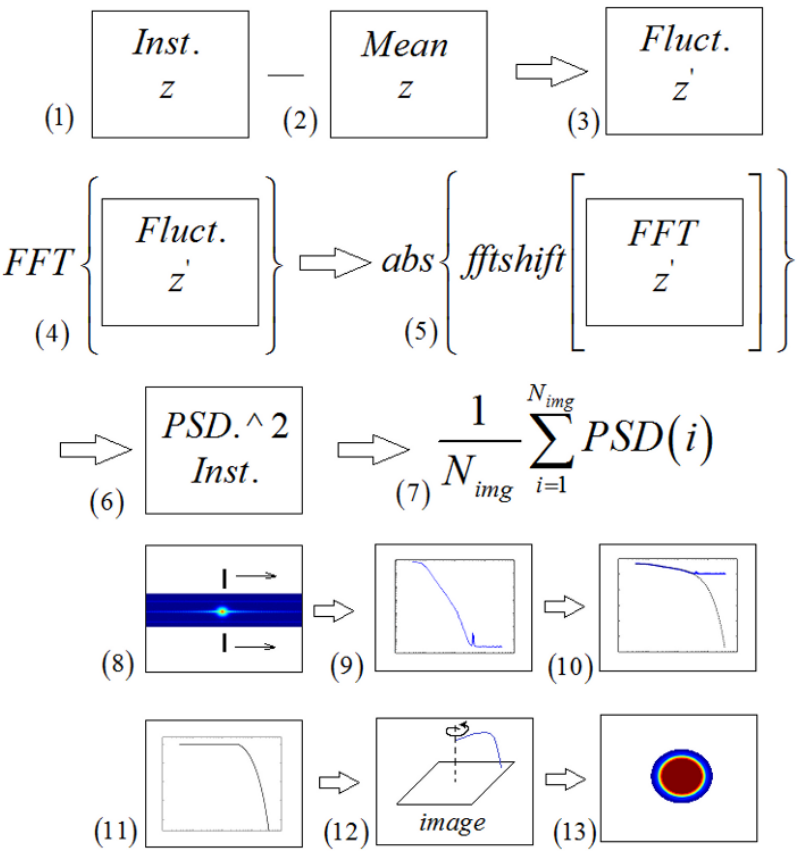

Figure 3.8: A general algorithmic interpretation of the design of 2D Wiener filter to be used in non−reacting measurements.

3.2.3 Rayleigh thermometry

In global Wiener filtering, the filter is applied over the whole image. This method does a good job for images that have similar local statistics throughout the entire image, e.g. mixture fraction images. However, in Rayleigh thermometry images, the local statistics can vary from one part of an image to another and hence the Wiener filter becomes far less optimal. The statement of non−similarity of the local statistics throughout the image was not confirmed by the experimental or theoretical studies to the best of the knowledge. In addition to the global Wiener filter, it is also possible to perform the Wiener filtering on a small block of an image so that the local statistics can also be accounted for.

Barlow (2011)[15] demonstrated wavelet denoising algorithm with application to temperature and mixture fraction fields. Unfortunately, no details of the algorithm implementation were given. According to the published algorithm block diagram, it was suggested that the algorithm was based on a stationary wavelet transform and a thresholding method.

The wavelet transform has entered the arena of image denoising since 1990th and is still one of the most popular methods (Donoho, 1995). Donoho presented a method for denoising images by thresholding the image wavelet[16] coefficients, which was named

[15] R.S. Barlow. Advances in Experimental Techniques for Premixed and Partially Premixed Combustion. Workshop on Advanced Measurement Techniques and Computational Methods for Premixed and Partially Premixed Combustion. Cagliari, Italy, Sept. 10−11, 2011.

[16] A wavelet is a wave−like oscillation with an amplitude that starts out at zero, increases and then

Soft Thresholding. Generally, a denoising procedure consists of the wavelet transform of the image, the modification of the wavelet coefficients and then the computation of the inverse wavelet transform. This denoising in wavelet domain procedure is actually similar to the denoising in Fourier domain. The most basic wavelet transform was the Haar transform, which was described by Alfred Haar[17] in 1910. A representation of a real or complex−valued signal by wavelet series is called the wavelet transform. The description of the wavelet transform is beyond the scope of the present work and only the filtering procedure assuming that the wavelet coefficients are known is briefly discussed.

In this work, an attempt of using wavelet based filtering procedure was performed. The filtering procedure for Rayleigh images is based on the theory of Wavelet denoising via empirical Wiener filter Ghael *et al.* (1997). Consider an image $s_{i,j}$, which has been corrupted by a zero−mean Gaussian noise $n_{i,j}$. A classical problem is to recover the true signal $s_{i,j}$ from degraded image $y_{i,j} = s_{i,j} + n_{i,j}$. In the context of wavelet transform, the values of $y_{i,j}$, $s_{i,j}$, $n_{i,j}$ represent the wavelet coefficients of the noisy image, the undegraded image and the coefficients of the noise. Let denote W an $M \times N$ orthonormal wavelet transform, where M and N is the number of rows and columns in the image. The number of rows and columns must satisfy $2^L = M$, $2^L = N$, where $L = 1, 2, 3...M, N$ is the number of wavelet transform levels. The wavelet coefficients of the noisy image are obtained by the wavelet transform of the original signal x (image) $y_{i,j} = Wx$. The orthogonality of the wavelet transform leads to the decorrelation property, i.e. the signal and the noise components are uncorrelated. The optimal filter minimizing the m.s.e. is the Wiener filter, which can be written as, where h_w is the weighting or Wiener transfer function, $\theta^2(i)$ is wavelet coefficients of the pilot signal estimate (modelled signal) and σ^2 is the noise variance.

$$h_w = \frac{\theta_{21}^2(i)}{\theta_{21}^2(i) + \sigma^2} \tag{3.23}$$

The Wiener filter requires knowledge of the signal and noise statistics, which is represented by the noise variance. However, these data are not known *a priory*. For solving this problem the noise variance must be estimated from the original noisy image, which is computed as $\sigma = MAD/0.6745$ with MAD the median absolute value of the fine−scale wavelet coefficients[18] Donoho (1995). The Donoho threshold T (sometimes called Universal threshold) is computed from the noise variance, and the base 10 logarithm of a number of samples as $T = \sigma\sqrt{2\log(n)}$. A representation of wavelet−based empirical Wiener filtering is shown in Figure 3.9. The hard thresholding formula is given to be as follows:

$$\hat{\theta} = y_{i,j}H_h = \begin{cases} y_{i,j} & \text{if } |y_{i,j}| \geq T \\ 0 & \text{if } |y_{i,j}| < T \end{cases} \tag{3.24}$$

The Wavelet−based empirical Wiener filtering procedure can be summarized as follows (according to Figure 3.9). Degraded image x is transformed into first wavelet domain by

decreases back to zero.

[17] Alfred Haar (11.10.1885−16.03.1933) was a Hungarian mathematician.

[18] The addition of noise to the original signal has the effect of adding noise to the wavelet coefficients as well. In statistics, the median absolute deviation (MAD) is defined as the median of the absolute deviations from the data's median $MAD = median(|X_i - median(X)|)$.

the wavelet transform W_1 thus giving the wavelet coefficients $y_{i,j}$.

$$y_{i,j} = W_1 x \tag{3.25}$$

Wavelet coefficients are hard thresholded by using the threshold function[19] H_h, thus leading to thresholded wavelet coefficients $\hat{\theta}$.

$$\hat{\theta} = H_h y_{i,j} \tag{3.26}$$

Inverse wavelet transform is computed from thresholded wavelet coefficients leading to the pilot signal estimate $\hat{s}$

$$\hat{s} = W_1^{-1} \hat{\theta} \tag{3.27}$$

The wavelet coefficients of the pilot signal estimate is then computed by the wavelet transform W_2 of the pilot signal estimate.

$$\theta_{21} = W_2 \hat{s} \tag{3.28}$$

Degraded image x is transformed into second wavelet domain by the wavelet transform W_2 thus giving the wavelet coefficients $\hat{y}_{i,j}$ in the second wavelet domain.

$$\hat{y}_{i,j} = W_2 x \tag{3.29}$$

Wiener filtered wavelet coefficients of the original noisy image $\hat{\theta}_2$ are computed by multiplication of the wavelet coefficients $\hat{y}_{i,j}$ in the second wavelet domain with designed empirical Wiener filter H_w. The Wiener filter is designed by using θ_{21} and noise variance computed from original noised image in the first wavelet domain W_1.

$$\hat{\theta}_2 = H_w \hat{y}_{i,j} \tag{3.30}$$

Inverse wavelet transform of the Wiener filtered wavelet coefficients of the original noisy image thus giving the denoised signal (image) y.

$$y = W_2^{-1} \hat{\theta}_2 \tag{3.31}$$

This procedure can be applied to each instantaneous thermal dissipation rate image in order to obtain the 'true' thermal dissipation. The algorithm, which was outlined above was implemented by using the linear shift invariant discrete wavelet transform based on Rice Wavelet Toolbox[20]. The wavelet−based denoising technique was also applied to mixture fraction images in order to test the algorithm. Figure 3.10 shows results of the application of the wavelet−based Wiener filter for different noise estimation criterion based on the MAD. The wavelet−based Wiener filtering procedure works quite well for images that have a relatively constant signal level across the image as, for example, images that are generated by conventional SDLR cameras. Unlike those images, the turbulent flow image does not have a constant signal level across the image and hence the noise variance

[19] The threshold function is simply equal 1 for $|y_{i,j}| \geq T$ and 0 for $|y_{i,j}| < T$.
[20] http://dsp.rice.edu/software/rice-wavelet-toolbox

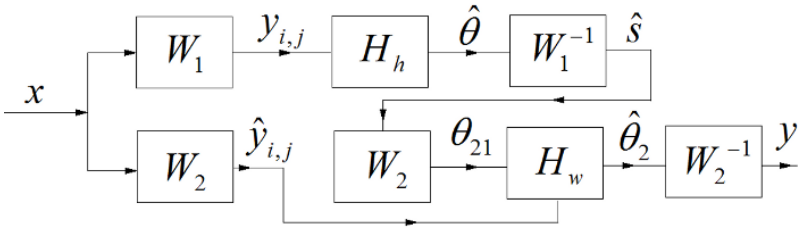

Figure 3.9: Wavelet−based empirical Wiener filtering. In the upper path, W_1 transform of original noisy image is used to design an empirical Wiener filter, which then applied in W_2 wavelet domain of the original noisy image. It is required that $W_1 \neq W_2$, i.e. one wavelet base is used for the design of the empirical Wiener filter and another one for its application (Ghael *et al.*, 1997).

based on the MAD may not be computed correctly. Donoho (1995) proposed MAD computation from fine−scale wavelet coefficients, which may lead to 'under denoising', as seen in Figure 3.10. Under the term 'under denoising' is understood the similarity between the raw image and the denoised one. As it can be seen, the resulting denoised image is highly affected by the computation of the noise variance, which was related to MAD. In this work, it was shown that the MAD can be computed from an entire image in spatial domain (i.e. from pixel intensities) and this would lead to more accurate results. However, this is not a general case and, therefore, requires a careful attention and further investigation.

Figure 3.11 shows filtered scalar dissipation rate as a function of wavelet transform levels L. Higher number leads to higher details in the reconstructed image. There is the limiting level of wavelet transform after which, the reconstructed image is not affected by an increasing number of levels. In the context of this work, the limiting level L was found to be 5, i.e. five levels of wavelet transform were used. Apparently, the wavelet−based algorithm is not an universal answer, because it is highly dependent on the threshold. Increasing or decreasing the threshold may lead to poorly denoised image or to other distortion artefacts in the reconstructed image. The most appropriate denoised algorithm will depend on the type of signal being processed. In non−reacting flows, the Wiener filter should be superior.

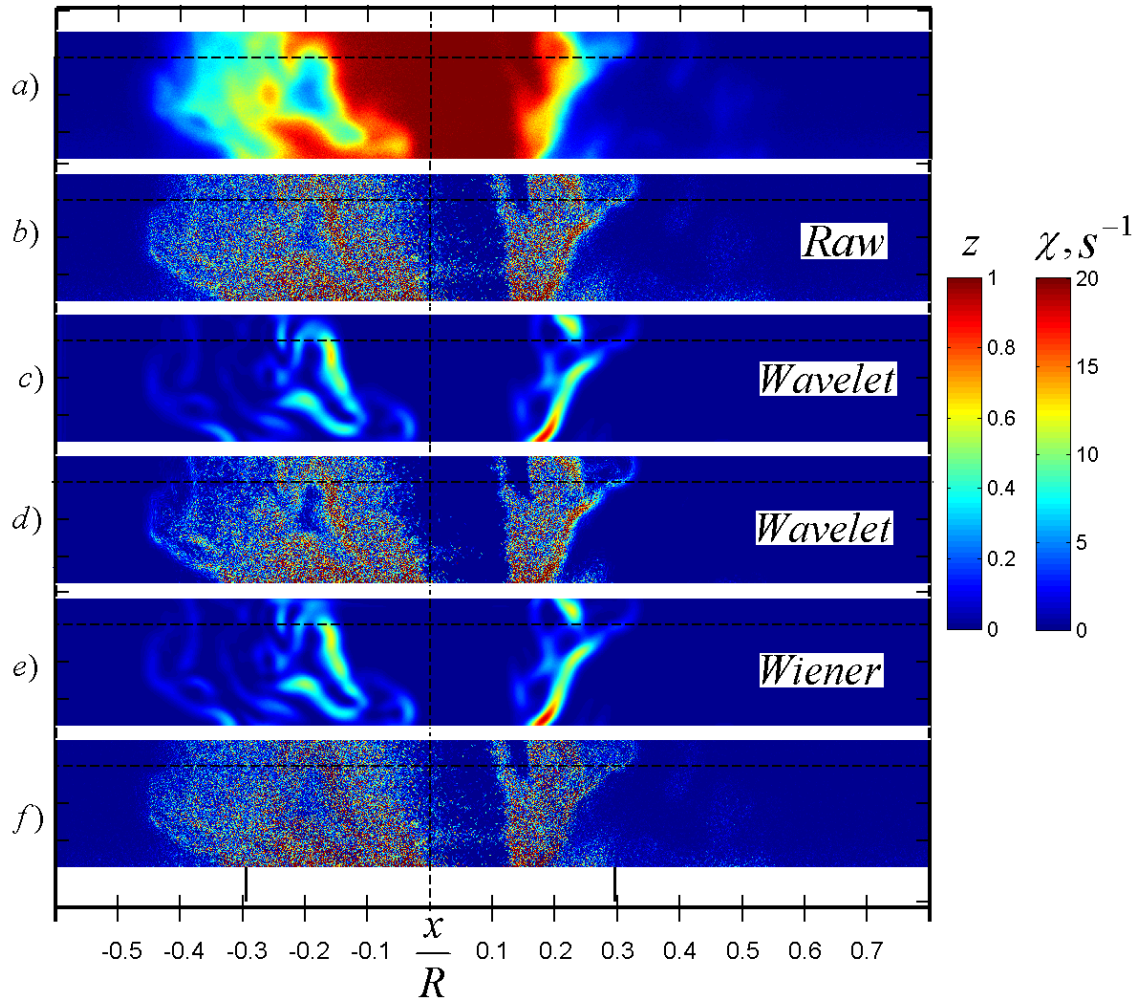

Figure 3.10: Results of the application of several Wiener filters to an instantaneous mixture fraction distribution.
a) Raw instantaneous mixture fraction image.
b) Raw scalar dissipation image computed from 'a'.
c) Wavelet−based Wiener filtered scalar dissipation image, where MAD was computed from a spatial domain of an entire image.
d) Wavelet−based Wiener filtered scalar dissipation image, where MAD was computed from the fine−scale wavelet coefficient.
e) Wiener filtered scalar dissipation in the Fourier domain.
f) Noise from wavelet−based filtered scalar dissipation with MAD being computed from an entire image in spatial domain.
The discrepancy between c) and e) is negligible.

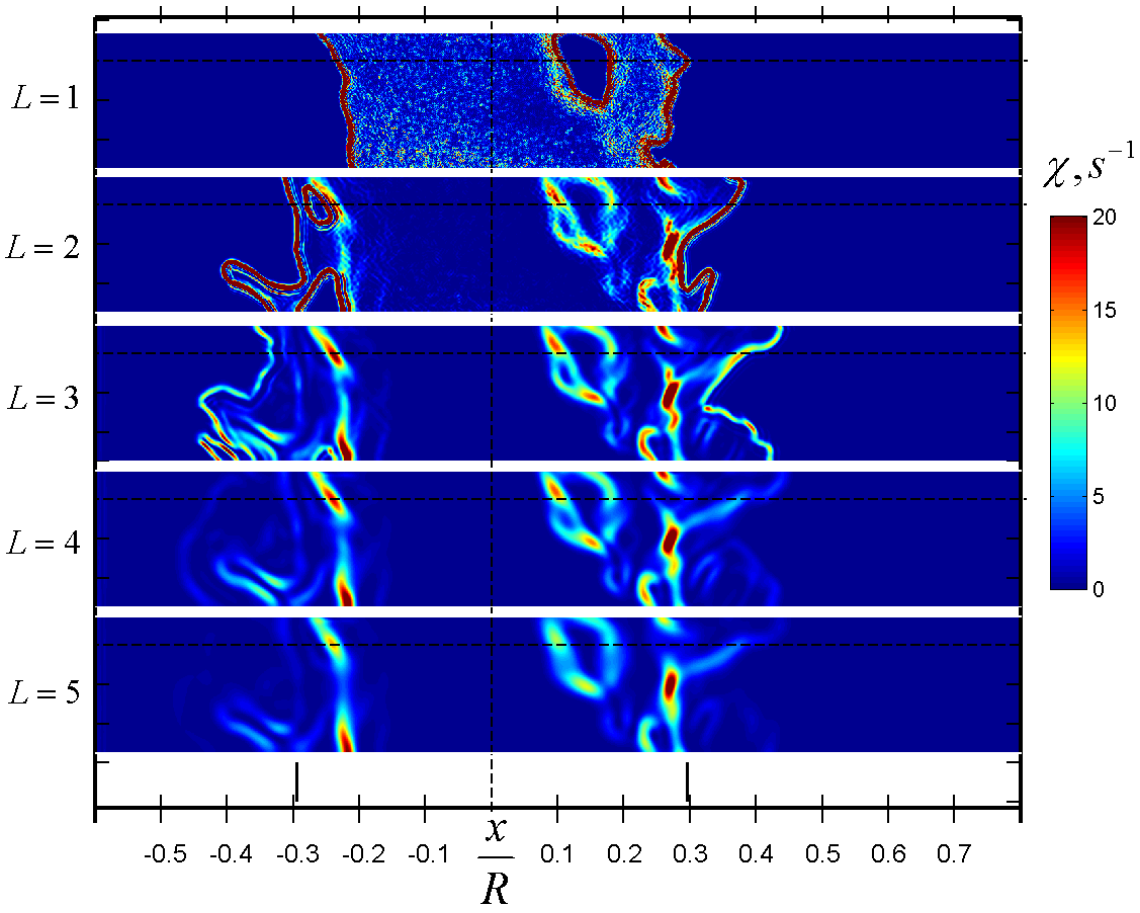

Figure 3.11: Filtered scalar dissipation after filtering with wavelet−based Wiener filter for different transform levels L. Five transform levels are shown $L = 1, 2...5$, where higher transform levels lead to higher details.

3.3 Summary

This chapter outlined data processing algorithms, which were based on Wiener filters in Fourier and wavelet domains. Two different filtering techniques were chosen due to the fact that non−reacting and reacting flows exhibited different characteristics, and hence no universal filtering procedure could be used. Image quality and spatial resolution were discussed in terms of point spread and modulation transfer functions. Two methods for the evaluation of PSF and MTF were presented and discussed.

4 Scalar mixing in swirling flows

> Bad times have a scientific value.
> These are occasions a good learner
> would not miss.
>
> Ralph Waldo Emerson

The main aerodynamic variable in swirling flow is the swirl number and thus the effects of increasing the swirl number on scalar mixing are studied in the near burner exit region downstream up to seven fuel nozzle diameters $y/D_f = 7$. Here 'y', is the axial downstream coordinate with origin on the centreline at the exit plane of the burner. The secondary air flow (swirling flow) had a Reynolds number of 28662 based on the bulk velocity of 8.46(m/s) and the outer diameter 50.8(mm) of the annulus, carrying swirling flow. The fuel jet (mixture of acetone vapour plus air) flow had a Reynolds number of 3770 based on the bulk velocity of 3.77(m/s) and the inner diameter D_f of 15(mm) of the annulus carrying axial jet fuel (acetone/air mixture). The measurements are reported for four swirl numbers S of 0, 0.3, 0.58 and 1.07 within non−dimensional coordinates, namely dimensionless centreline (axial) positions and dimensionless radial positions. Radius was dimensionalised by the burner radius $R = 25.4$(mm) and downstream positions were dimensionalised by a pipe diameter D_f delivering acetone vapour.

4.1 Instantaneous, mean and fluctuations of mixture fraction distribution

Instantaneous, two−dimensional mixture fraction images were recorded by using a conventional planar laser−induced fluorescence technique and processed by using commercial software MATLAB©. Sample instantaneous mixture fraction images at various axial downstream locations are shown in Figures 4.1−4.4. Figures 4.5−4.8 also show time averaged (mean) mixture fraction distributions for four swirl numbers. The mixture fraction time averaged fields were computed from 1500 instantaneous images. The figures show that the flow shape was symmetrical for $S = 0.3$, slightly non−symmetrical for 0.58-1.07 and had uniform scalar field near the centre line. As it was expected, the mixing levels were highly affected by swirling coflow and the mixing improved as the swirl number increased, which was quantified by uniform mixture fraction distributions and very low mixture fraction fluctuation levels at $y/D_f = 7$ (approximately 2 burner diameters) for $S = 1.07$. The results show the strongest acetone vapour signal along the centreline at each downstream position. As the acetone vapour jet diffuses into surrounding air flow and mixing occurs downstream of the jet, the acetone vapour spreads towards ambient surrounding air. This process is enhanced when swirl number increases due to higher turbulence levels (velocity data can be found in Chapter 7).

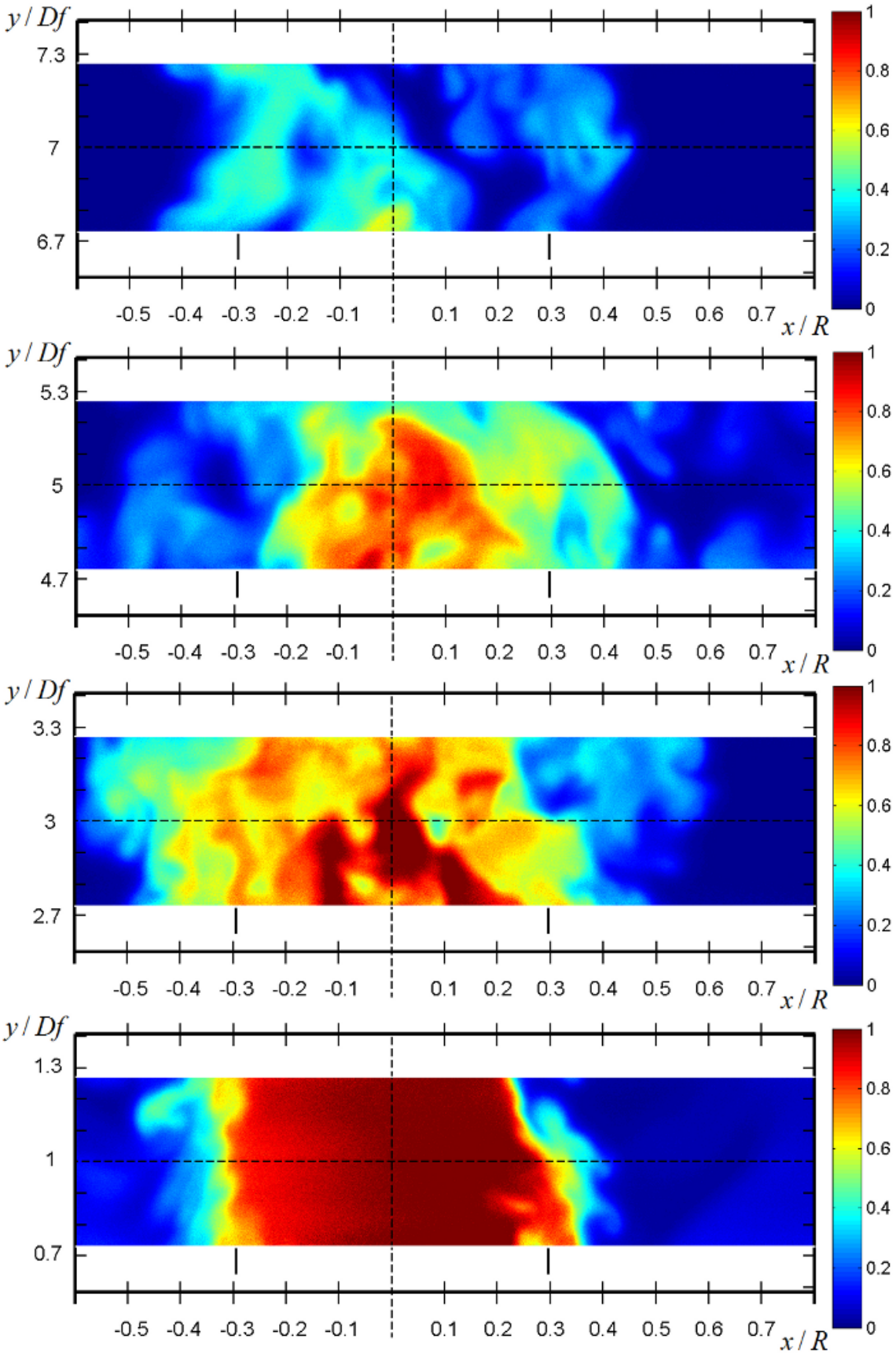

Figure 4.1: Instantaneous mixture fraction fields at $y/D_f = 1, 3, 5, 7$ for acetone vapour jet only without air coflow (no Wiener filter). Radial scale was normalised by burner radius R. The position of the edges of the central pipe delivering the acetone vapour jet is shown by the vertical short lines at $\approx \pm 0.3\ x/R$.

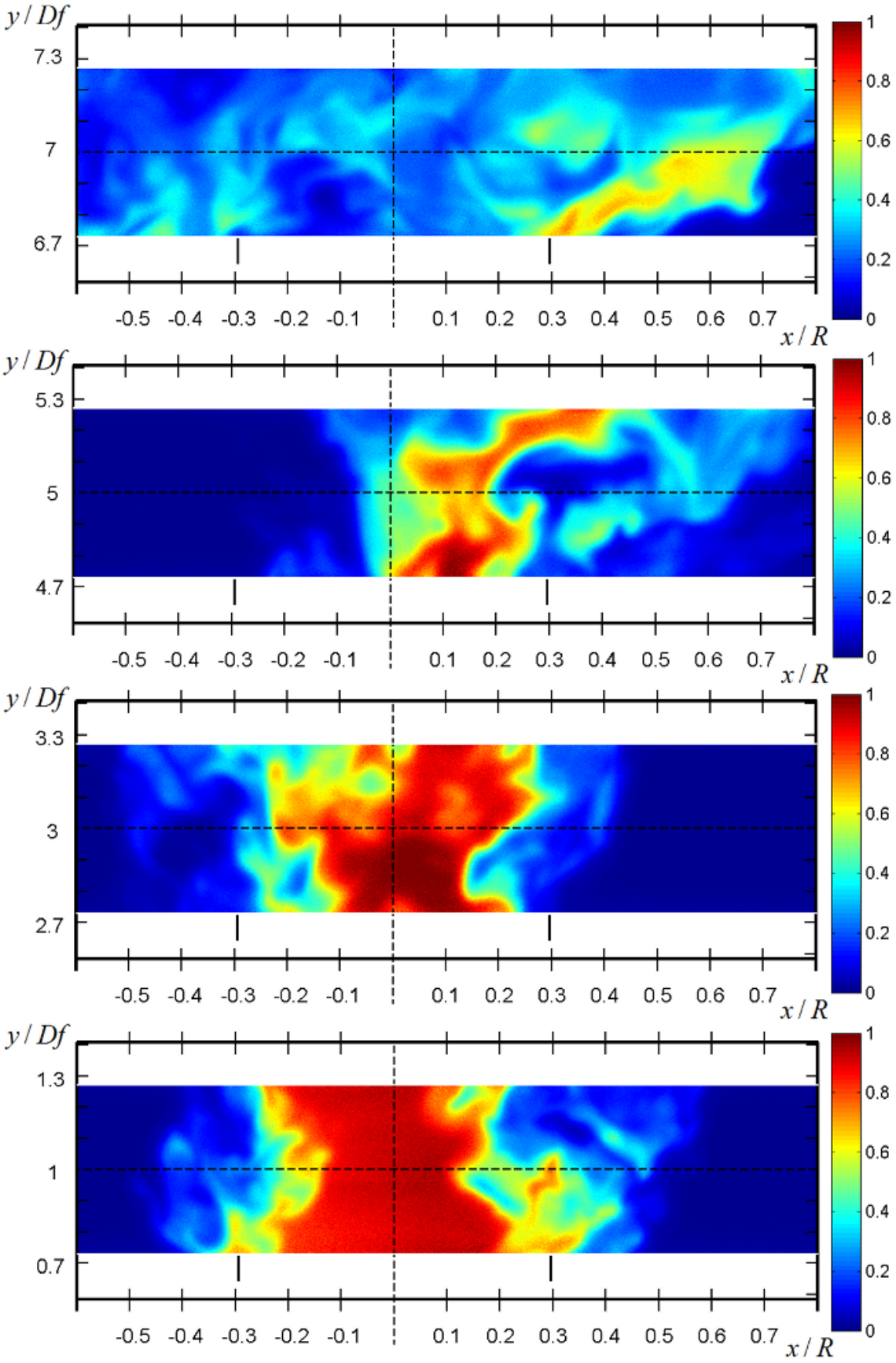

Figure 4.2: Instantaneous mixture fraction fields at $y/D_f = 1, 3, 5, 7$ for $S = 0.3$ (no Wiener filter). Radial scale was normalised by burner radius R. The position of the edges of the central pipe delivering the acetone vapour jet is shown by the vertical short lines at $\approx \pm 0.3\ x/R$.

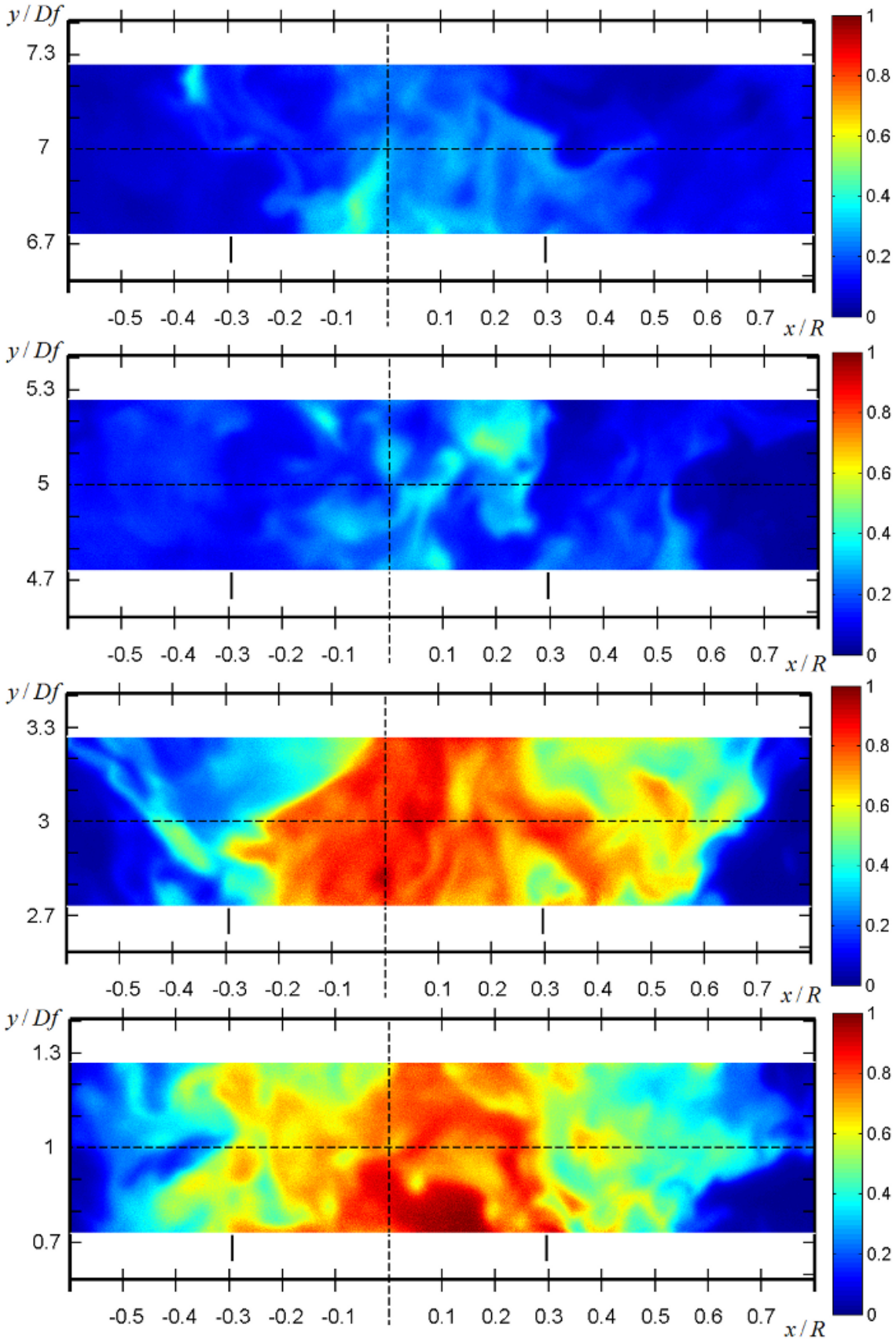

Figure 4.3: Instantaneous mixture fraction fields at $y/D_f = 1, 3, 5, 7$ for $S = 0.58$ (no Wiener filter). Radial scale was normalised by burner radius R. The position of the edges of the central pipe delivering the acetone vapour jet is shown by the vertical short lines at $\approx \pm 0.3\ x/R$.

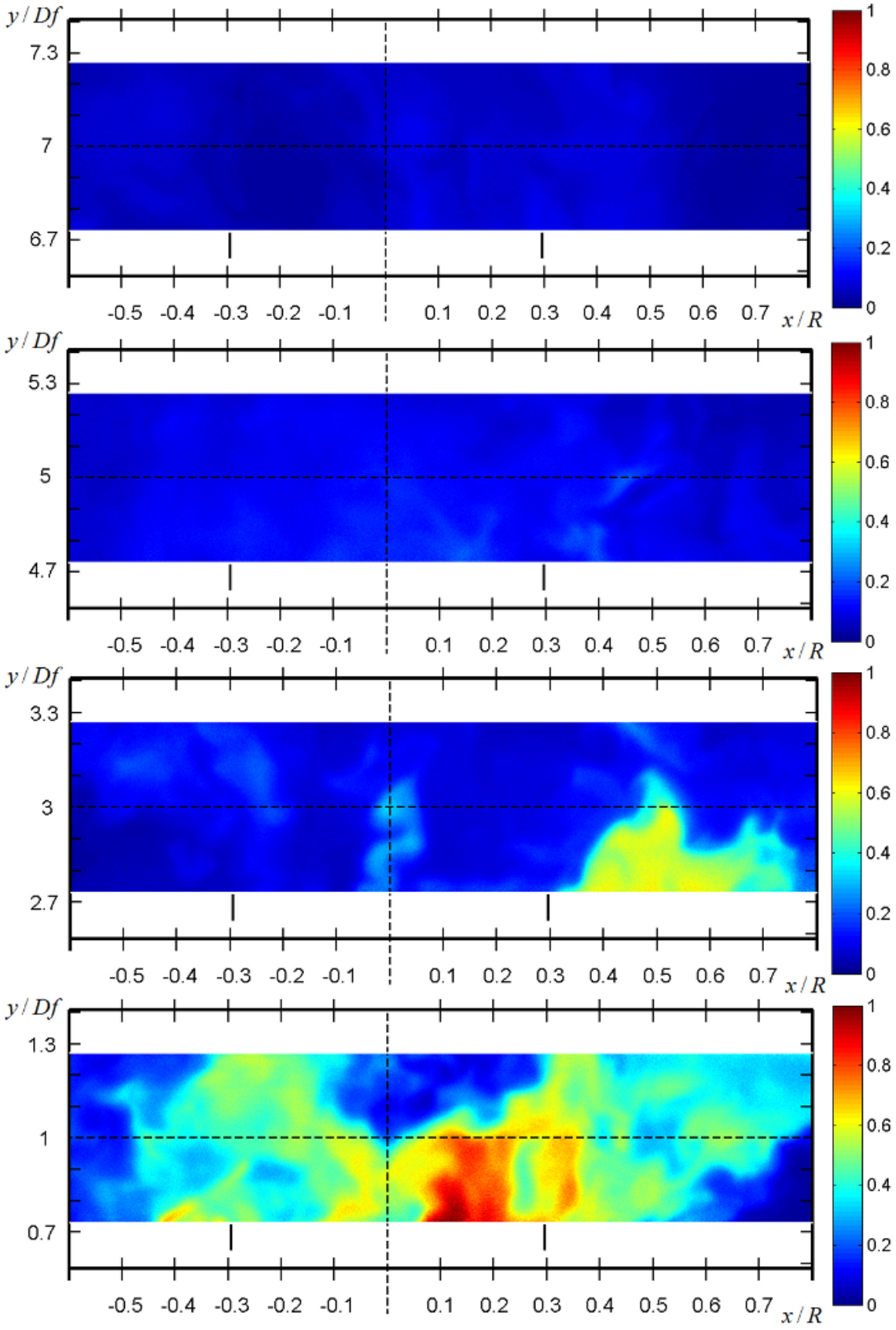

Figure 4.4: Instantaneous mixture fraction fields at $y/D_f = 1, 3, 5, 7$ for $S = 1.07$ (no Wiener filter). Radial scale was normalised by burner radius R. The position of the edges of the central pipe delivering the acetone vapour jet is shown by the vertical short lines at $\approx \pm 0.3\ x/R$.

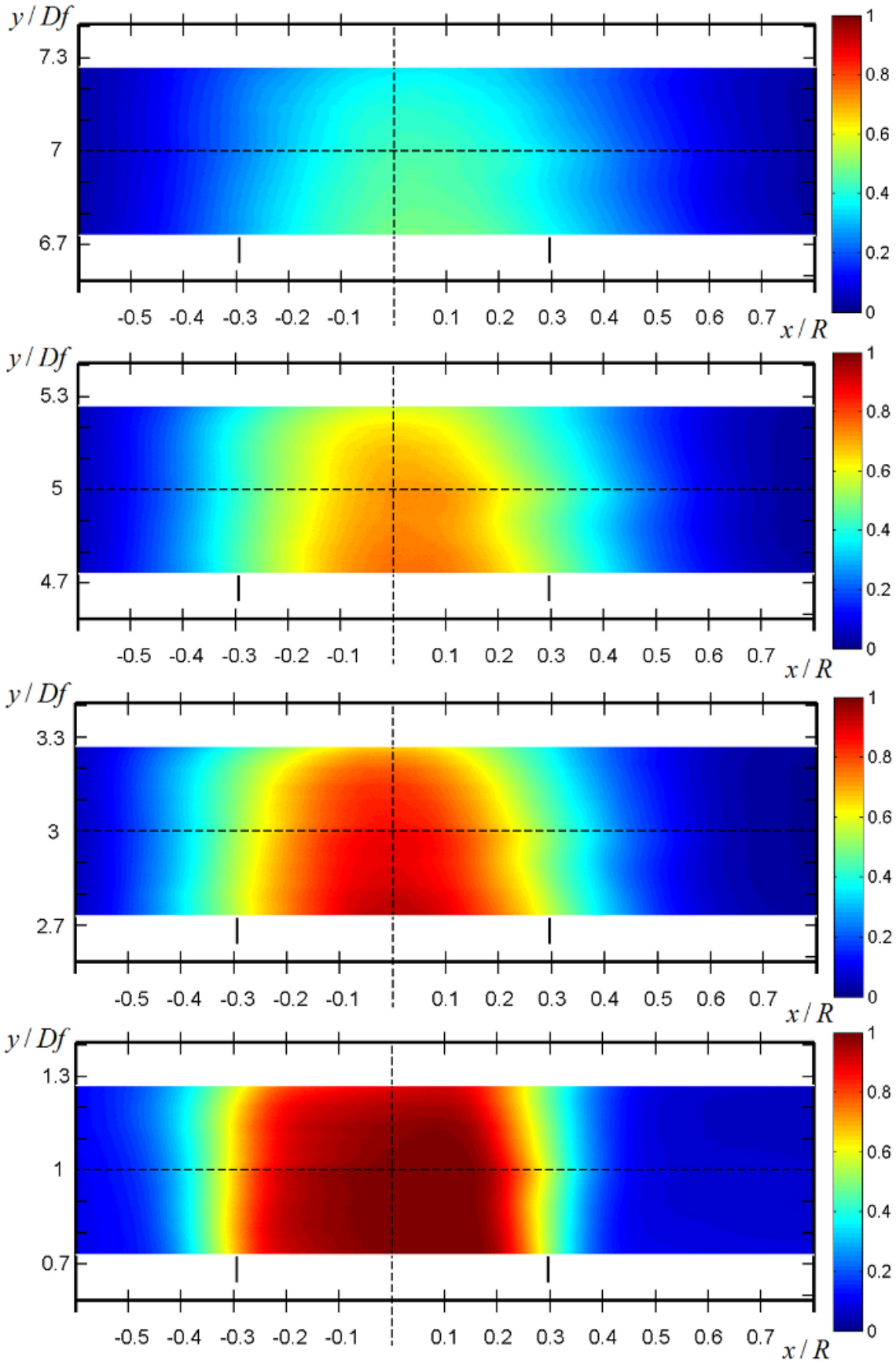

Figure 4.5: Mean mixture fraction fields at $y/D_f = 1, 3, 5, 7$ for acetone vapour jet only without air coflow (no Wiener filter). Radial scale was normalised by burner radius R. The position of the edges of the central pipe delivering the acetone vapour jet is shown by the vertical short lines at $\approx \pm 0.3\ x/R$.

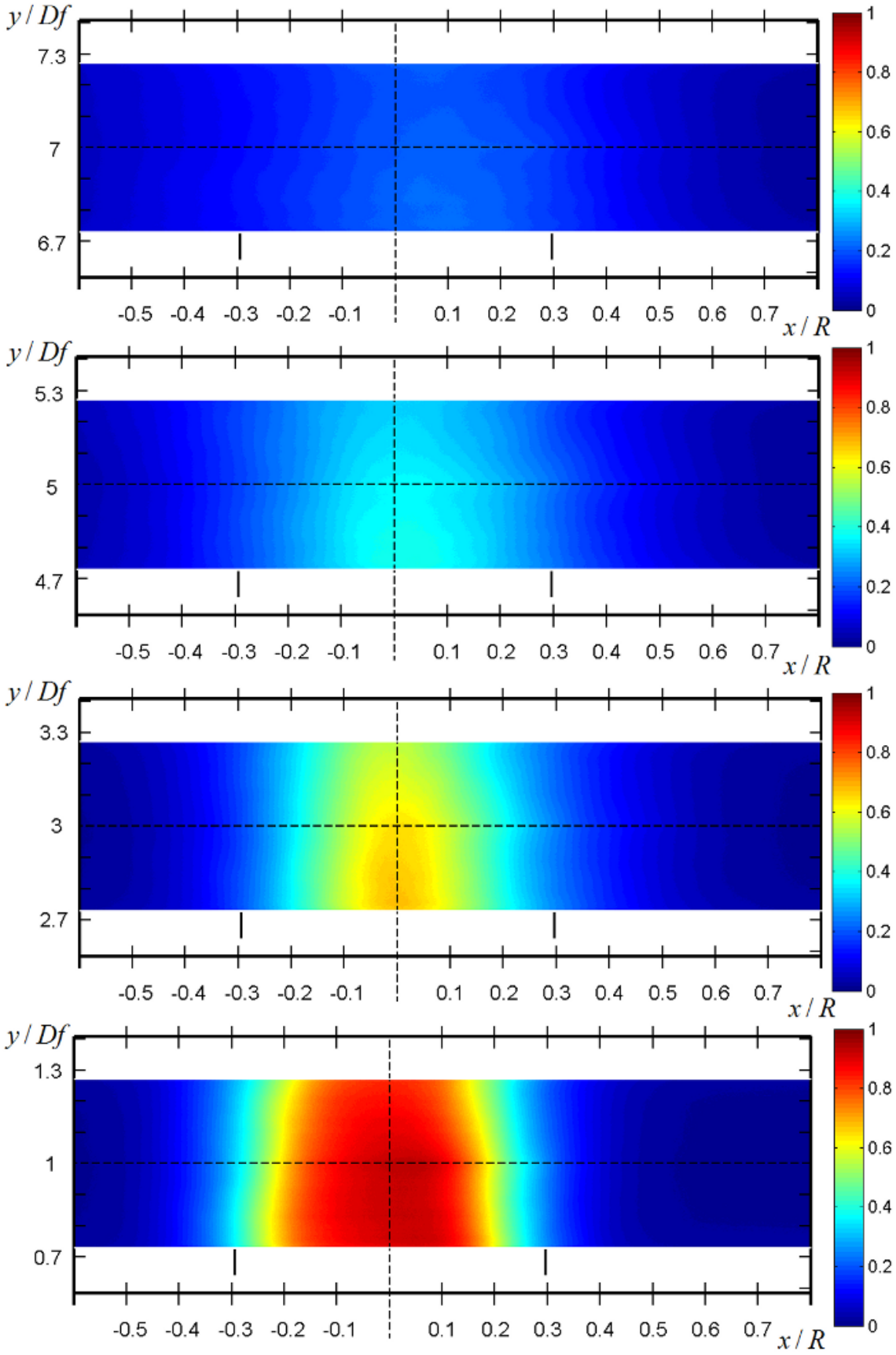

Figure 4.6: Mean mixture fraction fields at $y/D_f = 1, 3, 5, 7$ for $S = 0.3$ (no Wiener filter). Radial scale was normalised by burner radius R. The position of the edges of the central pipe delivering the acetone vapour jet is shown by the vertical short lines at $\approx \pm 0.3\ x/R$.

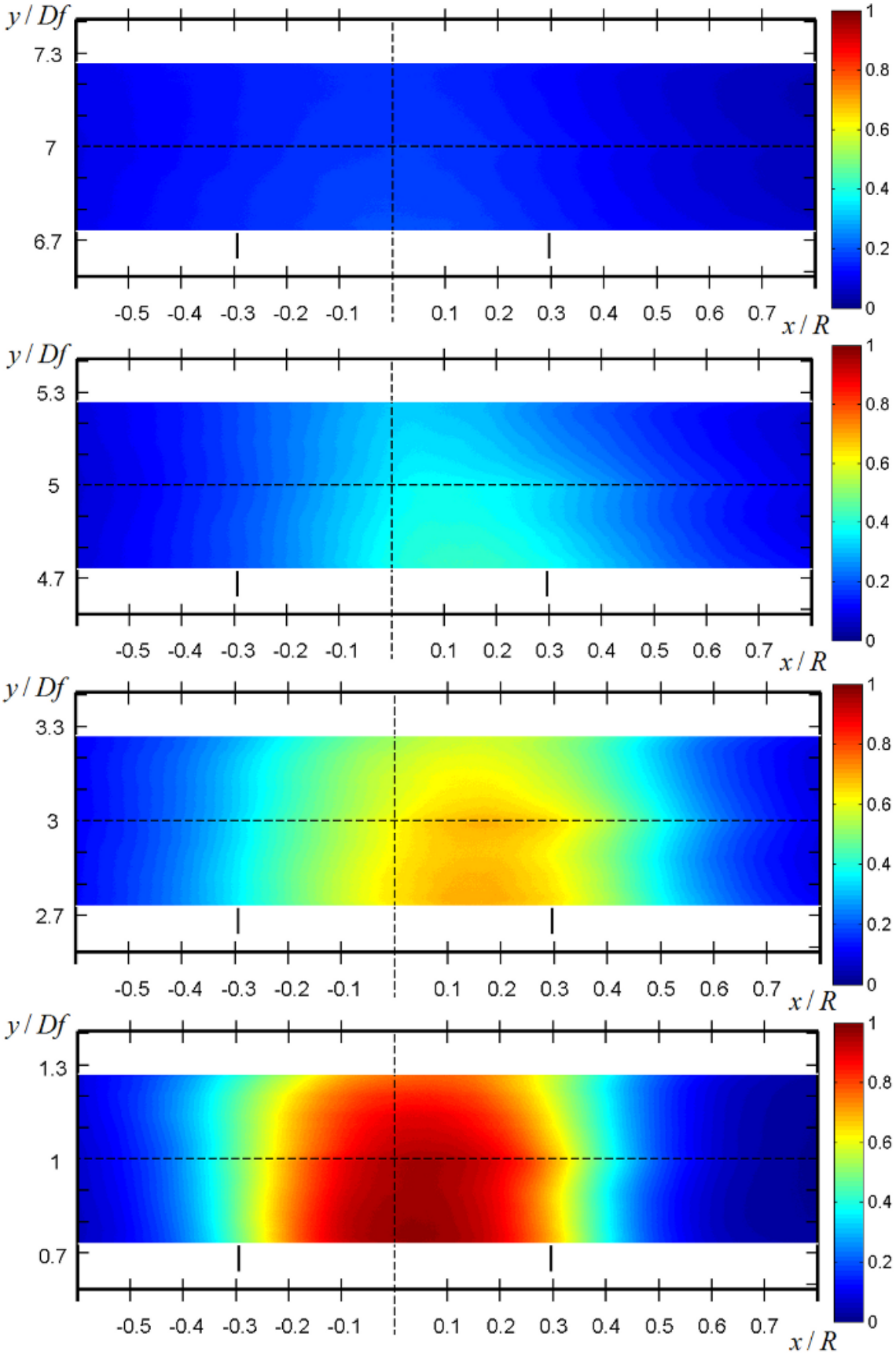

Figure 4.7: Mean mixture fraction fields at $y/D_f = 1, 3, 5, 7$ for $S = 0.58$ (no Wiener filter). Radial scale was normalised by burner radius R. The position of the edges of the central pipe delivering the acetone vapour jet is shown by the vertical short lines at $\approx \pm 0.3\ x/R$.

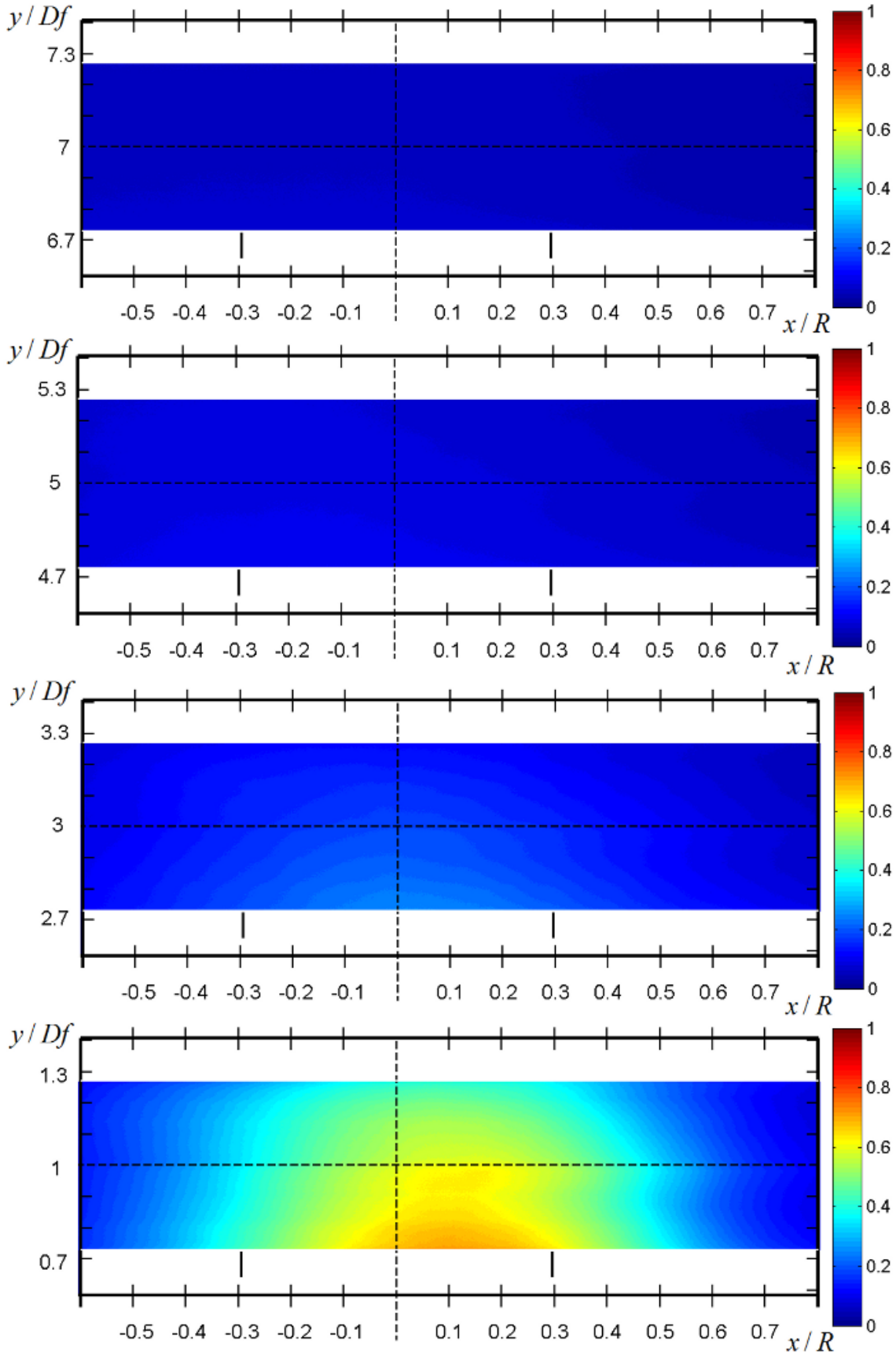

Figure 4.8: Mean mixture fraction fields at $y/D_f = 1, 3, 5, 7$ for $S = 1.07$ (no Wiener filter). Radial scale was normalised by burner radius R. The position of the edges of the central pipe delivering the acetone vapour jet is shown by the vertical short lines at $\approx \pm 0.3\ x/R$.

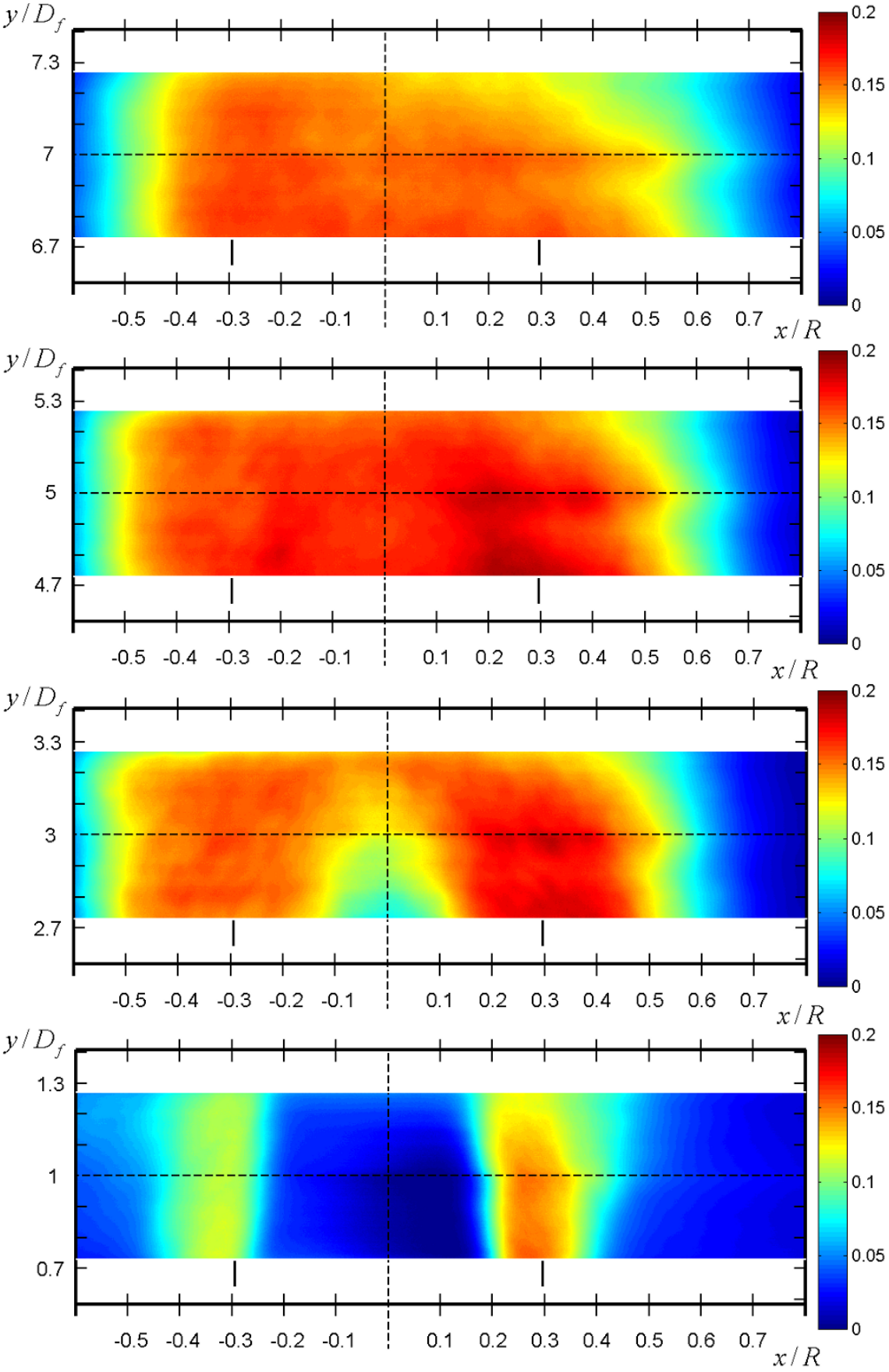

Figure 4.9: Standard deviation of fluctuations of mixture fraction at $y/D_f = 1, 3, 5, 7$ for the acetone vapour jet only without air coflow (no Wiener filter). Radial scale was normalised by burner radius R. The position of the edges of the central pipe delivering the acetone vapour jet is shown by the vertical short lines at $\approx \pm 0.3\ x/R$.

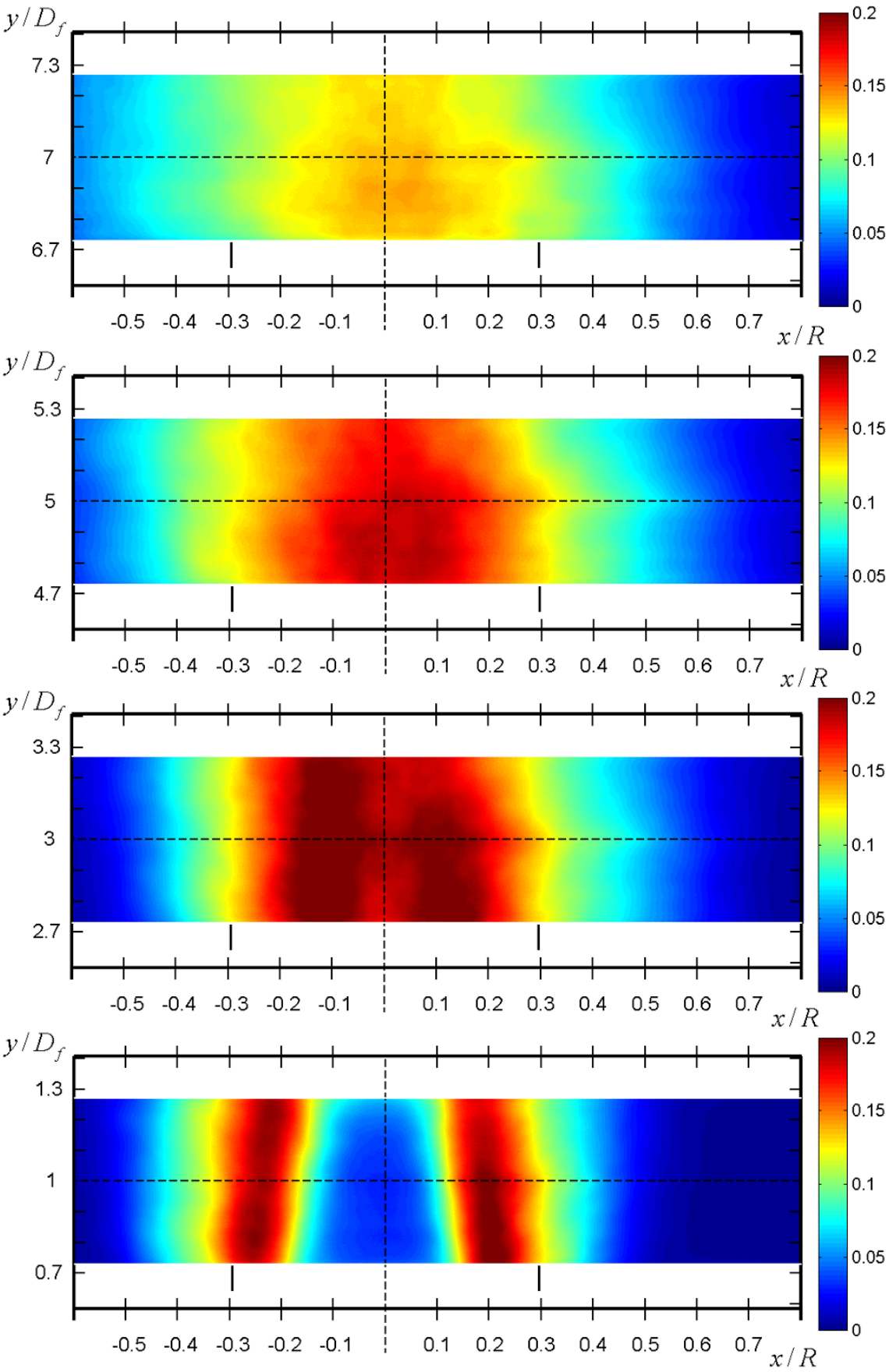

Figure 4.10: Standard deviation of fluctuations of mixture fraction at $y/D_f = 1, 3, 5, 7$ for $S = 0.3$ (no Wiener filter). Radial scale was normalised by burner radius R. The position of the edges of the central pipe delivering the acetone vapour jet is shown by the vertical short lines at $\approx \pm 0.3$ x/R.

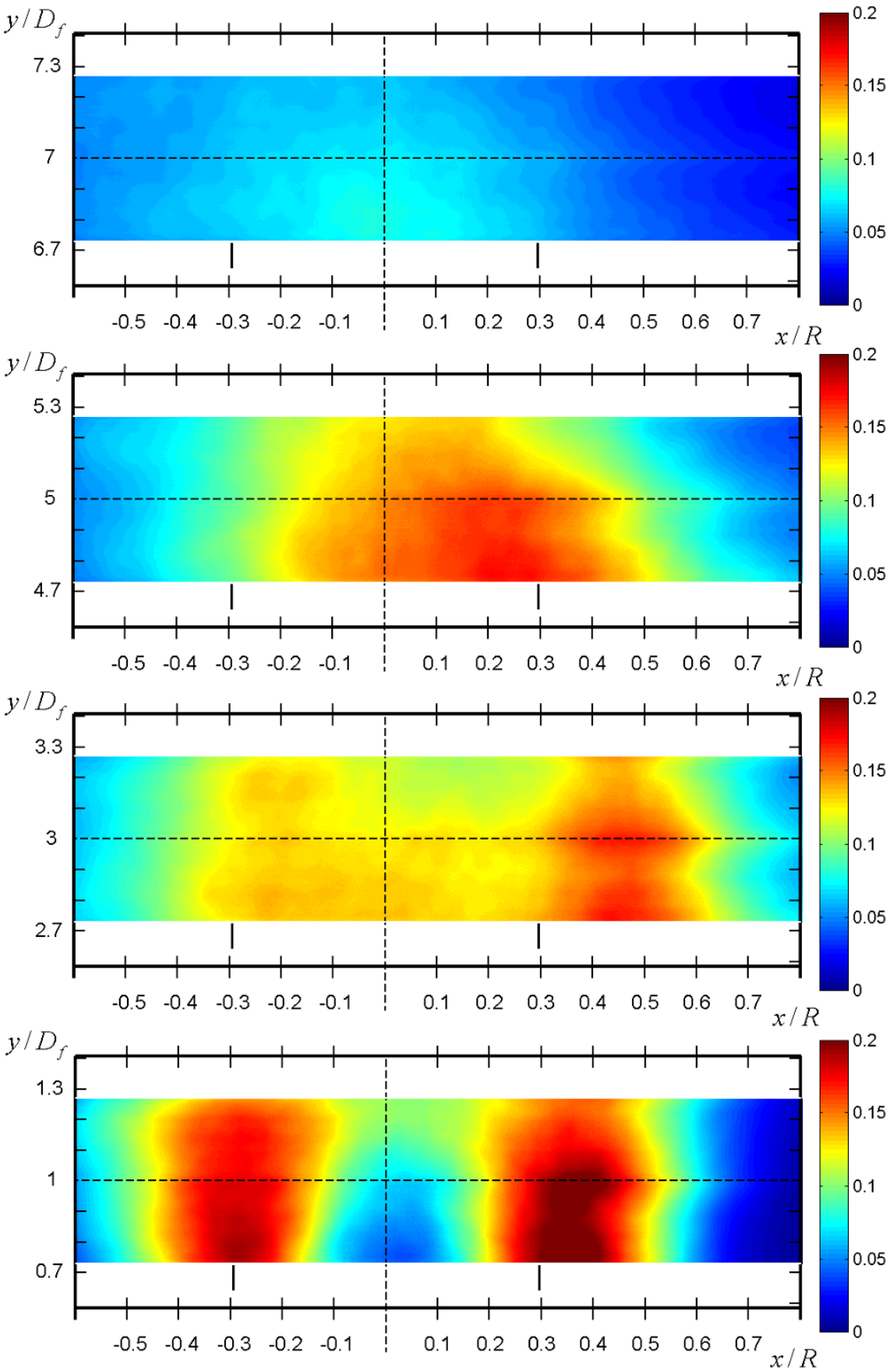

Figure 4.11: Standard deviation of fluctuations of mixture fraction at $y/D_f = 1, 3, 5, 7$ for $S = 0.58$ (no Wiener filter). Radial scale was normalised by burner radius R. The position of the edges of the central pipe delivering the acetone vapour jet is shown by the vertical short lines at $\approx \pm 0.3$ x/R.

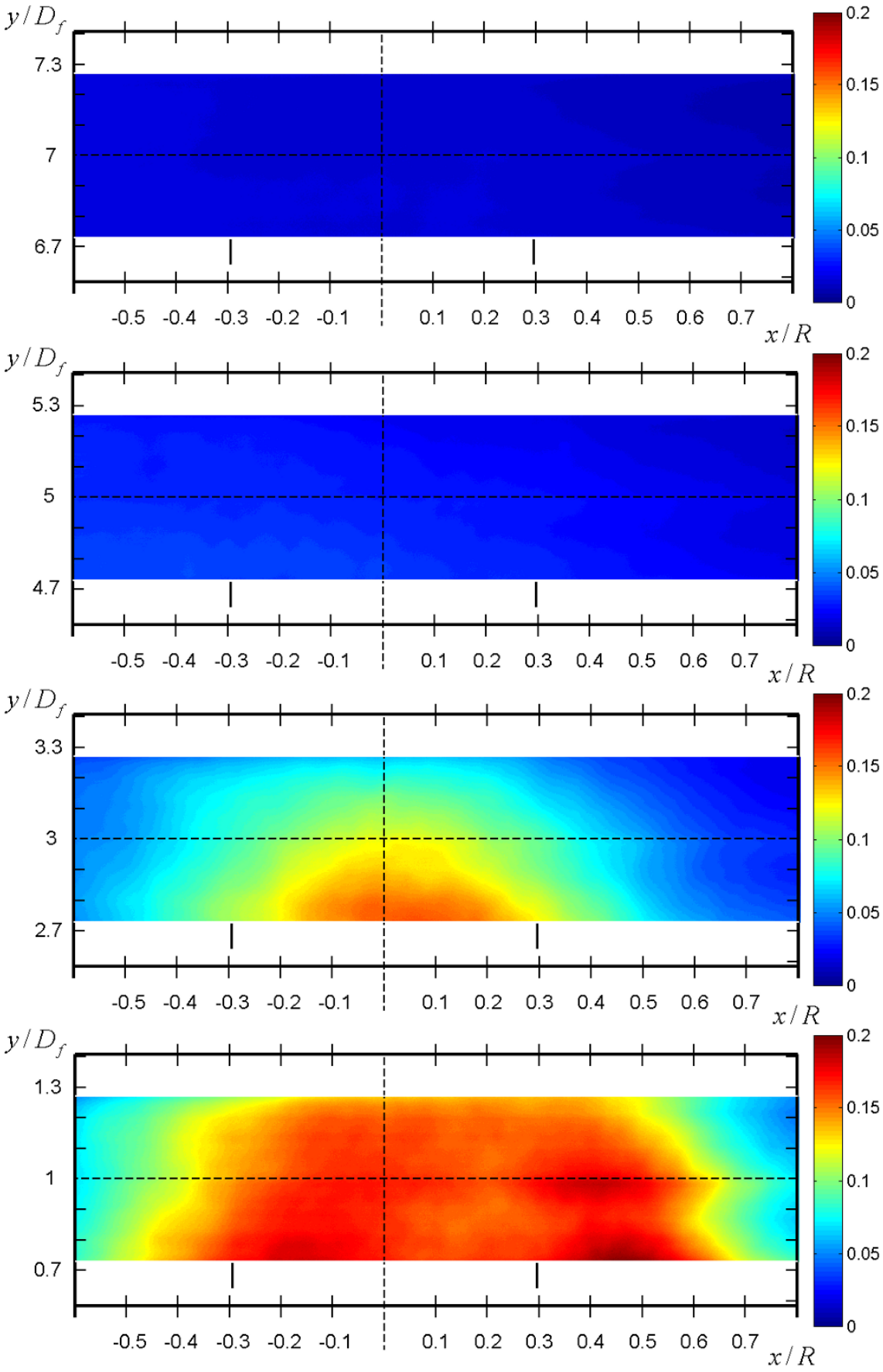

Figure 4.12: Standard deviation of fluctuations of mixture fraction at $y/D_f = 1, 3, 5, 7$ for $S = 1.07$ (no Wiener filter). Radial scale was normalised by burner radius R. The position of the edges of the central pipe delivering the acetone vapour jet is shown by the vertical short lines at $\approx \pm 0.3$ x/R.

Corresponding radial profiles of the mixture fraction at each measured axial positions are shown in Figures 4.13−4.14. It is interesting to note that the radial profiles of the mixture fraction at $y/D_f = 1$ are slightly affected by low and intermediate swirl numbers i.e. 0.3 and 0.58, which may be explained by the weak internal recirculation zone that always exists in swirling flows. It is unlikely that this was due to the wakes downstream of the three locking screws within the flow development section of the annular duct.

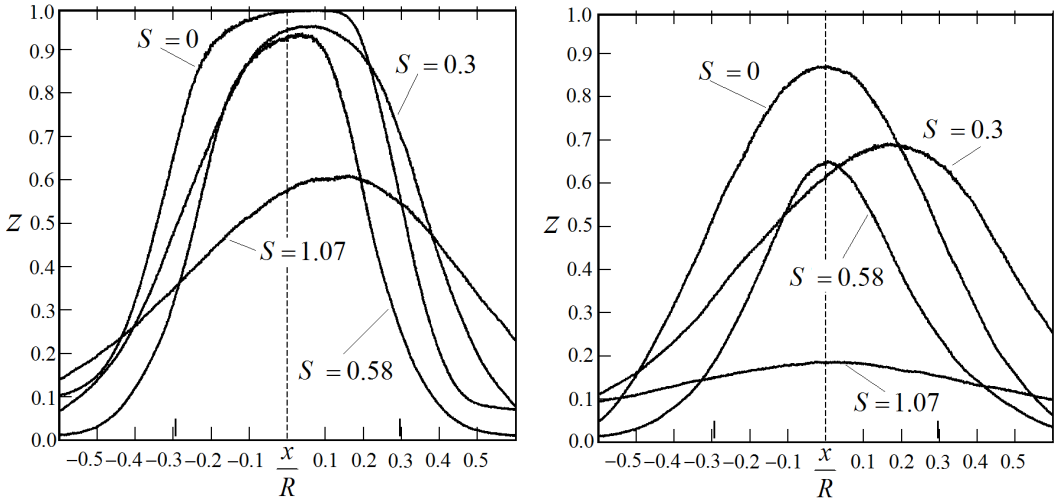

Figure 4.13: Mean mixture fraction radial profiles cut at the centre of laser sheet at $y/D_f = 1$ (left) and $y/D_f = 3$ (right) as a function of swirl number. $S = 0$ denotes acetone vapour jet only without swirling coflow of air.

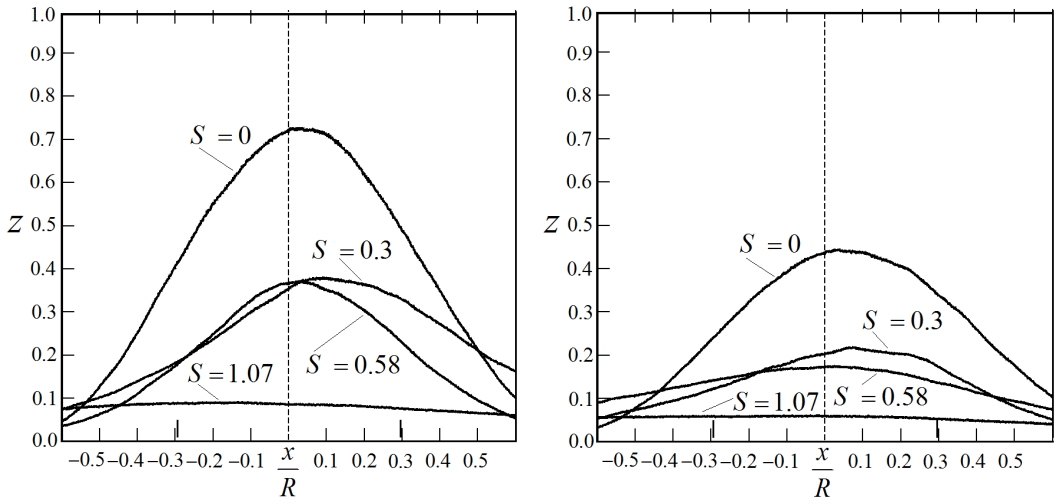

Figure 4.14: Mean mixture fraction radial profiles cut at the centre of laser sheet at $y/D_f = 5$ (left) and $y/D_f = 7$ (right) as a function of swirl number.

More evidence for enhanced mixing is shown in Figures 4.9 and 4.12, which show mixture fraction standard deviation distribution at $y/D_f = 1, 3, 5, 7$. The figures show a relatively uniform distribution of mixture fraction values around the mean at $y/D_f = 5$ and $y/D_f = 7$, especially for high swirl numbers. In contrast, acetone concentration is high within the region of the jet fuel pipe, indicating highly non−mixed region. Enhanced mixing can be associated with processing vortex core (PVC) as was reported by, e.g. Sloan *et*

al. (1986) and Syred (1973). Reacting and non−reacting swirling flow were also well documented by, e.g Landenfeld *et al.* (1998), Lawn (1987) and Beeller & Chigier (1983). However, most of the published papers were dedicated to velocity measurements (including associated statistics) and no systematic data of scalar mixing in swirling isothermal jets were reported.

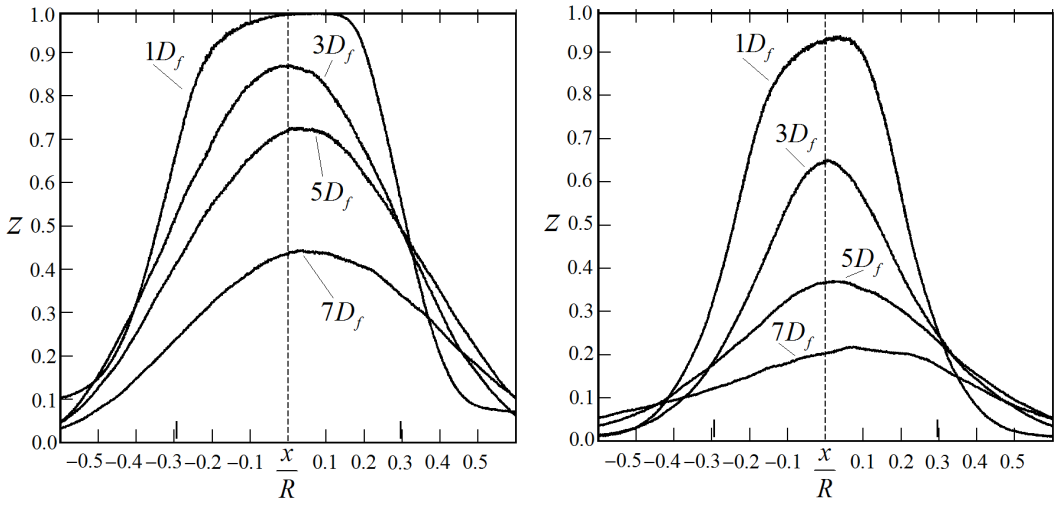

Figure 4.15: Mean mixture fraction radial profiles cut through the centre of laser sheet as a function of normalized axial distance y/D_f for the acetone vapour jet only (left) and for $S = 0.3$ (right)

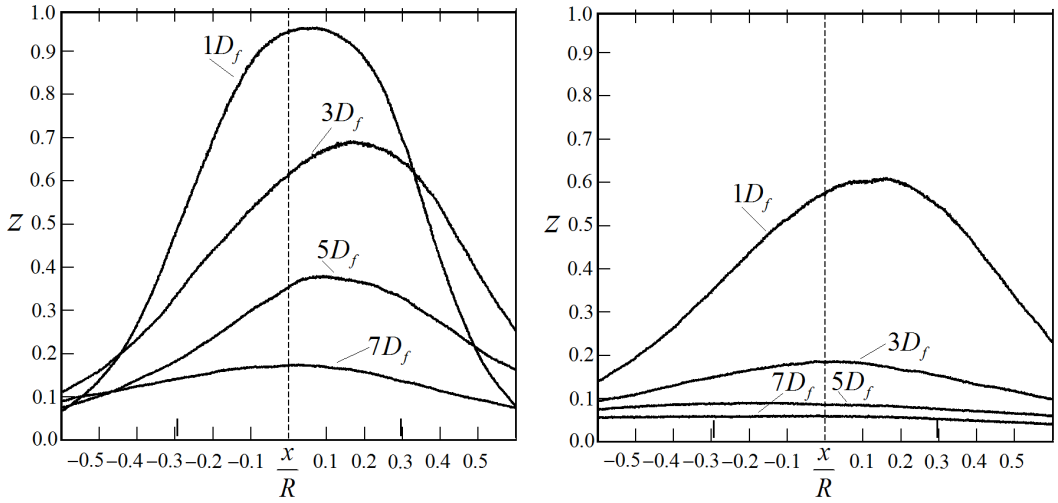

Figure 4.16: Mean mixture fraction radial profiles cut through the centre of laser sheet as a function of normalized axial distance y/D_f for $S = 0.58$ (left) and for $S = 1.07$ (right)

4.2 Mixture fraction dissipation rate

4.2.1 Instantaneous scalar dissipation

The scalar dissipation rate plays an important role in non−premixed combustion, because the combustion regime is usually governed by the diffusion time, which can be characterized

by the Damkohler number. In turn, the diffusion time is inverse of the scalar dissipation rate, which is directly related to mixture fraction gradients. It can be sought that the rate of fuel oxidation or depletion is also proportional to the scalar dissipation rate.

Though the computation of scalar dissipation rate generally involves the computation of the 3D gradients of the mixture fraction, it is practically hard to obtain the 3D distributions of mixture fraction distribution. In homogeneous and isotropic turbulent fields, the three−dimensional scalar dissipation rate can easily be computed, because the statistics of the mixture fraction fluctuations are the same in all three directions. In this case, one of the 3D−components can be measured and the calculation of the scalar dissipation rate is quite straightforward. In this work, the 2D gradients of the mixture fraction were computed from instantaneous mixture fraction distributions by using central finite−difference scheme and commercially available software MATLAB©.

The rate of mixing, quantified by the scalar dissipation rate, can be formally written as follows:

$$\chi = D\left[\left(\frac{\partial z}{\partial x_1}\right)^2 + \left(\frac{\partial z}{\partial x_2}\right)^2 + \left(\frac{\partial z}{\partial x_3}\right)^2\right] \tag{4.1}$$

$$\chi = 2D\left[\left(\frac{\partial z}{\partial x}\right)^2 + \left(\frac{\partial z}{\partial y}\right)^2\right] \tag{4.2}$$

where x_1, x_2, x_3 are spatial coordinates (x, y, z).

In this work the two−dimensional scalar dissipation rate is determined from the measured mixture fraction z fields according to Eq. 4.2, where x and y correspond to radial and axial components of the mixture fraction derivative. The local acetone diffusivity D was set constant and equalled to $12.4(mm^2/s)$.

Figure 4.17 shows an unfiltered scalar dissipation rate (raw scalar dissipation rate), computed from the raw mixture fraction image and the result of the application of the Wiener filter for acetone vapour jet only without air coflow at $y/D_f = 1$. Figure 4.18 shows filtered scalar dissipation rate for acetone vapour jet only without air coflow at $y/D_f = 3, 5, 7$. It can be seen that the largest scalar dissipation rate is concentrated within jet periphery where mixing of the central acetone vapour jet with ambient air takes place (note that there is no coflow). At higher downstream distances from the burner exit, i.e. $y/D_f = 3 - 7$, the central acetone vapour jet diffuses into surrounding air, thus decreasing local mixture fraction gradients, which leads to lower scalar dissipation rate.

Figures 4.19−4.21 show instantaneous scalar dissipation rate as the result of the application of the Wiener filter. The maximum of instantaneous scalar dissipation rate was found to be up to $35(s^{-1})$ depending on instantaneous realizations, downstream positions and the swirl numbers. The general observation was that the scalar dissipation rate increased with the increase in swirl number for axial positions $y/D_f = 1, 3, 5$. The reason the scalar dissipation rate increases with increase in the swirl number is highly non−homogeneous scalar field, especially at lower downstream positions. At higher downstream positions and high swirl numbers i.e. $y/D_f = 7$ and $S = 1.07$, the scalar dissipation rate decreases to very small values due to highly homogeneous scalar fields indicating well−mixed regime, in which mixture fraction gradients are small. As it was expected, the largest scalar dissi-

pation rate was observed at the interface between the acetone vapour jet and the coflow air stream i.e. at radial positions of $\approx \pm 0.3$ x/R, especially at lower axial locations e.g. $y/D_f = 1, 3$ and low swirl numbers ($S = 0.3$, 0.58).

4.2.2 Mean scalar dissipation rate

Figures 4.22−4.25 show the mean scalar dissipation rate computed from 1500 instantaneous images and a horizontal cut through the centre of laser sheet (horizontal dashed line). The values of scalar dissipation rate in these images are typically much smaller than the values found in instantaneous images Figures 4.18−4.21. Values of up to $35(s^{-1})$, assuming acetone diffusivity value of $12.4(mm^2/s)$, can be found in instantaneous realizations, while mean dissipation rate values are approximately $3(s^{-1})$ or less. The higher scalar dissipation rate values in the mean images correspond to lower downstream positions, where the mixture fraction gradients are larger due to highly segregated scalar fields. The second observation is that the mean scalar dissipation rate distribution is similar to the standard deviation distribution of the fluctuations of mixture fraction, which had been described earlier. The highest scalar dissipation rate values are observed at the fuel jet periphery, i.e. at $\pm 0.3\ x/R$ for $y/D_f = 1, 3$, and can be seen even in instantaneous images. However, at higher downstream distances, far away from the jet origin no distinct location can be easily observed.

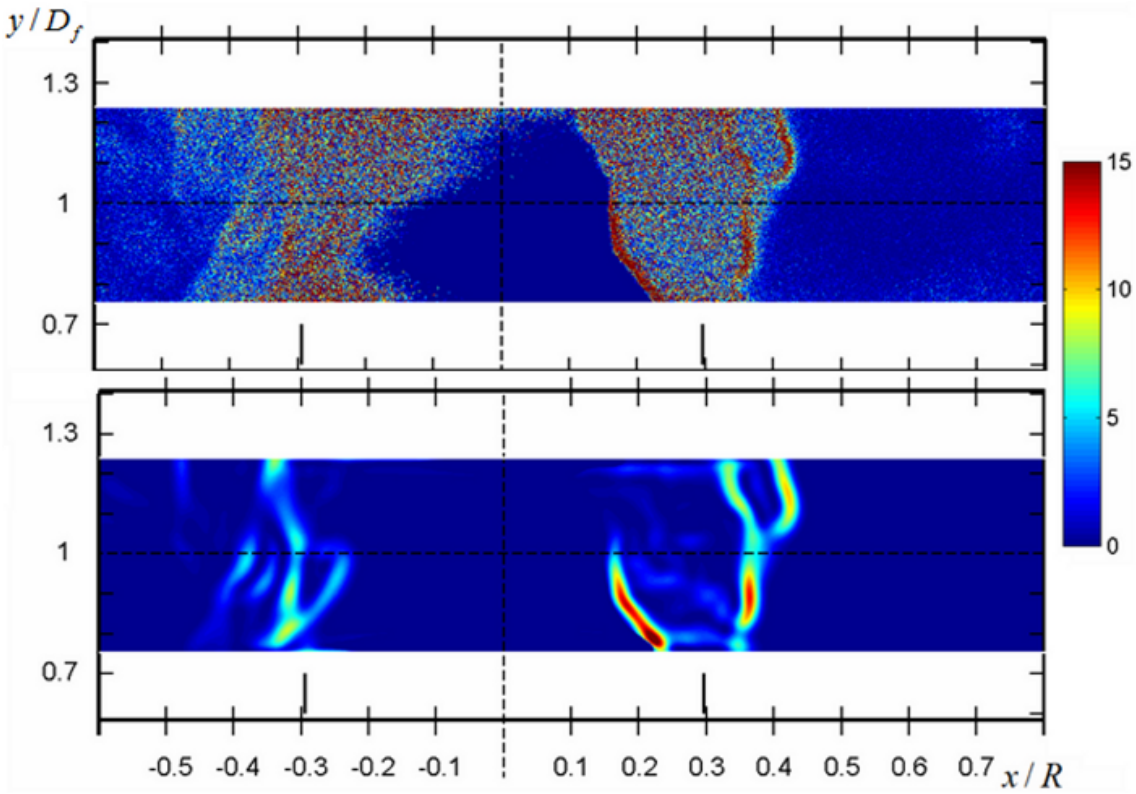

Figure 4.17: An example of instantaneous raw scalar dissipation rate (s^{-1}) and the result of the application of the Wiener filter (bottom) computed at $y/D_f = 1$ for acetone vapour jet only without swirling coflow of air. Radial scale was normalised by burner radius R. The position of the edges of the central pipe delivering the acetone vapour jet is shown by the vertical short lines at $\approx \pm 0.3$ x/R.

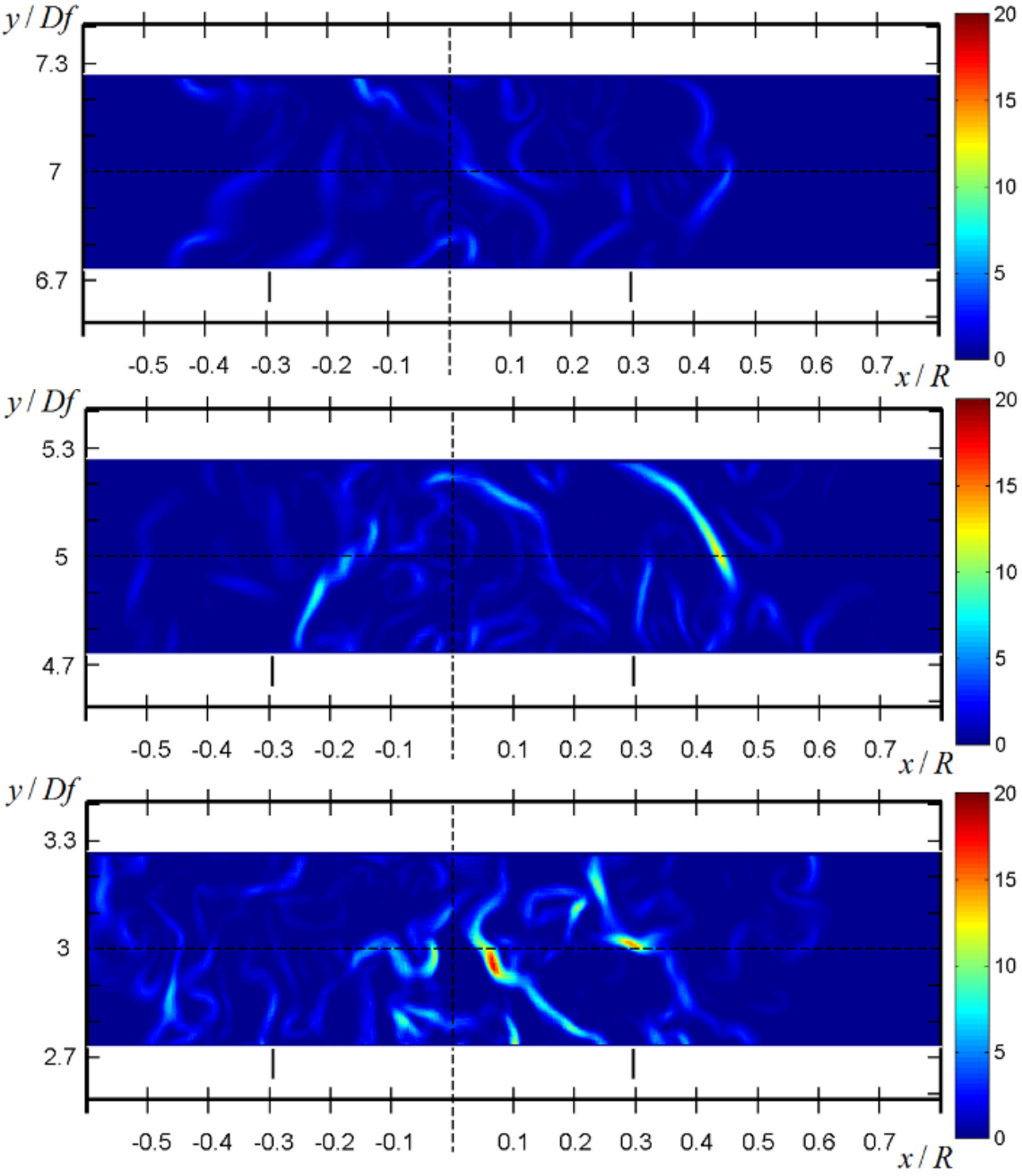

Figure 4.18: An instantaneous scalar dissipation rate (s^{-1}) computed at $y/D_f = 3, 5, 7$ for acetone vapour jet only without surrounding coflow of air. Scalar dissipation rate at $y/D_f = 1$ is reported in Fig. 4.17.

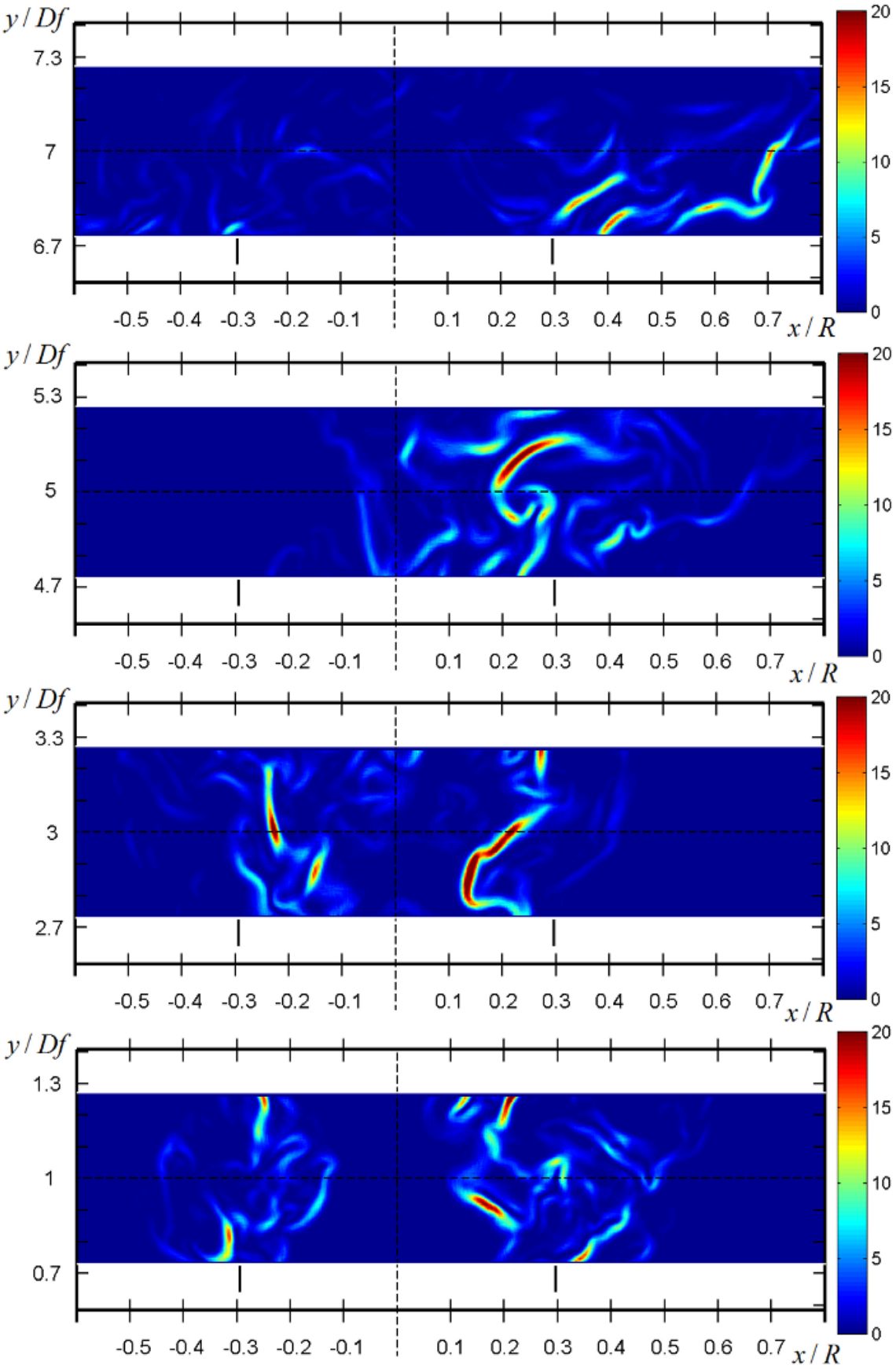

Figure 4.19: An instantaneous scalar dissipation rate (s^{-1}) computed at $y/D_f = 1, 3, 5, 7$ for $S = 0.3$. Radial scale was normalised by burner radius R. The position of the edges of the central pipe delivering the acetone vapour jet is shown by the vertical short lines at $\approx \pm 0.3$ x/R.

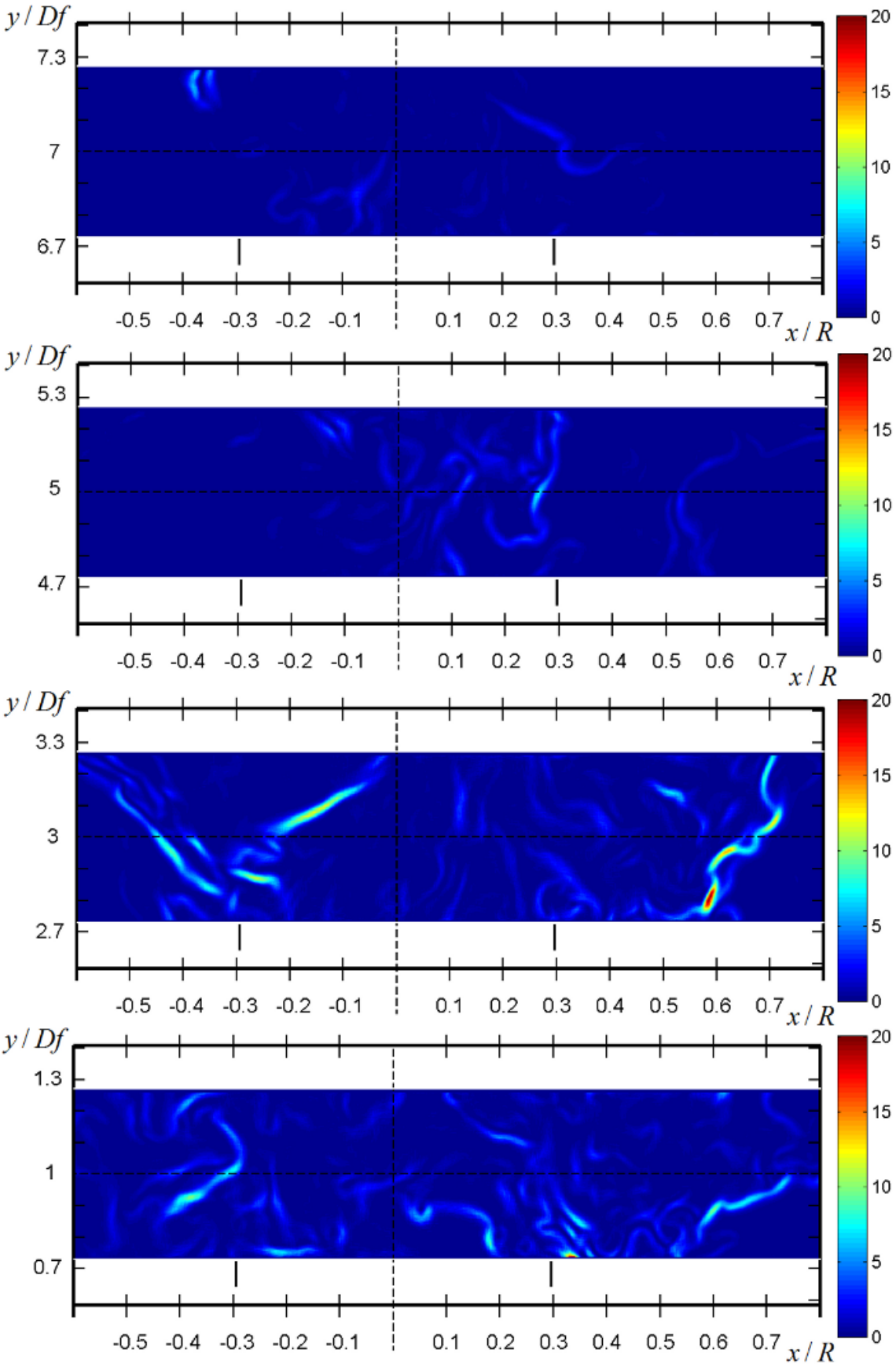

Figure 4.20: An instantaneous scalar dissipation rate (s^{-1}) computed at $y/D_f = 1, 3, 5, 7$ for $S = 0.58$. Radial scale was normalised by burner radius R. The position of the edges of the central pipe delivering the acetone vapour jet is shown by the vertical short lines at $\approx \pm 0.3$ x/R.

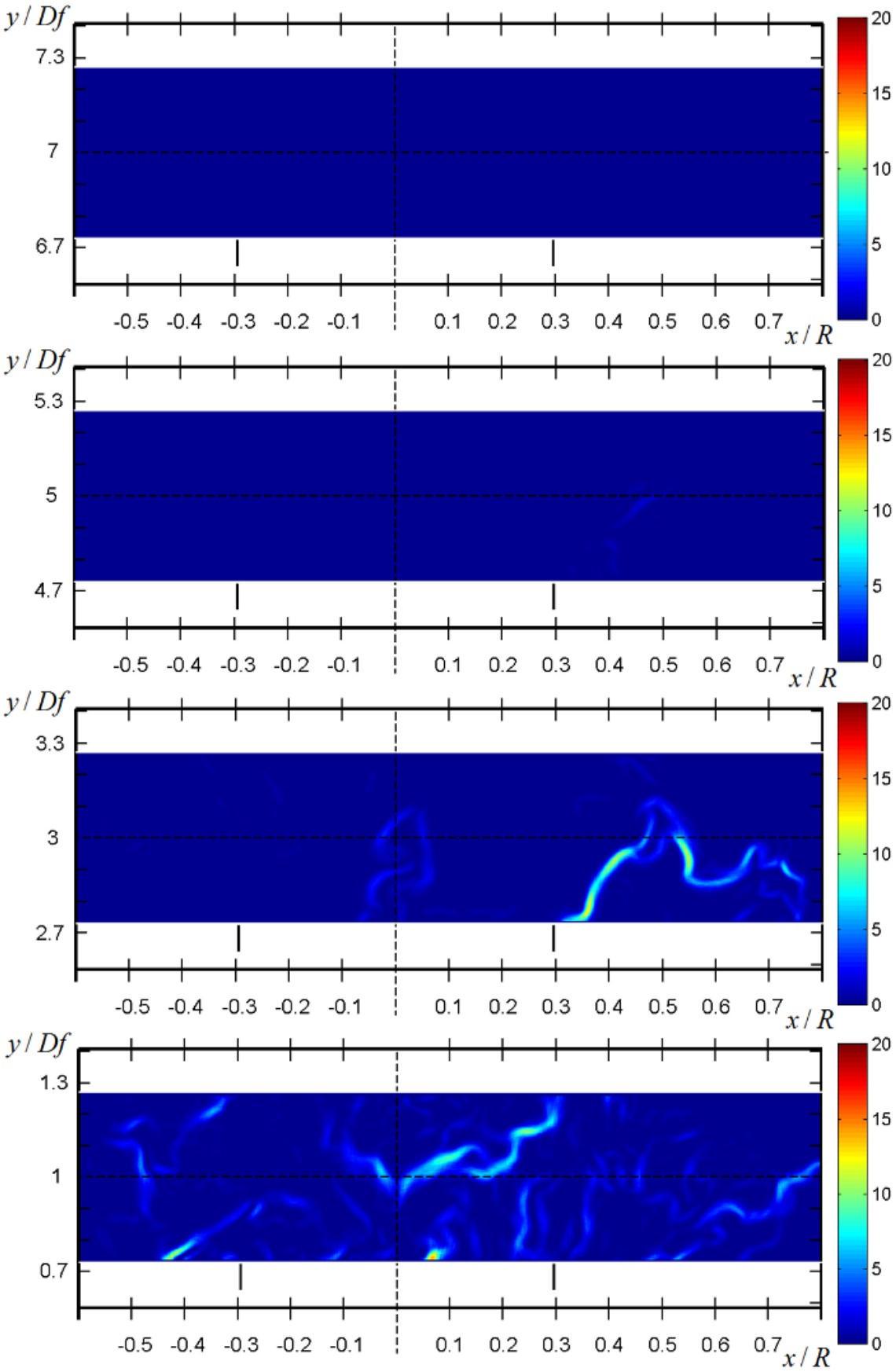

Figure 4.21: An instantaneous scalar dissipation rate (s^{-1}) computed at $y/D_f = 1, 3, 5, 7$ for $S = 1.07$. Radial scale was normalised by burner radius R. The position of the edges of the central pipe delivering the acetone vapour jet is shown by the vertical short lines at $\approx \pm 0.3$ x/R.

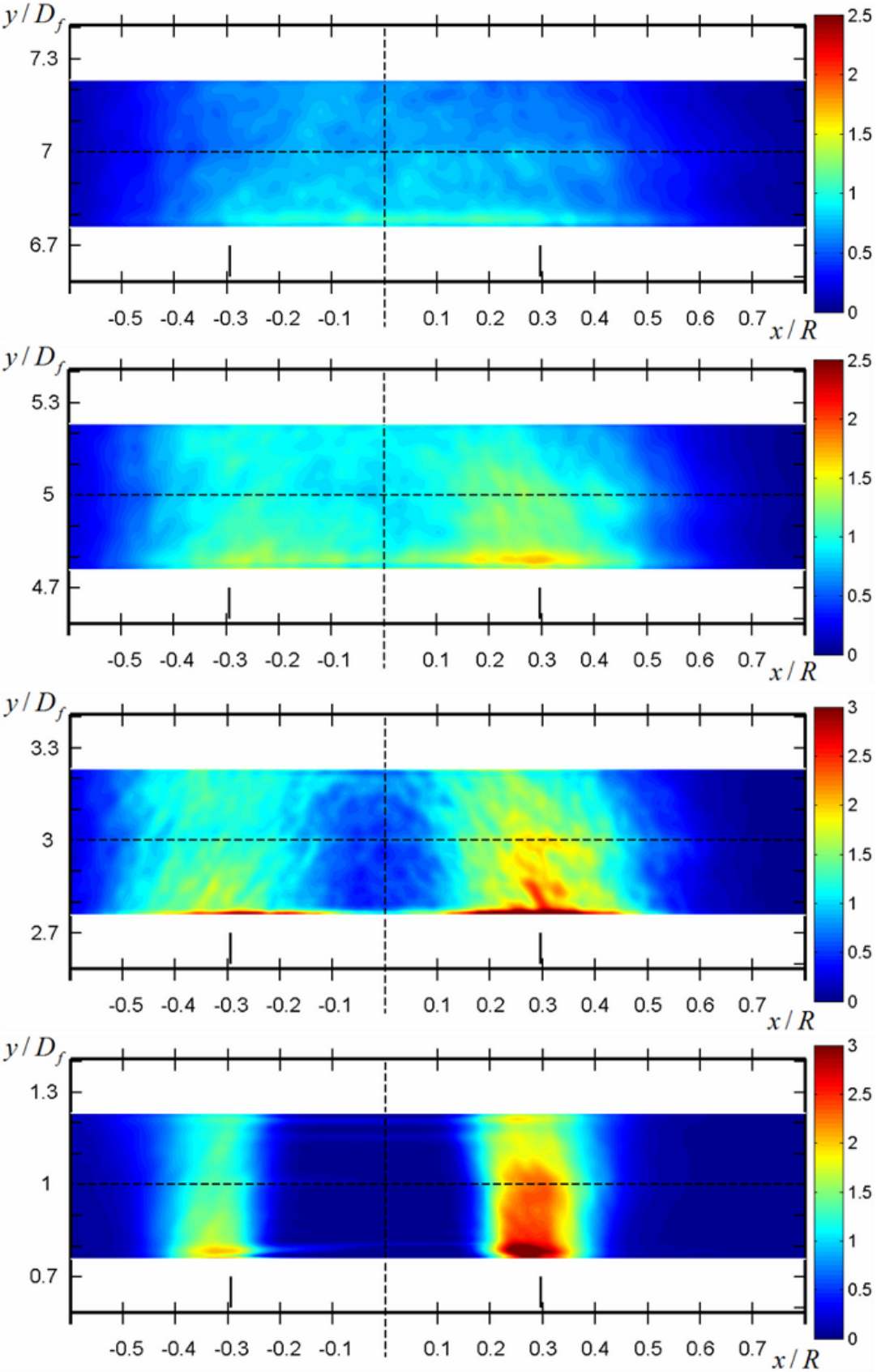

Figure 4.22: Mean scalar dissipation rate (s^{-1}), averaged over 1500 instantaneous images, at $y/D_f = 1, 3, 5, 7$ for acetone vapour jet only. Maximum scalar dissipation rate values are not the same for all images and are 2.5, 2.5, 3.0 and 3.0 (from top to bottom). Radial scale was normalised by burner radius R. The position of the edges of the central pipe delivering the acetone vapour jet is shown by the vertical short lines at $\approx \pm 0.3$ x/R.

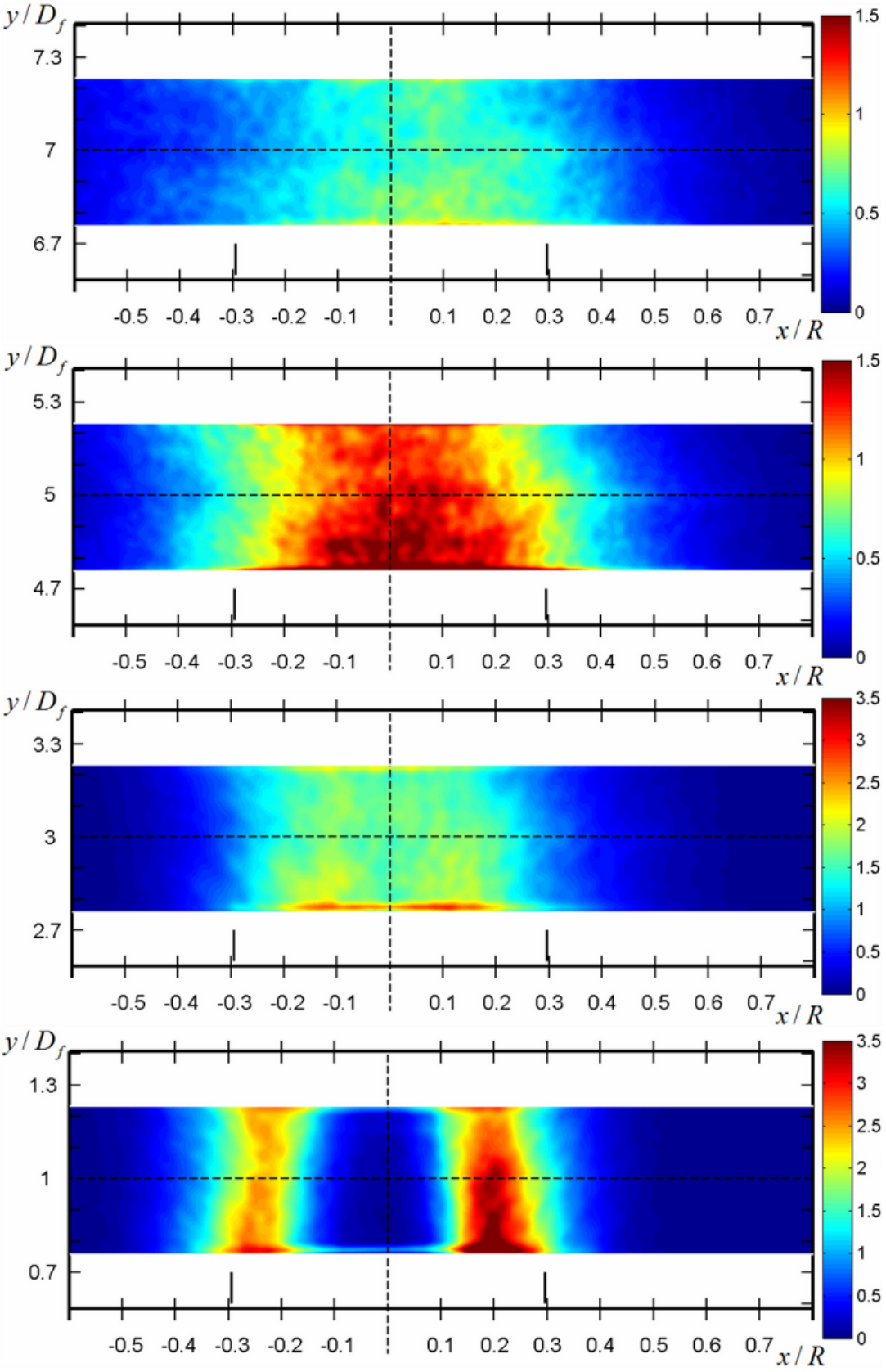

Figure 4.23: Mean scalar dissipation rate (s^{-1}), averaged over 1500 instantaneous images, at $y/D_f = 1, 3, 5, 7$ for $S = 0.3$. Maximum scalar dissipation values are not the same for all images and are 1.5, 1.5, 3.5 and 3.5 (from top to bottom). Radial scale was normalised by burner radius R. The position of the edges of the central pipe delivering the acetone vapour jet is shown by the vertical short lines at $\approx \pm 0.3$ x/R.

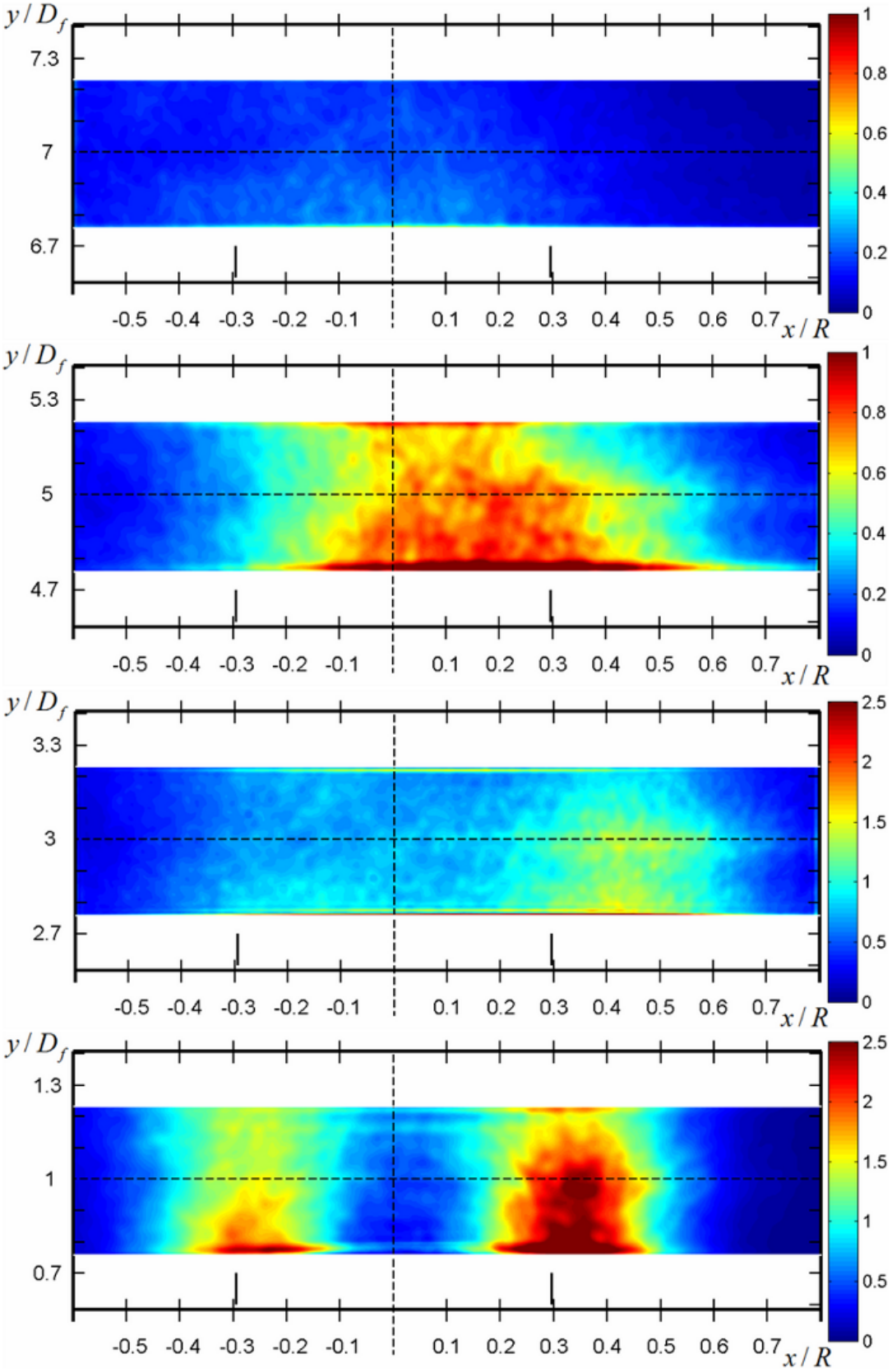

Figure 4.24: Mean scalar dissipation rate (s^{-1}), averaged over 1500 instantaneous images, at $y/D_f = 1, 3, 5, 7$ for $S = 0.58$. Maximum scalar dissipation rate values are not the same for all images and are 1.0, 1.0, 2.5 and 2.5 (from top to bottom). Radial scale was normalised by burner radius R. The position of the edges of the central pipe delivering the acetone vapour jet is shown by the vertical short lines at $\approx \pm 0.3$ x/R.

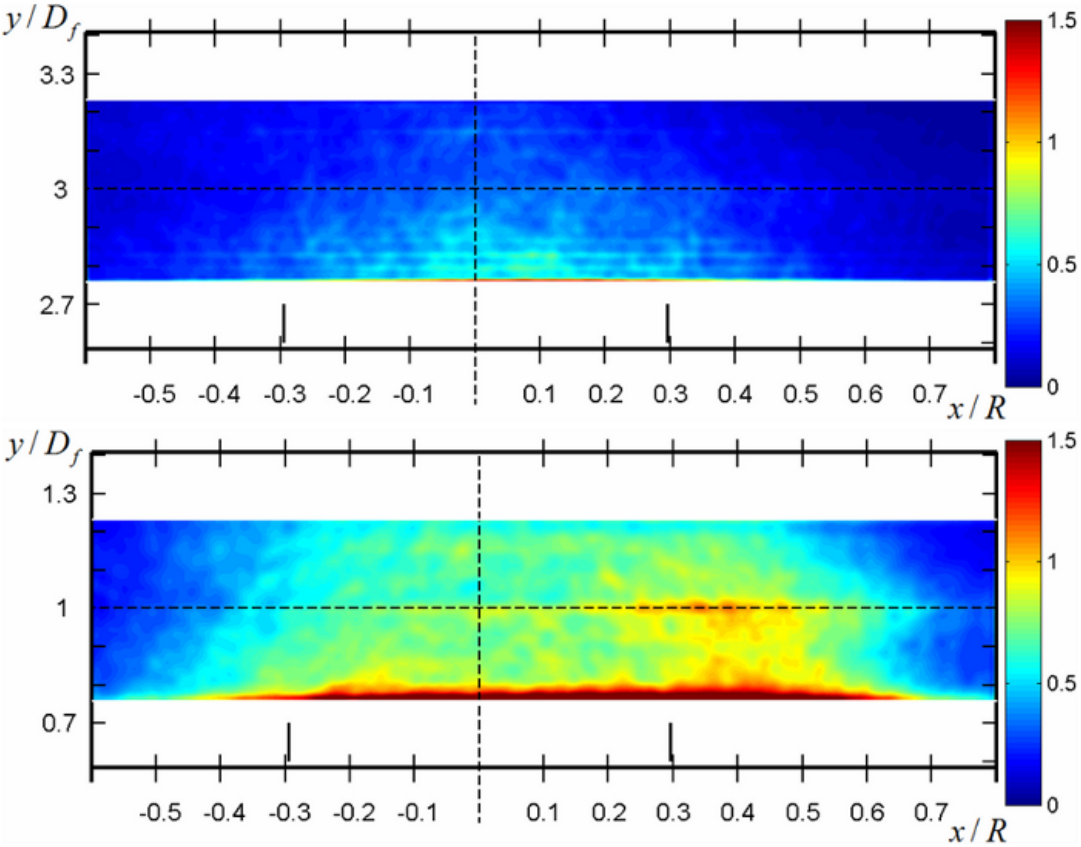

Figure 4.25: Mean scalar dissipation rate (s^{-1}), averaged over 1500 instantaneous images, at $y/D_f = 3$, and $y/D_f = 1$ (from top to bottom) for $S = 1.07$. Higher axial positions i.e. $y/D_f = 5$ and $y/D_f = 7$ are not shown, because the scalar dissipation distribution is similar to that found at $y/D_f = 3$ and is fully homogeneous with values $<< 1$. Radial scale was normalised by burner radius R. The position of the edges of the central pipe delivering the acetone vapour jet is shown by the vertical short lines at $\approx \pm 0.3$ x/R.

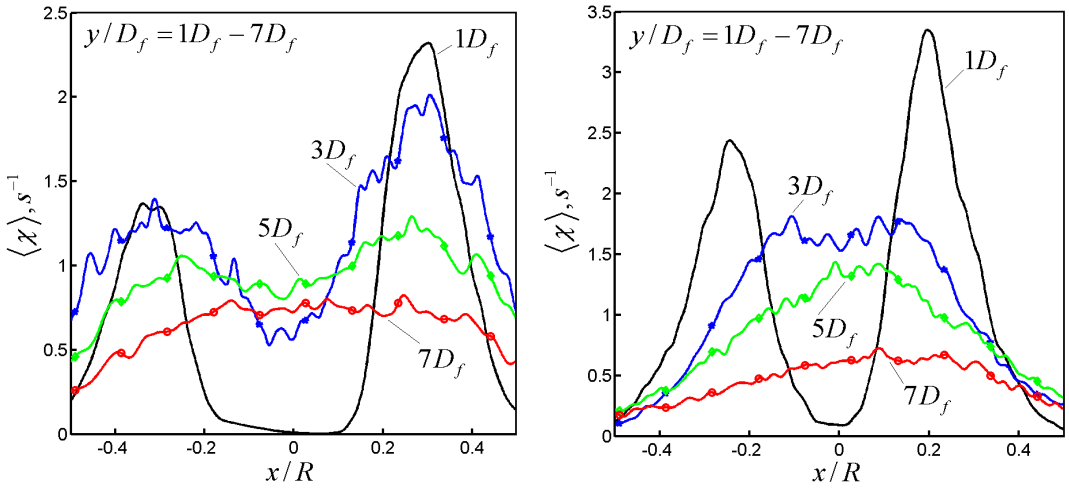

Figure 4.26: A horizontal profile along laser sheet axis of the mean scalar dissipation rate (s^{-1}) averaged over 1500 instantaneous images, for acetone vapour jet only (left) and $S = 0.3$ (right). Vertical $y-$axis is not the same in each figure and corresponds to the maximum value of 2.5 (left) and 3.5 (right).

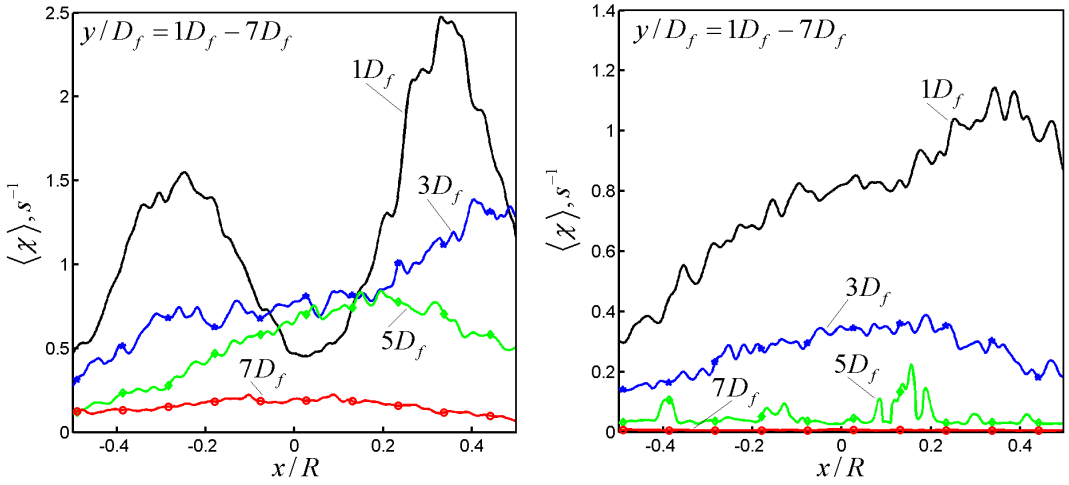

Figure 4.27: A horizontal profile along laser sheet axis of the mean scalar dissipation rate (s^{-1}) averaged over 1500 instantaneous images, for $S = 0.58$ (left) and $S = 1.07$ (right). Vertical $y-$axis is not the same in each figure and corresponds to the maximum value of 2.5 (left) and 1.4 (right).

Figures 4.26−4.27 show horizontal profile along laser sheet axis of the mean scalar dissipation rate averaged over 1500 instantaneous images, for acetone vapour jet only, S =0.3, 0.58 and 1.07 at different y/D_f. It is clearly seen that the mean scalar dissipation rate decreases with distance from the burner exit. Higher swirl numbers also lead to lower mean scalar dissipation rate.

4.2.3 Dissipative layer thickness

The structure of the scalar distribution can be characterized by the thickness of the dissipation layers, which are seen as wrinkled flake−like or layer−like structures. A characteristic width of the dissipative structures can be directly measured from instantaneous 2D images of dissipation rate distribution. The thickness of the dissipation rate layer can be defined as the region of the finite dissipation rate or as the thickness of the interface (Su & Clemens, 2003). For consistency with similar studies in non−swirling, non−reacting flows (Su & Clemens, 2003), the thickness of the dissipative structures (λ_D) was measured as the full width of 20% of the local dissipation layer maximum. The layer width was determined according to the following procedure.

Figure 4.28 shows the principle of computation the thickness of the scalar dissipation layers. The 20% half−width was measured on one side of the layer (defined as I_2 in Fig. 4.28) and then was subsequently doubled to yield the 20% full width. The 20% half width was measured along x−axis and after doubling was denoted as L_1 in Figure 4.28. Since, the layers were positioned at different angles with respect to x−axis, the true dissipation thickness can be determined by multiplying the measured L_1 with $cos(\alpha)$, where α is the layer angle (see Fig. 4.28). According to Figure4.28, the dissipative layer thickness can be computed as $\lambda_D = L_1 * cos(\alpha)$, where α the angle between the layer structure centreline and the radial direction, i.e. along x−axis and is computed via $tan(\alpha) = L_2/L_3$.

The PDFs of the dissipative layer thickness for acetone vapour jet only and $S = 0.3$ are shown in Figure 4.29. The PDFs of the dissipative layer thickness for $S = 0.58$

and $S = 1.07$ are shown in Figure 4.30. All PDFs were computed from 100 instantaneous images and were normalised by their corresponding maximum values. The PDFs computed from a single instantaneous image, demonstrated the same trends.

The peaks of the PDFs are at approximately $500-900(\mu m)$, depending on swirl number and downstream positions. All PDFs have long tails that extend toward larger values of dissipative layer thickness. These tails have been also reported for thermal dissipation layers by Kaiser & Frank (2007) where it was suggested that it could result from two−dimensional measurements of three−dimensional structures. Similar observations were reported by Su & Clemens, (2003) for planar turbulent jets. Kaiser & Frank (2007) suggested that cutoff length scales from dissipation spectral analysis were on the same order as the dissipative layer thickness at the peak of the measured PDFs. In this work, however, this statement is less valid, because the peak of PDFs of the layer thickness is $\approx$ 1.5-2 times larger than cuttoff length scales, which were computed as $\approx 300 - 500(\mu m)$. Note that the PDF of the layer thickness becomes almost delta−PDF when scalar field is almost homogeneous, i.e. $S = 1.07$ at $y/D_f = 7$ ($y/D_f = 7$ in Fig. 4.29).

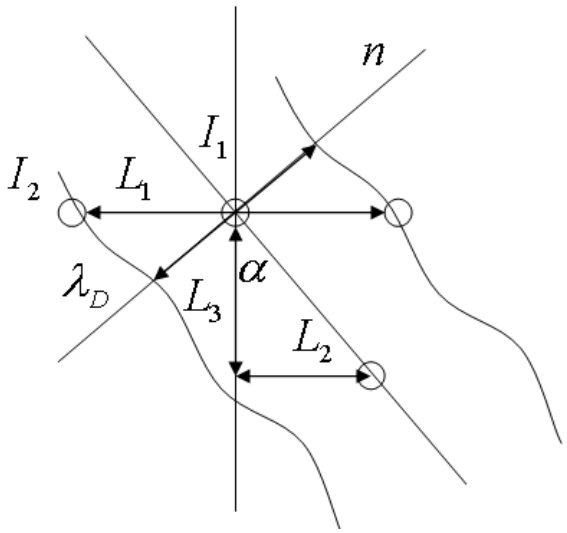

Figure 4.28: The principle of computation the thickness of scalar dissipation layers.

Ahmed (2012) used PLIF technique to examine a shearless mixing layer with isotropic decaying turbulence in opposed−jet flow and a plume in pipe flow, where the thickness of the scalar dissipation rate layer was also computed. The thickness of the scalar dissipation rate layer was computed to be $1250(\mu m)$ and not significant variations of the thickness along the layer length had been observed.

The thickness of the scalar dissipation rate layer may be different if all three components of the scalar dissipation rate are used. The dissipation layer thickness from three components was reported by Su & Clemens, (2003). If the turbulent flow is homogeneous and isotropic, meaning that the statistics of the fluctuations of the mixture fraction are the same in all three directions, the scalar dissipation rate can be obtained from a single component only. In this work, the turbulence is neither homogeneous nor isotropic and hence no assumptions can be invoked in order to define the full scalar dissipation rate from two−dimensional images. However, it is supposed that the scalar dissipation rate

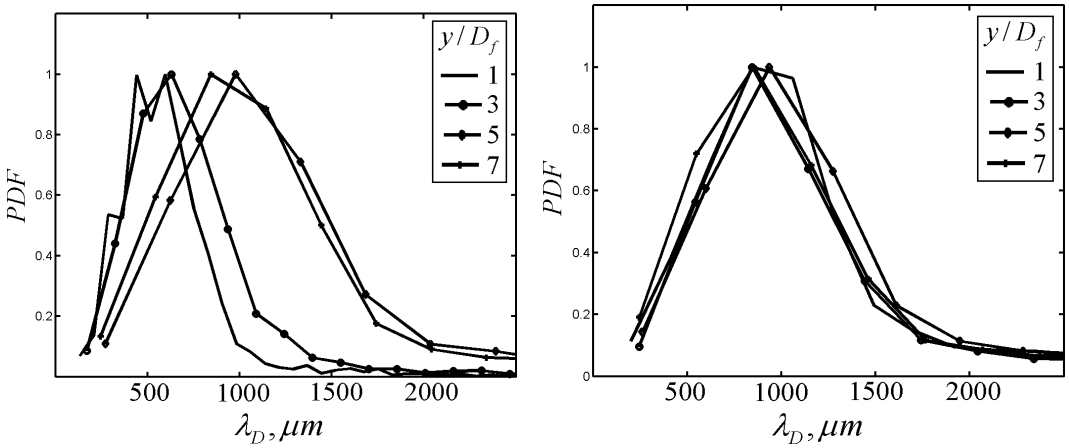

Figure 4.29: The probability distribution of the local scalar dissipation layer thickness, λ_D, for acetone vapour jet only (left) and $S = 0.3$ (right). The PDFs were computed from 100 instantaneous images and were normalised by corresponding maximum values.

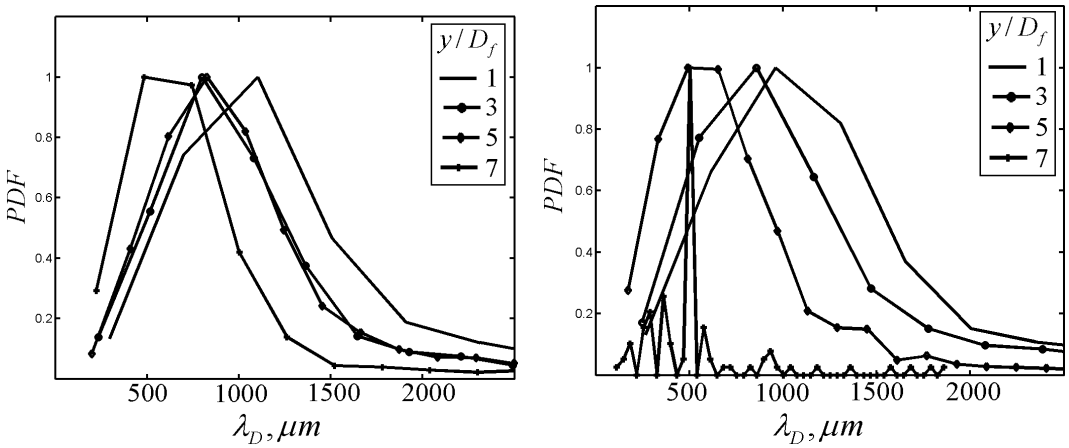

Figure 4.30: The probability distribution of the local scalar dissipation layer thickness, λ_D, for $S = 0.58$ (left) and $S = 1.07$ (right) at different y/D_f. The PDFs were computed from 100 instantaneous images and were normalised by corresponding maximum values.

statistics or at least their trends can be observed from the two components of the scalar dissipation rate.

Another important issue that should be brought to attention before discussing the scalar dissipation rate statistics in details is the issue of gradient vector orientation. A part of the gradient vector, not being measured, will depend on the orientation of the three dimensional vector in three−dimensional space, with respect to the plane measurements. It is quite obvious that the closer the inclination angle being parallel to the plane measurement the smaller the difference between the artificial estimate and the full scalar dissipation rate will be. However, the definition of gradient orientation in swirling flows is not straightforward and not trivial, especially when only two components of the scalar dissipation rate are measured.

4.2.4 Unconditional statistics

In this section, the unconditional statistics of the mixture fraction dissipation rate are presented in order to provide the necessary background needed for a better understanding of mixing in swirling jets. The results, presented in this sections are useful for turbulent reacting flow models, as for example, advanced flamelet and transported p.d.f. closures, which include the fluctuations of the scalar dissipation rate, e.g. Blanquart & Pitsch (2005), Pitch & Fedotov (2000). The unconditional statistics are presented here in terms of the probability density functions of the scalar dissipation rate fluctuations at various positions in the flow, for all normalized downstream positions y/D_f and swirl numbers S. Data for each p.d.f. was compiled by considering the local window of axial length of 1.58(mm) $\approx 5\lambda_\beta$ and radial length of 3.87(mm) $\approx 13\lambda_\beta$ containing 8820 data points and over 1500 images resulting in 13e9 scalar dissipation rate data points for each spatial location. This window was chosen on the basis of the sufficient number of samples for statistical computations. Five spatial locations were investigated and are shown in Figure 4.31. All probability density functions of the scalar dissipation rate of the mixture fraction are presented here in terms of $P(C)$, where P denotes probability density function and C is defined as follows:

$$C = \frac{\ln(\chi) - \overline{\ln(\chi)}}{\sigma_{\ln(\chi)}} \tag{4.3}$$

The p.d.f. of the scalar dissipation rate fluctuations was computed from the logarithm of the instantaneous scalar dissipation rate values minus their mean and normalizing by the standard deviation of the logarithm of the scalar dissipation rate. Models of p.d.fs. of scalar dissipation rate are typically based on log-normal fits and, hence, we use a logarithm notation in order to asses the possibility of having lognormal p.d.f. of the scalar dissipation rate, as it was also demonstrated experimentally by Gurvich & Yaglom (1967) and Soulopoulos (2009).

The range of the scalar dissipation rate values was divided in a number of equal bins (150 bins were typically used) and the number of occurrences in each bin was counted. The p.d.f. was computed as N/LW, where N is the count of values in each bin or frequency, W is the width of the bin and L is the total number of values (cardinality of a dataset). The width of the bin was assessed through a set of trial and error procedures and it was found that the convergence of the p.d.f. was almost independent on the number of bins.

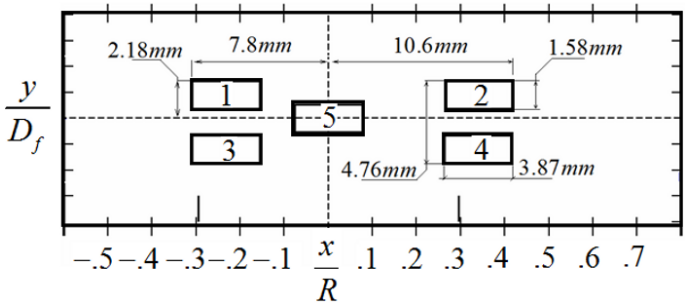

Figure 4.31: Window positions where scalar dissipation rate statistics were evaluated.

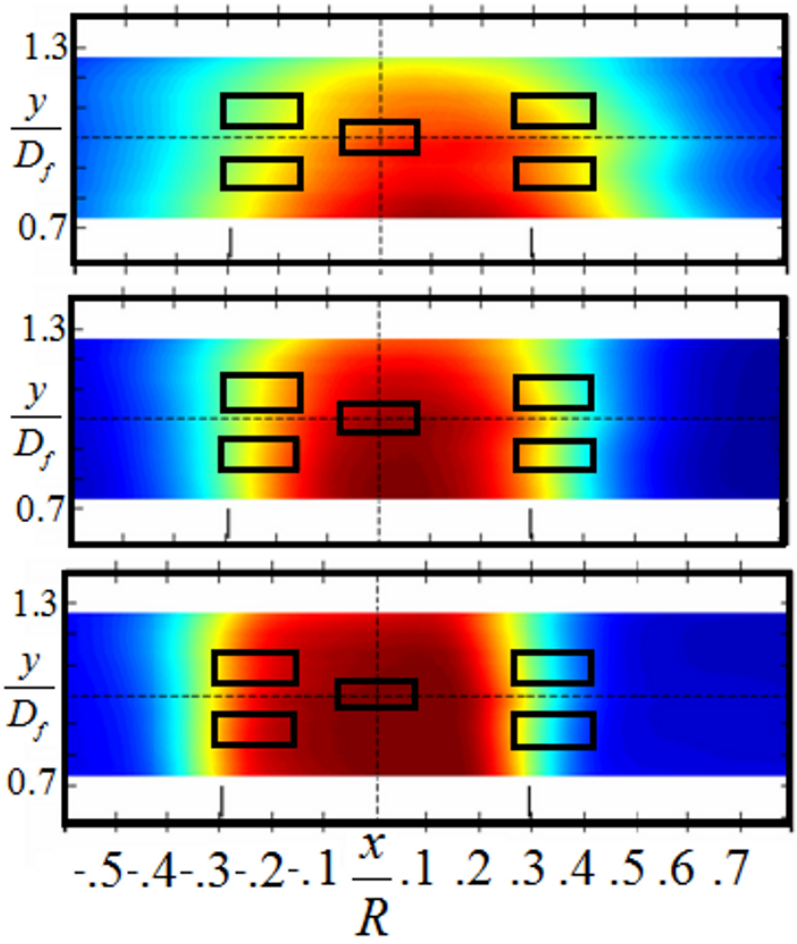

Figure 4.32: Window positions where scalar dissipation rate statistics were evaluated relative to the mean scalar field as a function of swirl number for $S = 1.07$, 0.58 and acetone vapour jet only (from top to bottom) at $y/D_f = 1$.

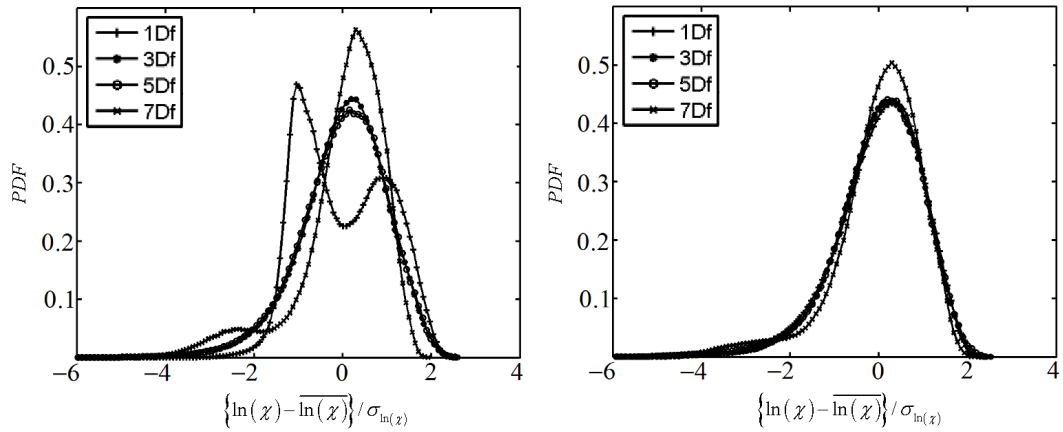

Figure 4.33: The p.d.f. of the fluctuations of the logarithm of the scalar dissipation rate $\left[\ln(\chi) - \overline{\ln(\chi)}\right]/\sigma_{\ln(\chi)}$ from window 1 (left) and 2 (right), computed at $y/D_f = 1, 3, 5, 7$ for acetone vapour jet only.

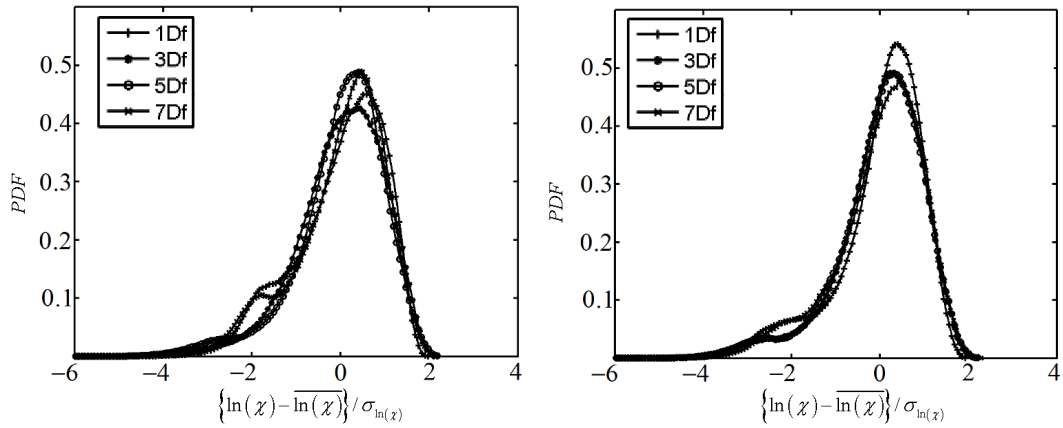

Figure 4.34: The p.d.f. of the fluctuations of the logarithm of the scalar dissipation rate $\left[\ln(\chi)-\overline{\ln(\chi)}\right]/\sigma_{\ln(\chi)}$ from window 1 (left) and 2 (right), computed at $y/D_f = 1, 3, 5, 7$ for $S = 0.3$.

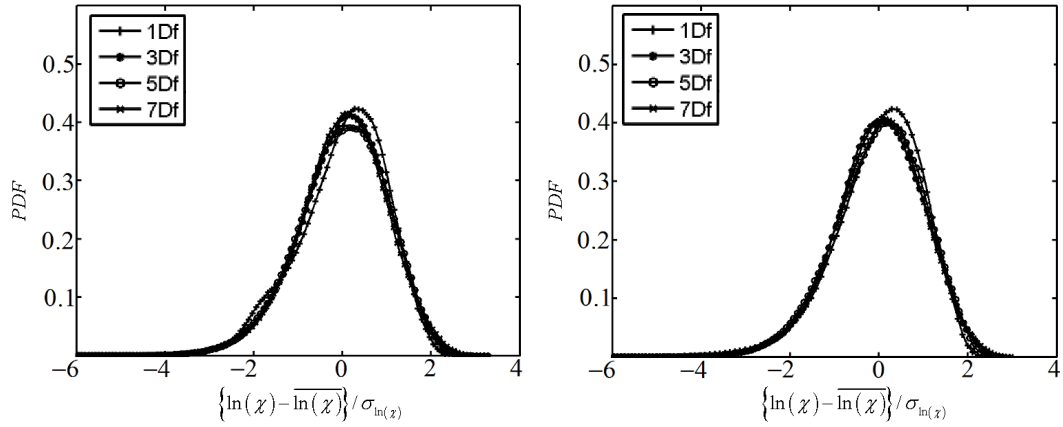

Figure 4.35: The p.d.f. of the fluctuations of the logarithm of the scalar dissipation rate $\left[\ln(\chi)-\overline{\ln(\chi)}\right]/\sigma_{\ln(\chi)}$ from window 1 (left) and 2 (right), computed at $y/D_f = 1, 3, 5, 7$ for $S = 0.58$.

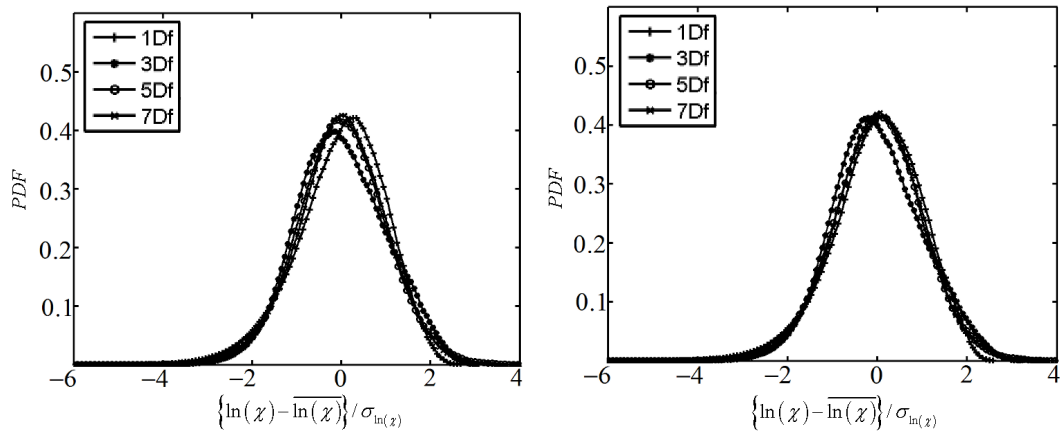

Figure 4.36: The p.d.f. of the fluctuations of the logarithm of the scalar dissipation rate $\left[\ln(\chi)-\overline{\ln(\chi)}\right]/\sigma_{\ln(\chi)}$ from window 1 (left) and 2 (right), computed at $y/D_f = 1, 3, 5, 7$ for $S = 1.07$.

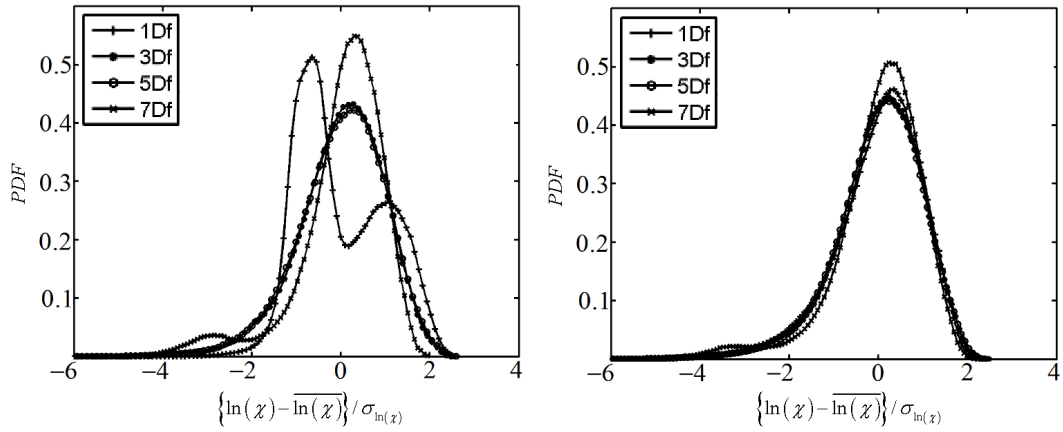

Figure 4.37: The p.d.f. of the fluctuations of the logarithm of the scalar dissipation rate $\left[\ln(\chi)-\overline{\ln(\chi)}\right]/\sigma_{\ln(\chi)}$ from window 3 (left) and 4 (right), computed at $y/D_f = 1, 3, 5, 7$ for acetone vapour jet only.

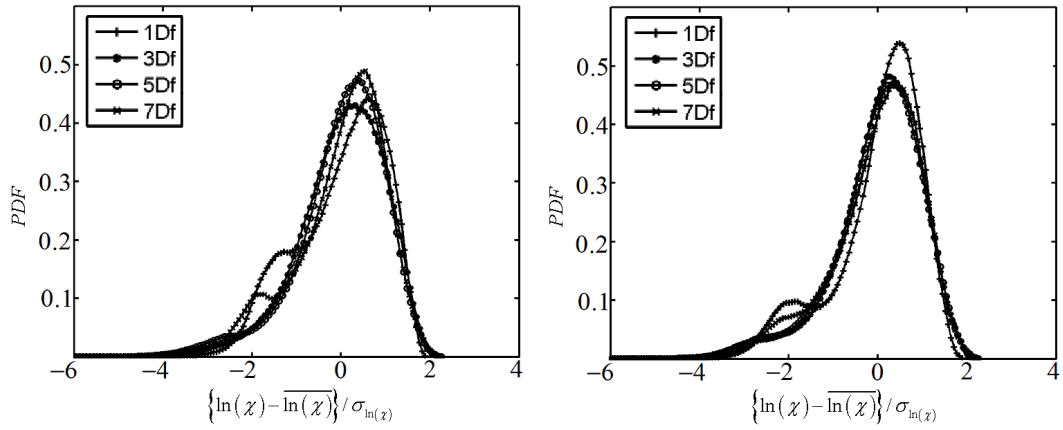

Figure 4.38: The p.d.f. of the fluctuations of the logarithm of the scalar dissipation rate from window 3 (left) and 4 (right), computed at $y/D_f = 1, 3, 5, 7$ for $S = 0.3$.

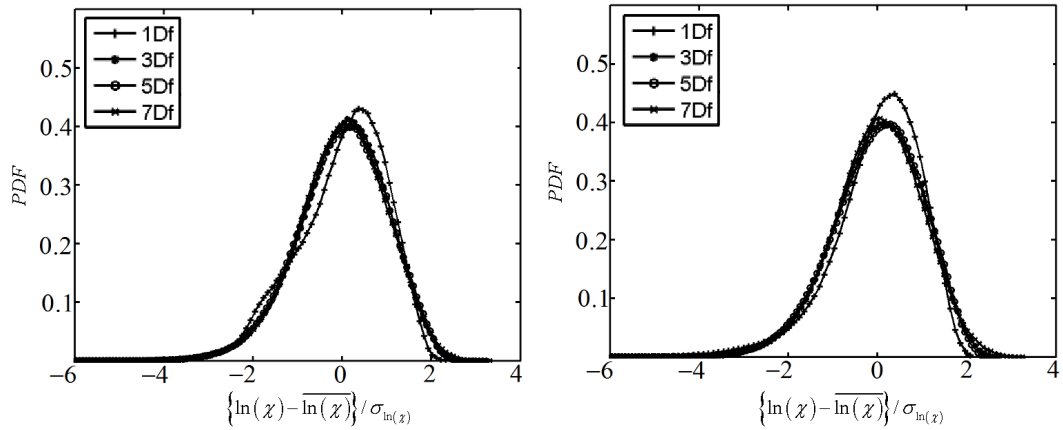

Figure 4.39: The p.d.f. of the fluctuations of the logarithm of the scalar dissipation rate $\left[\ln(\chi)-\overline{\ln(\chi)}\right]/\sigma_{\ln(\chi)}$ from window 3 (left) and 4 (right), computed at $y/D_f = 1, 3, 5, 7$ for $S = 0.58$.

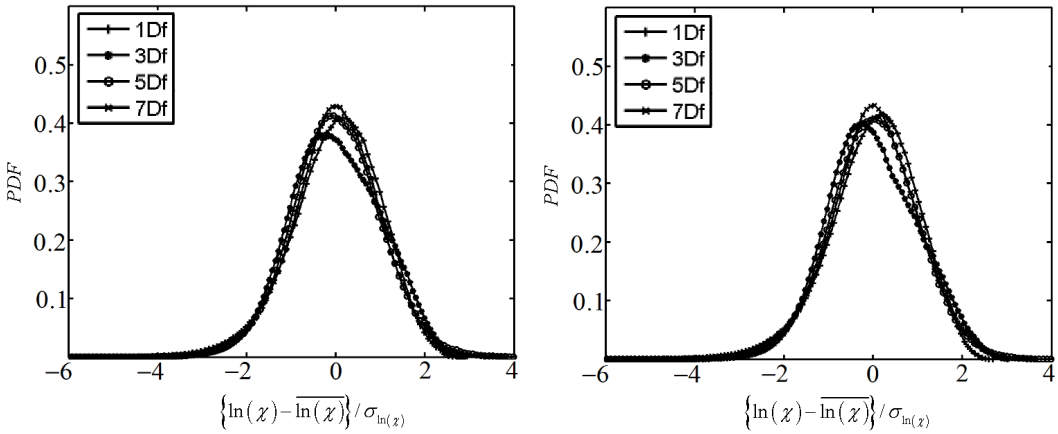

Figure 4.40: The p.d.f. of the fluctuations of the logarithm of the scalar dissipation rate $\left[\ln(\chi)-\overline{\ln(\chi)}\right]/\sigma_{\ln(\chi)}$ from window 3 (left) and 4 (right), computed at $y/D_f = 1, 3, 5, 7$ for $S = 1.07$.

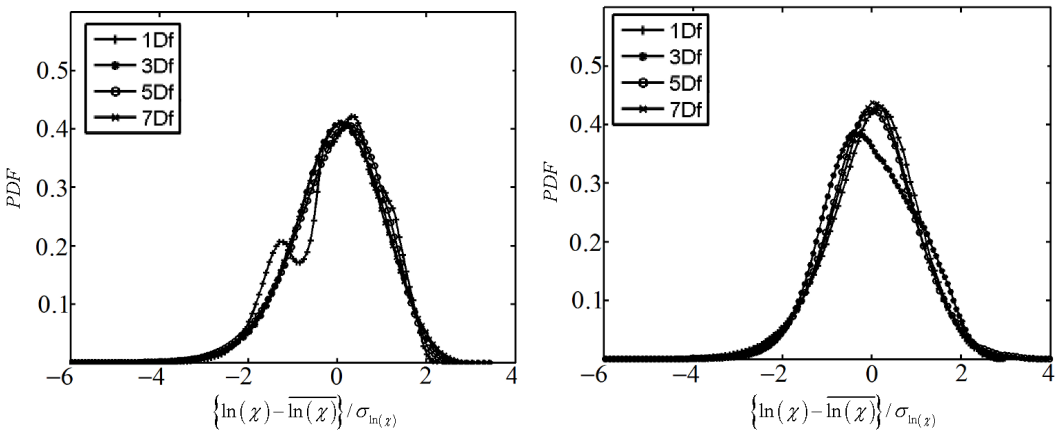

Figure 4.41: The p.d.f. of the fluctuations of the logarithm of the scalar dissipation rate $\left[\ln(\chi)-\overline{\ln(\chi)}\right]/\sigma_{\ln(\chi)}$ from window 5, computed at $y/D_f = 1, 3, 5, 7$ for $S = 0.58$ (left) and $S = 1.07$ (right).

The rest of this section discusses the p.d.f. of the fluctuations of the logarithm of the scalar dissipation rate, mainly in order to assess the applicability and the extent of the assumption of log−normality. The p.d.f. will be discussed in detail at different axial positions in the flow and for different swirl numbers. The Gaussian distribution will also be compared to the present measurements and the statistics will also be summarized. Figures 4.33−4.41 present the p.d.f. of the fluctuations of the logarithm of the scalar dissipation rate at all five spatial locations in the flow as well as at different axial positions and different swirl numbers. The p.d.f. of the scalar dissipation was found to be slightly negatively skewed at low swirl number (0.3) and almost symmetrical when swirl number increased to 0.58−1.07. This negative skewness was also reported in a number of previous publications, e.g. Ahmed (2012), Soulopoulos (2009), Sardi *et al.* (1998), Everest *et al.* (1995), Namazian & Kelly (1988) and Sreenivasan *et al.* (1977).

The assumption of a log−normal distribution of the scalar dissipation rate is usually employed in modelling of turbulent reacting flows. Nevertheless, this assumption might be questionable and the deviation from the log−normal distribution can be observed. Sardi *et al.* (1998) measured only one component of the scalar dissipation rate, discussed in detail the p.d.fs. in an opposed jet flow and observed deviations from log−normality. The same conclusions were drawn from the measurements mentioned in Ahmed (2012). It was generally reported that the deviation from log−normality of individual components of scalar dissipation rate can be explained by the intermittency effects. However, it was argued that the overall scalar dissipation rate p.d.f. can be adequately described by log−normal distributions. The latter is also partially confirmed in this work, where two components of the scalar dissipation rate are used. Tables 4.6−4.25 on pages 167−171 show the detailed statistics of the scalar dissipation rate at all downstream positions and windows as a function of swirl numbers. It is clearly seen that the probability density functions of the scalar dissipation rate are negatively skewed but become almost symmetrical when well−mixed regime is observed. In addition, the log−normal distribution was also computed and the parameters of the log−normal distribution (mean $\mu_{N(\mu,\sigma^2)}$ and standard deviation $\sigma_{N(\mu,\sigma^2)}$) were also reported. It is interesting to note that for swirl number of 1.07 at all axial positions and all five spatial locations the p.d.f. can be closely approximated by a standard log−normal distribution, i.e. with standard deviation of one and mean of zero. In fact, the standard deviation is not exactly equal to one but very close to this value, which is clearly seen in Tables 4.6−4.25 and Figure 4.42. The same can be applied to the mean, which is close to zero but not exactly zero. Therefore, it is suggested that the level of mixing directly affects the p.d.f. of the scalar dissipation rate and in case of well−mixed regime, i.e. far away from nozzle and high swirl numbers, no large deviation from log−normality can be observed.

In order to assess the effect of the chosen window size for calculation of the p.d.f., Figure 4.43 shows the p.d.f. of the scalar dissipation rate at four window spatial locations, at $y/D_f = 3$ and $S = 0.58$, computed by using a window of size 4×4 pixels. Similar computations are also shown in Figure 4.44 at $y/D_f = 1$ for $S = 0.3$. The p.d.f. computed from the larger window size 147×60 pixels is also shown for comparison. The p.d.f. reproduced from the smallest windows contained 24000 data points, while the p.d.f. reproduced from the larger windows consisted of circa 13e6 values. The p.d.f. from the

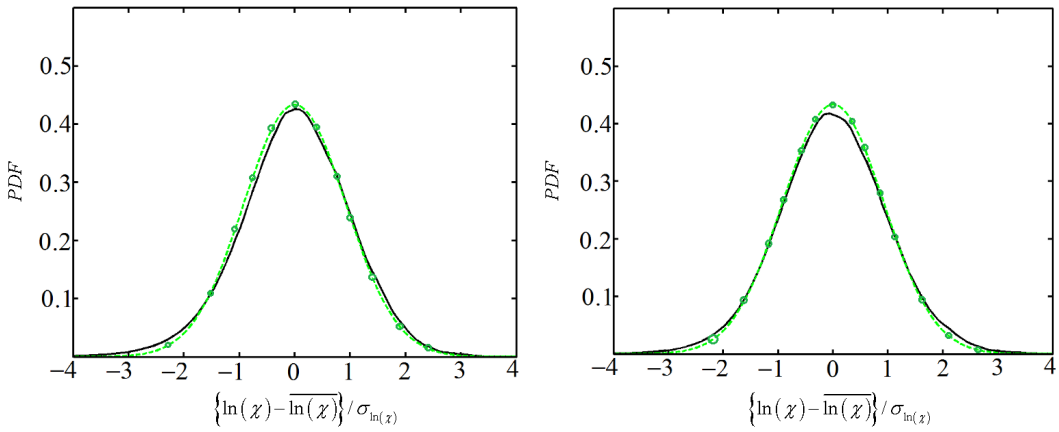

Figure 4.42: The p.d.f. of the fluctuations of the logarithm of the scalar dissipation rate $\left[\ln(\chi)-\overline{\ln(\chi)}\right]/\sigma_{\ln(\chi)}$ from window 1 for $S = 1.07$ at $y/D_f = 7$ (left) and $y/D_f = 5$ (right). An example of log−normal fitting is also shown as dashed line (circles) with expected value of $\mu_{N(\mu,\sigma^2)}$ =4.26e-6 and standard deviation of $\sigma_{N(\mu,\sigma^2)}$ =0.92.

smallest regions reproduced the p.d.f. computed from the larger sample windows and its trend was well captured at high swirl numbers, i.e. 0.58−1.07 and all spatial window locations. In contrast, for swirl number of 0.3 at location 1 and 3, the p.d.f. that was computed from the smallest windows has not converged. Nevertheless, the range of the dissipation rate fluctuations was well captured even if the p.d.f. was not converged. It can be suggested that in regions where high intermittency is observed the smallest window cannot provide an adequate description of the corresponding probability density function due to insufficient statistics. Following this discussion the next question arises, i.e. 'How many randomly generated samples N are needed in order to obtain a reliable probabilistic estimate. The minimum number of samples, which provides a reliable estimate, can in general be computed according to so−called Chernoff bound. The minimum number of samples is dependent on the accuracy $\varepsilon \in (0,1)$, the confidence $\delta \in (0,1)$ and can be computed as $N \geq \ln(2/\delta)/2\varepsilon^2$. For instance, if $\varepsilon = \delta = 0.005$ then $N \geq 119830$. The minimum number of samples can be seen from the next prospective, if ε and δ are small, then there is a high probability of $1-\delta$ that the estimated probability from the data set is within ε or it has a high degree of certainty. Therefore, the minimum number of samples is not a single parameter and is dependent on context and type of problems being analysed.

In order to assess the assumption of log−normality, quantile−quantile[1] plots (q−q plots) of the dissipation rate data for some swirl numbers and axial locations are reported in Figures 4.45−4.48. In these plots the inverse cumulative distribution function of the dissipation rate data is plotted against the inverse cumulative distribution function of the standard normal distribution. Empirical cumulative distribution function of the scalar dissipation rate data is computed as the proportion of values in the data set that are less than or equal to x. Practically, this means that the scalar dissipation rate data array (x) is

[1]Quantiles are points taken at regular intervals from the cumulative distribution function (CDF) of a random variable. In statistics, a Q−Q plot ('Q' stands for quantile) is a probability plot, which is a graphical method for comparing two probability distributions by plotting their quantiles against each other.

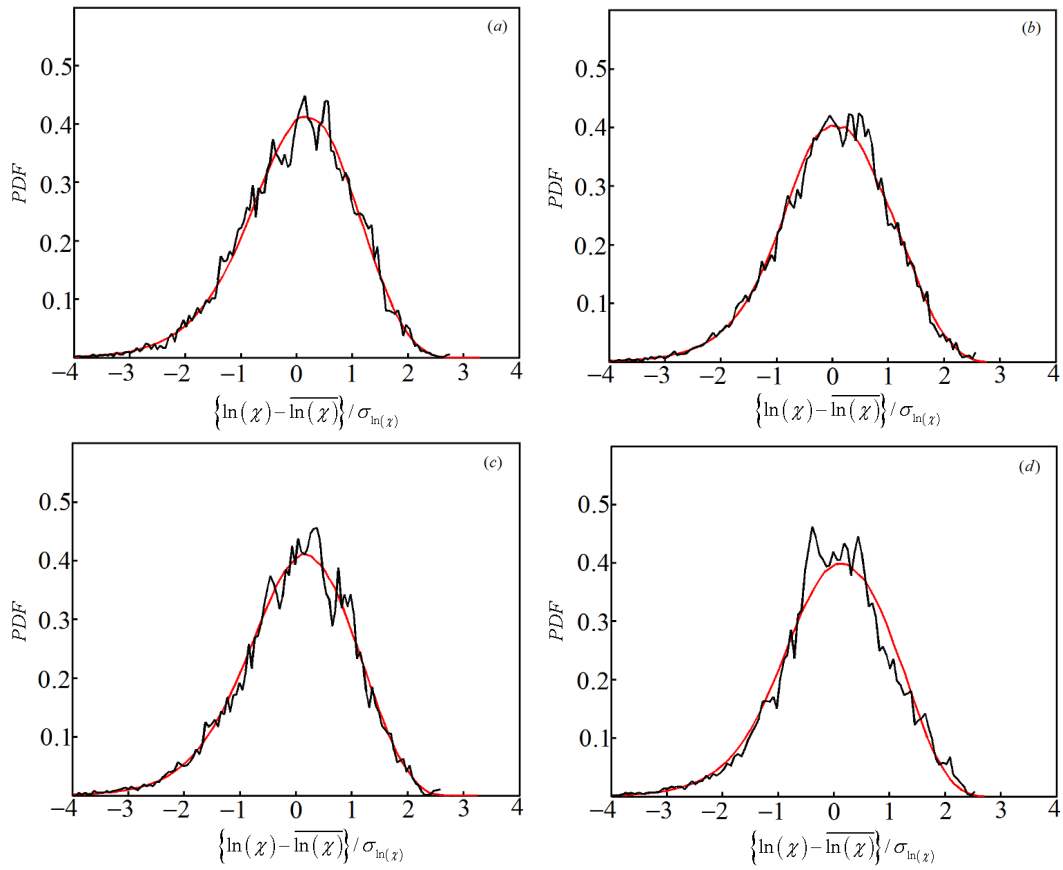

Figure 4.43: The p.d.f. of the fluctuations of the logarithm of the scalar dissipation rate $\left[\ln(\chi)-\overline{\ln(\chi)}\right]/\sigma_{\ln(\chi)}$ computed from windows 1 (a), 2 (b), 3 (c), 4 (d), at $y/D_f = 3$ for $S = 0.58$. The p.d.f., which is shown as smooth red line was computed by using a window of size 147×60 pixels. The p.d.f., which is shown as serrated black line was computed by using a window of 4×4 pixels. The smallest window contained 24000 data points (4×4×1500 images). The larger window contained 13e6 data points.

sorted in ascending order and plotted against the running indices for every x. All running indices are normalized with N, which is the cardinality of a set (measure of the numbers of elements of the set). The straight line that connects the first and the third quartiles of the two distributions is usually plotted in order to assess whether the dissipation rate data are log−normally distributed.

$$F_n(x) = \frac{\{i \in (1,2,3....N)\,; x_i < x\}}{N}, x \in R \tag{4.4}$$

The plots show that within the centre of the scalar dissipation rate distribution the scalar dissipation rate data do indeed follow the log−normal distribution. At the edges of the distribution the deviation from log−normality is evident and becomes less satisfactory. The difference is dependent on downstream positions and swirl numbers, as it was reported earlier. The discrepancy is mainly found at the lower end of the q−q distribution. However, this is valid for well−mixed regime i.e. high swirl number and at far away distances from the fuel nozzle. In case of binary mixing and bimodal p.d.f. as shown for instance in Figure 4.33 the deviation is large at both positive and negative ends of the distribution (Figure

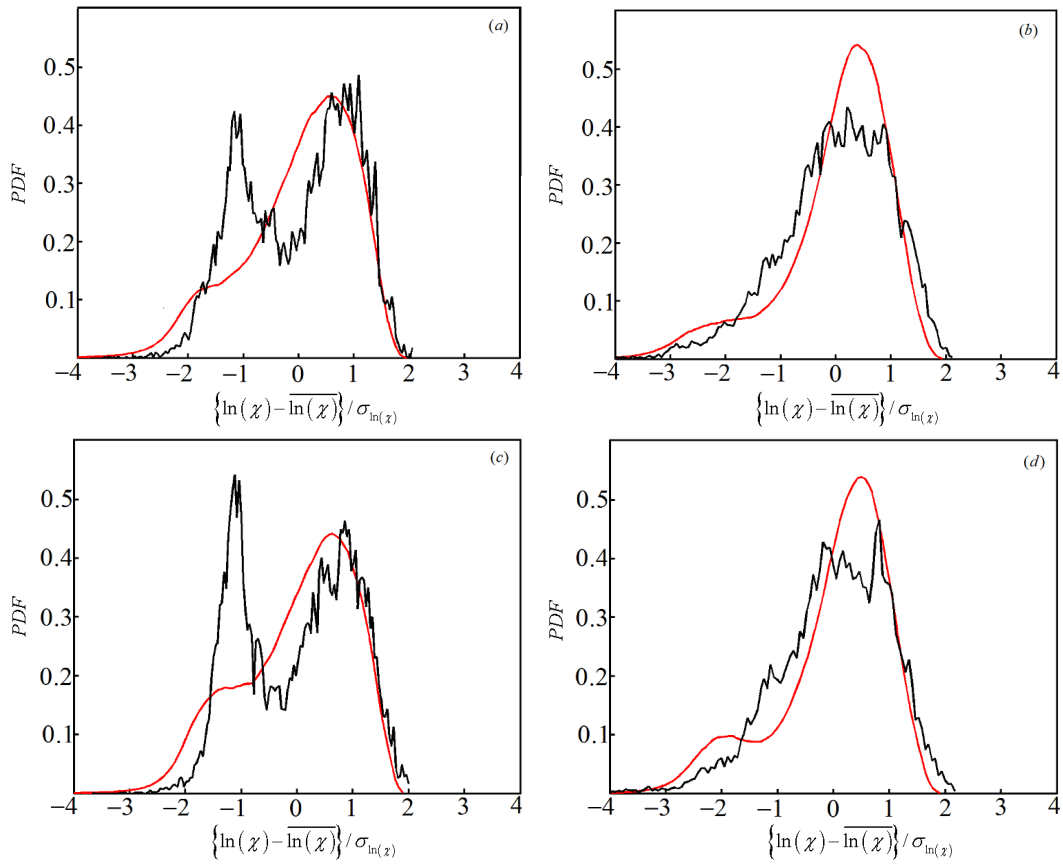

Figure 4.44: The p.d.f. of the fluctuations of the logarithm of the scalar dissipation rate $\left[\ln(\chi)-\overline{\ln(\chi)}\right]/\sigma_{\ln(\chi)}$ computed from windows 1 (a), 2 (b), 3 (c), 4 (d) at $y/D_f = 1$ for $S = 0.3$. The p.d.f., which is shown as smooth red line was computed by using a window of size 147×60 pixels. The p.d.f., which is shown as serrated black line was computed by using a window of 4×4 pixels. The smallest window contained 24000 data points (4×4×1500 images). The larger window contained 13e6 data points.

4.45). This difference tends to decrease with increasing swirl numbers and the log−normal distribution fits the scalar dissipation rate distribution over progressively large regions always around the centre of the distribution. It is also interesting to point out that the deviation from the log−normality is found in q−q plots at the same negative positions of the logarithm of the scalar dissipation rate. Figures 4.47−4.48 the deviation spans along negative axis starting at the same negative value of −2.

The bimodal p.d.f. of the scalar dissipation rate at sample window one and in some cases at five can suggest the large scale intermittency of the scalar dissipation rate distribution. The two distinct peaks at both negative and positive fluctuations are clearly visible. The amplitude of these peaks is typically different. The position of the higher peak is typically at negative values of the scalar dissipation rate fluctuations. The ratio of the maximum value of the positive peak to the maximum value of the negative peak was found to be up to 2 depending on the case.

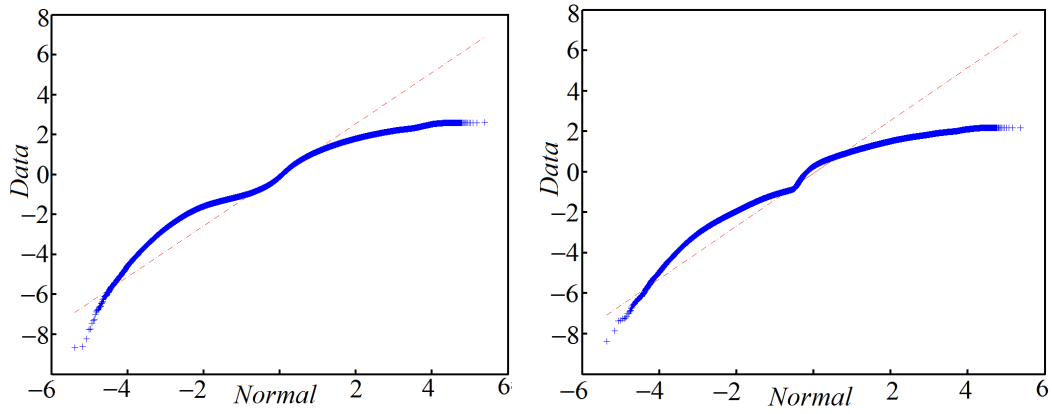

Figure 4.45: Quantile plots of the fluctuations of the logarithm of the scalar dissipation rate distribution (Data) with a standard normal (Normal) computed at $y/D_f = 1$, window 1 (left), $y/D_f = 3$, window 5 (right) for the acetone vapour jet only. The straight line connects the first and third quartiles of the distribution.

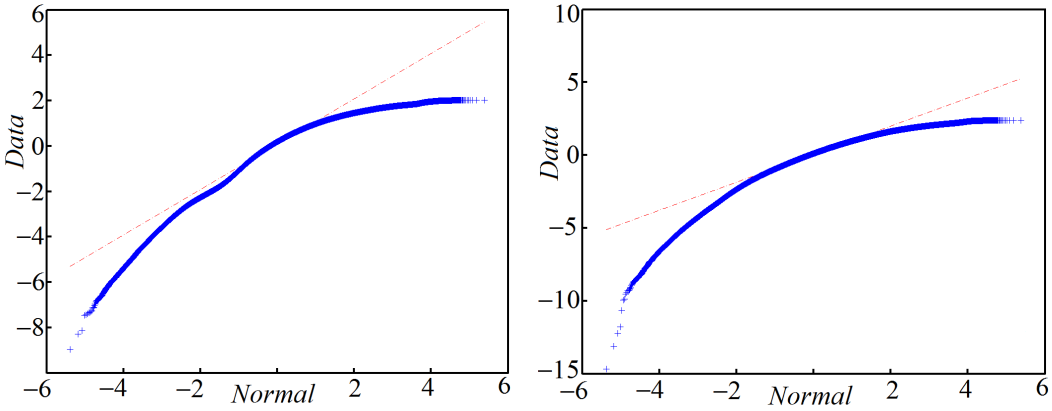

Figure 4.46: Quantile plots of the fluctuations of the logarithm of the scalar dissipation rate distribution (Data) with a standard normal (Normal) computed at $y/D_f = 1$, window 1, $S = 0.3$ (left), $y/D_f = 1$, window 2 and $S = 0.58$ (right). The straight line connects the first and third quartiles of the distribution.

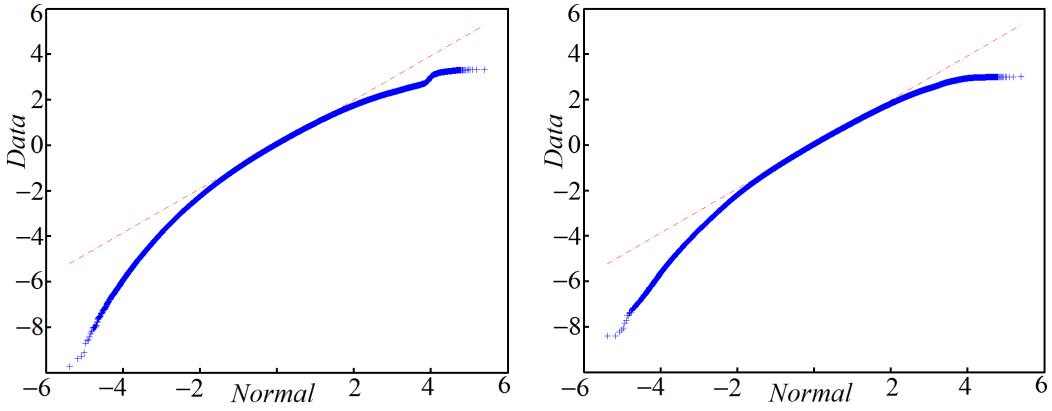

Figure 4.47: Quantile plots of the fluctuations of the logarithm of the scalar dissipation rate distribution (Data) with a standard normal (Normal) computed at $y/D_f = 3$, location 1, $S = 0.58$ (left), $y/D_f = 7$, location 2 and $S = 0.58$ (right). The straight line connects the first and third quartiles of the two distributions.

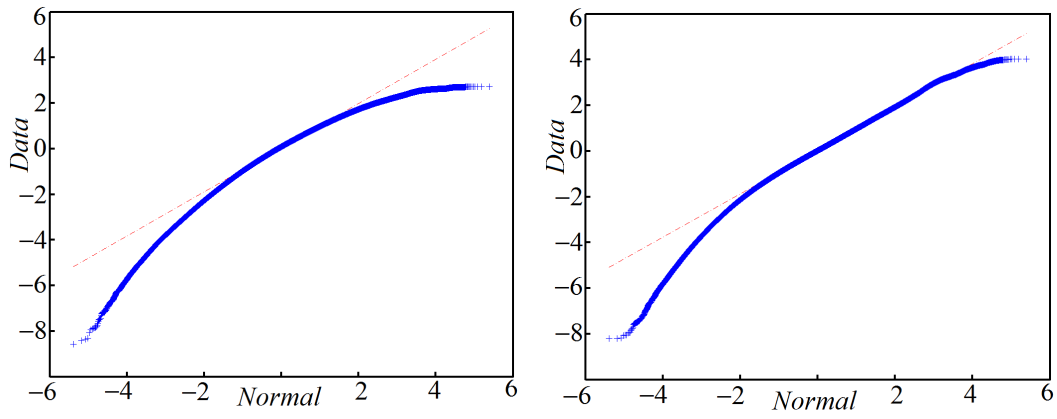

Figure 4.48: Quantile plots of the fluctuations of the logarithm of the scalar dissipation rate distribution (Data) with a standard normal (Normal) computed at $y/D_f = 1$(left), $y/D_f = 7$ (right), location 1 and $S = 1.07$. The straight line connects the first and third quartiles of the two distributions.

Tables 4.6−4.25 on pages 167−171 summarize the detailed unconditional statistics for different swirl numbers, downstream positions and sample windows. The statistics were computed from the larger windows (147×60 pixels). The statistical error in $\langle \ln(\chi) \rangle$ was computed as $\sigma_{\ln(\chi)}/N^{1/2} \approx 5.5048\text{e}-4$, where N is a number of data points. Notations that are used in Tables 4.6−4.25 are given in Table 4.25 on page 171 for convenience.

4.2.5 Joint statistics between scalar and its dissipation rate

This section quantifies the departures from statistical independence of the scalar fluctuations and their dissipation rate by comparing the joint p.d.fs. with the product of the individual p.d.fs. The joint p.d.f. is the association of the mixture fraction fluctuations with the fluctuations of the logarithm of the scalar dissipation rate. In modelling of reacting flows, it is usually assumed statistical independence between the scalar fluctuations and their dissipation rate. This approximation may introduce significant errors. Therefore, this issue must be addressed in detail, especially in swirling flows, where no prior data is available from existing literature. The concept of statistical independence between the scalar fluctuations and their dissipation rate appears in the modelling of turbulent mixing in both isothermal and reacting flows, where the joint p.d.f. is equal to the product of the individual p.d.f. (Hawarth *et al.*, 1988).

$$pdf\,(z,\chi) = pdf\,(z)\,pdf\,(\chi) \tag{4.5}$$

In statistics, the dependence of two random variables or two data sets can be assessed by the correlation coefficients. If the two random variables are independent, the correlation coefficient is zero. On the other hand, if the correlation coefficient is zero, it does not guarantee that the two random variables are statistically independent, because the coefficient detects only linear dependencies between these two. The correlation coefficient or Pearson's correlation coefficient when applied to a sample is commonly defined as the sample correlation coefficient according to the following equation, where X and Y are the mixture fraction and its dissipation rate.

$$r_{z,\chi} = \frac{\sum_{i=1}^{N} \left(X_i - \bar{X}\right)\left(Y_i - \bar{Y}\right)}{\sqrt{\sum_{i=1}^{N} \left(X_i - \bar{X}\right)^2}\sqrt{\sum_{i=1}^{N} \left(Y_i - \bar{Y}\right)^2}}; X = z; Y = \chi \tag{4.6}$$

The correlation coefficient ranges from -1 to $+1$. A value of -1 implies that all data points lie on a line for which X increases and Y decreases. A value of $+1$ implies that a linear equation describes the relationship between X and Y, and zero correlation coefficient implies that there is no linear correlation between variables. General interpretations of a correlation coefficient are in some ways arbitrary. It might depend on context and purposes. Tennekes & Limley (1972) pointed out that if the correlation coefficient of the scalar fluctuations and the scalar dissipation rate is zero the scalar and its dissipation rate is not necessarily statistically independent. For non−zero values of correlation coefficient the scalar fluctuations and the scalar dissipation rate are statistically related (Tennekes & Limley, 1972). Gao (1991) pointed out that in a homogeneous scalar field, the scalar fluctuations and their dissipation rate are statistically independent if and only if the scalar p.d.f. has a Gaussian distribution.

Generally speaking, the correlation coefficient can serve as an initial estimator of statistical independence and further investigation by comparing the joint p.d.f. to the product of the individual p.d.f. is usually required. The joint probability density functions of the scalar fluctuations and the scalar dissipation rate are presented in Figures 4.51−4.63 on pages 149−155. The joint p.d.f. was computed from the logarithm of the instantaneous values of the scalar dissipation rate minus the mean of the logarithm of the scalar dissipation rate, normalized by the standard deviation of the logarithm of the scalar dissipation rate and from the instantaneous values of the mixture fraction minus the mean of the mixture fraction, normalized by the standard deviation of the mixture fraction. The range of the scalar dissipation rate fluctuations and the mixture fraction fluctuations was divided in a number of two−dimensional bins (50 bins were typically used) and the number of occurrences in each bin was counted. The p.d.f. was computed as $N/(W * H * L)$, where W is the width of the bin along the mixture fraction set of data, H is the width of bin along the scalar dissipation rate set of data and L is the number of samples being analysed. In graphs of joint p.d.f. the $x-$axis and the $y-$axis are plotted according to:

$$x - Axis = \frac{\ln(\chi) - \langle \ln(\chi) \rangle}{\sigma_{\ln(\chi)}} \tag{4.7}$$

$$y - Axis = \frac{z - \langle z \rangle}{\sigma_z} \tag{4.8}$$

If the assumption of independence between the scalar fluctuations and the scalar dissipation rate is valid then by definition the joint probability distribution of the scalar fluctuations and their dissipation rate will be equal to the product of the individual p.d.f. Figures 4.51−4.63 (pages 149−151) are plotted to assess an assumption of statistical independence. These plots are arranged in two columns where left column corresponds to the joint p.d.f. of the scalar and its dissipation rate, while right column corresponds to the product of individual p.d.f. of the scalar and its dissipation rate. Typically, only one

window location is shown except for $S = 1.07$, where p.d.fs. from all five windows are shown (Figures 4.51−4.55). The plotting range was the same for all plots and ranged from −4 to 4. The product of two p.d.f. was computed by using the same bin number as in the joint p.d.f. The joint p.d.f. and the product p.d.f. were plotted by using 20 contour lines.

At all five sample windows at $y/D_f = 1$ and for $S = 1.07$ the contours of the product of the individual p.d.f. appear close to circular, even though not entirely symmetric. The joint p.d.f. had a little oval shape and seemed skewed towards both negative and positive dissipation rate fluctuations. The centre of the joint p.d.f. and the product of individual p.d.f. seemed to have the same origin. The assumption of statistical independence was therefore in better agreement with the experimental data under assumptions of homogeneous flow field or well−mixed regime. As it was showed earlier, the scalar field at high axial position and swirl number is nearly homogeneous with small scalar fluctuations. However, the deviations from the assumption of statistical independence are clearly observed, where the flow is not homogeneous with large scalar fluctuations. The joint p.d.f. for acetone vapour jet only, is skewed towards negative values of scalar dissipation rate with large negative fluctuations of mixture fraction, while the product of the individual p.d.f. displays bimodal features (figures not presented here). Figures are not presented here because the acetone vapour jet only case is not relevant for this work and is only mentioned here for convenience.

As a result, the assumption of statistical independence is not held, since the two shapes are quite different in nature, i.e. shapes, location etc. In fact, the product of the individual p.d.f. reproduces the probability of occurrence of values lower than the mean, i.e. large negative fluctuations, even though the shape is quite different from that of joint p.d.f. On top of that, the joint p.d.fs. demonstrate that intermittency[2] plays an important role and can affect the shape of the p.d.fs., even though not much, which is not taken into account by the product of individual p.d.fs. The intermittency causes the joint p.d.fs. to be skewed towards negative values of the logarithm of scalar dissipation rate fluctuations. It is expected that the assumption of statistical independence is less valid in flows with high levels of intermittency. For lower swirl numbers 0.3 and 0.58 and axial positions $y/D_f = 3, 5$ the product of individual p.d.fs. appears to remain circular, even though the shape of the p.d.f. is dependent on window positions. The product of individual and the joint p.d.f. in Figure 153 ($S = 0.3$, $y/D_f = 7$) seem to have 'clipped region' at a value approximately equalled to -1, corresponding to the negative mixture fraction fluctuations. Similar clipped regions can be observed from other sample windows. This clipped regions mean that there are no fluctuations beyond a certain limit and this effect is not quite well understood.

In order to understand the effect of clipped p.d.fs., Figures 4.64−4.66 on page 155 are presented. In these figures, a set of 500 mixture fraction samples from a window 2 for $S = 0.3$ at $y/D_f = 7$ is shown. The large fluctuations along with low mean indicate that the flow within the window is highly segregated. Since the mixture fraction is within 0−1 limit, the minimum of the mixture fraction fluctuations is close to zero. For a given mean, which is 0.167 in this case, it leads to $z - \langle z \rangle$, i.e. 0−1.167=−0.167 and when it

[2]Such rare events of large scalar dissipation rate fluctuations are called intermittency, even though the understanding of this process is still lacking.

is normalized with given standard deviation (e.g. 0.142) it leads to negative fluctuations, i.e. in this case of -1.17. Since the minimum fluctuations of mixture fraction are not zero, this limits the negative fluctuations to -1 minus one and that is why the 'clipped region' is seen in the figures of the joint p.d.fs. However, the mixture fraction fluctuations close to zero do not provide an answer whether it is a physical phenomenon or so called digitization error.

The digitization error can be described as follows: Modern CCD cameras use N−bits to represent the data and one bit for the sign. The dynamic range for example for 12 bit camera is $2^{12} - 1 = 4095$ or 4095 counts (discretisation levels). If for example, the mixture fraction is measured at full dynamic range i.e. 4095, the associated minimum mixture fraction that in theory can be measured is 1/4095 or $2.4e^{-4}$. This value is indeed very close to zero, even though not exactly. However, if the dynamic range or the signal is much lower, e.g. if the mixture fraction is measured with 1200 counts only (as in this work) the minimum value of mixture fraction that can be measured is 1/1200 or $8.3e^{-4}$ and in case of very low signal from a CCD camera 1/400 leads to $2.5e^{-3}$. Therefore, any smaller value than the theoretical limit will be rounded to the minimum theoretical limit, i.e. 0 will become $2.4e^{-4}$. This type of error is called discretisation error or round−off error and is related to the CCD gain factor.

There are two possibilities to examine where the round−off errors affect the measurements. The first is quite straightforward and is related to the minimum value of the mixture fraction that is being measured. If this value is much larger than the theoretical limit then it can be concluded that this is indeed a physical phenomenon. The second is based on the cumulative distribution function (c.d.f) of the mixture fraction. This principle can be seen in Figure 4.66 on page 156 where a cumulative distribution function of the mixture fraction, computed from Figure 4.64 and a c.d.f. representation shown in cartoon form when round−off errors are present in the experimental data. If the round−off errors are present in the experimental data the cumulative distribution function at small values will be step−shaped. However, the experimental c.d.f. does not confirm that the round−off errors affect the measured values of the mixture fraction and fluctuation are indeed close to zero but not exactly zero.

Preliminary conclusions on statistical independence of the scalar fluctuations and the scalar dissipation rate can be summarized as follows: It was found that the scalar fluctuations were strongly correlated at the boundaries of the mixing layer or shear layer, especially for low swirl numbers. The assumption of statistical independence between the scalar fluctuations and their dissipation rate, commonly introduced in modelling of turbulent reacting flows was therefore not tenable in case of low swirl number, i.e. $S = 0.3$. On the other hand, the assumption of statistical independence between the scalar and their dissipation rate was justified in case of high swirling flows. This can serve as an initial indicator that the present models that are based on statistical independence are more suitable for reacting and non−reacting swirling flows, especially for those with high swirl numbers. It was also found that the skewness of the joint p.d.f. was dependent on the swirl numbers as well as on intermittency. The intermittency was not found when the swirl number was large namely 1.07 and the shape of the joint p.d.f. was close to circular.

Table 4.1: Pearson's correlation coefficients as a function of downstream positions for acetone vapour jet only.

y/D_f	Window 1	Window 2	Window 3	Window 4	Window 5
1	-0.45	0.21	-0.51	0.26	-0.51
3	-0.11	0.09	-0.14	0.07	-0.31
5	0.01	0.10	-0.003	0.08	-0.14
7	0.12	0.11	0.10	0.09	-0.03

Table 4.2: Pearson's correlation coefficients as a function of downstream positions for $S = 0.3$.

y/D_f	Window 1	Window 2	Window 3	Window 4	Window 5
1	-0.06	0.45	-0.14	0.45	-0.49
3	0.29	0.37	0.28	0.38	-0.17
5	0.34	0.36	0.33	0.36	0.23
7	0.41	0.38	0.39	0.36	0.36

Table 4.3: Pearson's correlation coefficients as a function of downstream positions for $S = 0.58$.

y/D_f	Window 1	Window 2	Window 3	Window 4	Window 5
1	-0.15	-0.04	-0.19	-0.01	-0.48
3	0.11	-0.1	0.08	-0.11	-0.04
5	0.32	0.27	0.31	0.21	0.19
7	0.37	0.36	0.34	0.36	0.36

Table 4.4: Pearson's correlation coefficients as a function of downstream positions for $S = 1.07$.

y/D_f	Window 1	Window 2	Window 3	Window 4	Window 5
1	0.17	0.013	0.13	-0.03	-0.0012
3	0.4	0.41	0.38	0.38	0.36
5	0.22	0.18	0.24	0.18	0.29
7	0.38	0.31	0.3	0.34	0.26

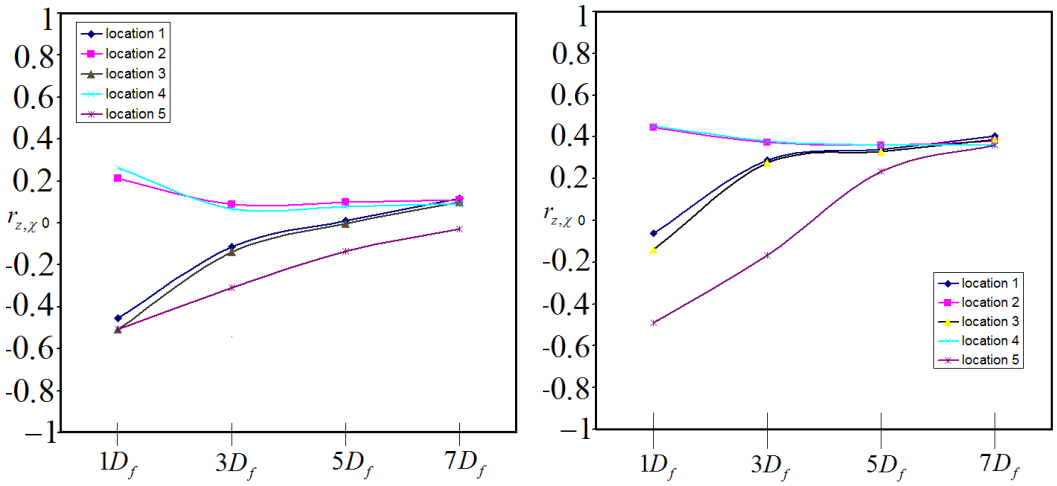

Figure 4.49: Pearson's correlation coefficients between scalar and its dissipation rate, as a function of axial distances and window locations for acetone vapour jet only (left) and for $S = 0.3$ (right).

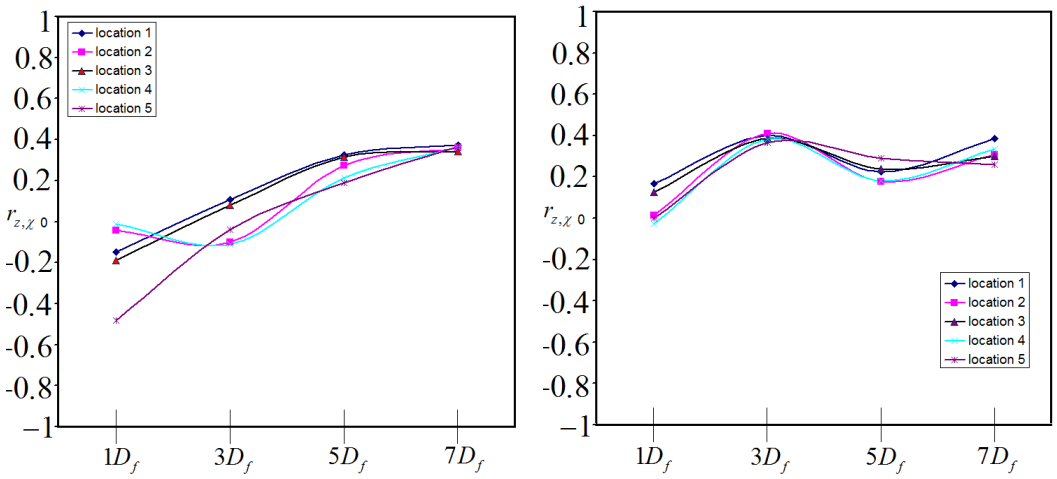

Figure 4.50: Pearson's correlation coefficients between scalar and its dissipation rate, as a function of axial distances and window locations for $S = 0.58$(left) and for $S = 1.07$ (right).

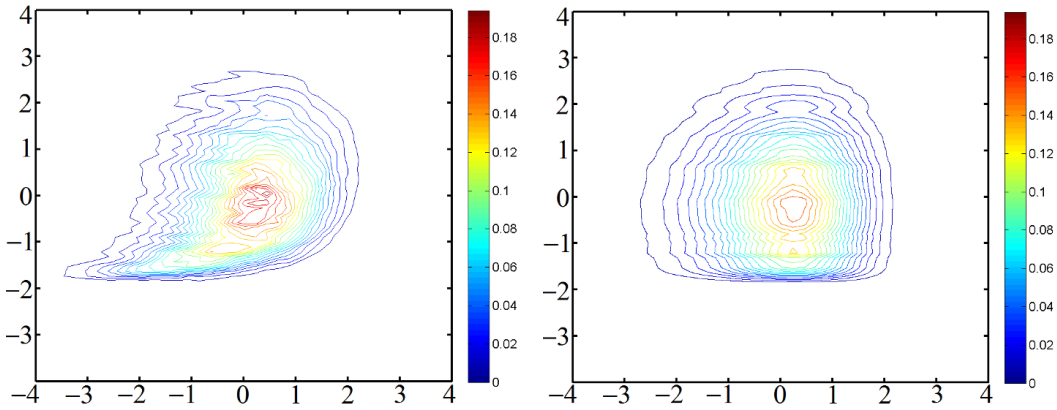

Figure 4.51: Joint p.d.fs. of scalar and its dissipation rate (left) and product of individual p.d.fs. (right) at $y/D_f = 1$ for $S = 1.07$ computed from window 1. Horizontal scale corresponds to p.d.f of $\left[\ln(\chi) - \overline{\ln(\chi)}\right]/\sigma_{\ln(\chi)}$ while vertical scale corresponds to p.d.f of $[z - \langle z \rangle]/\sigma_z$.

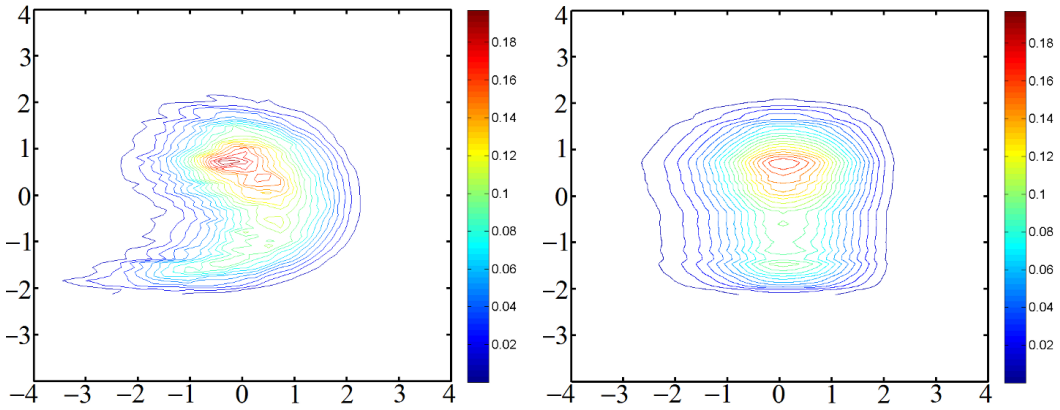

Figure 4.52: Joint p.d.fs. of scalar and its dissipation rate (left) and product of individual p.d.fs. (right) at $y/D_f = 1$ for $S = 1.07$ computed from window 2. Horizontal scale corresponds to p.d.f of $\left[\ln(\chi) - \overline{\ln(\chi)}\right]/\sigma_{\ln(\chi)}$ while vertical scale corresponds to p.d.f of $[z - \langle z \rangle]/\sigma_z$.

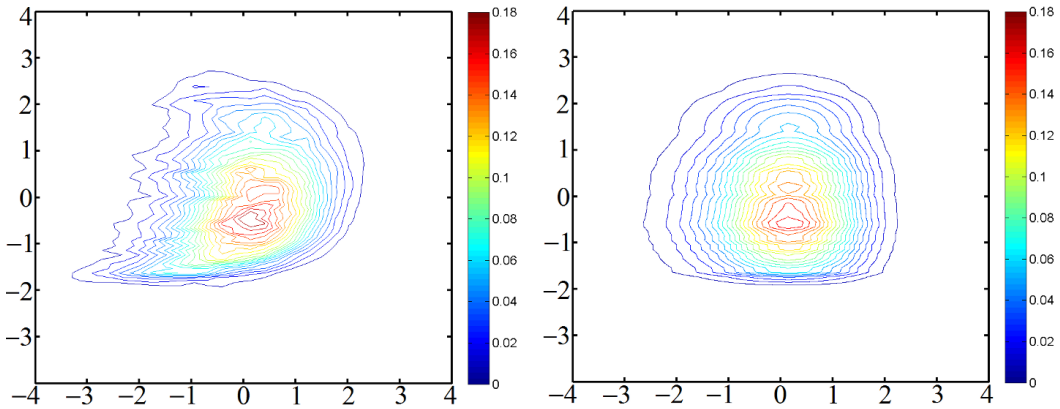

Figure 4.53: Joint p.d.fs. of scalar and its dissipation rate (left) and product of individual p.d.fs. (right) at $y/D_f = 1$ for $S = 1.07$ computed from window 3. Horizontal scale corresponds to p.d.f of $\left[\ln(\chi) - \overline{\ln(\chi)}\right]/\sigma_{\ln(\chi)}$ while vertical scale corresponds to p.d.f of $[z - \langle z \rangle]/\sigma_z$.

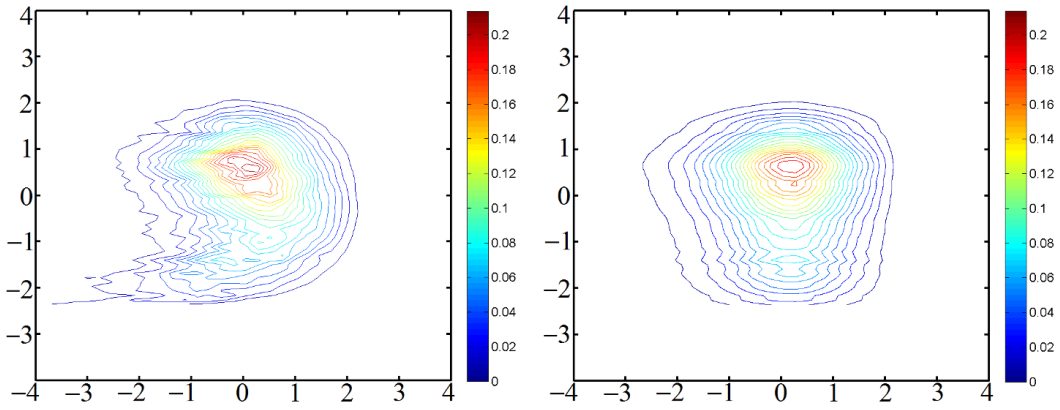

Figure 4.54: Joint p.d.fs. of scalar and its dissipation rate (left) and product of individual p.d.fs. (right) at $y/D_f = 1$ for $S = 1.07$ computed from window 4. Horizontal scale corresponds to p.d.f of $\left[\ln(\chi) - \overline{\ln(\chi)}\right]/\sigma_{\ln(\chi)}$ while vertical scale corresponds to p.d.f of $[z - \langle z \rangle]/\sigma_z$.

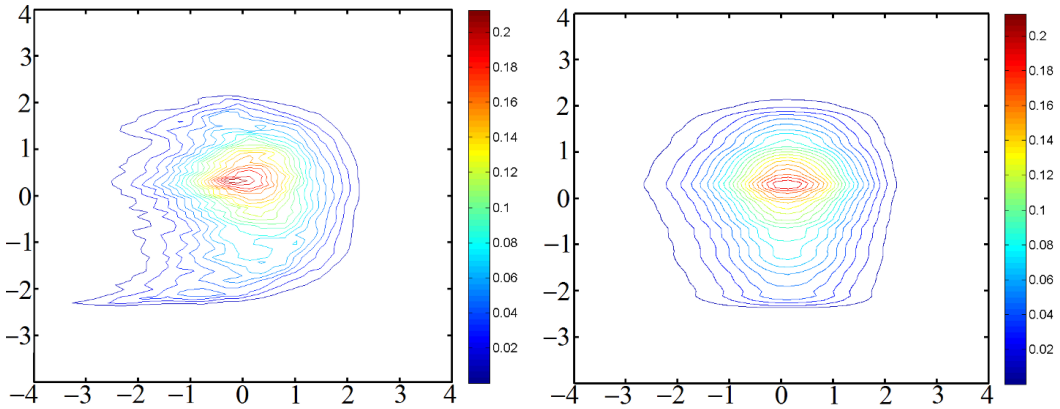

Figure 4.55: Joint p.d.fs. of scalar and its dissipation rate (left) and product of individual p.d.fs. (right) at $y/D_f = 1$ for $S = 1.07$ computed from window 5. Horizontal scale corresponds to p.d.f of $\left[\ln(\chi) - \overline{\ln(\chi)}\right]/\sigma_{\ln(\chi)}$ while vertical scale corresponds to p.d.f of $[z - \langle z \rangle]/\sigma_z$.

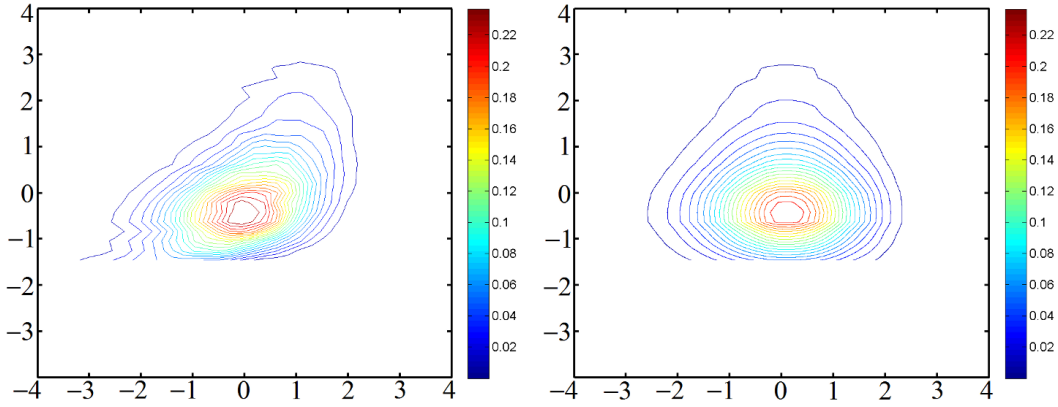

Figure 4.56: Joint p.d.fs. of scalar and its dissipation rate (left) and product of individual p.d.f. (right) at $y/D_f = 7$ for $S = 0.58$, computed from window 2. Horizontal scale corresponds to p.d.f of $\left[\ln(\chi) - \overline{\ln(\chi)}\right]/\sigma_{\ln(\chi)}$ while vertical scale corresponds to p.d.f of $[z - \langle z\rangle]/\sigma_z$.

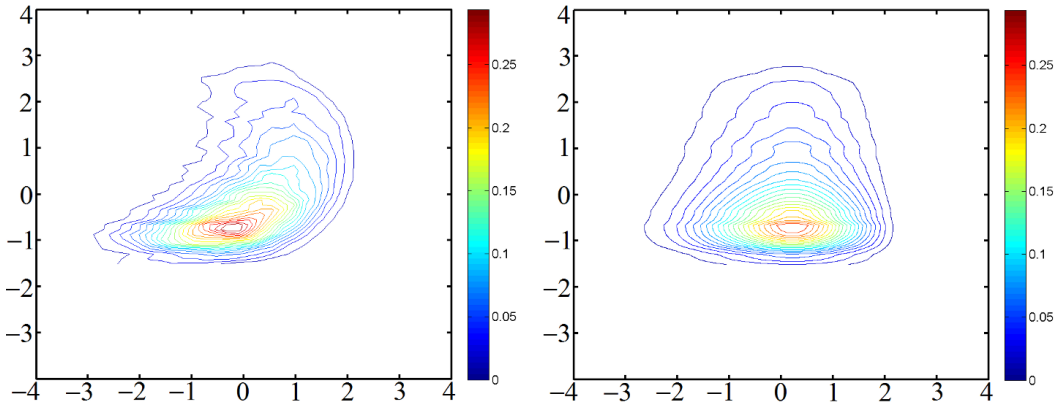

Figure 4.57: Joint p.d.f. of scalar and its dissipation rate (left) and product of individual p.d.fs. (right) at $y/D_f = 5$ for $S = 0.58$, computed from window 2. Horizontal scale corresponds to p.d.f of $\left[\ln(\chi) - \overline{\ln(\chi)}\right]/\sigma_{\ln(\chi)}$ while vertical scale corresponds to p.d.f of $[z - \langle z\rangle]/\sigma_z$.

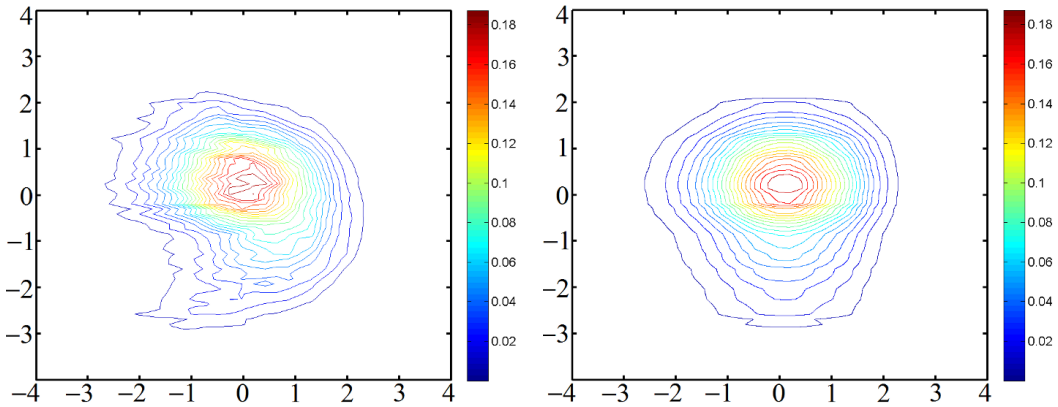

Figure 4.58: Joint p.d.fs. of scalar and its dissipation rate (left) and product of individual p.d.fs. (right) at $y/D_f = 3$ for $S = 0.58$, computed from window 2. Horizontal scale corresponds to p.d.f of $\left[\ln(\chi) - \overline{\ln(\chi)}\right]/\sigma_{\ln(\chi)}$ while vertical scale corresponds to p.d.f of $[z - \langle z\rangle]/\sigma_z$.

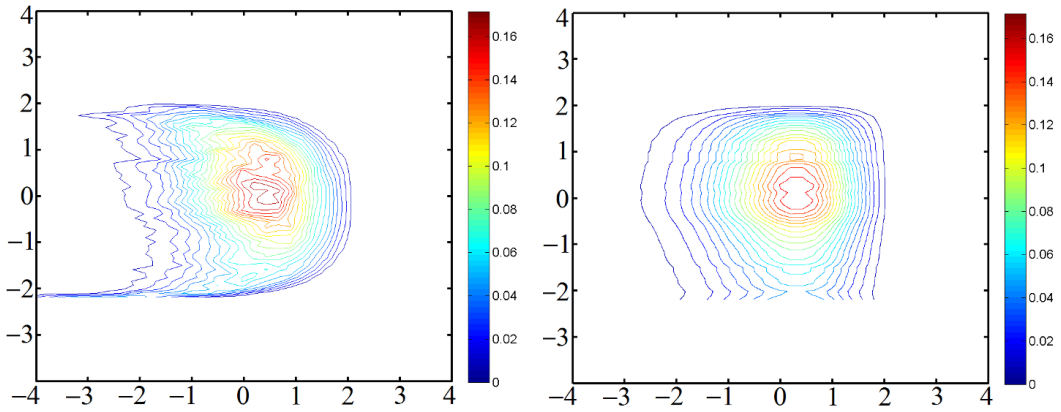

Figure 4.59: Joint p.d.fs. of scalar and its dissipation rate (left) and product of individual p.d.fs (right) at $y/D_f = 1$ for $S = 0.58$ computed from window 2. Horizontal scale corresponds to p.d.f of $\left[\ln(\chi) - \overline{\ln(\chi)}\right]/\sigma_{\ln(\chi)}$ while vertical scale corresponds to p.d.f of $[z - \langle z \rangle]/\sigma_z$.

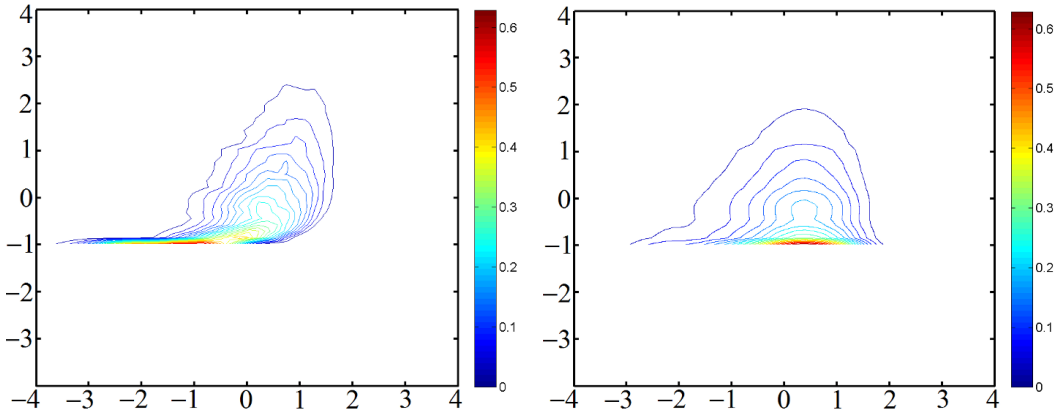

Figure 4.60: Joint p.d.fs. of scalar and its dissipation rate (left) and product of individual p.d.f. (right) at $y/D_f = 7$ for $S = 0.3$ computed from window 2. Horizontal scale corresponds to p.d.f of $\left[\ln(\chi) - \overline{\ln(\chi)}\right]/\sigma_{\ln(\chi)}$ while vertical scale corresponds to p.d.f of $[z - \langle z \rangle]/\sigma_z$.

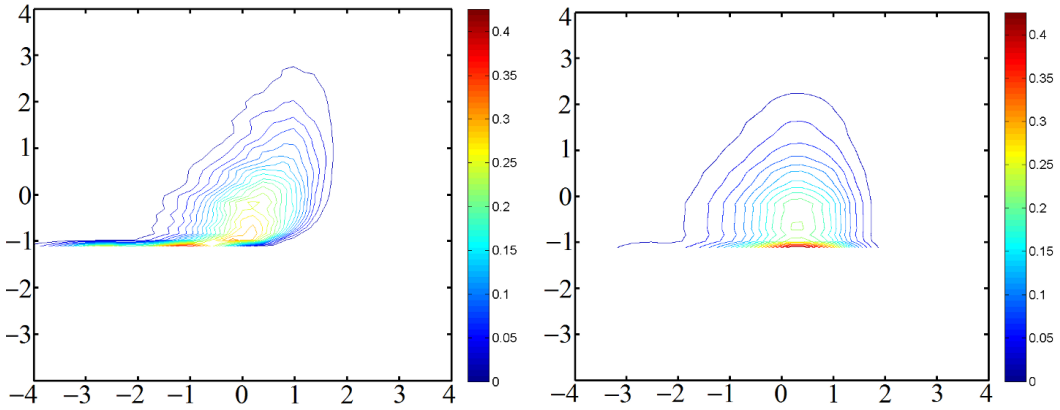

Figure 4.61: Joint p.d.fs. of scalar and its dissipation rate (left) and product of individual p.d.f. (right) at $y/D_f = 5$ for $S = 0.3$ computed from window 2. Horizontal scale corresponds to p.d.f of $\left[\ln(\chi) - \overline{\ln(\chi)}\right]/\sigma_{\ln(\chi)}$ while vertical scale corresponds to p.d.f of $[z - \langle z \rangle]/\sigma_z$.

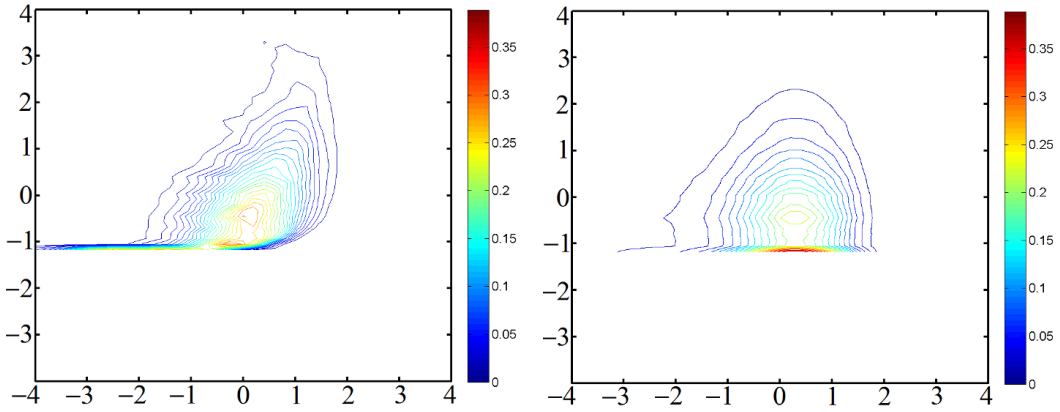

Figure 4.62: Joint p.d.fs. of scalar and its dissipation rate (left) and product of individual p.d.f. (right) at $y/D_f = 3$ for $S = 0.3$ computed from window 2. Horizontal scale corresponds to p.d.f of $\left[\ln(\chi) - \overline{\ln(\chi)}\right]/\sigma_{\ln(\chi)}$ while vertical scale corresponds to p.d.f of $[z - \langle z \rangle]/\sigma_z$.

The joint p.d.f. gives the measure of the joint probability between scalar fluctuations and their dissipation rate, even though does not provide a physical explanation for the processes that give rise to the correlation between the scalar fluctuations and their dissipation rate. This can give the conditions under which the assumption of statistical hypothesis breaks down. This is useful information but incomplete, because it is unknown, which components contribute more, i.e. axial or radial components of scalar dissipation rate. The contribution of each part of the scalar fluctuations and the scalar dissipation rate to their overall correlation can be understood by using a weighting function. The weighting function $w(z, \ln(\chi))$ approach was used e.g. in Soulopoulos (2009), Sardi *et al.* (1997) and Anselmet *et al.* (1994) and is defined as product of mixture fraction z, logarithm of the scalar dissipation rate and their joint p.d.f., so that the double integral over scalar fluctuations and the dissipation rate is the correlation coefficient Soulopoulos (2009) and Sardi *et al.* (1997).

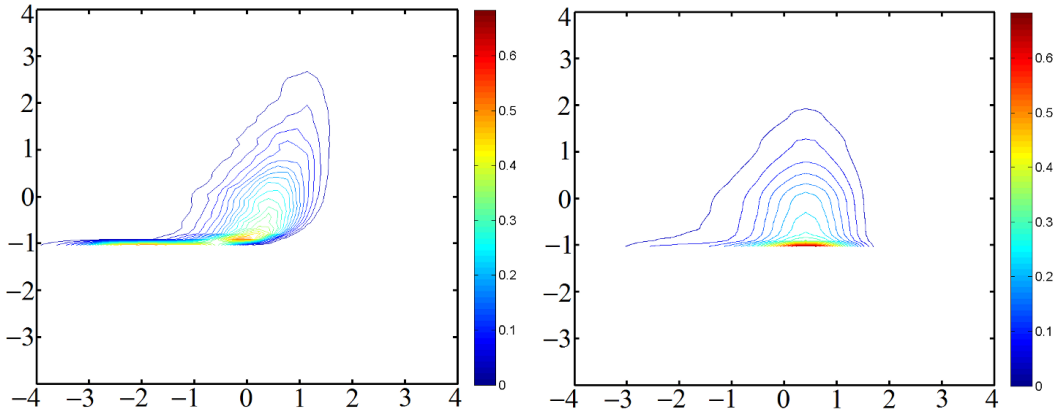

Figure 4.63: Joint p.d.f. of scalar and its dissipation rate (left) and product of individual p.d.f. (right) at $y/D_f = 1$ for $S = 0.3$ computed from window 2. Horizontal scale corresponds to p.d.f of $\left[\ln(\chi) - \overline{\ln(\chi)}\right]/\sigma_{\ln(\chi)}$ while vertical scale corresponds to p.d.f of $[z - \langle z \rangle]/\sigma_z$.

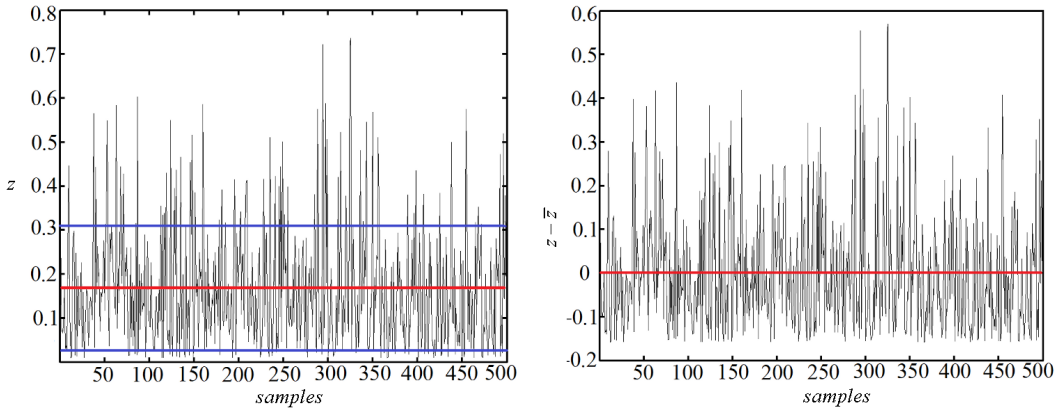

Figure 4.64: Plot of 500 mixture fraction samples from window 2 for $S = 0.3$ at $y/D_f = 7$ (left) and plot of corresponding fluctuations $z - \langle z \rangle$ (right).

$$w\left(z^{'},\chi^{'}\right) = z^{'}\chi^{'}pdf\left(z^{'},\chi^{'}\right) \tag{4.9}$$

$$r_{z',\chi'} = \int_{-\infty}^{\infty}\int_{-\infty}^{\infty} z^{'}\chi^{'}pdf\left(z^{'},\chi^{'}\right) \tag{4.10}$$

$$z^{'} = \frac{z - \bar{z}}{\sigma_z} \tag{4.11}$$

$$\chi^{'} = \frac{\ln(\chi) - \overline{\ln(\chi)}}{\sigma_{\ln(\chi)}} \tag{4.12}$$

It is also possible to assess the relative importance of the axial, radial or both components of the scalar dissipation rate to the overall correlation by computing the weighted integrands from single components of the scalar dissipation rate (axial or radial). This approach provides a rapid overview of identifying the origin of the correlation between

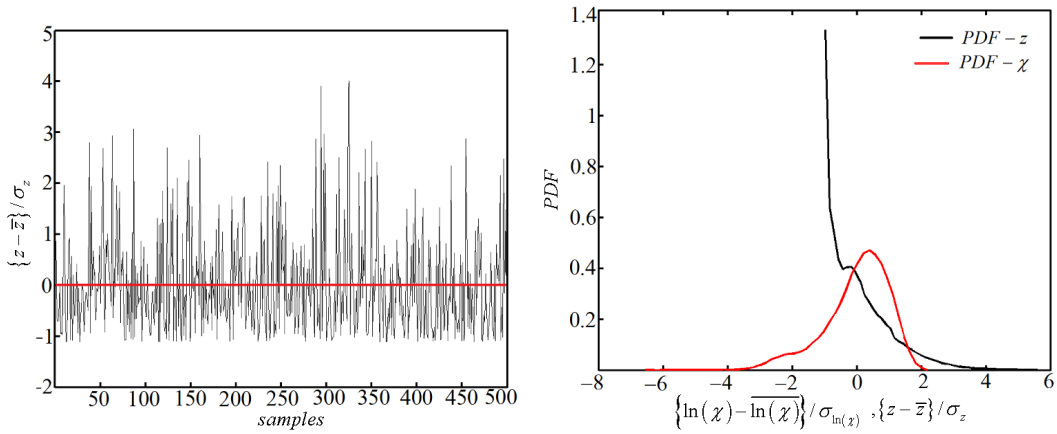

Figure 4.65: Plot of normalized (by standard deviation) of mixture fraction fluctuations $[z - \langle z \rangle]/\sigma_z$ (left) for $S = 0.3$ at $y/D_f = 7$ computed from window 2. Figure on the right shows corresponding p.d.f. of mixture fraction fluctuations as well as the p.d.f of the scalar dissipation rate computed from the same window.

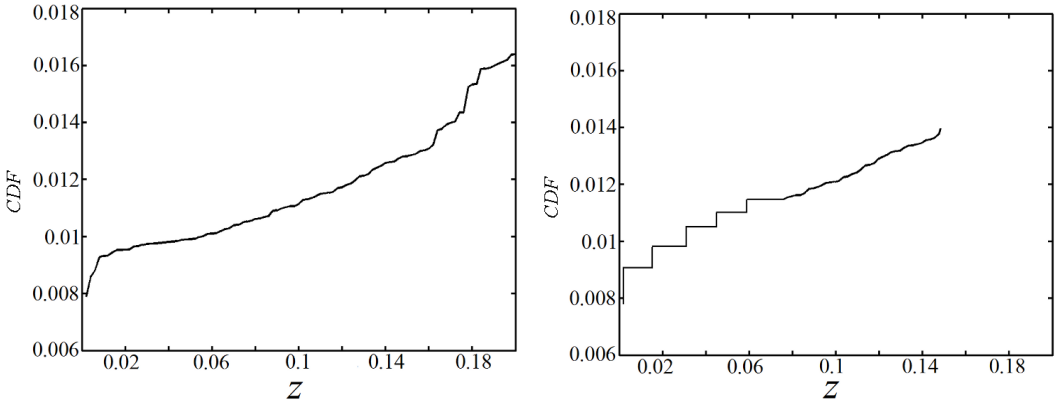

Figure 4.66: Cumulative distribution function of the mixture fraction, computed from Figure 4.65 (left) and a c.d.f. representation shown in cartoon form when round−off errors are present in the experimental data. Figure on the right hand side does not represent experimental data and is drawn to illustrate the principle of round−off errors.

the scalar and its dissipation rate. The weighted integrands computed from axial and radial components of the joint p.d.f. are presented in Figures 4.67−4.68. On the left hand side, the weighted integrands computed from the axial component of the scalar dissipation rate are presented, while on the right hand side the integrands computed from the radial components of the scalar dissipation rate are shown.

In each figure the plotted values (isocountors) of the weighted integrands may not be equal and colorbars indicate this. This was done in order to improve visual interpretations and allow better understanding of which component contributes more to the overall scalar dissipation rate. The weighted integrands computed from window 2 from components (radial and axial) of the scalar dissipation rate for acetone vapour jet only demonstrated that correlations were primarily from large negative scalar dissipation rate fluctuations (Fig. 4.69). For the flow conditions without swirling motion i.e. for $S = 0$ (acetone vapour jet only) the radial component contributes more to the overall correlation than

the axial component (Figure 4.69), which is also consistent with the previously published data. It is also evident for $S = 0.3$ and $S = 0.58$ (not shown here) at all axial positions of the laser sheet.

However, for $S = 1.07$ the contour demonstrated (Figure 4.67) that the correlation was mainly associated with small negative and positive scalar dissipation rate fluctuations (± 1 standard deviation of the scalar dissipation rate) and the plots are close to circular, which means that all fluctuations contribute equally. The contribution of the axial and the radial components becomes nearly equally as the level of mixing increases i.e. for $S = 0.3$, 0.58 and 1.07. It should be noted that for the sake of brevity the weighted integrand computed from the overall scalar dissipation rate are not presented here. The contribution to the overall correlation can be seen from the axial and the radial components of the scalar dissipation rate. A general conclusion is that in swirling flow the contribution from the axial and the radial component of the scalar dissipation rate is equal or almost equal and is directly related to the degree of mixing i.e. the swirl number.

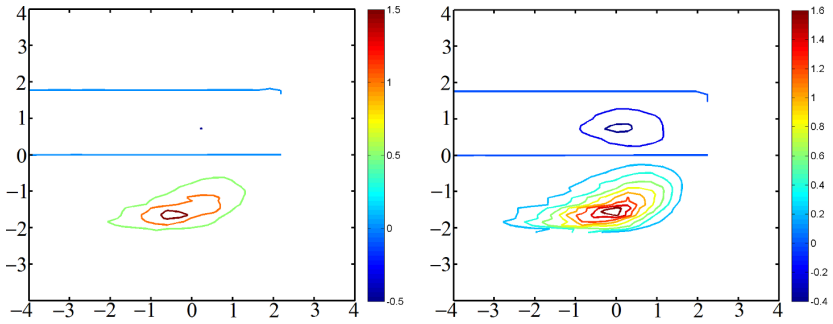

Figure 4.67: The weighted integrands from window 2 for the fluctuations of mixture fraction, the fluctuations of the axial component of the dissipation rate (left) and the radial component (right), computed by using the joint p.d.f. at $y/D_f = 1$ for $S = 1.07$. Horizontal scale corresponds to $\left[\ln(\chi) - \overline{\ln(\chi)}\right]/\sigma_{\ln(\chi)}$ while vertical scale corresponds to $[z - \langle z \rangle]/\sigma_z$.

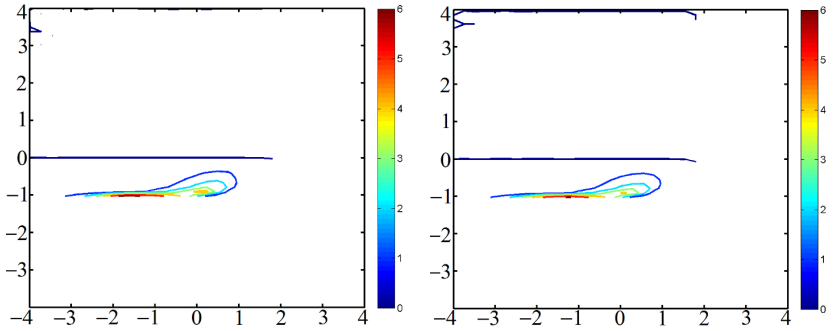

Figure 4.68: The weighted integrands from window 2 for the fluctuations of mixture fraction, the fluctuations of the axial component of the dissipation rate (left) and the radial component (right), computed by using the joint p.d.f. at $y/D_f = 1$ for $S = 0.3$. Horizontal scale corresponds to $\left[\ln(\chi) - \overline{\ln(\chi)}\right]/\sigma_{\ln(\chi)}$ while vertical scale corresponds to $[z - \langle z \rangle]/\sigma_z$.

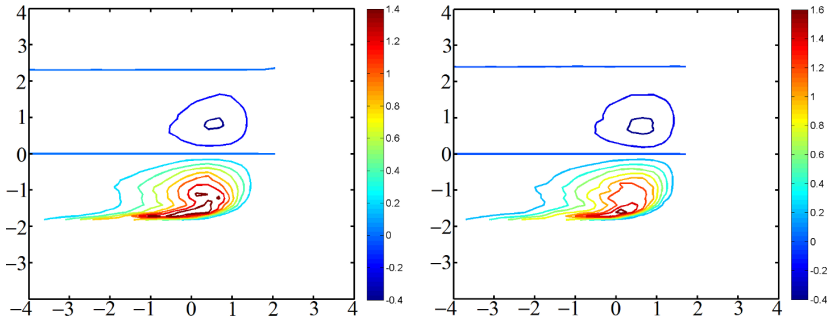

Figure 4.69: The weighted integrands from window 2 for the fluctuations of mixture fraction, the fluctuations of the axial component of the dissipation rate (left) and the radial component (right), computed by using the joint p.d.f. at $y/D_f = 1$ for the acetone vapour jet only. Horizontal scale corresponds to $\left[\ln(\chi) - \overline{\ln(\chi)}\right]/\sigma_{\ln(\chi)}$ while vertical scale corresponds to $[z - \langle z \rangle]/\sigma_z$.

4.2.6 Conditional scalar dissipation rate

Conditional scalar statistics are often required in turbulent flows and combustion modelling (Soulopoulos, 2009). In the context of combustion calculations, three parameters are usually required, which are the mean scalar dissipation rate conditional on the stoichiometric mixture fraction $\langle \chi | z_{st} = z^* \rangle$, the weighted probability of occurrence of the mean conditional scalar dissipation rate $E_{\chi|z}$ and the standard deviation of the conditional scalar dissipation rate $\left\langle \chi^{'} | z_{st} = z^* \right\rangle$. The conditional averaging is denoted by the angular brackets and only carried out for the events that satisfy the conditions to the right of the vertical rule, where N_{st} is the number of scalar dissipation rate samples corresponding to the stoichiometric mixture fraction.

$$\langle \chi | z_{st} = z^* \rangle \equiv \int_0^\infty \chi P\left(\chi | z_{st}\right) d\chi = \frac{1}{N_{st}} \sum_{i=1}^{N_{st}} \left(\chi | z_{st}\right) \tag{4.13}$$

$$E_{\chi|z} \equiv \langle \chi | z_{st} = z^* \rangle \, P\left(z = z_{st}\right) \tag{4.14}$$

$$\begin{aligned} \left\langle \chi^{'} | z_{st} = z^* \right\rangle &\equiv \left(\int_0^\infty \left(\chi - \langle \chi | z_{st} \rangle\right)^2 P\left(\chi | z_{st}\right) d\chi \right)^{1/2} = \\ &= \left(\frac{1}{N_{st}} \sum_{i=1}^{N_{st}} \left(\chi | z_{st} - \langle \chi | z_{st} \rangle\right)_i^2 \right)^{1/2} \end{aligned} \tag{4.15}$$

The mean and the standard deviation of the conditional dissipation rate are related to the location (mean) and scale (squared variance) parameters of the log−normal distribution according to the following relationships.

$$\langle \chi | z_{st} = z^* \rangle = e^{(\mu_{st} + \sigma/2)} \tag{4.16}$$

$$\left\langle \chi^{'} | z_{st} = z^* \right\rangle = \left(\langle \chi | z_{st} = z^* \rangle^2 \, e^{\left(\sigma_{st}^2 - 1\right)} \right)^{1/2} \tag{4.17}$$

The weighted probability of occurrence of the mean conditional scalar dissipation rate represents the molecular diffusion in scalar space in the transport equation for the scalar p.d.f. Sahay & O'Brien (1993) and is proportional to the mean reaction rate Bilger (1980). The relationship between the conditional scalar dissipation rate and the mean reaction rate for non−premixed combustion and under assumption of fast chemistry limit is given by the following expression Bilger (1976a).

$$\bar{\omega} = -\frac{1}{2} \bar{\rho} \frac{Y_{F,1}}{1 - z_{st}} \tilde{\chi}_{st} \tilde{P}\left(z = z_{st}\right) \tag{4.18}$$

where: $\bar{\omega}$ is the mean reaction rate, $\bar{\rho}$ is the mean density, $Y_{F,1}$ is the fuel mass fraction in the fuel stream, z_{st} is the stoichiometric mass fraction, $\tilde{\chi}_{st}$ is the Favre average scalar dissipation rate conditional on stoichiometric mixture fraction, $\tilde{P}$ is is the Favre p.d.f. of the stoichiometric mixture fraction.

Mastorakos *et al.* (1997) demonstrated that the most probable autoignition in a binary air/fuel mixture was a point with maximum of conditional scalar dissipation rate. The

maximum of conditional scalar dissipation rate was found to be not the stoichiometric mixture fraction as it would have been intuitively expected. On top of that, the extinction of a diffusion flame occurred when the cumulative probability of the conditional scalar dissipation rate exceed a certain threshold. The probability of extinction is given by Peters (1983) according to the following expression.

$$P_c = \int_0^{\chi_q} P\left(\chi|z_{st}\right) d\chi P_{ext} = 1 - P_c \tag{4.19}$$

A relatively new approach, which is based on conditional statistics is the conditional moment closure (CMC) method Bilger (1993, 1991a,b), Klimenko (1990), where moments conditional on the mixture fraction are of particular interest. The conditional dissipation rate is therefore the area of great interest, which needs to be addressed in details.

The conditional statistics of the scalar dissipation rate were computed by dividing the mixture fraction space in a number of bins, of typical width less than 0.01 and a typical size of 150000 samples in each bin. Averaging takes place in each bin so that the conditional mean of the scalar dissipation rate is computed. Similarly, the conditional standard deviation is computed from the data in each bin. Typically, 110 equally spaced bins were used to split the mixture fraction space containing 12e6 values, which resulted in 107000-280000 samples in the bins (depending on the bin number). The conditional means and the standard deviation of the scalar dissipation rate are shown in Figures 4.72−4.75 (pages 162−164) for window 2 at all axial positions ($y/D_f = 1, 3, 5, 7$), as a function of mixture fraction. The weighted probability of occurrence of the mean conditional scalar dissipation rate and the conditional probability are also shown in Figures 4.76−4.79 (pages 164−166).

The conditional means and the standard deviation of the scalar dissipation rate have a well−defined hyperbolic−shaped structure in the mixture fraction space. General observation of the mean scalar dissipation rate reveals that the mean increases with the mixture fraction, reaching a maximum value, then gradually decreases and reaches zero. With increasing swirl number the conditional mean decreases and its maximum shifts to lower mixture fraction values and this trend is similar for all axial positions ($y/D_f = 1, 3, 5, 7$). The location of the peak conditional mean shifts from 0.7 mixture fraction units for axial jet only to 0.6 units for $S = 0.3$, 0.4 for $S = 0.58$ and 0.3−0.4 units for the highest swirl number of 1.07. The peak conditional mean attains its maximum values (s^{-1}) of 2.3 ($y/D_f = 1$), 1.5 ($y/D_f = 3$), 1 ($y/D_f = 5$) and 0.6 ($y/D_f = 7$) for acetone vapour jet only, while for $S = 0.3$, 0.58, 1.07 the maximum values of the conditional mean are 3.5;2.5;1.4 ($D_f = 1$), 2;1.5;1.8 ($y/D_f = 3$), 2;1.2;1 ($y/D_f = 5$) and 1.8;0.8;0.4 ($y/D_f = 7$). For lower swirl numbers the conditional mean has clearly visible smooth shape, which somehow resembles the bell curve, while for higher swirl number and higher degree of mixing, the conditional mean 'breaks down' showing sparse scatter plot. The conditional average following the bell−shaped curve is consistent with the measurements given in Ahmed (2012), Soulopoulos (2009), Geyer *et al.* (2005) and Sardi *et al.* (1998). The variation of the conditional mean is consistent with the fact that the mean approaches zero at large and small mixture fraction values. This is due to the fact that larger and smaller mixture fraction values correspond to either jet fluid or ambient fluid, where scalar gradients are zero.

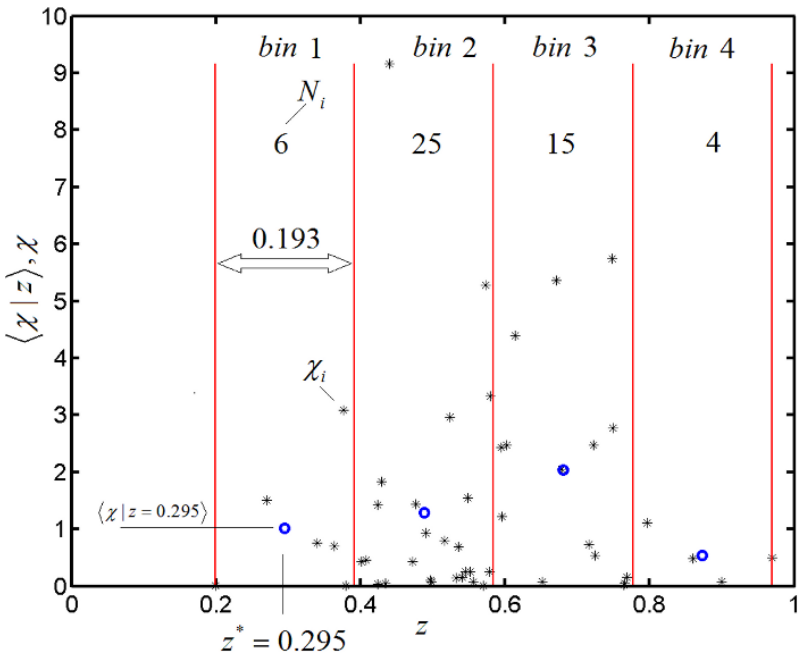

Figure 4.70: The principle of computation of the mean scalar dissipation rate conditional on the mixture fraction.

A set containing 50 samples is shown along with four bins used for computations. The principle of computation of the mean scalar dissipation rate conditional on the mixture fraction is described here for convenience as follows: Consider a set of data containing 50 values of the scalar dissipation rate and corresponding 50 values of the mixture fraction as is shown in the figure above. A mixture fraction set is divided in a number of bins, which is equal in this case to four equal bins, labelled as bin 1, 2, 3 and 4. Each bin contains a certain set of scalar dissipation rate values, i.e. bin one contains 6, bin two contains 25 etc. The scalar dissipation rate values are averaged in each bin giving the mean scalar dissipation rate. The mean scalar dissipation rate is assigned to the centre of bin, so that for example, the mean conditional scalar dissipation rate in bin one is equal to 1.009 at 0.295 (denoted as z^*) as result of averaging six scalar dissipation rate values ((0+1.512+0.7542+3.092+0.6956+0.000459)/6). Similar procedure is done for each bin so that the mean scalar dissipation rate conditional on the mixture fraction can be computed. Similarly, the standard deviation is computed in each bin as the root square of variance. In practice, the number of bins should be chosen on the principle of sufficient number of sample in the bin, especially in the case of large standard deviations, because the number of samples in each bin and the standard deviation of the set are related to the statistical error in the conditional mean. The conditional p.d.f can also be computed from the bins by using the standard procedure for the p.d.f. computations.

The standard deviation of the scalar dissipation rate conditioned on the mixture fraction demonstrates (Figures 4.72−4.75, pages 162−164) similar trend as the conditional mean with similar bell−shaped curve. The maximum values of the standard deviation attain maximum at the same mixture fraction units as the conditional mean and are equal to 3;3.5;3.5;2 ($y/D_f = 1$), 3;2.5;2.5;2.5 ($y/D_f = 3$), 2;3;2;2 ($y/D_f = 5$), 1;2.5;1;0.5 ($y/D_f = 7$) for axial jet only, $S = 0.3$, 0.58 and 1.07. Even though the peak of the standard deviation of the scalar dissipation rate is approximately constant irrespective of swirl number or the degree of mixing, the distribution is dependent on the swirl numbers. The distribution of the standard deviation follows the conditional mean pattern and for high

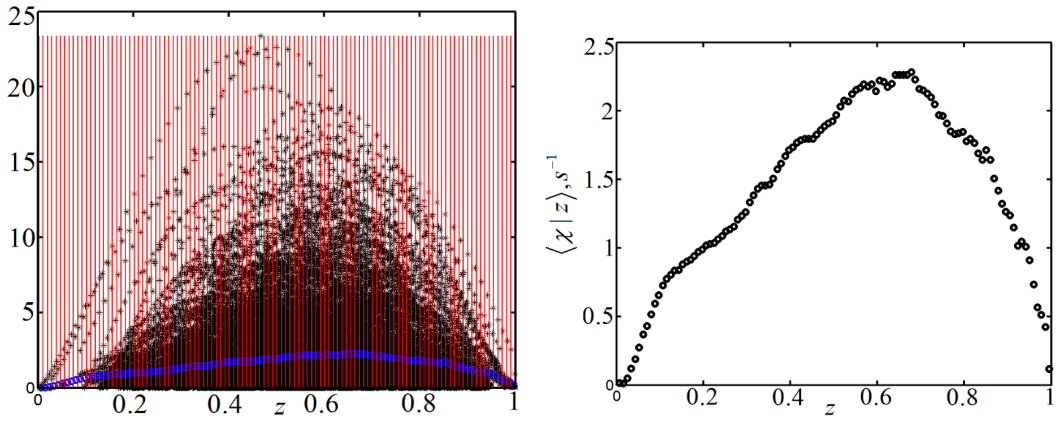

Figure 4.71: Mean scalar dissipation rate (s^{-1}) conditional on mixture fraction, as a function of mixture fraction computed from window 2 for acetone vapour jet only at $y/D_f = 1$. Figure on the left hand side shows first 50 thousand values of the scalar dissipation rate along with the mean scalar dissipation rate, computed from 12e6 samples. Vertical red lines indicate the 110 bins used in the computation. Blue circles indicate the mean scalar dissipation rate plotted on the scatter plot. On the right, the mean scalar dissipation rate from 12e6 values is shown.

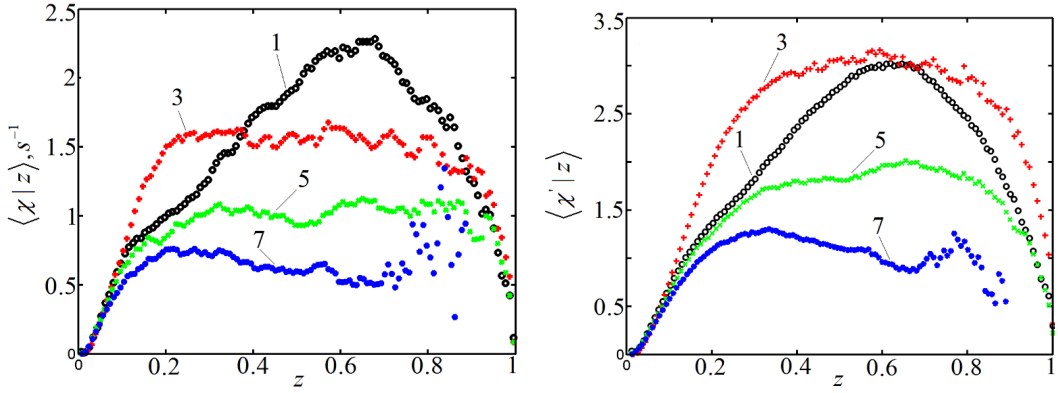

Figure 4.72: Mean scalar dissipation rate (s^{-1}) conditional on mixture fraction as a function of mixture fraction for window 2 (left) and standard deviation (right) for acetone vapour jet only at $y/D_f = 1, 3, 5, 7$.

swirl numbers becomes 'sparse scattered'. However, the absence of published data on the standard deviation of the scalar dissipation rate from similar rotating flows does not allow commenting on the generality of the results.

Sardi *et al.* (1998) reported that the standard deviation of the scalar fluctuations was almost equal to the mean conditional dissipation rate and was similarly distributed. An alternative explanation can be given in terms of probability of scalar dissipation rate, both conditional and unconditional. The probability of the scalar dissipation rate (not logarithm) was characterized by high probability at small values of dissipation rate with long tail approaching zero probability, which somehow resembled an exponential distribution. In the exponential distribution the standard deviation is equal to its mean by definition, and hence the standard deviation will resemble the conditional mean. Namazian (1988) and Sreenivasan *et al.* (1977) reported that the p.d.f. of scalar dissipation rate charac-

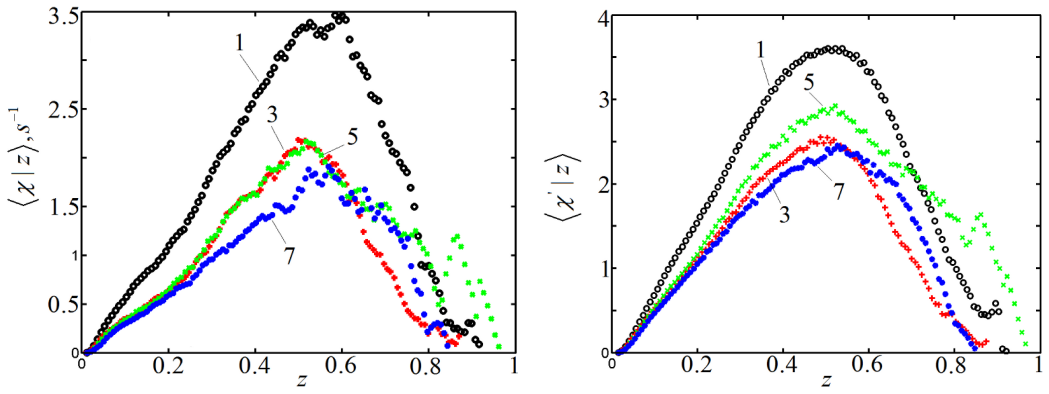

Figure 4.73: Mean scalar dissipation rate (s^{-1}) conditional on mixture fraction as a function of mixture fraction for window 2 (left) and standard deviation (right) for $S = 0.3$ at $y/D_f = 1, 3, 5, 7$.

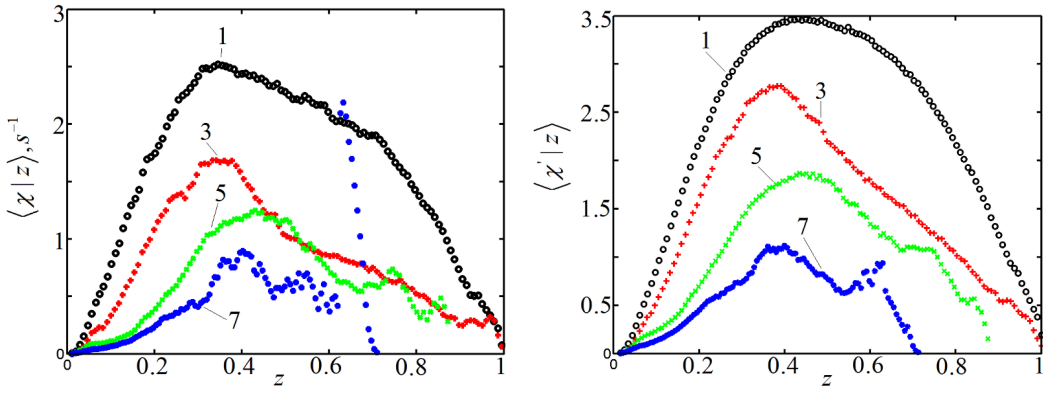

Figure 4.74: Mean scalar dissipation rate (s^{-1}) conditional on mixture fraction as a function of mixture fraction for window 2 (left) and standard deviation (right) for $S = 0.58$ at $y/D_f = 1, 3, 5, 7$.

terized by a high probability regions at small values of scalar dissipation rate and long exponential tails, which is also consistent with the present work. Even though it seems that the standard deviation is related to the conditional mean, because the p.d.f. of scalar dissipation rate is exponentially−distributed, the conclusions regarding particular interpretation in swirling or other flows will not be made. The interpretation is left as is and requires further investigations. However, to support these facts the conditional probability distributions of the scalar dissipation rate (not logarithm) computed for acetone vapour jet only and $S = 1.07$ from window 2 at $y/D_f = 1, 3, 5, 7$ are shown in Figure 4.80. In these plots the conditional p.d.f. of the scalar dissipation rate was approximated by a standard exponential distribution with different scale parameters. The scale parameters are summarized in Table 4.5 on page 167. The exponential distribution is given by the following formula, where the location parameter is equal to zero.

$$y = f\left(x; \mu\right) = \frac{1}{\mu} e^{\frac{-x}{\mu}} \tag{4.20}$$

It is clearly seen from Figure 4.80 that the scalar dissipation rate is indeed characterized by high probability at small values of dissipation rate with long tails. The exponential

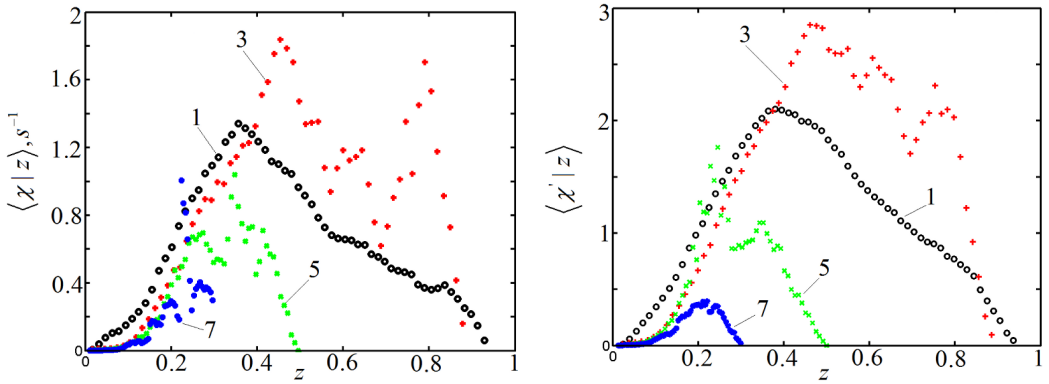

Figure 4.75: Mean scalar dissipation rate (s^{-1}) conditional on mixture fraction as a function of mixture fraction for window 2 (left) and standard deviation (right) for $S = 1.07$ at $y/D_f = 1, 3, 5, 7$.

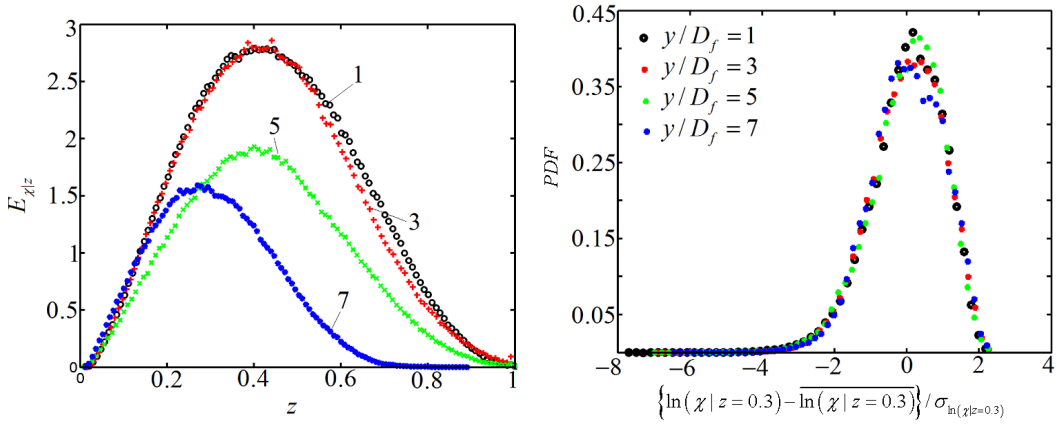

Figure 4.76: Weighted probability of occurrence of the mean conditional scalar dissipation rate (left) and conditional p.d.f. $\left[\ln(\chi|z=0.3) - \overline{\ln(\chi|z=0.3)}\right] / \sigma_{\ln(\chi|z=0.3)}$ (right) for the acetone vapour jet only at $y/D_f = 1, 3, 5, 7$ computed from window 2.

function approximation seems to be plausible assumption, because the exponential p.d.f. function follows the general trend of the scalar dissipation. As the level of mixing increases, the probability shift towards smaller values of the scalar dissipation rate and hence the scale parameter in the exponential p.d.f. decreases as well.

In addition, the conditional probability density functions of the scalar dissipation rate evaluated at 0.3 and 0.1 mixture fraction units are presented here (Figures 4.76−4.79). The conditional p.d.f. was evaluated from the logarithm of the scalar dissipation rate minus the mean of the logarithm of the scalar dissipation rate, normalized by the standard deviation of the logarithm of the scalar dissipation rate. This is similar to the unconditional p.d.f. mentioned earlier. The conditional and unconditional p.d.f. are very similar with small deviation from log−normal distribution and large negative fluctuation around the mean. This contradicts the findings reported by Ahmed (2012), where the deviation of the conditional p.d.f. from the Gaussian shape was more prominent than the unconditional p.d.f. Similar observations of the conditional p.d.f have been made for other values of the scalar dissipation rate and the conclusions can be extended to all mixture fraction

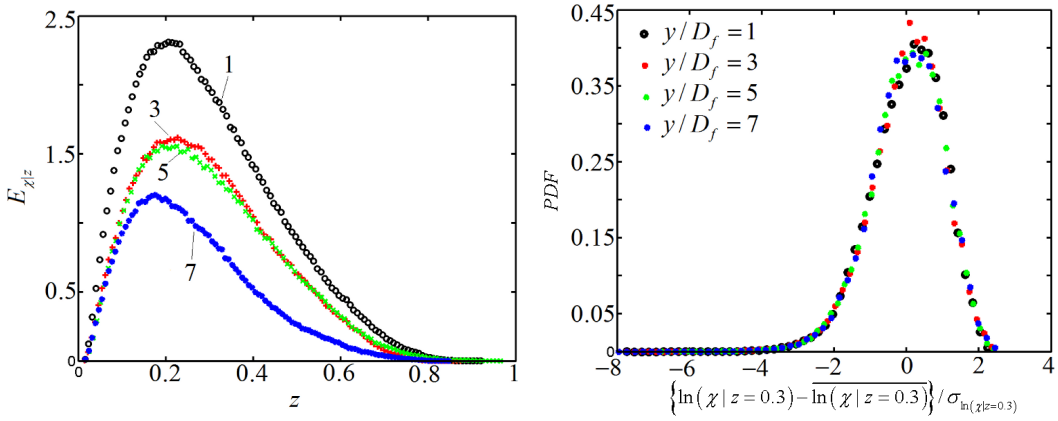

Figure 4.77: Weighted probability of occurrence of the mean conditional scalar dissipation rate (left) and conditional p.d.f $\left[\ln(\chi|z=0.3) - \overline{\ln(\chi|z=0.3)}\right]/\sigma_{\ln(\chi|z=0.3)}$(right) for $S = 0.3$ at $y/D_f = 1, 3, 5, 7$ computed from window 2.

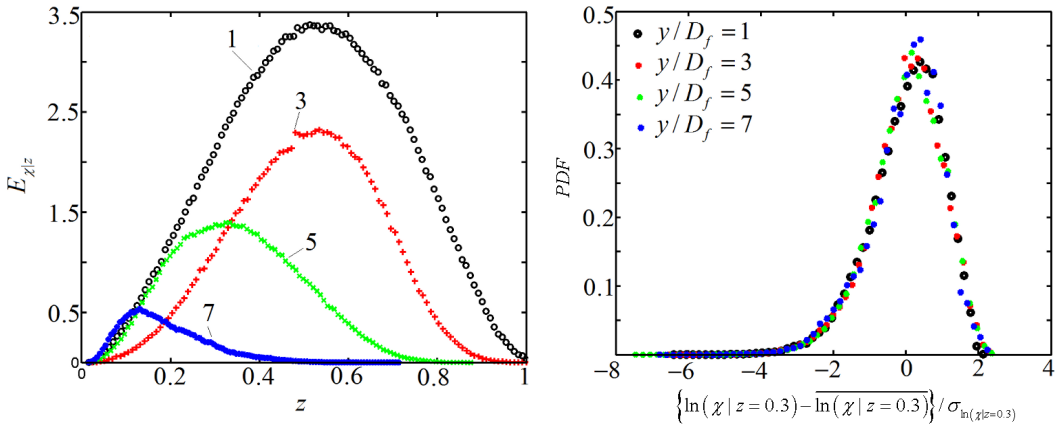

Figure 4.78: Weighted probability of occurrence of the mean conditional scalar dissipation rate (left) and conditional p.d.f. $\left[\ln(\chi|z=0.3) - \overline{\ln(\chi|z=0.3)}\right]/\sigma_{\ln(\chi|z=0.3)}$ (right) for $S = 0.58$ at $y/D_f = 1, 3, 5, 7$ computed from window 2.

units. This means that the conditional p.d.f. can be approximated by the Gaussian p.d.f. and the deviation can be small. However, an effect of spatial location, i.e. the location from which the statistics were evaluated, can alter the shape of the conditional p.d.f. On the other hand an assumption of log−normality in case of conditional p.d.f. seems to be plausible.

The weighted probability of occurrence is given in Figures 4.76−4.79 as a function of mixture fraction for different axial locations and swirl numbers computed from window 2. The weighted probability of occurrence is presented here as in Soulopoulos (2009) and Sardi *et al.* (1998), and is in fact the measure of how probable the observations of the particular conditional mean are. The weighted probability of occurrence has bell−shaped positively skewed curve and generally follows the conditional mean. The maximum values of the weighted probability are similar to those in the conditional mean for small and moderate swirl numbers. The actual location of the weighted probability peak is dependent on swirl

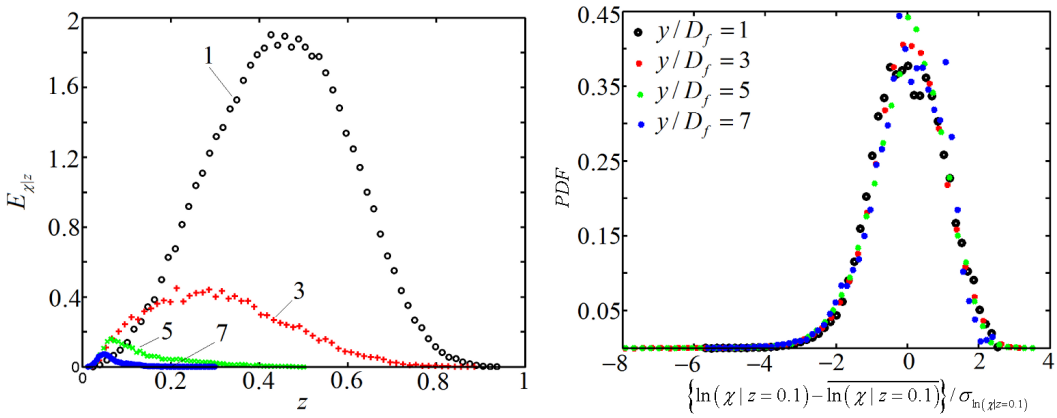

Figure 4.79: Weighted probability of occurrence of the mean conditional scalar dissipation rate (left) and conditional p.d.f. $\left[\ln(\chi|z=0.1) - \overline{\ln(\chi|z=0.1)}\right]/\sigma_{\ln(\chi|z=0.1)}$ (right) for $S = 1.07$ at $y/D_f = 1, 3, 5, 7$ computed from window 2.

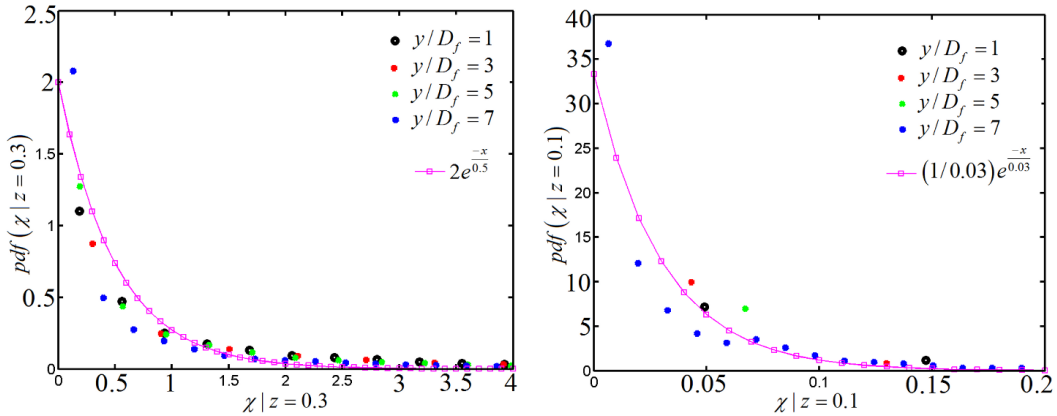

Figure 4.80: Conditional p.d.f. of the scalar dissipation rate $P(\chi|z=z^*)$ computed from window 2 as a function of axial positions for acetone vapour jet only (left) and $S = 1.07$ (right). Exponential distribution is also shown for scale parameter being equal to 0.5 (left) and 0.03 (right). Plotting range is not the same and is not equal in both figures.

number and axial position y/D_f in the flow. The weighted probability for axial jet only, shifts from 0.6 mixture fraction units to 0.4, i.e. to lower values of the mixture fraction and this is more prominent for higher downstream location ($y/D_f = 5$, and $y/D_f = 7$). Similar behaviour is observed for $S = 0.3$ where even smaller values of mixture fraction indicate the location of the peak, namely 0.2. For higher swirl numbers, the effect of peak location is partially reversed. The weighted probability of occurrence for $S = 0.58$ shifts from 0.4 to 0.6 for $y/D_f = 1, 3$; for $y/D_f = 5$ the position is roughly the same.

Table 4.5: Scale parameters μ for an exponential approximation $f(x;\mu) = \frac{1}{\mu}e^{-x/\mu}$ of conditional probability distribution $P(\chi|z=z^*)$ computed from window 2; z^* is equal to 0.3 for $y/D_f = 1, 3, 5$ and to 0.1 for $y/D_f = 7$.

S	$y/D_f = 1$	$y/D_f = 3$	$y/D_f = 5$	$y/D_f = 7$
S=0	1	1	0.8	0.8
S=0.3	1	0.8	0.8	0.8
S=0.58	0.5	1	0.5	0.3
S=1.07	0.1	0.1	0.1	0.025

Table 4.6: Unconditional statistics of scalar dissipation rate for acetone vapour jet only computed from window 1.

y/D_f	$\langle\chi\rangle$	$\mathrm{Var}(\chi)$	$\sigma_{\ln(\chi)}$	γ_1	$\langle\ln(\chi)\rangle$	$\sigma_{N(\mu,\sigma^2)}$	$\mu_{N(\mu,\sigma^2)}$
1	0.605	1.399	2.0147	0.1205	-2.179	b/m	b/m
3	1.124	5.204	1.9143	-0.8528	-1.447	0.90	0.22
5	0.960	2.774	1.7332	-0.7321	-1.209	0.93	0.22
7	0.652	1.378	2.6256	-1.4521	-2.081	0.7	0.3

Table 4.7: Unconditional statistics of scalar dissipation rate for acetone vapour jet only computed from window 2.

y/D_f	$\langle\chi\rangle$	$\mathrm{Var}(\chi)$	$\sigma_{\ln(\chi)}$	γ_1	$\langle\ln(\chi)\rangle$	$\sigma_{N(\mu,\sigma^2)}$	$\mu_{N(\mu,\sigma^2)}$
1	1.469	5.138	1.7964	-0.9173	-0.716	0.92	0.3
3	1.400	7.246	2.0620	-1.0691	-1.072	0.92	0.23
5	0.924	2.789	1.9138	-0.9295	-1.337	0.92	0.23
7	0.585	1.138	2.2926	-1.3538	-2.000	0.8	0.25

Table 4.8: Unconditional statistics of scalar dissipation rate for acetone vapour jet only computed from window 3.

y/D_f	$\langle\chi\rangle$	$\mathrm{Var}(\chi)$	$\sigma_{\ln(\chi)}$	γ_1	$\langle\ln(\chi)\rangle$	$\sigma_{N(\mu,\sigma^2)}$	$\mu_{N(\mu,\sigma^2)}$
1	0.625	1.684	1.9568	0.2575	-2.243	b/m	b/m
3	1.233	6.710	1.9547	-0.8464	-1.616	0.92	0.25
5	1.085	3.501	1.7145	-0.7097	-1.079	0.94	0.25
7	0.769	1.980	2.4836	-1.5291	-1.808	0.72	0.3

Table 4.9: Unconditional statistics of scalar dissipation rate for acetone vapour jet only computed from window 4.

y/D_f	$\langle\chi\rangle$	$\mathrm{Var}(\chi)$	$\sigma_{\ln(\chi)}$	γ_1	$\langle\ln(\chi)\rangle$	$\sigma_{N(\mu,\sigma^2)}$	$\mu_{N(\mu,\sigma^2)}$
1	1.742	7.199	1.8429	-0.9556	-0.587	0.85	0.3
3	1.791	11.672	2.0056	-0.9651	-0.815	0.9	0.2
5	1.145	3.943	1.8663	-0.9563	-1.081	0.9	0.2
7	0.668	1.499	2.2179	-1.3894	-1.805	0.8	0.3

Table 4.10: Unconditional statistics of scalar dissipation rate for acetone vapour jet only computed from window 5.

y/D_f	$\langle\chi\rangle$	Var(χ)	$\sigma_{\ln(\chi)}$	γ_1	$\langle\ln(\chi)\rangle$	$\sigma_{N(\mu,\sigma^2)}$	$\mu_{N(\mu,\sigma^2)}$
1	0.012	0.0013	1.9308	-0.1593	-6.744	b/m	b/m
3	0.585	2.917	3.4919	-0.3998	-4.446	b/m	b/m
5	0.871	2.608	1.8604	-0.8353	-1.795	0.9	0.22
7	0.738	1.704	1.7963	-0.7790	-1.480	0.93	0.22

Table 4.11: Unconditional statistics of scalar dissipation rate for S=0.3 computed from window 1.

y/D_f	$\langle\chi\rangle$	Var(χ)	$\sigma_{\ln(\chi)}$	γ_1	$\langle\ln(\chi)\rangle$	$\sigma_{N(\mu,\sigma^2)}$	$\mu_{N(\mu,\sigma^2)}$
1	2.016	9.305	2.1349	-0.7720	-0.679	0.88	0.55
3	1.238	4.895	2.1638	-0.9536	-1.260	0.92	0.3
5	0.845	3.705	2.5091	-1.1316	-1.983	0.82	0.3
7	0.417	1.398	3.1498	-0.7944	-3.500	0.8	0.45

Table 4.12: Unconditional statistics of scalar dissipation rate for S=0.3 computed from window 2.

y/D_f	$\langle\chi\rangle$	Var(χ)	$\sigma_{\ln(\chi)}$	γ_1	$\langle\ln(\chi)\rangle$	$\sigma_{N(\mu,\sigma^2)}$	$\mu_{N(\mu,\sigma^2)}$
1	0.923	3.343	2.7545	-1.1969	-1.952	0.75	0.45
3	0.643	1.749	2.4062	-1.1864	-2.091	0.8	0.3
5	0.632	2.086	2.5826	-1.1011	-2.341	0.8	0.3
7	0.411	1.075	2.8096	-0.8970	-3.086	0.83	0.4

Table 4.13: Unconditional statistics of scalar dissipation rate for S=0.3 computed from window 3.

y/D_f	$\langle\chi\rangle$	Var(χ)	$\sigma_{\ln(\chi)}$	γ_1	$\langle\ln(\chi)\rangle$	$\sigma_{N(\mu,\sigma^2)}$	$\mu_{N(\mu,\sigma^2)}$
1	2.084	10.661	2.1895	-0.6023	-0.754	0.9	0.55
3	1.401	6.416	2.1450	-0.9231	-1.124	0.93	0.3
5	0.902	4.050	2.4827	-1.0448	-1.901	0.83	0.3
7	0.480	1.818	3.0156	-0.7873	-3.213	0.83	0.45

Table 4.14: Unconditional statistics of scalar dissipation rate for S=0.3 computed from window 4.

y/D_f	$\langle\chi\rangle$	Var(χ)	$\sigma_{\ln(\chi)}$	γ_1	$\langle\ln(\chi)\rangle$	$\sigma_{N(\mu,\sigma^2)}$	$\mu_{N(\mu,\sigma^2)}$
1	1.095	4.892	2.8518	-1.0310	-1.919	0.75	0.45
3	0.714	2.078	2.3221	-1.0756	-1.940	0.82	0.35
5	0.718	2.703	2.4976	-0.9673	-2.181	0.83	0.35
7	0.496	1.589	2.7815	-0.8423	-2.897	0.84	0.4

Table 4.15: Unconditional statistics of scalar dissipation rate for S=0.3 computed from window 5.

y/D_f	$\langle\chi\rangle$	Var(χ)	$\sigma_{\ln(\chi)}$	γ_1	$\langle\ln(\chi)\rangle$	$\sigma_{N(\mu,\sigma^2)}$	$\mu_{N(\mu,\sigma^2)}$
1	0.195	1.271	1.5889	0.9666	-3.838	0.84	-0.15
3	1.623	7.310	2.0931	-0.6463	-0.945	0.93	0.45
5	1.318	5.932	2.0278	-0.8719	-1.118	0.93	0.3
7	0.611	2.109	2.7378	-1.0455	-2.536	0.82	0.3

Table 4.16: Unconditional statistics of scalar dissipation rate for S=0.58 computed from window 1.

y/D_f	$\langle\chi\rangle$	Var(χ)	$\sigma_{\ln(\chi)}$	γ_1	$\langle\ln(\chi)\rangle$	$\sigma_{N(\mu,\sigma^2)}$	$\mu_{N(\mu,\sigma^2)}$
1	1.314	4.862	1.7835	-0.6151	-0.889	0.93	0.3
3	0.671	1.90	1.8040	-0.5169	-1.670	0.95	0.2
5	0.381	0.810	2.0635	-0.4136	-2.596	0.99	0.2
7	0.161	0.211	2.0167	-0.3837	-3.503	0.98	0.15

Table 4.17: Unconditional statistics of scalar dissipation rate for S=0.58 computed from window 2.

y/D_f	$\langle\chi\rangle$	Var(χ)	$\sigma_{\ln(\chi)}$	γ_1	$\langle\ln(\chi)\rangle$	$\sigma_{N(\mu,\sigma^2)}$	$\mu_{N(\mu,\sigma^2)}$
1	1.838	8.333	1.7687	-0.8043	-0.515	0.95	0.25
3	0.975	3.861	1.7548	-0.4228	-1.279	0.99	0.1
5	0.550	1.374	2.0383	-0.4667	-2.145	0.99	0.1
7	0.110	0.096	2.0339	-0.3945	-3.885	0.99	0.1

Table 4.18: Unconditional statistics of scalar dissipation rate for S=0.58 computed from window 3.

y/D_f	$\langle\chi\rangle$	Var(χ)	$\sigma_{\ln(\chi)}$	γ_1	$\langle\ln(\chi)\rangle$	$\sigma_{N(\mu,\sigma^2)}$	$\mu_{N(\mu,\sigma^2)}$
1	1.542	5.937	1.8358	-0.6602	-0.817	0.92	0.3
3	0.774	2.308	1.7721	-0.5045	-1.487	0.95	0.2
5	0.420	0.939	2.0860	-0.4123	-2.526	0.99	0.2
7	0.206	0.360	2.0480	-0.3637	-3.280	0.99	0.15

Table 4.19: Unconditional statistics of scalar dissipation rate for S=0.58 computed from window 4.

y/D_f	$\langle\chi\rangle$	Var(χ)	$\sigma_{\ln(\chi)}$	γ_1	$\langle\ln(\chi)\rangle$	$\sigma_{N(\mu,\sigma^2)}$	$\mu_{N(\mu,\sigma^2)}$
1	2.318	12.375	1.8446	-1.0363	-0.420	0.9	0.25
3	1.125	4.839	1.8129	-0.4769	-1.169	0.99	0.15
5	0.70	1.985	2.0036	-0.4834	-1.841	0.99	0.15
7	0.145	0.199	2.0374	-0.3228	-3.664	0.99	0.15

Table 4.20: Unconditional statistics of scalar dissipation rate for S=0.58 computed from window 5.

y/D_f	$\langle\chi\rangle$	Var(χ)	$\sigma_{\ln(\chi)}$	γ_1	$\langle\ln(\chi)\rangle$	$\sigma_{N(\mu,\sigma^2)}$	$\mu_{N(\mu,\sigma^2)}$
1	0.53	2.747	3.1364	-0.4457	-4.622	b/m	b/m
3	0.747	2.223	1.7267	-0.4701	-1.517	0.99	0.15
5	0.666	1.668	1.9219	-0.5414	-1.771	0.99	0.15
7	0.189	0.253	2.0059	-0.3389	-3.319	0.99	0.15

Table 4.21: Unconditional statistics of scalar dissipation rate for S=1.07 computed from window 1.

y/D_f	$\langle\chi\rangle$	Var(χ)	$\sigma_{\ln(\chi)}$	γ_1	$\langle\ln(\chi)\rangle$	$\sigma_{N(\mu,\sigma^2)}$	$\mu_{N(\mu,\sigma^2)}$
1	0.587	1.623	1.9827	-0.5645	-1.993	0.99	0.15
3	0.209	0.593	2.3917	0.0226	-4.075	0.99	-0.15
5	0.035	0.275	2.0232	-0.0516	-5.568	0.94	-0.05
7	5e-3	3.94e-4	1.7986	-0.2536	-6.747	0.94	-0.05

Table 4.22: Unconditional statistics of scalar dissipation rate for S=1.07 computed from window 2.

y/D_f	$\langle\chi\rangle$	Var(χ)	$\sigma_{\ln(\chi)}$	γ_1	$\langle\ln(\chi)\rangle$	$\sigma_{N(\mu,\sigma^2)}$	$\mu_{N(\mu,\sigma^2)}$
1	0.776	2.339	1.8853	-0.5505	-1.602	0.94	0.05
3	0.187	0.628	2.3718	0.0748	-4.288	0.94	-0.15
5	0.026	0.20	1.9948	-0.1324	-5.748	0.94	0.1
7	4.7e-3	5.07e-4	1.8138	-0.2304	-6.935	0.94	0.1

Table 4.23: Unconditional statistics of scalar dissipation rate for S=1.07 computed from window 3.

y/D_f	$\langle\chi\rangle$	Var(χ)	$\sigma_{\ln(\chi)}$	γ_1	$\langle\ln(\chi)\rangle$	$\sigma_{N(\mu,\sigma^2)}$	$\mu_{N(\mu,\sigma^2)}$
1	0.73	2.529	1.9008	-0.5094	-1.731	0.94	0.1
3	0.34	1.264	2.4396	-0.0523	-3.529	1.05	-0.05
5	0.075	1.987	2.0548	-0.0109	-5.212	0.98	-0.05
7	6.6e-3	7.14e-4	1.7682	-0.2581	-6.525	0.93	-0.05

Table 4.24: Unconditional statistics of scalar dissipation rate for S=1.07 computed from window 4.

y/D_f	$\langle\chi\rangle$	Var(χ)	$\sigma_{\ln(\chi)}$	γ_1	$\langle\ln(\chi)\rangle$	$\sigma_{N(\mu,\sigma^2)}$	$\mu_{N(\mu,\sigma^2)}$
1	0.898	3.04	1.8225	-0.5823	-1.378	0.94	0.15
3	0.328	1.697	2.4452	0.0555	-3.771	0.98	-0.05
5	0.037	0.596	1.9839	-0.1155	-5.424	0.98	-0.05
7	5.4e-3	3.32e-4	1.7653	-0.2718	-6.660	0.92	-0.05

Table 4.25: Unconditional statistics of scalar dissipation rate for S=1.07 computed from window 5.

y/D_f	$\langle\chi\rangle$	Var(χ)	$\sigma_{\ln(\chi)}$	γ_1	$\langle\ln(\chi)\rangle$	$\sigma_{N(\mu,\sigma^2)}$	$\mu_{N(\mu,\sigma^2)}$
1	0.727	2.693	1.8062	-0.4936	-1.659	0.92	0.15
3	0.334	1.422	2.5443	6.8e-5	-3.756	0.98	-0.15
5	0.031	0.057	1.9758	-0.0880	-5.527	0.93	0.05
7	6.2e-3	2.6e-3	1.7942	-0.2137	-6.747	0.93	0.05

Note: Notations in Tables 4.6 - 4.25 are given below for convenience

- $\langle\chi\rangle-$Mean of scalar dissipation rate $(1/s)$.
- Var(χ)$-$Variance of scalar dissipation rate $(1/s^2)$.
- $\sigma_{\ln(\chi)}-$Standard deviation of the logarithm of the scalar dissipation rate.
- γ_1-Skewness of the p.d.f. of the fluctuations of the logarithm of the scalar dissipation rate.
- $\langle\ln(\chi)\rangle-$Mean of the logarithm of the scalar dissipation rate.
- $\sigma_{N(\mu,\sigma^2)}-$Scale parameter of Gaussian distribution that approximates given p.d.f.
- $\mu_{N(\mu,\sigma^2)}-$Location parameter of Gaussian distribution that approximates given p.d.f.
- $b/m-$Bi$-$modal p.d.f. cannot be represented by Gaussian distribution.

4.3 Summary

Scalar mixing in turbulent isothermal swirling flows was studied in this chapter. The measurements were carried out in swirling non$-$reacting jets as a function of downstream locations as well as a function of the degree of mixing that was quantified by the swirl number. Three swirl numbers were covered, i.e 0.3, 0.58 and 1.07, as well as non$-$swirling flow without coflow of air (denoted as acetone vapour jet). A different degree of mixing was achieved by splitting the two air streams (axial and swirl) and mixing them together within flow development section of the burner. The imaging technique used in this work was planar laser induced fluorescence of acetone. Quantitative, instantaneous and two dimensional mixture fraction images were recorded by using this technique and processed by using conventional software MATLAB©. The signal$-$to$-$noise ratio for the scalar measurements was circa 100.

It was shown that scalar mixing was highly dependent on swirl number. Highly non-homogeneous scalar field near to burner exit was observed regardless of swirl number. These highly non$-$homogeneous scalar fields lead to high scalar dissipation rates, especially within shear layer. The scalar dissipation rate resembled mixture fraction variance and was characterized by the so$-$called scalar dissipation rate layer thickness, which was measured as $\approx$1(mm). Scalar mixing statistics (mean, standard deviation) as well as scalar dissipation were highly dependent on both, swirl number and spatial locations. The detailed conclusions are given in Chapter 8.

5 Experimental assessment of presumed filtered density function models

> Science is wonderfully equipped to answer the question How? but it gets terribly confused when you ask the question Why?.
>
> Erwin Chargaff

In a general sense, complex chemistry cannot be easily incorporated in the reacting flow computation procedures. A certain degree of simplification is usually required, which results in a number of 'turbulence−chemistry' interaction models and approaches. The description of turbulence−chemistry interaction may be achieved by using a variety of numerical models. This chapter focuses on turbulence−chemistry interaction relevant for the LES method, as the most promising approach for computing reacting flows. Presumed Filtered Density Functions (FDF) of mixture fraction are studied both experimentally and theoretically by using the experimental data from isothermal non−reacting swirling jet with different degree of swirl. The filtered density functions are measured at different locations in the flow and are reported as a function of downstream positions (stream−wise) and as a function of swirl number. The presumed FDFs are computed from the resolved mixture fraction, which is obtained by applying a low−pass filter to measured instantaneous mixture fraction fields, and the resolved 'subgrid scale' scalar variance (SGS). The resolved SGS variance was also measured and studied numerically by using two common models.

5.1 Laminar flamelet approach

Large Eddy Simulation (LES) uses a type of spatial filtering procedure in order to remove smaller scales of a flow so that resulting equations can be solved on relatively coarse grid. Therefore, only resolved or spatially averaged quantities are known from a CFD solver. A laminar flamelet approach is typically used in commercial CFD codes due to the simplicity and flexibility. The flamelet approach is based on a concept of thin, laminar, locally one−dimensional structures (called laminar flamelet) embedded into the turbulent flow field. The main idea behind this approach is to separate the detailed and complex chemistry calculations and the flow solver. The laminar flamelet approach reduces the complex chemistry to a function of only two variables, which are the mixture fraction and the scalar dissipation rate.

A common laminar flame that is used to describe laminar flamelet is the counterflow diffusion flame. Precomputed variables that are known from counterflow diffusion flame

simulations, e.g. temperature, species mass fraction etc., are now a function of the mixture fraction and the scalar dissipation only. This reduces computation cost considerably. In order to embed locally one−dimensional laminar flamelets into the turbulent flow a concept of probability density function (in RANS context) or filtered density function (in LES context) is typically used. Under fast−chemistry assumption the temperature can be assumed to be a function of mixture fraction only and this assumption will be used in this work. In general, the temperature is also a function of scalar dissipation rate, which can be linked to the strain rate in opposed−flow diffusion flames. However, the relation between the temperature, scalar dissipation and the mixture fraction in laminar flamelet computations is beyond the scope of the present work.

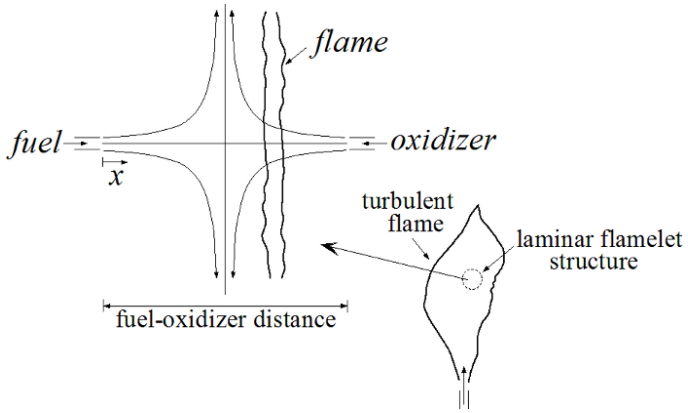

Figure 5.1: Laminar Opposed−flow diffusion flamelet. (Bray & Peters 1994).

In this work, the relationship between the temperature and the mixture fraction was computed by using commercial software CHEMKIN−Pro©. The CHEMKIN-Pro© is made of different Fortran[1] subroutines that allow modelling of different reacting system under different operating conditions. This software uses detailed chemical mechanism with a number of elementary reactions to compute chemically reacting flows. The detailed chemical mechanism that is included by default is GRI−3.0. However, in this work the San Diego mechanism, thermodynamic database and the transport database were chosen (published by University of California San Diego−UCSD). In the San Diego mechanism the number of species and reaction is kept to the appropriate minimum needed to accurately describe the modelled system, thus minimizing the uncertainties in the rate parameters. This approach differs from other data sets, e.g. GRI−3.0. The other data sets attempt to include all potentially relevant elementary steps that can lead to the uncertainties, especially when large number of steps is used[2].

A subroutine (OPPDIF) was used to compute the flame temperature of methane/air diffusion flame at atmospheric pressure of 1(bar) and temperature of 300(K). Injection velocities were constant and equal 100(cm/s) for both the oxidizer and the fuel sides. The OPPDIF simulates the flame structure in an opposite flow configuration for axisymmetric or planar diffusion flames between two opposite nozzles. The OPPDIF solution is based

[1]Fortran (previously FORTRAN) is a general-purpose, imperative programming language that is especially suited to numeric computation originally developed by IBM at their campus in south San Jose, California.

[2]The San Diego Mechanism. Chemical-kinetic mechanisms for combustion applications. http://web.eng.ucsd.edu/mae/groups/combustion/mechanism.html

on a model that was originally proposed by Kee et al. (1988) for premixed opposed−flow flames. A detailed derivation of the governing equations that are used in the OPDIFF can be found in Kee et al. (1988) and is not presented here.

The laminar opposed−flow diffusion flamelet solution generates a number of tables (called laminar flamelet tables) with all the required information, which is given as a function of the mixture fraction and the scalar dissipation rate. Since the opposed−flow solution is given as a discrete dataset it is convenient to interpolate the dataset between any two or more discrete points in order to compute the resolved mean temperature (the flame temperature in the LES context) as a function of any arbitrary mixture fraction value. The arbitrary instantaneous temperature can be computed from calculated discrete dataset by performing linear, cubic, or polynomial approximation between any two or more discrete points. In this work, a joint polynomial−cubic approximation was used to compute the instantaneous temperature as a function of any arbitrary mixture fraction value in the interval $z \in [0\ 1]$ (Figure 5.2). The system of approximating equations is then written as follows:

$$\begin{aligned} T_{|0\leq z\leq 0.5} &= a_1 z^8 + a_2 z^7 + a_3 z^6 + a_4 z^5 + a_5 z^4 + a_6 z^3 + a_7 z^2 + a_8 z + a_9 \\ T_{|0.5>z\leq 1.0} &= a_{11} z^3 + a_{22} z^2 + a_{33} z + a_{44} \end{aligned} \tag{5.1}$$

$$\begin{aligned} &a_1 = -1.8279e+013; a_2 = 6.6546e+012; a_3 = 9.3974e+011; a_4 = -6.5622e+010 \\ &a_5 = -2.4166e+009; a_6 = 5.065e+007; a_7 = -1.2237e+006; a_8 = 61761; \\ &a_9 = 300; a_{11} = -2083.5; a_{22} = 4796.3; a_{33} = -4675; a_{44} = 2256.6 \end{aligned} \tag{5.2}$$

The approximation error between the discrete set (from flamelet simulation) and the approximated solution was computed according to the following Eq. 5.3. As shown in Figure 5.2 the maximum approximating error is less than 1.6% for z >0.8 and less than 1% for 0< z <0.7. The average approximation error was less than 0.5%.

$$\varepsilon(z) = \left| \frac{T_C(z) - T_A(z)}{T_C(z)} \right| \cdot 100\% \tag{5.3}$$

Any resolved dependant variables (resolved temperature in this context) can be computed according to the following formulas[3]. The variable that is being integrated is called the dependant variable and in a broad sense can be any variable, e.g. mass fraction, reaction rate etc.

$$\overline{T}_{f_z}(x,t) = \int_0^1 T(z) f_z(x,t)\, dz \tag{5.4}$$

[3]Let X be a discrete random variable taking values $x_1, x_2, x_3, ...x_n$ with probabilities $p_1, p_2, p_3, ...p_n$ respectively. Then the expected value (resolved mean) of this random variable is by definition infinite sum $E[X] = \sum_{i=1}^{\infty} x_i p_i$. It is equivalent to computing the resolved mean, where probabilities $p_1, p_2, p_3, ...p_n$ are actually the values of the FDF/FMDF in the context of LES, and discrete random variables $x_1, x_2, x_3, ...x_n$ are precomputed quantities stored in the flamelet tables.

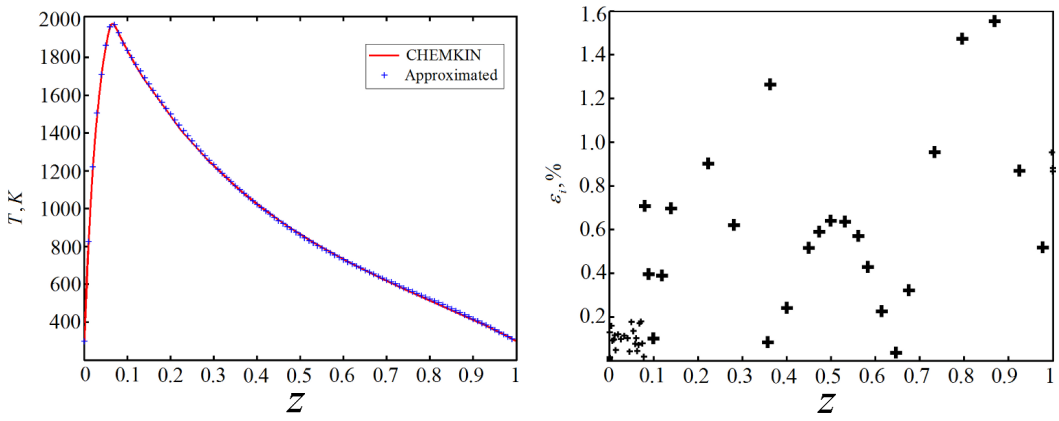

Figure 5.2: Temperature as a function of the mixture fraction from laminar flamelet solution with discrete data approximation by polynomials (left) and approximation errors (right). Temperature solution was obtained from opposed-flow simulation of CH_4+Air combustion at 300(K), 1(bar) for the strain rate of 100$(1/s)$.

$$\overline{T}_{\beta}\left(\tilde{z},\tilde{z}''^2\right) = \int_0^1 T(z) B_z\left(\tilde{z},\tilde{z}''^2\right) dz \tag{5.5}$$

$$\overline{T}_{\Pi_l}\left(\tilde{z},\tilde{z}''^2\right) = \int_0^1 T(z) \Pi_l\left(\tilde{z},\tilde{z}''^2\right) dz \tag{5.6}$$

5.2 Mixture fraction filtered mass density functions

The FDF[4] are used to integrate the flamelet tables and hence must be defined. There are two general approaches that can be used in order to define the shape of the FDF. The first is based on the FDF transport equations (similar to that RANS−PDF). This approach hardly can be incorporated in modern commercial LES codes due to high transported FDF dimensionality and hence additional complexity associated with the solution of the transport equation. The solution of this transported FDF equation is typically found by using a Monte−Carlo statistical technique (Pope, 1985). The high complexity of transported FDFs led to a concept of presumed FDFs. The presumed FDFs do not require heavy computational calculations and are easily incorporated into modern CFD codes. The FDF are usually approximated to be a β−FDF or a top−hat one.

The β−FDF as well as the top−hat presumed FDF proposed by Borghi (1988) and Mao (1970) have been extensively studied both theoretically and experimentally. The validity and the extent of presumed FDF methods were assessed by using the experimental data obtained either from turbulent non−premixed reacting Drozda *et al.* (2008), Tong (2006), Wang *et al.* (2007) and non−reacting flows Wang *et al.* (2004), Tong (2001) or from direct numerical simulations (DNS) Colucci *et al.* (1998), Cha & Trouillet (2002), Cook & Riley (1994) and Floyd *et al.* (2009).

The FDF is also an important model variable in several others LES approaches such

[4]FDF refers to the presumed filtered density function, while FMDF refers to the measured filtered density function.

as for example conditional moment closure. However, at present there is still not enough information on FDFs in swirling isothermal flows. Therefore, in order to understand, develop accurate and improved presumed FDF models for the LES of turbulent reacting flows, especially in swirling flows, understanding of the mixing of the subgrid scale (SGS) scalar is essential. As a step towards this goal, the structure and statistics of the SGS scalar mixing in terms of filtered mass density functions are studied in this section. This chapter can provide a physical base and further insight for the presumed FDF methods for conserved scalars used in Large Eddy Simulation of turbulent non−premixed isothermal swirling flows.

Measurements of the FDFs were carried out in non−premixed turbulent swirling flow at constant atmospheric pressure and temperature according to operating conditions outlined in Chapter 2. Nine different spatial locations at each axial downstream position (stream−wise), i.e. at each y/D_f were studied in the FDFs evaluation. The specific positions are shown in Figure 5.3 allowing the effects of swirl and spatial locations to be examined. Six spatial locations were chosen to be somehow within shear layer and three within axial centreline. Two box filters were used namely 0.3(mm), $\Delta/\lambda_\beta \approx 1$ and 1.0(mm), $\Delta/\lambda_\beta \approx 3.3$ allowing the influence of box filter width on the FDF statistics to be assessed. The smaller filter was chosen to ensure that the SGS scalar variance was small because the filter size was around the Batchelor scale.

The process of computation of the FDF from two−dimensional data involved binning the scalar data in 10−15 equally spaced bins. The discrete scalar data that fell in each bin was counted so that frequency could be computed[5]. The value of FDF was then obtained by normalizing calculated frequencies by the corresponding bin width and the total number of samples in all bins (Eqn. 5.7).

$$f_z(i) = \frac{n_i}{\Delta_{bin} N_{samples}} \tag{5.7}$$

The total number of samples depended on the box filter sizes. For instance if the box filter was 1(mm), $\Delta/\lambda_\beta \approx 3.3$, which corresponded to 38 pixels, then the total number of samples would be 38×38. It should be noted that the FDF computations are presented for three locations (first, second and third) only, because similar trends can be observed at other positions. In addition, the spatial location, where measured filtered mass density functions (FMDFs) were evaluated are presented for completeness. This trend and the behaviour of the FMDF should not be linked to any specific locations in the flow or to operating conditions (swirl number) because by definition the FMDFs/FDFs are computed from instantaneous realisation.

The rest of this section discusses the measured filtered mass density functions in terms of the effects of the box filter size on the resulting shape of the FMDF. An example of filtered mass density function computation from experimentally measured mixture fraction field for two different filter sizes is shown in Figure 5.4. The smallest filter, which was comparable to the Batchelor scale ($\approx 300(\mu m)$) contained almost uniformly distributed mixture fraction values within the confines of the filter. In this case, the FMDF would be expected to be unimodal, as it is illustrated in Figure 5.5. On the other hand, if the filter

[5]This is a standard way to compute a histogram.

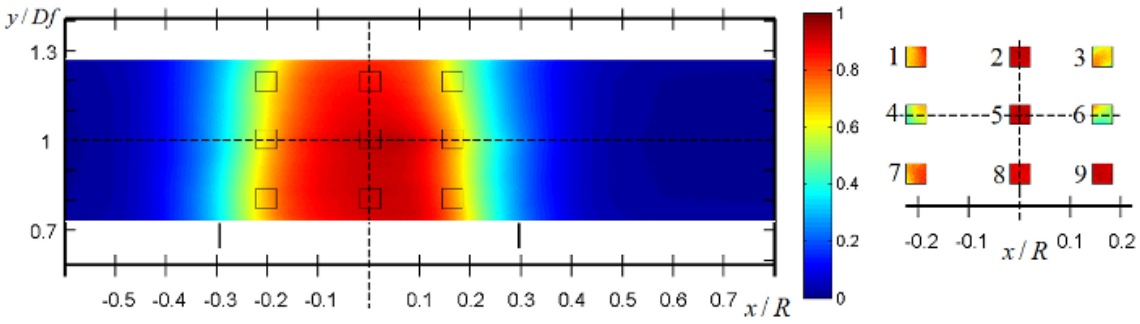

Figure 5.3: Spatial locations used to measure the FMDF ($f_z(x,t)$). Time averaged mixture fraction distribution ($\bar{z}$, computed from 1500 realizations) is also shown for $y/D_f = 1$ for $S = 0.3$. The spatial location used to compute the FMDF was chosen within the shear layer and the burner centreline, which is denoted as vertical dashed line.

contains highly segregated mixture fraction values, i.e. with larger fluctuations around the mean, the resulting FMDF would be expected to be bimodal (Fig. 5.5 left bottom picture).

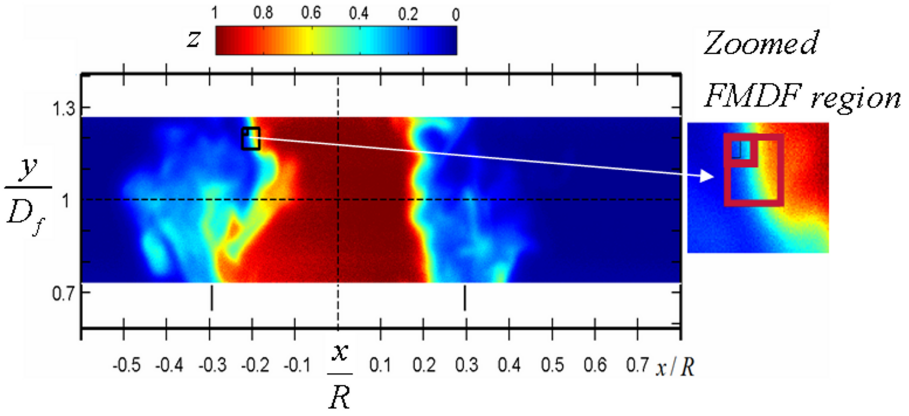

Figure 5.4: An example of filtered mass density function computation from experimentally measured mixture fraction field. The box filter of two different sizes are shown 1.0(mm), $\Delta/\lambda_\beta \approx 3.3$ and 0.3(mm), $\Delta/\lambda_\beta \approx 1$. Instantaneous mixture fraction distribution for S=0.3 at $y/D_f = 1$ is shown as an example of highly non-homogeneous mixture fraction field.

Figure 5.7 shows measured FMDF for two different filter sizes (mm) of 1.0; $\Delta/\lambda_\beta \approx$3.3 (left) and 0.3; $\Delta/\lambda_\beta \approx$1 computed from filters shown in Figure 5.4. The measured FMDF is in fact probability density function of mixture fraction, such that $\int_0^1 FMDF\,(z)dz = 1$. The bimodal distribution is clearly observable for the largest filter size and approximately unimodal distribution for the smallest filter size. It should be noted that for fixed filter size, the shape of the FMDF will be different as filter moves along the spatial domain. This is also illustrated in Figure 5.6, where for fixed filter size, the SGS scalar variance is different and hence the FMDFs will also be different. It should be noted that large filter size of 1.0(mm) is quite small for LES simulations and quite often larger sizes are used. However, for this moderately large filter size, bimodal FDFs are observed. On the other hand, for filter sizes that are exactly equal to the Batchelor scale (0.3(mm)) the

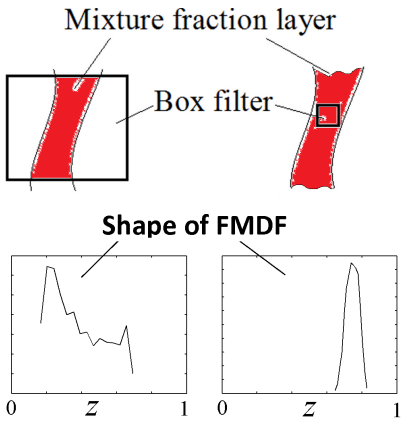

Figure 5.5: Schematic illustration in the cartoon form of the effect of the box filter size on the FMDF. On the left hand side, large filter size is shown ($\Delta/\lambda_\beta > 3$) on the right hand side, a small filter size is presented ($\Delta/\lambda_\beta \approx 1$). A steep gradient of the mixture fraction is shown as an example; when the mixture fraction field is highly segregated within the filter confines, the FMDF is expected to be bimodal. For actual data, see Figure 5.6.

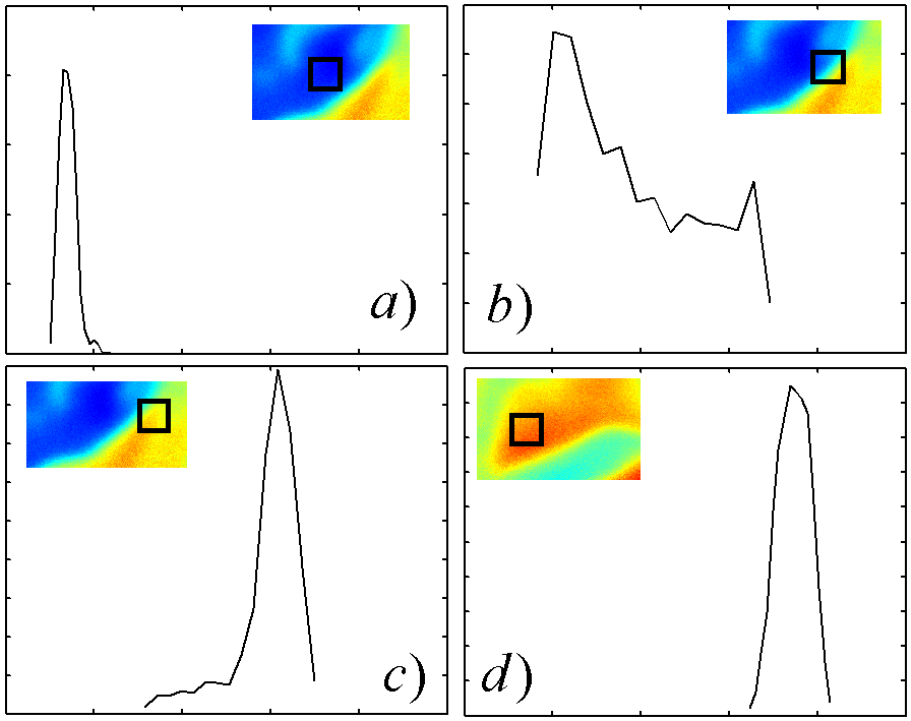

Figure 5.6: Effect of the box filter size on the FMDFs for a fixed filter size of 1.0(mm), $\Delta/\lambda_\beta \approx 3.3$ for different filter positions. The resulting FMDFs were computed from corresponding filters shown in each figure. Note that a), c) and d) are unimodal, b) is bimodal.

corresponding FMDFs were always unimodal.

In addition, the shape of the FMDF was studied as a function of the SGS scalar variance. By using trial and error procedures it a threshold SGS scalar value was experimentally found, above which the FMDF would be bimodal. The threshold was computed to be approximately $\tilde{z}''^2$ =0.02. This value was found by plotting the measured FMDF as a

function of the SGS scalar variance and examining the resulting shape. In this work, two SGS scalar variance terms were also defined, namely 'high' and 'low' SGS scalar variance as values relative to the threshold value, i.e. $\tilde{z}''^2 > 0.02$ and $\tilde{z}''^2 < 0.02$.

An interesting observation can be seen in Figure 5.8, which shows measured FMDF computed from filter size of Δ/λ_β =1.5. Presumed $\beta-$FDF and top$-$hat FDF are also shown, which were calculated from measured resolved mean and measured SGS scalar variance from the same filter. The figure shows that even for such small filter, which is comparable to the Batchelor scale, the bimodal FMDF distribution can still be observed. In fact, Figure 5.8 demonstrates a typical picture of 'filter overlapped state', which is shown in Figure 5.5. In addition, the presumed FDF cannot represent bimodal distribution, which is also clearly seen from Figure 5.8.

In addition, the unimodal FMDF distribution can be found, e.g. in jet potential core, where no mixing takes place and hence for any arbitrary filter size, the distribution of the mixture fraction values within confines of the filter is nearly homogeneous. Similarly, under well-mixed conditions, e.g. at far away distances from the nozzle exit or highly swirling flows, where rapid mixing takes place, the shape of the FMDF is likely to be unimodal. Figure 5.9 shows an example of measured FMDFs from two spatial locations for large filter sizes and well-mixed regime at $y/D_f = 7$ for S=0.58. As it can be clearly seen, even for large filter sizes, the shape of the FMDF can be unimodal.

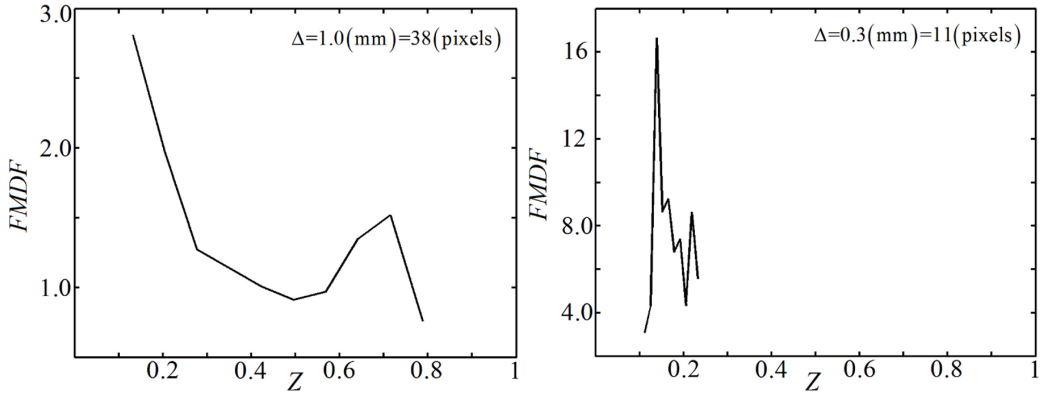

Figure 5.7: Measured FMDF for two different filter sizes (mm) of 1.0; $\Delta/\lambda_\beta \approx 3.3$ (left) and 0.3; $\Delta/\lambda_\beta \approx 1$ (right) computed from filters shown in Figure 5.4. Plotting range along vertical scale represents probability density function of mixture fraction, such that $\int_0^1 FMDF\,(z)dz = 1$. Vertical scale is not the same in each figure.

The effect of the swirl number cannot be readily assessed from the shape of the FMDF, because the FMDF is by definition computed from the instantaneous realisations. General remarks, which will be supported later by examining the p.d.f. of the SGS scalar variance, are given here as follows. Increase in the level of mixing increases homogeneity of the flow field, which in turn means that the scalar is locally well-mixed. Well-mixed regime indicates that the SGS scalar variance tends to be lower, which results in unimodal FMDF distribution. It was generally found that unimodal distributions were observed at all locations in the flow at $y/D_f = 7$ for S=1.07 for all filter sizes $\Delta/\lambda_\beta >> 1$. This is also consistent with Wang & Tong(2005) where it was pointed out that the conditional FMDF

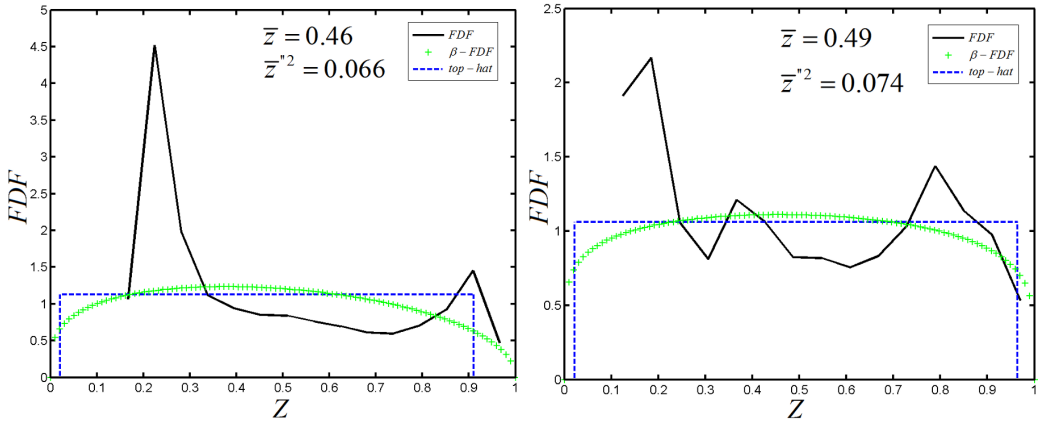

Figure 5.8: Measured FMDF computed from instantaneous realizations for filter size of Δ/λ_β =1.5; $\beta-$FDF and top−hat FDF are also shown, which are calculated from measured resolved mean and measured SGS scalar variance, computed from the same filter.

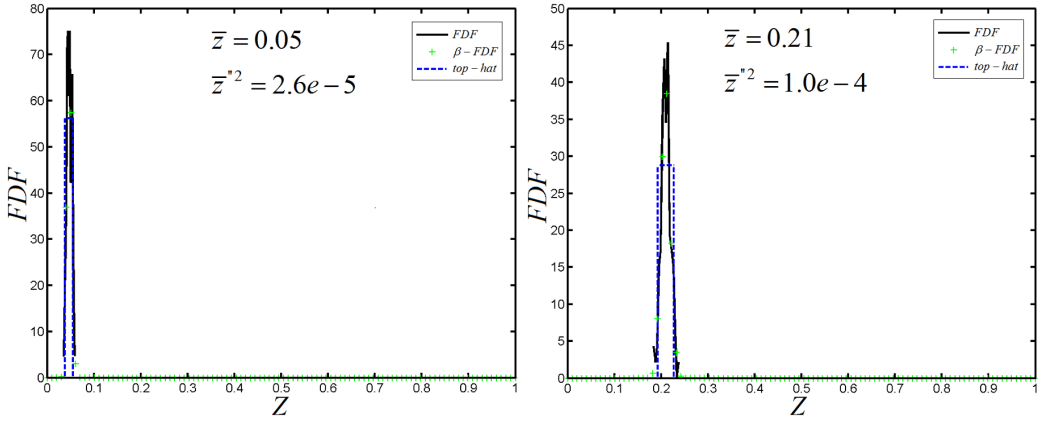

Figure 5.9: An example of measured FMDFs from two different spatial locations for large filter sizes and well-mixed regime at $y/D_f = 7$ for S=0.58; $\beta-$FDF and top−hat FDF are shown as green dashed and blue dashed lines respectively. The $\beta-$FDF and top−hat FDF coincide becoming delta functions and almost not distinguishable. The filter size is $\Delta/\lambda_\beta = 4$.

was found to be unimodal, and not far from Gaussian, when the SGS variance was small.

It is also necessary to examine the convergence of the FMDF being computed from the larger number of samples, because previously mentioned FMDFs were computed from a single box filter only. The measured FMDF was computed by using the same filter of 38×38 pixel 1.0(mm) from an instantaneous realisation from all spatial location within this realisation for $0.35 \leq \tilde{z} \leq 0.38$ and $\tilde{z}''^2 > 0.02$. Figure 5.10 show measured FMDF computed from single instantaneous realisation for the resolved mean in the range $0.35 \leq \tilde{z} \leq 0.38$ and for $\tilde{z}''^2 > 0.02$(left) and $\tilde{z}''^2 > 0.03$(right). The FMDF on the left and right were computed from different instantaneous realisations from 101080 (left) and 40432 (right) samples from all positions in the instantaneous mixture fraction field. The figures confirm that the FMDF computed from large variance demonstrate bimodal distribution regardless of a number of samples.

The SGS scalar variance[6] is the key parameter and is the measure of the level of mixing

[6]If a random variable X has the mean $\mu = E[X]$ then the variance is given by $Var(X) =$

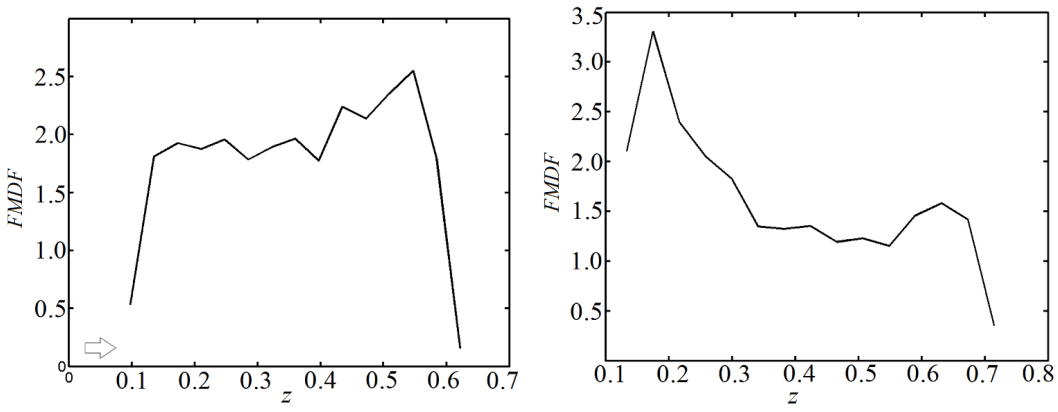

Figure 5.10: Measured FMDF computed from single instantaneous realisation for the resolved mean in the range $0.35 \leq \bar{z} \leq 0.38$ and for $\bar{z}''^2 > 0.02$ (left) and $\bar{z}''^2 > 0.03$ (right) for the filter size of 1.0(mm), $\Delta/\lambda_\beta \approx 3.3$. The FMDF on the left and right were computed from different instantaneous realisations from 101080 (left) and 40432 (right) samples from all positions in the instantaneous mixture fraction field. Scales in each figure are not the same.

within one LES cell. It is convenient to relate the measured SGS scalar variance to specific positions in the flow or to operating conditions by considering the probability density function of the SGS scalar variance fluctuations. Probability density mass function of the SGS scalar variance is reported here, as an example, for one position in the flow (window 3 of Figure 5.3). The p.d.f. of SGS scalar variance is computed as follows:

$$P_{\bar{Z}''^2} = \frac{\ln\left(\bar{z}''^2\right) - \overline{\ln\left(\bar{z}''^2\right)}}{\sigma_{\ln\left(\bar{z}''^2\right)}} \tag{5.8}$$

A box filter of given size, e.g. 1.0(mm) is fixed at a specific position in the flow and the SGS scalar variance is computed from the filter for each instantaneous realisations. The SGS p.d.f. is then computed from time series of the SGS scalar variance. In this work, 1500 instantaneous realisations were used to compute the SGS p.d.f. The SGS p.d.f. convergence was also checked and found that the p.d.f. of the SGS scalar variance converged even for 1000 realisations.

The measured p.d.f. of the SGS scalar variance computed from 1500 realisations for window 3 at $y/D_f = 5 - 7$ for a fixed filter size of 1.0(mm) and different swirl numbers is shown in Figure 5.11. The vertical lines denote threshold positions where $\bar{z}''^2$ =0.02 for different swirl number. The first observation provides a quick estimate of probability of having a bimodal distribution at a specific position in the flow and specific operating conditions. As expected, the probability of having bimodal FMDF distribution shifted to very low values for higher swirl numbers of 0.58 and 1.07, which indicated that the distribution is generally unimodal. Note that the p.d.f. of the SGS scalar variance was

$E\left[(X-\mu)^2\right]$. Similarly, the SGS variance can be written as $\bar{\phi}''^2_{(x)} = \int \left\{\phi_{(x)} - \bar{\phi}_{(x)}\right\}^2 G(x - x')dx$. It is convenient to rewrite the SGS variance as $\bar{\phi}''^2_{(x)} = \int \left\{\phi_{(x)} - \bar{\phi}_{(x)}\right\}^2 G(x - x')dx = \int \left[\left(\phi_{(x)}\right)^2 - 2\left(\phi_{(x)}\bar{\phi}_{(x)}\right) + \left(\bar{\phi}_{(x)}\right)^2\right] G(x - x')dx$. After some manipulations $\int \left(\phi_{(x)}\right)^2 G(x - x')dx - 2\bar{\phi}_{(x)} \int \phi_{(x)} G(x - x')dx + \bar{\phi}^2_{(x)} \int G(x - x')dx$, and by taken into account that filter is normalized i.e. $\int G(x - x')dx = 1$ it yields to $\int \left(\phi_{(x)}\right)^2 G(x - x')dx - 2\bar{\phi}^2_{(x)} + \bar{\phi}^2_{(x)} = \int \left(\phi_{(x)}\right)^2 G(x - x')dx - \bar{\phi}^2_{(x)}$

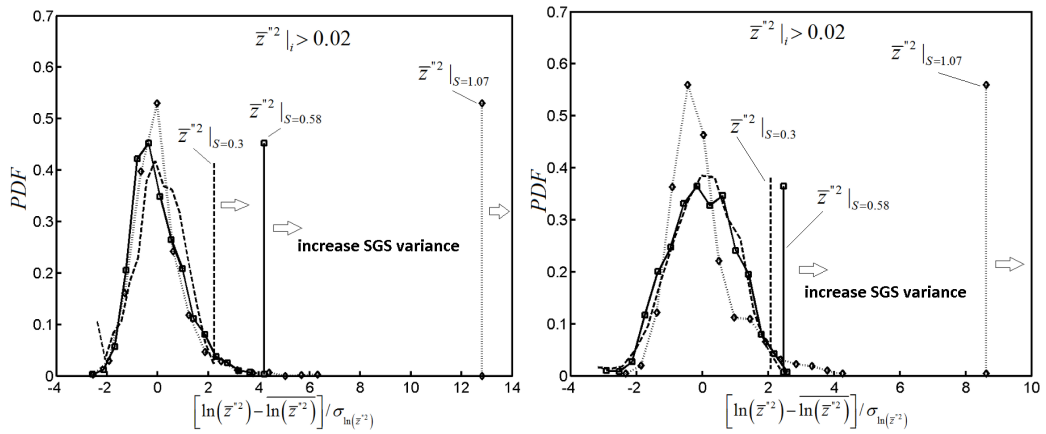

Figure 5.11: The measured p.d.f. of the SGS scalar variance computed from 1500 realisation from window 3 at $y/D_f = 7$ (left) and the same window at $y/D_f = 5$ (right) for a fixed filter size of 1.0(mm) and different swirl numbers. The vertical lines denote threshold positions for different swirl number where $\bar{z}''^2$ =0.02 and arrows indicate increase in the SGS variance.

close to a log-normal distribution, because, by definition, the log-normal distribution is the distribution of a random variable whose logarithm is normally distributed.

The last comment is on the integration errors between the temperature computed by integration of the laminar flamelet solution with the presumed FDF and with the measured FMDF. In this work, for simplicity and for the sake of brevity, the dependent variable was chosen to be the temperature obtained from the laminar flamelet solution. We point out that the resolved temperature was computed only for realisation with high SGS scalar variance $\bar{z}''^2$ >0.02, i.e. only when bimodal FMDF distribution was observed. The majority of the integration errors from several realisations seemed to be below 1% and a direct correlation between the shape of the presumed $\beta-$FDF and the associated integration error was not found. The weakest correlation between the temperatures computed by the presumed FDF and the measured FMDF suggests that the SGS scalar variance models and not the presumed $\beta-$FDF are perhaps the main source of error in the LES simulations that are based on presumed FDF methods. This is also consistent with Floyd *et al.*(2009) and Cook & Riley (1994).

In addition, several integrations of the laminar flamelet solution with the measured FMDF, the $\beta-$FDF and the top−hat FDF are shown in a table form. Table 5.1 summarizes several numerical cases for both large and small SGS scalar variances fro different filter. It is seen that there is no direct correlation between the integration of the laminar flamelet solution based on the measured FMDF or the presumed FDF, except that of top−hat functions, if the 'true' SGS scalar variance is used in the presumed filtered density functions.

Last final remark is on the SGS scalar variance and its relation to the box filter size. Figure 5.12 presents the measured 'true' SGS scalar variance as a function of box filter sizes normalized to the Batchelor length scale of 300(μm). Two extreme cases were studied, well−mixed regime i.e. $y/D_f = 7$ for $S = 1.07$ and highly segregated flow field i.e. at $y/D_f = 1$ for $S = 0.3$. The SGS scalar variance was computed from three windows 1−3 from a single instantaneous realisation and was normalized by the corresponding maximum

value. A highly non−linear dependence is observed and is dependant on the degree of mixing and spatial locations in the flow. For example, if the flow is highly homogeneous then there is no SGS scalar variance dependence on the box filter size up to $\Delta/\lambda_\beta \approx 6$. It should be noted that the SGS scalar variance would be different for different realisations and hence no direct conclusions are made here except that the SGS dependence on the box filter size is highly non−linear.

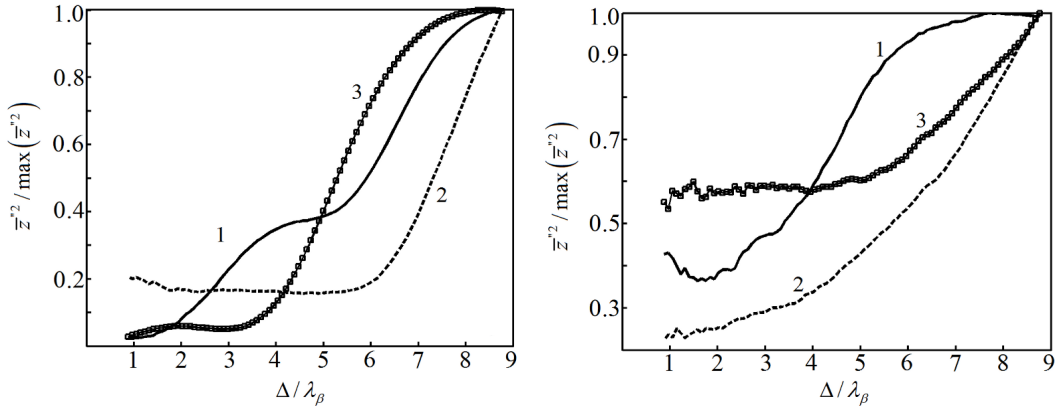

Figure 5.12: SGS scalar variance as a function of box filter size computed from single realisation for windows 1-3 at $y/D_f = 7$ for S=1.07 (left) and at $y/D_f = 1$ for $S = 0.3$ (right). Lines 1,2 and 3 were computed from windows 1,2 and 3 correspondingly. Box filter size was normalized to Batchelor scale of 300(μm).

Table 5.1: Resolved mean temperature obtained by integration of the laminar flamelet solution with measured FMDF, presumed $\beta-$FDF and the presumed top−hat FDF. Large and small SGS scalar variance were considered. The associated temperature errors were computed. Large and small SGS variance was obtained from filter sizes in the range of $1.5 < \Delta/\lambda_\beta < 4$

$\bar{z}$	$\bar{z}''^2$	$\bar{T}_{f_z}$,K	$\bar{T}_\beta$,K	$\bar{T}_{\prod_l}$,K	Δ_β, %	$\Delta_{\prod_l}$,%
0.493	0.0741	993	978	807	1.510	18.731
0.465	0.0659	1017	1019	826	0.197	18.780
0.682	0.0299	654	687	668	5.046	2.141
0.584	0.0265	783	790	841	0.894	7.407
0.430	0.0112	989	1040	1003	5.157	1.415
0.507	2.3e−3	852	863	862	1.290	1.174
0.171	1.2e−3	1594	1611	1604	1.066	0.627
0.440	1.2e−3	956	966	961	1.046	1.046
0.514	8.8e−4	842	851	845	1.069	0.356
0.210	1e−4	1471	1486	1472	1.020	0.021
0.047	2.6e−5	1816	1837	1802	1.156	0.771

5.3 Assessment of SGS scalar variance models

In flamelet combustion models, the combustion temperature, species mass fractions etc. can be computed as a function of resolved mean mixture fraction, mixture fraction 'subgird' scale scalar variance and scalar dissipation rate by integrating the flamelet solution (Eq.

5.3). The SGS scalar variance is used in computation of presumed filtered density functions of the mixture fraction and hence modelling is necessary. The transport equation for the SGS scalar variance can in principle be also solved during LES simulation. However, the equation contains the triple velocity−scalar correlation terms, which also need to be modelled (Chumakov, 2005). In addition, the SGS scalar variance transport equation, which is regarded as the most accurate in prediction of the SGS scalar variance can in some cases result in non realistic solution. Kaul et al. (2009) showed that the variance transport equation tended to underpredict the SGS scalar variance due to numerical errors. The numerical errors can be related to numerical approximations of the SGS scalar transport equations.

The scalar dissipation rate is usually modelled proportionally to the SGS scalar variance. Cabra et al. (2005) and Domingo et al. (2008) pointed out that LES solution was sensitive to the modelling of the scalar dissipation rate and therefore an accurate prediction of the SGS scalar variance is paramount. The importance of the SGS scalar variance can be illustrated by the following formula, where resolved species mass fractions are computed by direct integration of the laminar flamelet solution $Y_k\left(z,\chi_{st}\right)$ with the presumed FDF $P\left(\bar{z},\bar{z}''^2\right)$.

$$Y\left(\bar{z},\bar{z}''^2,\bar{\chi}_{st}\right)=\int_0^1 Y_k\left(z,\chi_{st}\right)P\left(\bar{z},\bar{z}''^2\right)dz \tag{5.9}$$

There are mainly two different models that can be used to compute the SGS scalar variance. The first approach is based on a gradient assumption Pierce & Moin (1998) and is used in many commercial CFD codes. According to this model, the SGS scalar variance $\bar{z}''^2$ is directly related to the gradient of the resolved scalar field $\nabla\bar{z}$ via a modelling constant C_z and the filter width Δ as follows:

$$\bar{z}''^2=C_z\Delta^2\left|\nabla\bar{z}\right|^2 \tag{5.10}$$

The second approach is based on the fact of similarity between large and small scales. The relationship between large and small scales is often approximated by an assumption of so called self−similarity. Self−similarity is the property that is found in fractal−like structures, where smaller parts are identical (or approximately identical) to the larger parts. Models that are based on this assumption are called self−similarity models and the SGS scalar variance can be computed from the larger scales by applying so called test−level filtering. The test filtering operation is applied to the resolved field and SGS scalar variance is computed according to the following formula, where $(\wedge)$ denotes a test filter, which is often taken to be two times larger than the LES filter. Similarity models for the SGS scalar variance were first proposed by Cook & Riley (1994).

$$\bar{z}''^2=C_{ss}\left(\bar{z}^{\wedge}\cdot\bar{z}-\hat{\bar{z}}\cdot\hat{\bar{z}}\right) \tag{5.11}$$

The scalar similarity coefficient can be prescribed or defined by using a dynamic procedure, which requires another test filter that must be larger than the test filter used in the model. However, the assumption of self−similarity is not correct for arbitrary LES filters. Carati & Eijnde (1997) pointed out that both the base filter (LES filter) and the

test filter had to be similar. This means that if for instance a box filter is used in the LES simulation, the test filter must be also a box filter. The similarity concept and the similarity assumption model have been evaluated both numerically and experimentally, e.g. in the work of Liu et al. (1994). It was generally found that the scale similarity model performed better than the gradient assumption model.

In this work, a comparison of these two models with experimental data was performed. A priory test was used to validate both the scalar similarity concept and the gradient assumption model. A priory test uses well resolved turbulent field from either experiments or from DNS data to compare with modelled predictions. This approach was first introduced by Clark et al. (1979), and used by many others Piomelli et al. (1988), Domaradski et al. (1993) etc. In this work, a priory test uses experimental data from the PLIF experiments in non−reacting turbulent swirling isothermal flows. The main reason for this attempt is that previous model validations mentioned in literature, were done using either DNS data or experiments, where experimental data was obtained from turbulent non−swirling flows. In this work, however, the experimental data from swirling jets is used. An evaluation of the models was done by direct comparison with the SGS scalar variance, obtained from the experimental data, and the models output.

The instantaneous mixture fraction field was spatially averaged by using a box filter of different size (normally 0.3 and 1.0 mm) and the resolved mean values were used to compute the SGS scalar variance by two different models. First a gradient assumption was tested and the SGS variance from model predictions and the experiment was plotted. The scalar similarity approach was tested by using a test filter, which was 2 times larger than the base filter. The smaller filter $\Delta/\lambda_\beta \approx 1$ was used in order to test an assumption that the LES approach would provide better SGS scalar variance agreement with experimental data when filter resolves small turbulent length scales.

Figures 5.13−5.14 show scatter plots of the SGS variance, obtained from a single instantaneous image at various axial positions, for $S = 0.3$ and $S = 0.58$ from experimental data and two different models predictions (filter size is $\Delta/\lambda_\beta \approx 1$). The red straight line is a linear relationship between the experimental and the modelled SGS scalar variance. As it was expected, the model predictions were perfect correlated with the experimental data because the smallest turbulence length scale was resolved $\Delta/\lambda_\beta \approx 1$. A perfect linear correlation between the gradient assumption model and the experimental data was observed. However, when swirl number increased the scatter plot tended to broaden out. This could be related to smaller local Batchelor scale.

On the other hand the scale similarity model appears to overestimate or underestimate (depending on the model constant) the variance when compared with the experimental data (Figure 5.14) even when smallest filter was used. This different behaviour indicates that a dynamic procedure should be used to determine the model constant. In addition to the computational cost due to additional filtering procedure, the scale similarity model seems to lead to worse estimation of the SGS scalar variance. If a dynamic procedure is used and the model constant is adjusted at each time, the discrepancy between the measured SGS scalar variance and the modelled predictions, can still be large. Similar conclusion regarding scale similarity model was made in work of Jimenez et al. (2001). Jimenez used DNS data to compute the SGS scalar variance and the dissipation of a scalar

field. The SGS scalar variance, computed from the DNS was compared with the values that were predicted by the scale similarity model. It was also concluded that the scale similarity model underpredicts or in some cases overpredicts the DNS data.

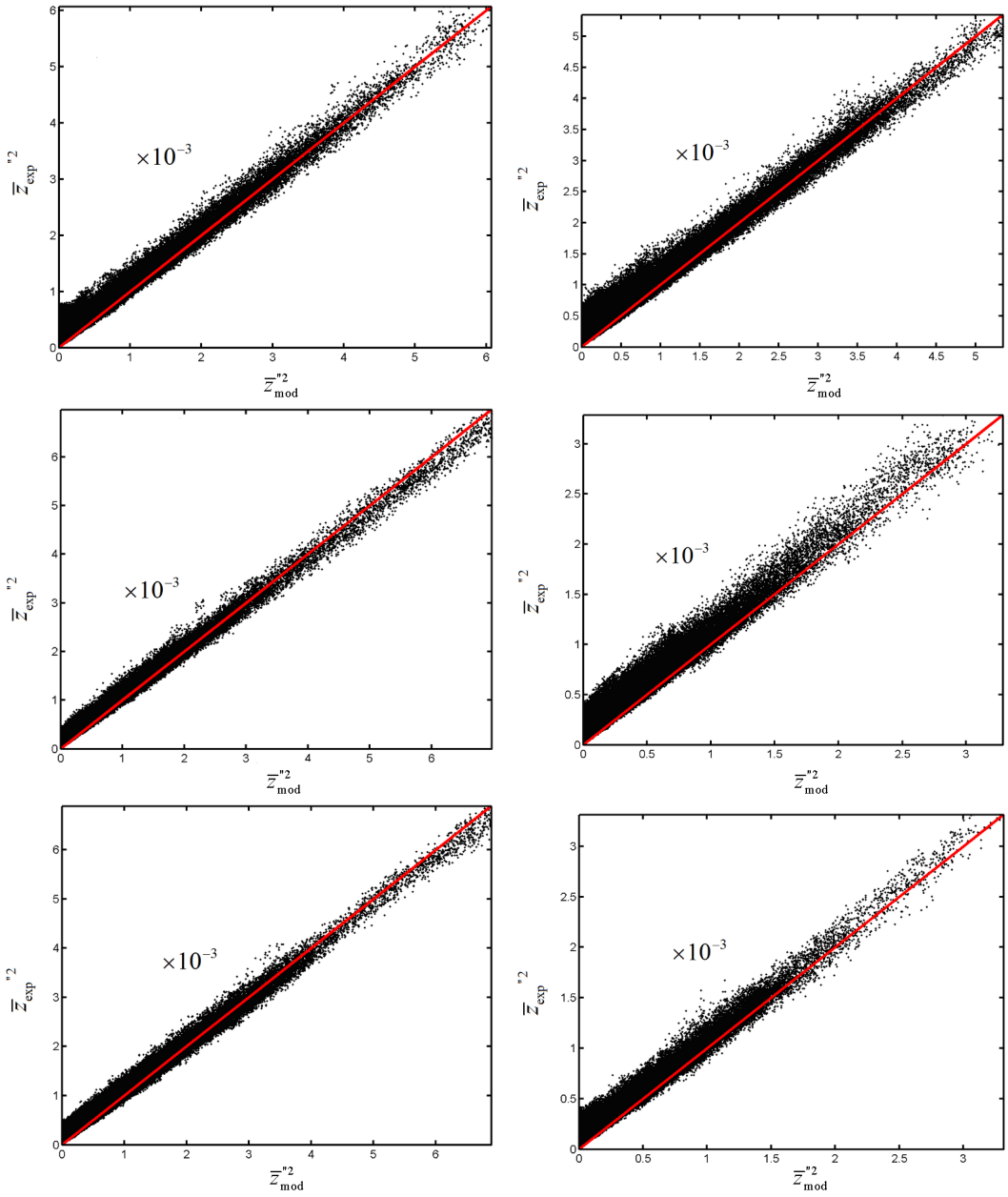

Figure 5.13: Scatter plots of the SGS variance computed from several instantaneous images and from the gradient assumption model output for box filter of 0.3 (mm), S=0.3 (left) and S=0.58 (right). Model constant is 0.09. Note that the scatter plots of the SGS scalar variance were obtained from the entire instantaneous image and not from the specific image area. Plotting range along x and $y-$axis is equal but not the same in each image. Straight red line represents a linear relationship between the experimentally obtained SGS variance and the model output.

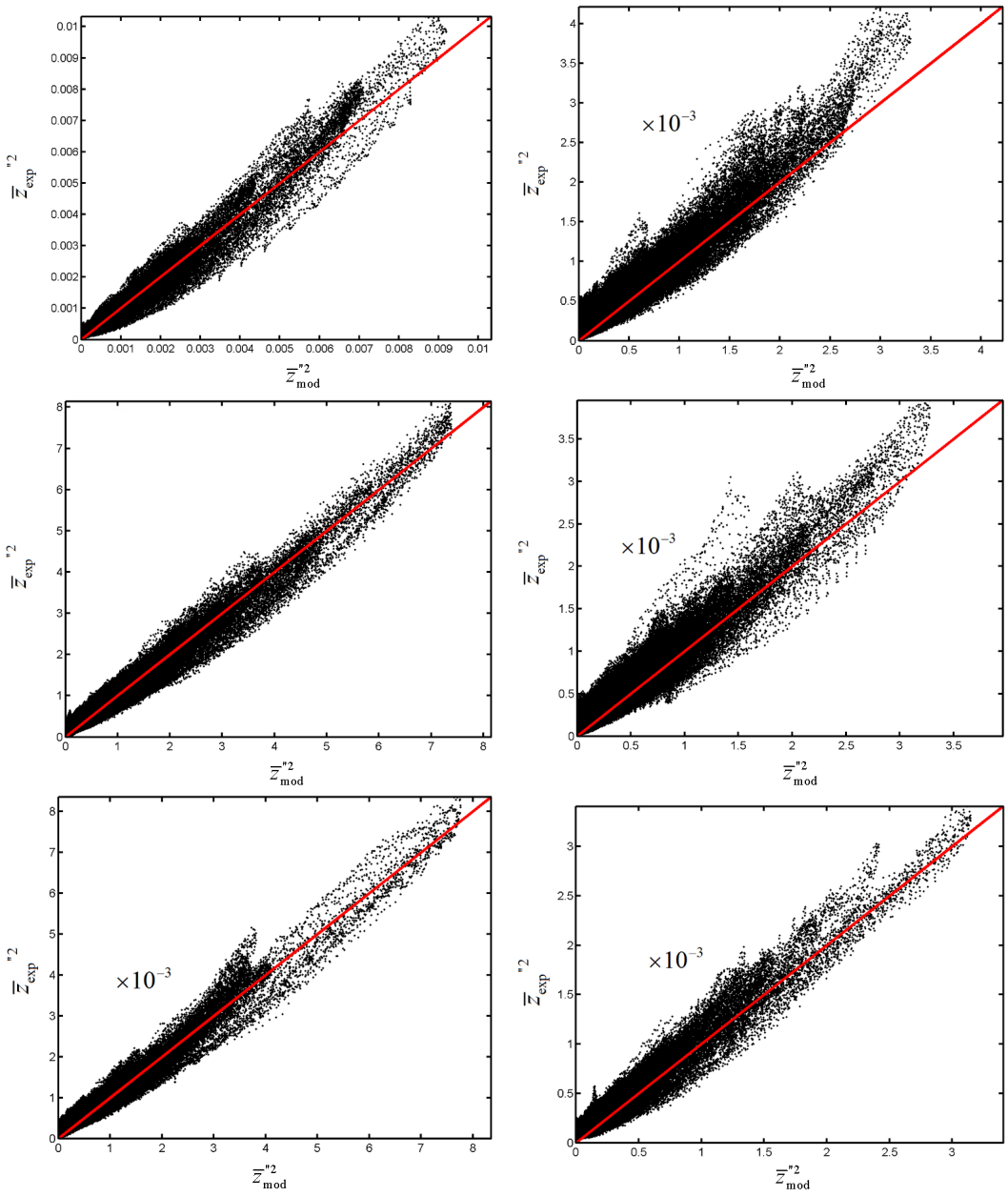

Figure 5.14: Scatter plots of the SGS variance computed from several instantaneous images and scale similarity model output for box filter of 0.3 (mm), S=0.3 (left) and S=0.58 (right). Note that model constant was changed to 0.12. Also, the scatter plots of the SGS scalar variance were obtained from the entire instantaneous image and not from the specific image area. Plotting range along x and $y-$axis is equal but not the same in each image. Straight red line represents a linear relationship between the experimentally obtained SGS variance and the model output. Finger$-$like structures that are observed in the figure, come form different spatial locations in the flow.

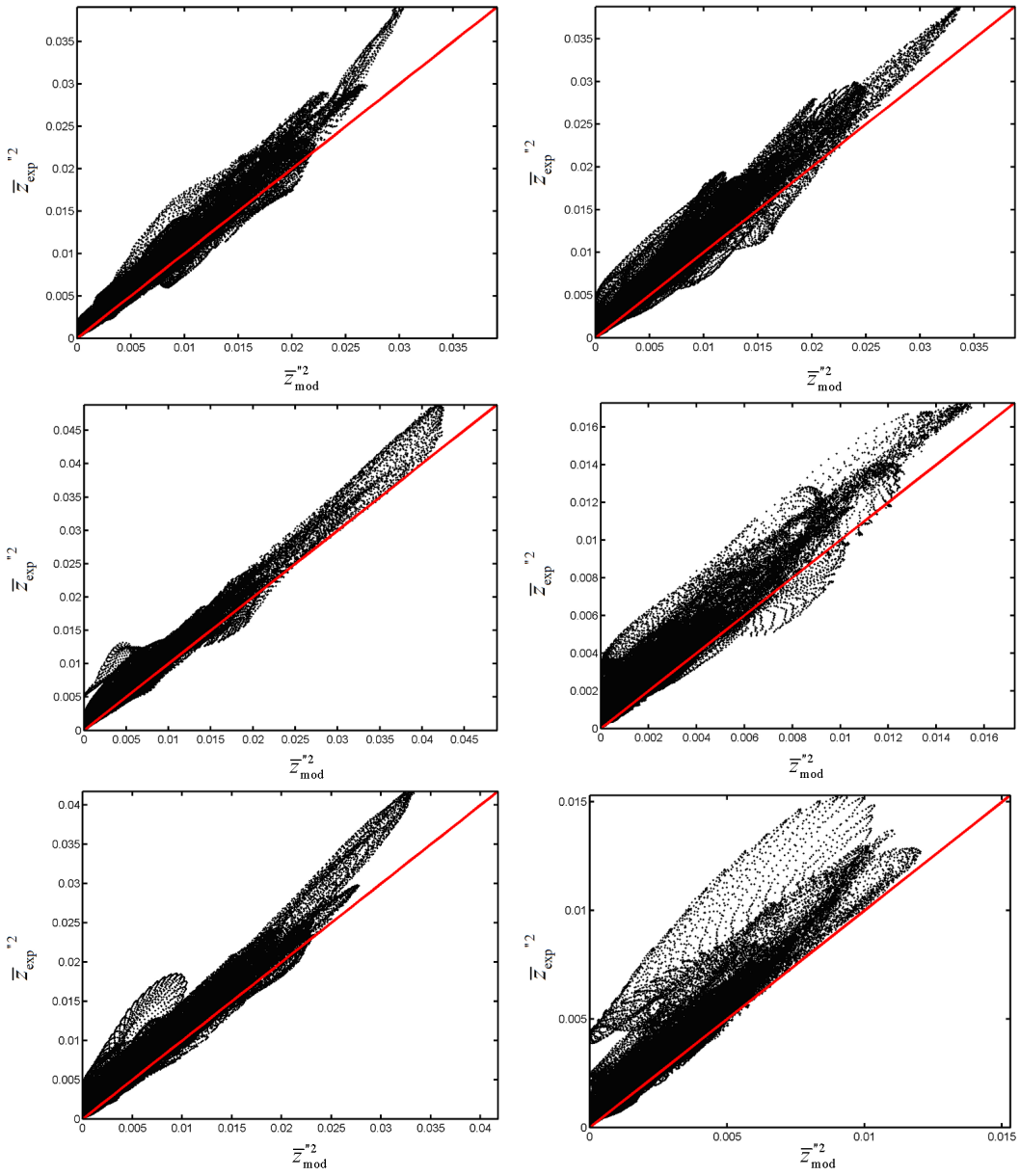

Figure 5.15: Scatter plots of the SGS scalar variance computed from several instantaneous images and from the gradient assumption model output for box filter of 1.0(mm), S=0.3 (left) and S=0.58 (right). Model constant is 0.09. Note that the scatter plots of the SGS scalar variance were obtained from the entire instantaneous image and not from the specific image area. Plotting range along x and $y-$axis is equal but not the same in each image. Straight red line represents a linear relationship between the experimentally obtained SGS variance and the model output. Finger$-$like structures that are observed in the figure, come form different spatial locations in the flow.

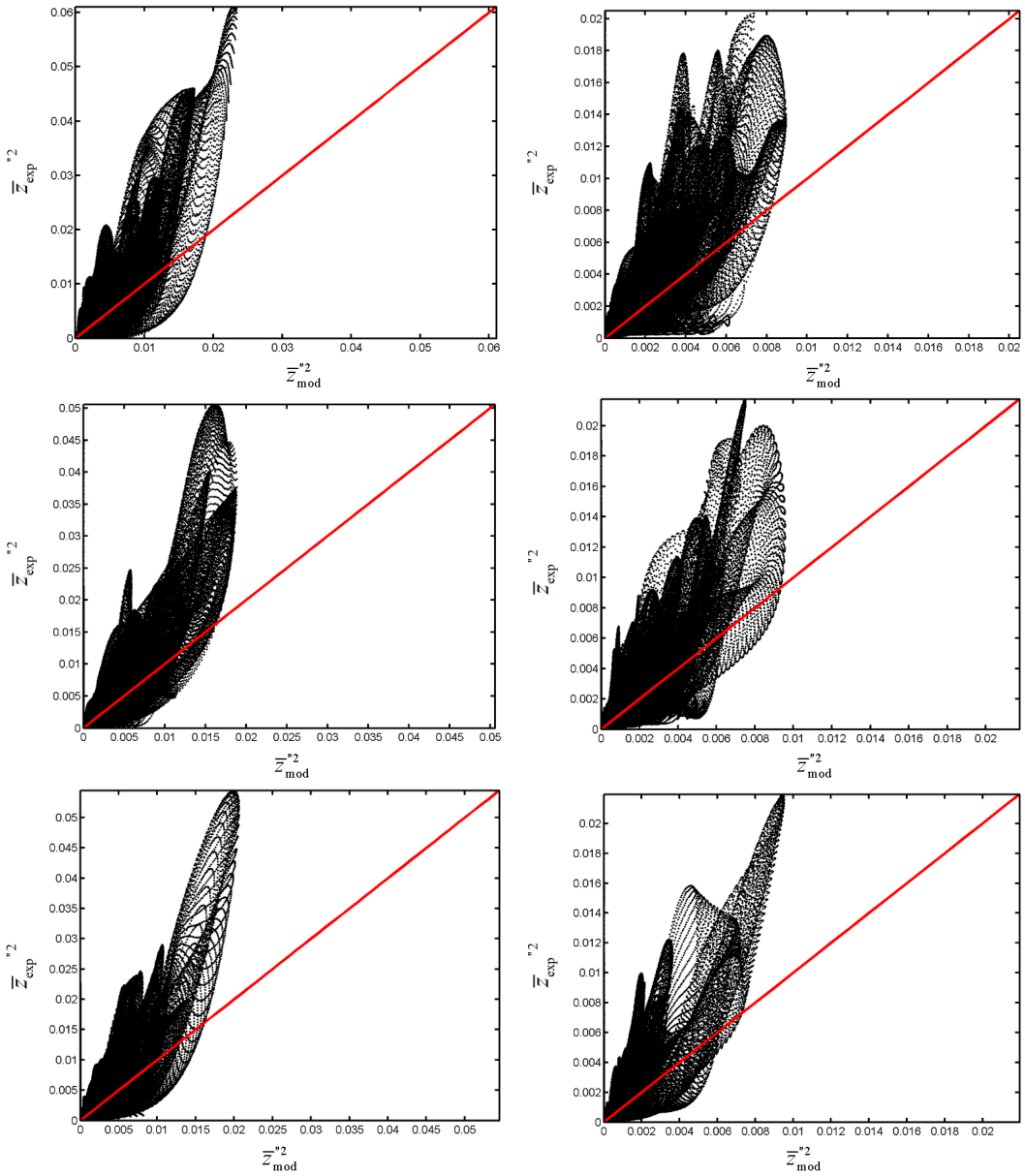

Figure 5.16: Scatter plots of the SGS scalar variance computed from several instantaneous images and from the scale similarity model output for box filter of 1.0(mm), S=0.3 (left) and S=0.58 (right). Model constant is 0.09. Note that the scatter plots of the SGS scalar variance were obtained from the entire instantaneous image and not from the specific image area. Plotting range along x and $y-$axis is equal but not the same in each image. Straight red line represents a linear relationship between the experimentally obtained SGS variance and the model output. Finger−like structures that are observed in the figure, come form different spatial locations in the flow.

The preliminary observations based on different box filter sizes suggest that additional factors may affect the validity of the models. For example it is hard to relate the size of the digital box filters used in this work to the real LES filter size. It is generally observed that the larger filter size affects both the distribution of the SGS scalar variance (SGS deviates from the linear model−experiment relationship) and its magnitude. The SGS scalar variance increases with increase of the box filter size. However, the box filter, which is used in this work, can be related to the smallest dissipative scales, which is easy to determine in most cases. In both cases, the two models are highly dependant on the model coefficients that must be specified by prior calculations or calculated by using the dynamic procedure. However, when the gradient assumption model is employed and when the LES filter size is sufficiently small $\Delta/\lambda_\beta \approx 1$ the gradient assumption model may be used with a single initially prescribed constant without performing the dynamic procedure. On the other hand, when $\Delta/\lambda_\beta \approx 1$ the LES becomes equivalent to DNS and all the LES advantages vanish.

The modelling constant, which was found to be 0.09 for a certain filter to integral scale[7] ratio l/Δ_x=170 can be used without the need of employing Germano identity that in turn can speed up LES calculations, because no additional test filtering is used. Germano with co−workers (1991) studied the concept of the scale similarity and the validity of dynamic approach in determination of the scale similarity constant using filtered DNS data. They found that the scale similarity constant was dependant on the size of LES grid, i.e. the degree of resolution of large eddies. Due to lack of comparable experimental data, especially in swirling turbulent flows a rough comparison was made with Cook (1997) by using the test filter two times larger than the box filter $\hat{\Delta}/\Delta_x$. The constant was shown to depend on the size of the sampling filter, i.e. the test filter, the turbulent Reynolds number and the degree of resolution of the large eddies. In the present work the model constant was found to be independent of swirl number and was 0.6 and 0.5 for l/Δ_x. Cook[8] (1997) presented modelling constants of 0.64 and 0.54 for the same integral scale to box filter width ratio.

The last comment concerning the SGS scalar variance is related to the effect of the filter size on the SGS scalar variance model predictions. The box filter size or more precisely the turbulent resolution length scale directly affects both the magnitude and the distribution of the SGS scalar variance, which is demonstrated in Figures 5.15−5.16. A quick observation confirms that the gradient assumption model performs better in case of smaller filter size because a linear relationship between the experimentally measured SGS scalar variance and the model output is maintained. However, the discrepancy between the experimental data and the model predictions becomes larger and this discrepancy increases with swirl number. However, the modelling constant does not remain unchanged for the larger box filters (Figure 5.15). It should be noted that this modelling constant was initially prescribed by employing a trial−and−error procedure and should not be regarded as a universal constant for a given filter width to turbulence scale ratio. It was generally observed that the higher the swirl number the higher the discrepancy between the measured SGS scalar variance and the gradient assumption model output was.

[7] The integral length scale was assumed to be the diameter of the burner (50.8mm).

[8] A. W. Cook. Determination of the constant coefficient in scale similarity models of turbulence, Phys. Fluids 9, 1485, 1997.

The scale similarity model generally demonstrates completely inadequate behaviour and non-linear relationship between the model predictions and the measured data, which is seen in Figure 5.16, where an initially prescribed modelling constant is used with the model. The modelling constant that was found to be 0.12 for filter size of 0.3(mm) was completely wrong for larger filter size of 1.0(mm). It is, therefore, suggested that in case of larger filter size and by using the scale similarity approach the modelling constant should be adjusted at each time step and determined by using the dynamic procedure. The discrepancy between the scale similarity model output and the measured SGS scalar variance is larger for larger filter size than in case of gradient assumption model for the same filter width.

5.4 Summary

This chapter focused on the computational models used to describe turbulence−chemistry interactions and in particular on laminar flamelet approach coupled with presumed filtered density functions methods. The presumed filtered density functions were chosen to be a $\beta-$FDF and a top−hat FDF, which were typically used in commercial CFD codes. Filtered mass density functions of the mixture fraction were obtained from instantaneous mixture fraction fields by applying a box filter of given size. Subgrid scale scalar variance was also studied in this chapter both experimentally and theoretically. The measured resolved SGS scalar variance and the resolved mean were used to parametrize the presumed FDF functions. The resolved mean was computed as a convolution of a box filter with measured non−resolved mixture fraction fields. Different spatial locations in the flow were also investigated. The measured FMDF and the presumed FDF were used to integrate the laminar opposed−flow diffusion flamelet solution and a relative integration error was computed.

The conserved scalar measured FMDF demonstrated two clear visible regimes, which were denoted as homogeneous and non−homogeneous. In homogeneous regime, the FMDFs had clear visible unimodal distribution with single mode. This was due to the fact that the scalar distribution within a box filter was nearly homogeneous. In homogeneous regime, the SGS scalar variance was found to be small, which was consistent with Tong et al. (2007). In addition, it was found that for $\Delta/\lambda_\beta = 1$ the corresponding FMDFs were unimodal.

For larger SGS scalar variance (for filter sizes $\Delta/\lambda_\beta > 1.5$)the FMDF demonstrated bimodal distribution. It was also pointed out that the measured FMDF could not be linked to any spatial position in the flow or operating conditions because the FMDF computed from a single instantaneous realization. For the same spatial position and the same filter width, the shape of the FMDF will be different for different realizations and, therefore, it is convenient to relate both the FMDF and the FDF to a single parameter only. The single parameter in this context was the SGS scalar variance. It was also demonstrated that bimodal distribution of the measured FMDF did not automatically introduce errors when integrating the laminar flamelet data and was compared with $\beta-$FDF. As it was known, the $\beta-$FDF was unable to represent a bimodal distribution and hence it was initially supposed that this bimodality would introduce errors in the integrated laminar

flamelet solution. However, integration errors between the flamelet solution integrated with measured bimodal FMDF and the corresponding unimodal $\beta-$FDF, were not found.

Subgrid scale scalar variance was measured for different filter sizes and swirl numbers. A direct comparison between the measured SGS scalar variance and the modelled one was made. Two SGS variance models were chosen, i.e. a gradient assumption model and a scale similarity approach, for their simplicity and common use in commercial CFD codes. The discrepancy between the measured SGS scalar variance and the model outputs were negligible with filter width close to Batchelor scale for both gradient assumption and scale similarity models, as it was expected. For larger filter size the gradient assumption model performed better than the scale similarity model for a constant modelling constant. Based on the fact that the bimodal FMDFs and the corresponding presumed FDF were not correlated in terms of associated flamelet solution integration errors, it has been therefore suggested that the actual source of error in turbulence$-$chemistry interaction could possibly be found in the subgrid scale models and not in presumed FDF methods.

6 Combustion and temperature statistics in swirl stabilised flames

The science of today is the technology of tomorrow.

Edward Teller

The chapter presents the characteristics of the temperature field produced by the swirl stabilized burner. The main goal of this chapter is to fulfil the gap in understanding the characteristics and properties of swirling reacting flows. Temperature, power spectral density of temperature fluctuations, probability density functions of the temperature fluctuations and thermal dissipation rate measurements in a non−premixed turbulent swirling jet flame are reported in this chapter. Rayleigh scattering measurement technique was used to obtain the temperature fields as inverse of the Rayleigh signal that was recorded by the CCD camera. The Reynolds numbers for air and fuel streams were 28662 and 2134 correspondingly. The measurements were reported within non−dimensional radial and axial coordinates. Radial coordinates x/R were dimensionalised by the burner radius R and the axial centreline positions y/D_f were dimensionalised by the fuel pipe diameter $D_f = 15$(mm). The temperature measurements were carried out in the region extending up to 10 fuel nozzle diameters at 1, 3, 5, 7 and 10 correspondingly.

Mixture fraction fields usually provide all the required information and hence the measurements in non−reacting flows are highly important. On the other hand, the measurements in reacting flows may not be regarded as important as the mixture fraction measurements. However, it can be argued that the temperature measurements and especially temperature higher statistics do provide important information about underlying mixture fraction structure as well as about the underlying process. It has been argued that the length scales of temperature and the mixture fraction dissipation structures are similar[1] (Wang *et al.*, 2007).

However, it is expected that temperature gradients modify the flow structure and impact on the flow field (the temperature is not passive scalar). It is also expected that the thermal dissipation rate is several times larger than the corresponding scalar dissipation rate computed from non−reacting field. It is also expected that the power spectral density of temperature fluctuations computed from reacting and the spectra from mixture fraction fluctuations computed from non−reacting flows are quite different. Higher temperature should increase the dumping effects of turbulence due to higher viscosity and must be analysed in detail.

This chapter is organized in several sections. The first section outlines the temperature calibration and technique validation, which was performed on a flat flame burner, while

[1] G. Wang *et al.* Combustion and Flame 148, pp.62−75, 2007.

the following subsequent sections consider the swirl stabilized burner.

6.1 Temperature calibration

Flat flames stabilized on a porous material have spatially and temporally uniform temperature distribution, which are valuable tools for calibration of temperature. The most popular laminar flat flame burner is probably the McKenna burner[2]. The flame holder of this burner is typically manufactured from a sintered porous material and water cooling is provided to protect from elevated temperature. The flame of this burner is attached to or stabilizes on the flame holder. The flame stabilization is dependent of the velocity of fresh mixture. The low velocity (low flow rates) causes the flame to stabilize on the surface of the flame holder and significant heat losses are expected due to conduction via the flame holder, which in turn lowers the flame temperature. The deviation of the measured flame temperature from the adiabatic flame temperature can be quite significant. Higher flow rate leads to higher velocity, which in turn can lead to rapid blow−off.

Additional complexity arises from the fact that the porous material of the flame holder must be clean to be able to provide spatially uniform temperature. In addition, a precise control of the mass flow rate through the flat flame burner is often needed. However, even with these practical constrains the flat flame burner remains popular tool for temperature calibration within combustion community. In this work, the flat flame burner, based on McKenna design was used as a tool for temperature calibration and verification of Rayleigh thermometry. The burner, which is seen in Figure 6.1[3] was used without cooling to minimize heat losses to the flame holder. The additional requirement was a quick installation and removal from the swirl−stabilized test rig. The burner consisted of a porous stainless steel plate of 60(mm) diameter and a water cooled ring below it. The burner could be operated with an annular shielded coflow. The flame holder and coflow were separated from each other by a concentric ring. However, this option was not used due to objective reasons. The flow of $25\%H_2$ + $75\%N_2$ and air were controlled by volumetric flow meters with maximum flow rates of 50, 44 and 100 (l/min). The flows of hydrogen, nitrogen and air were combined via a standard cross union and mixed in a flexible long hose before being supplied to the McKenna burner. For the measured temperatures and the corresponding stoichiometries the corresponding adiabatic flame temperature was computed by using perfect stirred reactor model (PSR) and commercial software CHEMKIN®. Measurements were performed with the same CCD camera and laser power setting as later for the swirl−stabilized burner in the central region of the flame holder. Since no cooling was used, the burner was not allowed to run continuously more than 5−10 minutes.

Temperature measurements that were performed on the McKenna burner for the mixture of $25\%H_2$+$75\%N_2$ (by volume) by applying Rayleigh thermometry 10(mm) above the burner flame holder clearly indicated two combustion regimes. The first regime was found when the flow rate and hence the velocity of the mixture was low, which corresponded to

[2]McKenna Burner Flat Flame Burner, Holthuis & Associates, P.O. Box 1531, Sebastopol, CA 95473 U.S.A., http://www.flatflame.com.

[3]Picture of the burner was taken from 'A flat flame burner as calibration source for combustion research. Temperatures and species concentrations of premixed H_2/air flames. S.Prucker, W.Meier and W.Stricker, Rev. Sci. Instrum. 85(9), September 1994.'

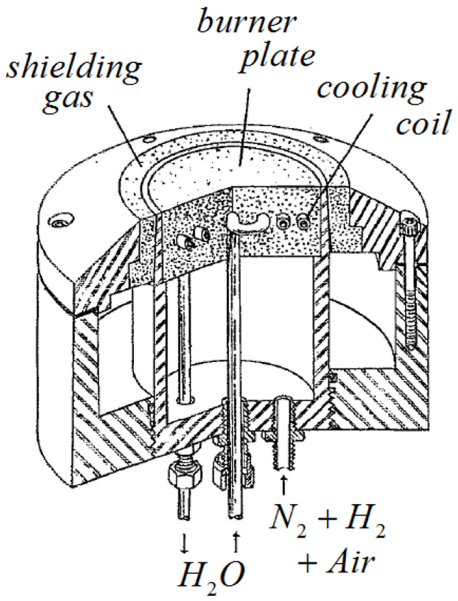

Figure 6.1: A cross−section view of the Mckenna burner. [Prucker *et al.*, 1994]

overall flow rate of fuel and air of 40(l/min), in which 7.5 (l/min) was hydrogen flow rate and 22.5 (l/min) nitrogen flow rate[4].

The thermal behaviour and hence the flame holder temperature was dependent on the flow rate and, therefore, flow velocity. At low flow velocity and low axial distance from the burner plate the flame was composed of individual narrow flames issuing from individual pores. The flame was attached to the flame holder resulting in significant heat losses to the porous plate. At high velocity the individual flames issuing from the pores broaden out interlacing with each other at lower axial distances from the burner head. The flame was also detached from the flame holder porous plate, which was indicated by almost ambient temperature measured by the thermocouple inside the flame holder. The flame holder temperature corresponding to low velocity was ≈353(K), while at high velocity case was slightly above the ambient temperature of 293(K).

The mean temperature was computed from 200 instantaneous realisations taken at 10(Hz) for two equivalence ratios of slightly lean Φ =0.9 and rich Φ =1.78 flames. The unsteady thermal behaviour of the McKenna burner was prevented by allowing the flame holder to heat up, which was monitored by the thermocouple (typically required less than 5 minutes). However, this thermal steady−state estimation was rough due to only one installed thermocouple in the centre of the burner. The radial temperature gradient could exist in unevenly heated burner flame holder. However, for calibration purposes, it was supposed to be unimportant, especially when the flame was detached and heat losses to the burner porous plate were minimized. Heat losses arise due to heat conduction between the flame holder and the flat flame as well as due to gas radiation.

Deviations from the adiabatic flame temperature for arbitrary chosen equivalence ratios were computed by using a detailed chemical mechanism GRI−3.0, which was included in commercial software CHEMKIN®. Figure 6.2 shows temporal history of temperature radial profile (T_{radial}), mean temperature (T_m) and the adiabatic flame temperature com-

[4]The definition of 'low' and 'high' velocity regimes is somehow arbitrary.

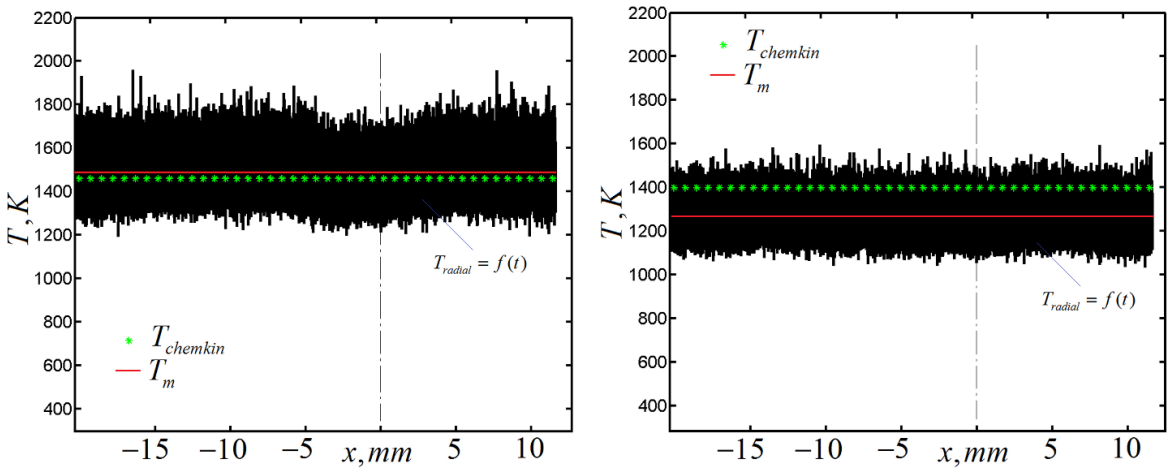

Figure 6.2: Temporal history of temperature radial profile (T_{radial}), mean temperature (T_m) and the adiabatic flame temperature computed from perfect stirred reactor model ($T_{chemkin}$) of the laminar flat flame produced by the McKenna burner at 10(mm) above the flame holder. Left picture corresponds to equivalence ratio Φ=0.9, velocity of 0.29 (m/s) and total flow rate of 50 (l/min) while right corresponds to Φ=1.78, velocity of 0.23(m/s) and total flow rate of 40(l/min). The difference between adiabatic flame temperature and the measured one is due to heat losses primary into the flame holder.

puted from perfect stirred reactor model ($T_{chemkin}$) of the laminar flat flame produced by the McKenna burner at 10(mm) above the flame holder. Temporal history of temperature radial profile was plotted from all 200 instantaneous realisations at the same axial distance from the burner holder 10(mm). The discrepancy between the measured temperature and the adiabatic flame temperature showed that a significant amount of heat was released to the burner porous plate, which was also indicated by an elevated temperature of the plate. With increasing flow rate, the distance between the flame holder and the flame reaction zone increases and the heat transfer is reduced, which is clearly seen in Figure 6.2. The temperature measurements were repeatedly performed at time intervals of three−four days during three weeks. The reproducibility was found to be satisfactory, which led to the conclusions that Rayleigh thermometry was adequately calibrated and provided acceptable accuracy. Figures 6.3−6.4 show results of repeated measurements with stoichiometric conditions $\Phi = 1.0$ performed on different days. The total flow rate ranged from 24 (l/min) to 60 (l/min), which corresponded to velocity of 0.14−0.35 (m/s). The burner generated quasi−adiabatic flame when flow rate increased, which lead to detached flame and higher flame temperature.

Noise from many sources can contribute to the measured light intensity in the Rayleigh scattering system, which leads to erroneous results. The fluctuations in the laser output power, drifting of electronic equipment, unwanted reflections from apparatus, dark noise, Mie scattered light from the dust particles, fluctuations in the equivalence ratio, deviation of Rayleigh scattering cross−section of the post flame species etc. are the most important sources of noise in the experimental data. In experiments, the contribution from the fluctuations of laser intensity can be kept at minimum by using long warm−up times (typically not less than 20 minutes was used in this work) and by monitoring the laser output energy. The Mie scattering from dust particles is somehow unavoidable, es-

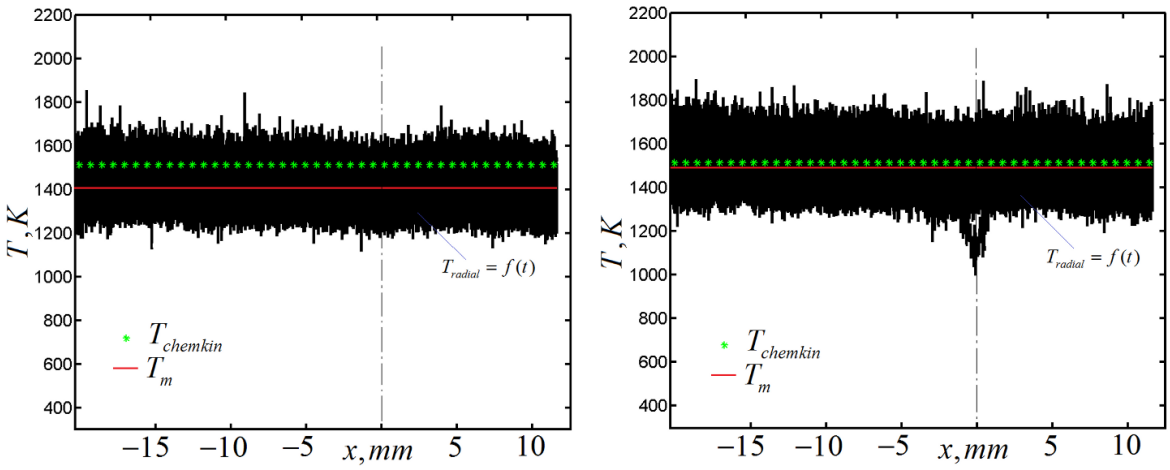

Figure 6.3: Temporal history of temperature radial profile (T_{radial}), mean temperature (T_m) and the adiabatic flame temperature computed from perfect stirred reactor model ($T_{chemkin}$) of the laminar flat flame produced by the McKenna burner at 10(mm) above the flame holder for stoichiometric mixture $\Phi = 1.0$. Left picture corresponds to fuel and air flow rates of 15 and 9 (l/min) with velocity of 0.14(m/s) based on the total mass flow rate. Right picture corresponds to fuel and air flow rates of 22.5 and 13.5 (l/min) with velocity of 0.21(m/s).

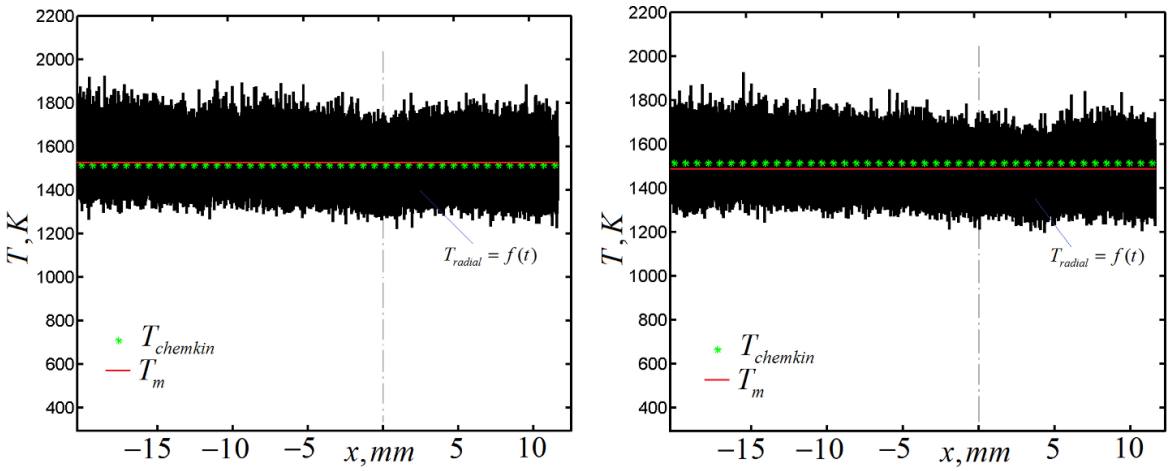

Figure 6.4: Temporal history of temperature radial profile (T_{radial}), mean temperature (T_m) and the adiabatic flame temperature computed from perfect stirred reactor model ($T_{chemkin}$) of the laminar flat flame produced by the McKenna burner at 10(mm) above the flame holder for stoichiometric mixture $\Phi = 1.0$. Left picture corresponds to fuel and air flow rates of 30 and 18 (l/min) with velocity of 0.28(m/s) based on the total mass flow rate. Right picture corresponds to fuel and air flow rates of 37.5 and 22.5 (l/min) with velocity of 0.35(m/s).

pecially in swirling flows, where ambient air entrainment is observed. A software filtering is possible and necessary to remove the Mie scattering contamination from the Rayleigh signal. Fortunately, the intensity of the Mie scattering signal is several times larger than Rayleigh signal, which simplifies the removal. Even though, the fluctuations in the equivalence ratio can be the potential source of error in premixed flames may not be relevant in non−premixed diffusion flames.

6.2 Direct swirl-stabilized flame photography

Direct flame photography is used to document the characteristics of the flames. The main characteristic features are dimensions, shapes and structures, which can highlight the main features of the swirling flame under miscellaneous conditions, i.e. swirl numbers. A Cannon EOS 550D digital camera was used to take the flame photographs. This camera has 18 million effective pixels and was equipped with 18−75(mm) lens. In this study, an aperture of f5.6 was used for each photography along with typical exposure time of 1/10th of a second.

A photograph of DLR flames operating with 0.9 overall equivalence ratio and swirl numbers equal to 0.3, 0.58 and 1.07 is shown in Figure 6.5. A thermocouple that is seen in the images was used to detect the flame temperature in order to provide a safety protection from incidental blow−off.[5]. The flame is blue−coloured tulip cup shaped for moderate and highest swirl numbers of 0.58 and 1.07, while for the lowest swirl number the flame seems to have cylindrical shape without significant divergence and resembles a long jet flame. The higher swirl number 0.58 and 1.07 produce wider flame, which could be the representation of positive radial stretch as a result of the large tangential velocity gradients. The positive radial stretch also shortens the flame height and increases the volumetric burning rate due to larger surface area.

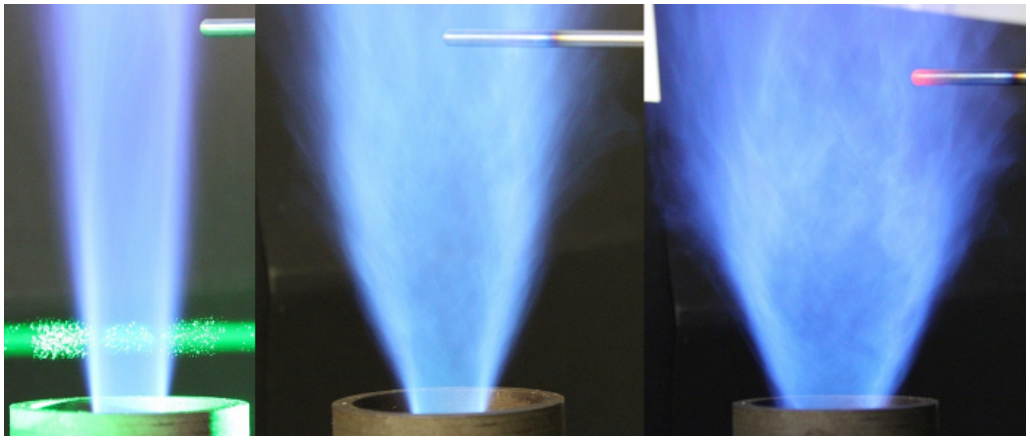

Figure 6.5: A photograph of the flame (side view) as a function of the swirl number. From left to right S=0.3, 0.58 and 1.07, overall stoichiometric ratio = 0.9. A thermocouple that is seen in the images was used to detect the flame temperature in order to provide a safety protection from incidental blow−off. A position of laser sheet is also shown at $y/D_f = 1$ with clearly visible Mie scattering from dust particles.

The flame is stably attached to the fuel nozzle for all three swirl numbers, which can be seen in Figure 6.6. These flames seem to be stabilized by the recirculation of hot gases, because no combustion can be sustained when no swirl is used i.e. $S = 0$. It is particularly hard to conclude whether internal, external or both recirculation zones are responsible for the flame stabilization without considering velocity data or at least the temperature fields. However, some observations from the direct photography allows commenting on general

[5]When flame is not detected, i.e. the temperature is below 600(K), a specially designed control system switches off the power thus cutting off the supply of fuel.

findings as follows. Increasing the swirl leads to flame expansion, which may decrease lower axial speeds while increasing tangential momentum. The shear is expected to increase at the fuel jet boundaries, which in turn provides better mixing between the fuel and the oxidiser. The centreline temperature seems to be lower at locations close to the fuel nozzle, which can be seen from unburned dust particles along centreline in Figure 6.5. More detailed analysis will be made in the next section in which instantaneous and mean temperature fields are discussed.

Figure 6.6: A photograph of the flame (angled view) as a function of swirl number. From left to right S=1.07, 0.58 and 0.3; overall equivalence ratio is 0.9. A position of laser sheet is also shown at $y/D_f = 1$.

6.3 Instantaneous and mean temperature fields

Experimental data was obtained from the Rayleigh measurements, where the reference signal was obtained from the air at known temperature (291K) and is shown in Figure 6.7. A CCD camera high temperature raw image recorded as the result of the laser sheet illumination is shown in Figure 6.8. The corresponding temperature image was obtained by the division of the reference signal in Figure 6.7 by the Rayleigh raw image (I) shown in Figure 6.8 and subsequent multiplication with the reference temperature of 291(K).

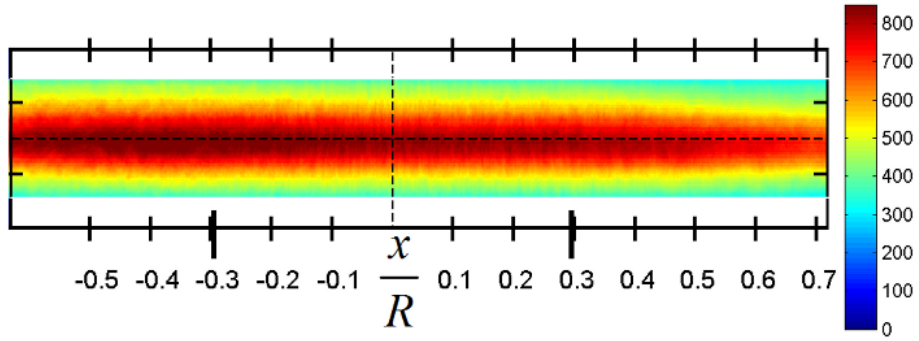

Figure 6.7: The camera image of the laser Rayleigh scattered light from the ambient air, which was used as the reference signal in the Rayleigh thermometry. Scale is given in terms of counts (camera discretization levels). More than 5000 instantaneous images were averaged in order to eliminate the influence of the Mie scattering from the dust particles.

An initial image processing for the temperature computation involved two steps. The most important issue was the elimination of bright spots (due to overexposed pixels),

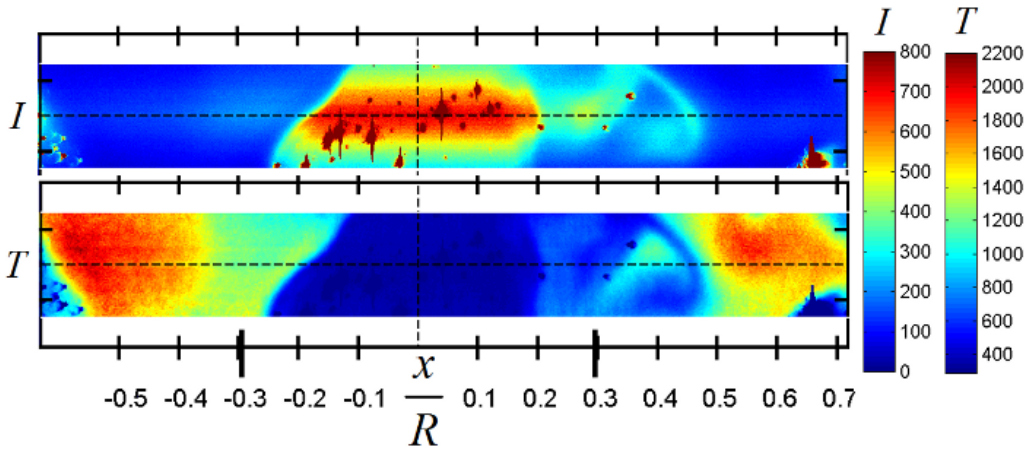

Figure 6.8: The raw image of the scattered light intensity as recorded by the CCD camera I and the corresponding temperature image T. Bright spots in the top image I are due to the Mie scattering from dust particles that were present in the ambient and the combustion air. The resulting temperature image T was thresholded to eliminate the bright Mie scattered spots and subsequently median filtered by using the kernel of 3 by 3 pixels.

which were due to the Mie scattering from the dust particles. Even though, the combustion air was supplied through a set of filters installed in the air supply system, the ambient air contained a certain amount of dust particles, which penetrated into the flame zone. In addition to unwanted reflection from dust particles, which propagates to the final temperature image, the overexposed pixels can generate an excess of electrons that can migrate to neighbouring pixels. This effect is known as 'blooming', which leads to darker and brighter structures in the image[6].

The elimination of the bright spots from the raw images was done by a thresholding, which is the simplest method of image denoising. During the thresholding process, individual pixels in computed temperature image are compared to the threshold value, which is the reference temperature. The measured temperature is given as the ratio of the reference signal over the measured signal at unknown temperature S_{ref}/S_{meas}. This ratio is multiplied with the reference temperature T_{ref}, which gives the measured temperature. If a dust particle is present and illuminated by the laser sheet, the Mie scattering intensity from the particle creates the bright spot in the image, with the intensity much higher than the Rayleigh scattering light, meaning that $S_{meas} >> S_{ref}$ or $S_{ref}/S_{meas} < 1$. This leads to the measured temperature T, which is less than the reference temperature $T < T_{ref}$ that is not realistic. The threshold filtering is therefore simply $T = T_{ref}$ if the measured temperature is less than the reference one $T < T_{ref}$. Finally, the thresholded temperature images were filtered by using a median filter with a kernel of 3×3 pixels. The median filter is proven to be effective when the goal is to simultaneously reduce noise and preserve image structures Chan *et al.* (2005)[7].

[6] CMOS sensors unlike CCD sensors are not prone to this effect. However, CMOS sensors are more susceptible to noise than CCD ones.

[7] The main idea of the median filter in 2D image processing is to go through the image, replacing each pixel value with the median of neighboring pixel values. The neighboring pixels values are called the 'window'. The window is translated over the entire image. If the window has an odd number of pixels, then the median is simply the middle value after all pixels in the window are sorted numerically.

Several authors used a Gaussian filter[8] to reduce noise in the temperature images e.g. Frank & Kaiser (2006). The Gaussian filter is equivalent to low−pass filtering, which means that this filter suppresses high frequency details (noise), while preserving the low frequency content of the temperature image. In other words, the filter blurs everything that is smaller than the filter size. It is quite apparent that the lost of contrast is inevitable and there is an trade−off between the suppression of noise and the reduction of spatial resolution as was pointed by Mi & Nathan (2003). Homogeneous Gaussian smoothing is commonly used, which is not optimal for the images containing a wide range of length scale. An alternative inhomogeneous smoothing with an isotropic Gaussian kernel can be used (Frank & Kaiser, 2006).

Instantaneous temperature fields are shown in Figures 6.9−6.11. Time averaged temperature fields and standard deviation of temperature fluctuations are shown in Figures 6.12−6.14 and in Figures 6.15−6.17. In addition, radial and axial profiles of the mean temperature are also presented in Figures 6.18−6.20. All the temperature data is reported here for three swirl numbers $S = 0.3, 0.58, 1.07$ and up to 10 fuel diameters downstream $y/D_f = 1, 3, 5, 7, 10$. The SNR[9] computed from a small rectangular window for $1100 < T < 1300$ was 60. The SNR of the Rayleigh signal in air at 291(K) was 95. The relative standard error[10] in temperature computations was computed to be within 1-2% depending on operating conditions (swirl number, downstream locations etc.)

Two−dimensional instantaneous images of temperature at several[11] downstream positions $y/D_f = 1 - 10$ are shown in Figures 6.9−6.11. At lower axial downstream positions $y/D_f = 1 - 3$ the temperature is seen as narrow zones of high temperature (seen as red), which are embedded into cold field (seen as blue). At higher positions, the temperature field becomes more homogeneous, in which no distinct high temperature zones can be observed. In addition, for lowest swirl number of 0.3 and at lower axial positions, the high temperature zone fluctuates within the shear layer, i.e. $x/R \approx \pm 0.3$. Centreline temperature at lower axial positions seems to be close to the ambient temperature (or air stream temperature), while at higher positions due to enhanced mixing, the centreline temperature increases. At intermediate swirl number of 0.58 the temperature is more affected by the level of mixing, which is seen as more distributed high temperature zones, especially at lower downstream location. At higher downstream positions, the temperature distribution tends to be more uniform (Fig. 6.12-6.14), which is seen even at instantaneous images (Fig.6.9−6.11). As in case of low swirl number of 0.3, the centreline temperature increases with the distance from the jet origin, or more precisely from the burner exit. The temperature field seems to be nearly homogeneous at the highest downstream positions $y/D_f = 10$ for $S = 1.07$ and no significant temperature fluctuations are observable. The centreline temperature expresses the same trend as in previous cases of low and moderate swirl numbers, i.e. gradually increases with the distance from the burner exit. It is also

[8] The visual effect of this smoothing technique is a smooth blur resembling that of viewing the image through a translucent screen.

[9] The definition of SNR is the ratio of mean to standard deviation of a signal or measurement $SNR = \mu/\sigma$.

[10] The relative standard error (RSE) is simply the temperature standard error divided by the mean and expressed as a percentage $RSE = \left[\left(\frac{\sigma_T}{\sqrt{n}}\right)/\bar{T}\right] \times 100\%$. The temperature standard error is computed from the temperature standard deviation σ_T and a number of images n.

[11] Laser sheet axial downstream positions no higher than 10 fuel diameters were covered. The reason for that was simply due to hardware limitations.

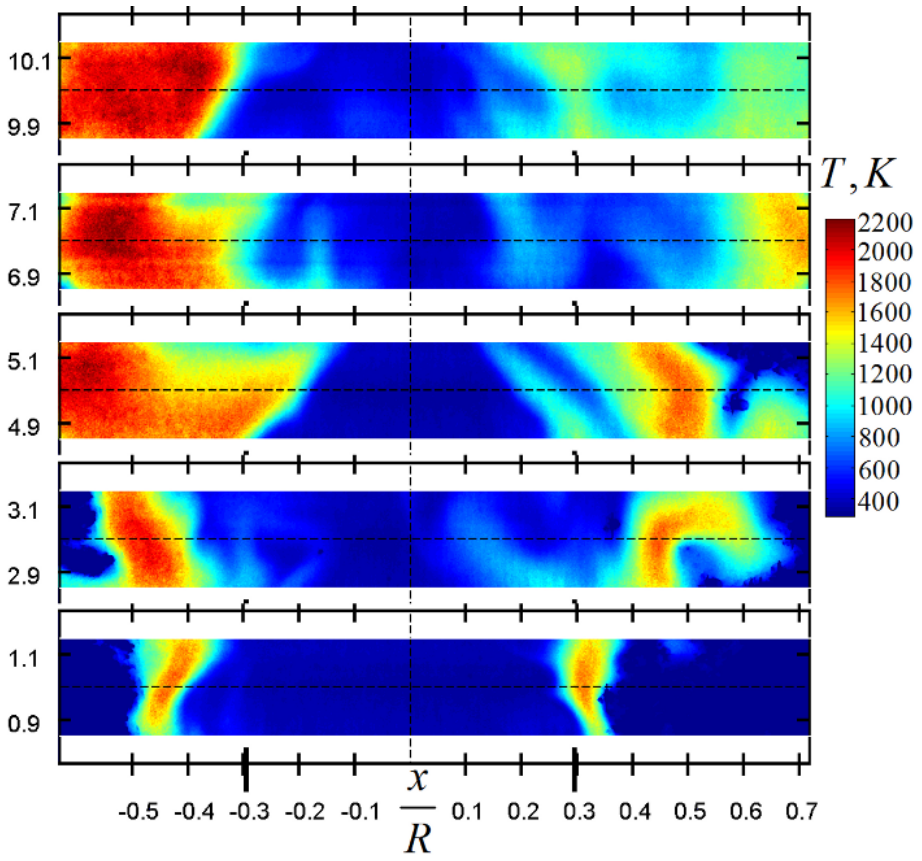

Figure 6.9: Instantaneous temperature fields for $S = 0.3$ at $y/D_f = 10, 7, 5, 3, 1$ (from top to bottom). Note that instantaneous images at various y/D_f were taken from different realisations.

possible to asses the level of temperature fluctuations by considering the standard deviation, which is reported in next images along with the mean temperature computed from 1000 instantaneous realisations.

Figures 6.15−6.17 show standard deviations of temperature fluctuations for three swirl numbers $S = 0.3, 0.58$ and 1.07. At low swirl number, the standard deviation is highly non−uniform, especially at lower downstream positions, which indicates highly non−uniform temperature distribution. In contrast, for intermediate and the highest swirl numbers, the standard deviation becomes smaller and more distributed. Low standard deviations indicate that most of the temperature is close to the average, which in turn means that the fluctuations are low. High standard deviations indicate high temperature fluctuations[12].

Figures 6.18−6.20 show radial profiles of the mean temperature distribution and the mean temperature distribution along the centreline. The temperature distribution along the centreline for $S = 0.3$ is non−linear with distinctive flat region at the distances, which are close to the burner exit. The temperature does not increase with distance, up to approximately 4 fuel pipe diameters (y/D_f =4) and slightly increases with distance afterwards, reaching circa 800(K). This indicates that the recirculation zone is not present, which is consistent with the measurements that are reported in Chapter 7. It can be

[12]A coefficient of variation c_v can be also used to describe the dispersion. The coefficient of variation c_v is defined as the ratio of the standard deviation to the mean $c_v = \sigma/\mu$. Coefficient of variation is sometimes multiplied by 100% and written as a percentage.

also suggested that there must be an alternative mechanism of flame stabilisation. The radial profiles of temperature distribution for the lowest swirl numbers confirm previous observations that temperature distribution along centreline increases with distance. The maximum recorded mean temperature was circa 1400(K).

A quite different picture is seen for $S = 0.58$ and $S = 1.07$. The distribution of the mean temperature along the centreline is almost linear, i.e. the temperature linearly increases with distance, reaching ≈1400(K) for $S = 0.58$ and ≈1800(K) for the highest swirl number of 1.07. This a clear indication of the recirculation zone. Pressure gradient within swirling jet is created due to jet swirling motion, which results in flow reversal and formation of recirculation zone. The recirculation zone enhances mixing between fresh reactants, which are supplied by the fuel pipe, and burnt products and acts as the source of 'hot fluid'. This results in higher centreline temperatures and almost linear relationship between temperature and distance. This effect is also confirmed by velocity measurements in Chapter 7.

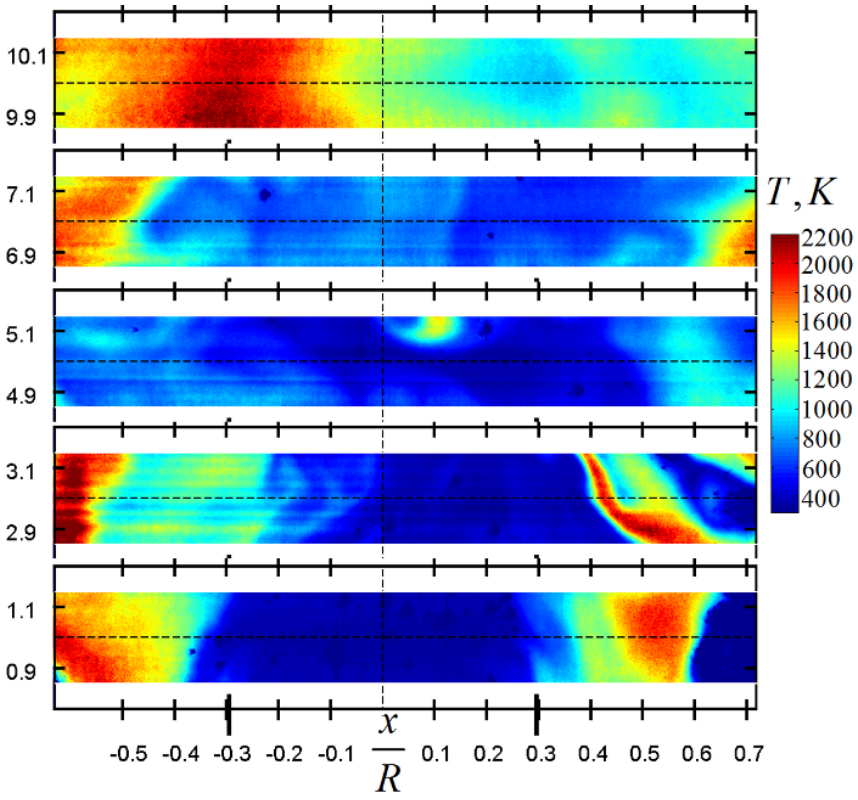

Figure 6.10: Instantaneous temperature fields for $S = 0.58$ at $y/D_f = 10, 7, 5, 3, 1$ (from top to bottom). Note that instantaneous images at various y/D_f were taken from different realisations.

Similar temperature distribution is observed for the highest swirl number $S = 1.07$ as for $S = 0.58$, which is reported in Figure 6.14. The mean temperature increases with the distance from the burner exit reaching ≈2000K (1800(K)@$S = 0.58$). The mean temperature distribution is almost uniform at the highest downstream location, which is also consistent with non−reacting measurements. At lower downstream locations the mean temperature is almost the same for all swirl numbers and is approximately equal to 1200K.

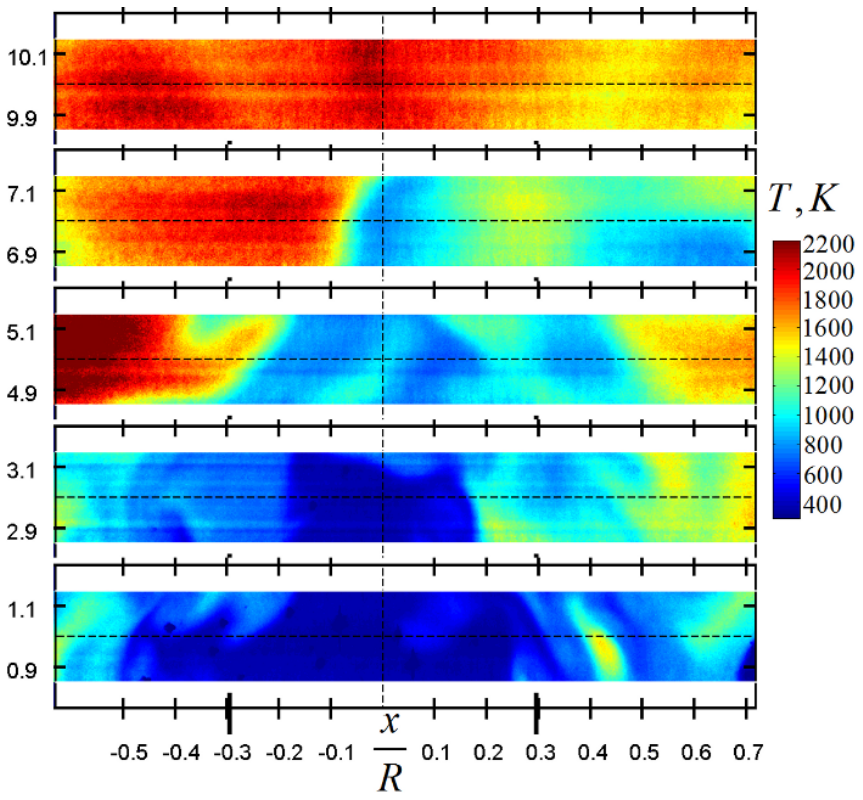

Figure 6.11: Instantaneous temperature fields for $S = 1.07$ at $y/D_f = 10, 7, 5, 3, 1$ (from top to bottom). Note that instantaneous images at various y/D_f were taken from different realisations.

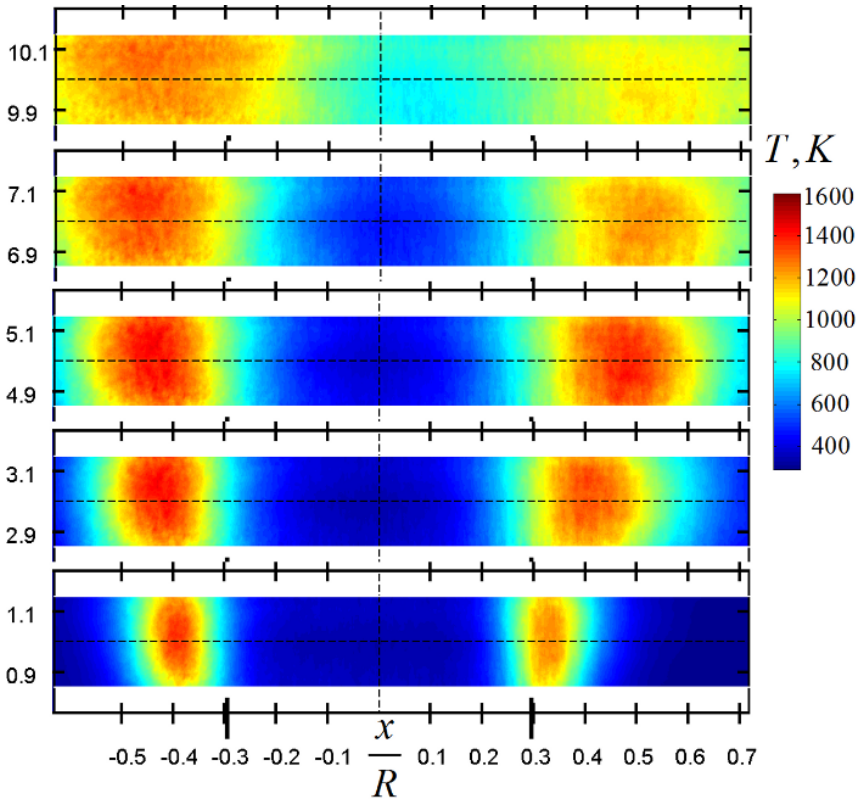

Figure 6.12: Mean temperature computed from 1000 instantaneous images for $S = 0.3$ at y/D_f=10,7,5,3,1 (from top to bottom).

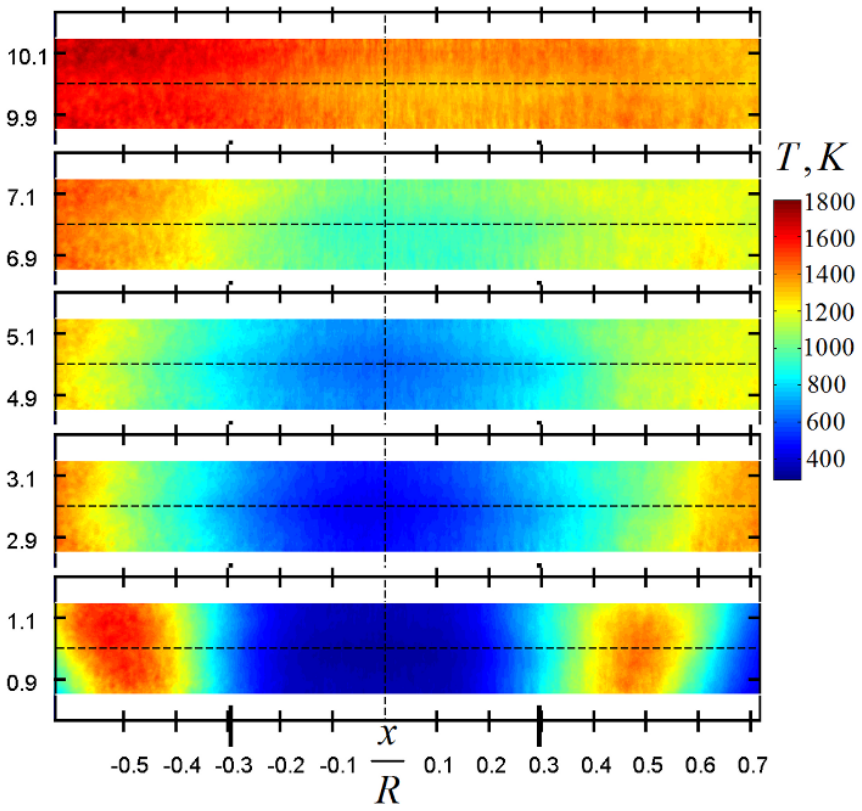

Figure 6.13: Mean temperature computed from 1000 instantaneous images for $S = 0.58$ at y/D_f=10,7,5,3,1 (from top to bottom).

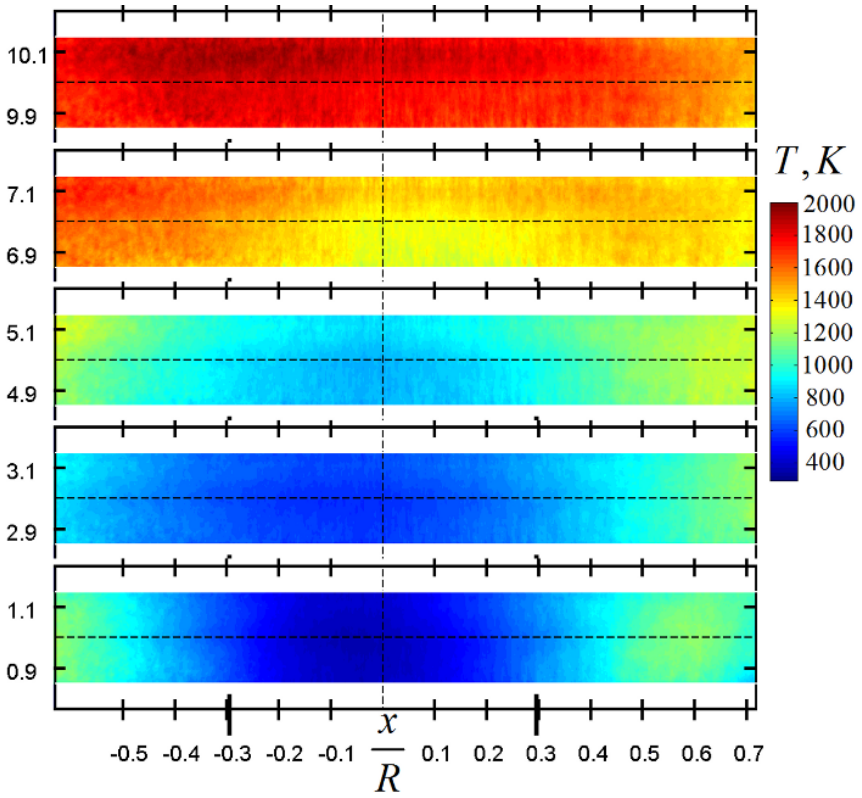

Figure 6.14: Mean temperature computed from 1000 instantaneous images for $S = 1.07$ at y/D_f=10,7,5,3,1 (from top to bottom).

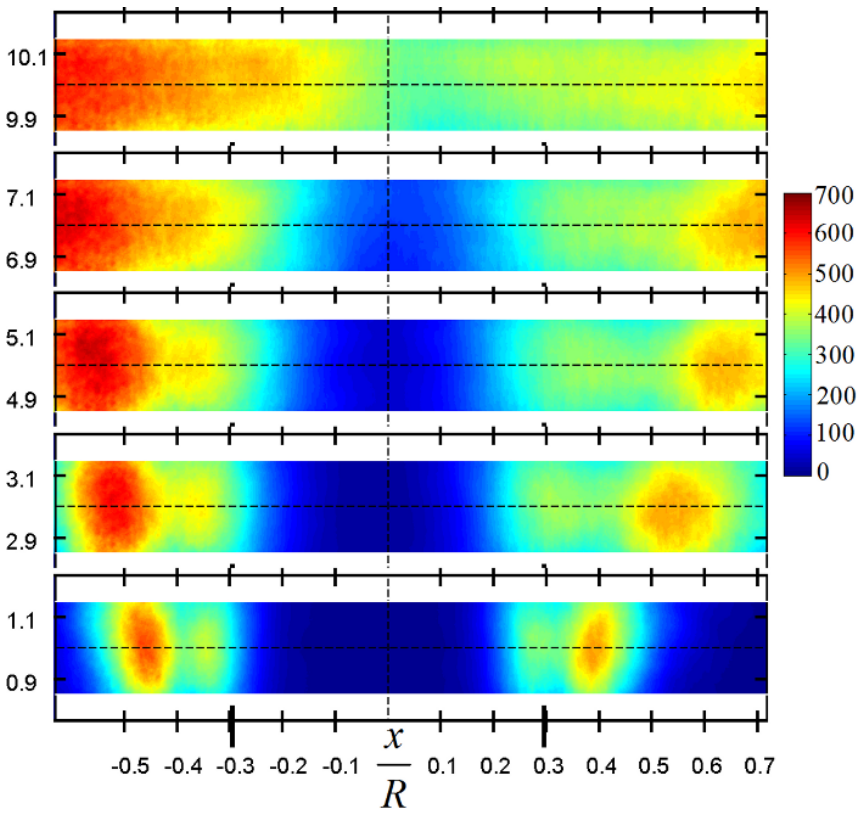

Figure 6.15: Standard deviation of temperature fluctuations (K), computed from 1000 instantaneous images for $S = 0.3$ at y/D_f=10,7,5,3,1 (from top to bottom).

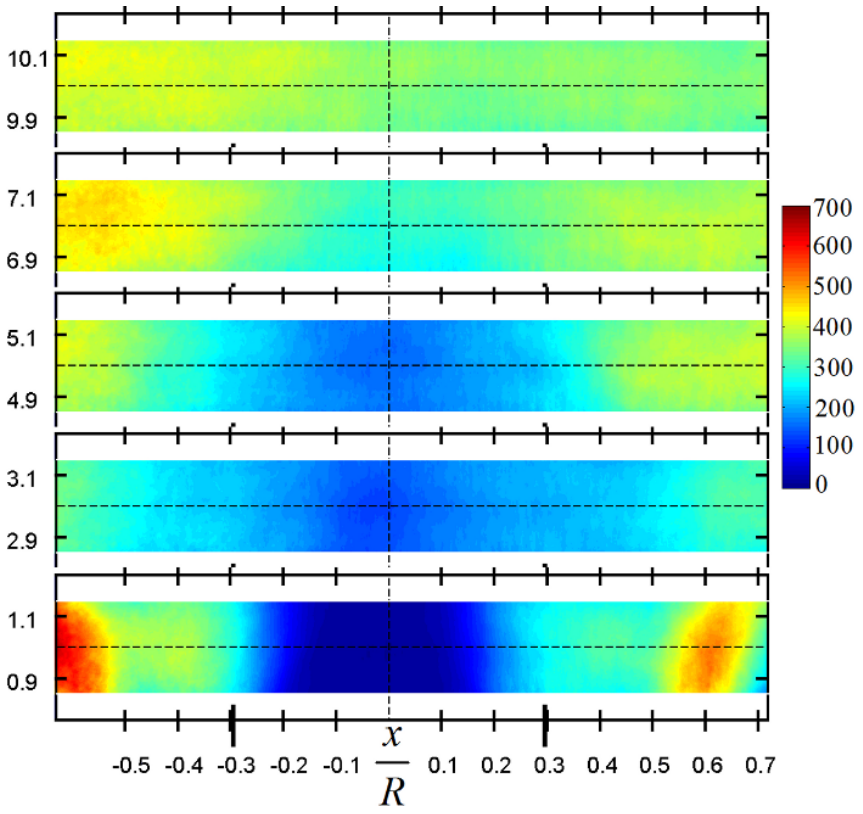

Figure 6.16: Standard deviation of temperature fluctuations (K), computed from 1000 instantaneous images for $S = 0.58$ at y/D_f=10,7,5,3,1 (from top to bottom).

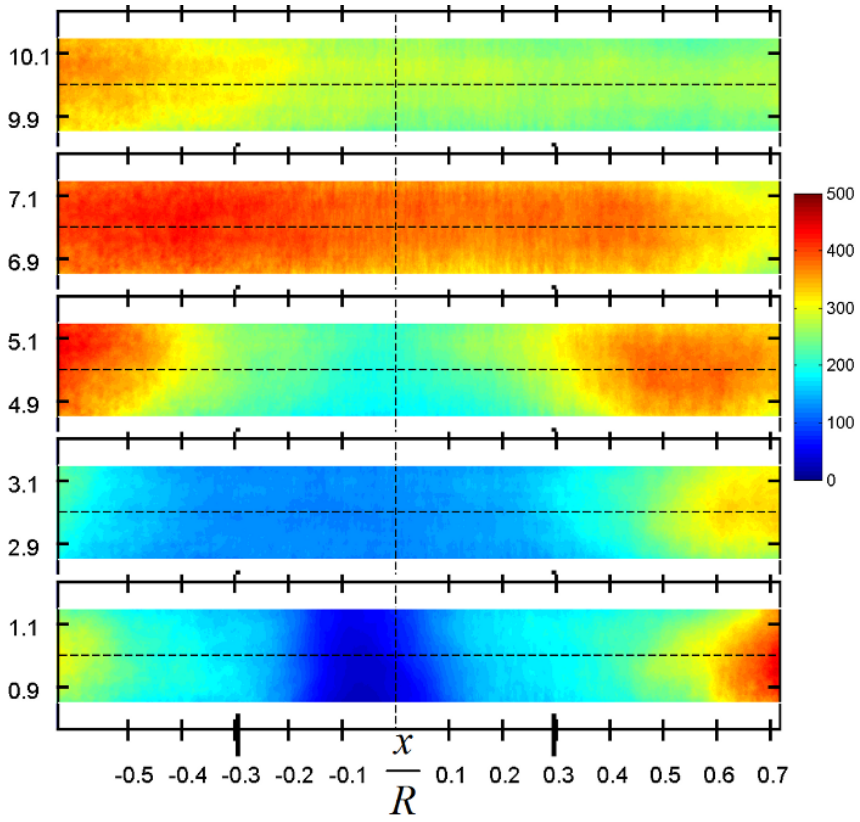

Figure 6.17: Standard deviation of temperature fluctuations (K), computed from 1000 instantaneous images for $S = 1.07$ at y/D_f=10,7,5,3,1 (from top to bottom).

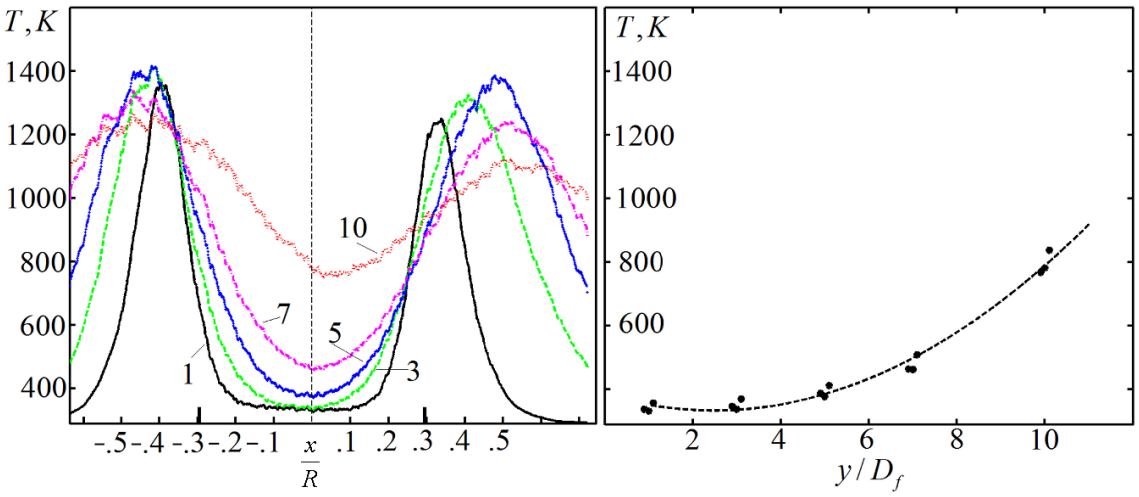

Figure 6.18: Mean temperature radial profiles (left) and the centreline axial temperature (right) for $S = 0.3$ as a function of downstream positions y/D_f.

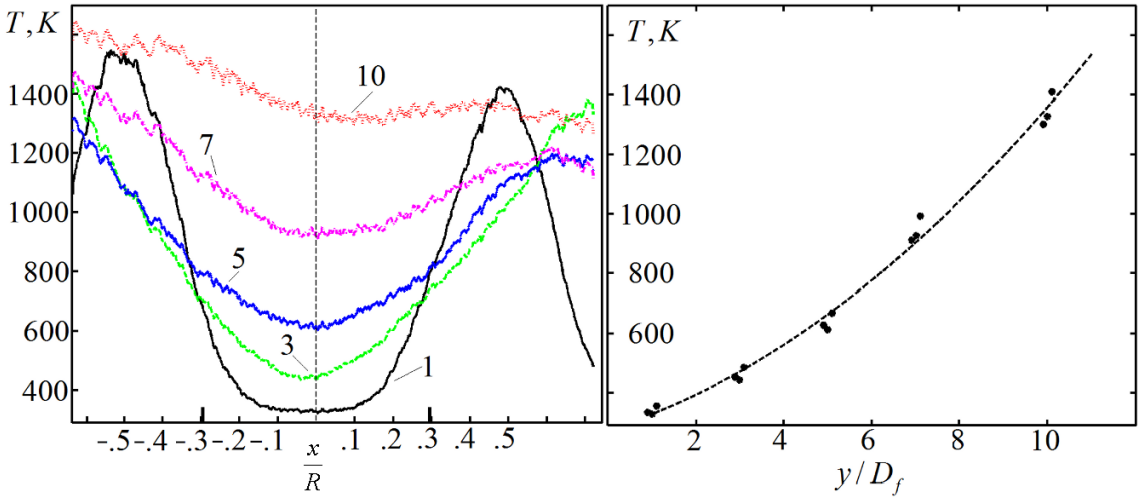

Figure 6.19: Mean temperature radial profiles (left) and the centreline axial temperature (right) for $S = 0.58$ as a function of downstream positions y/D_f.

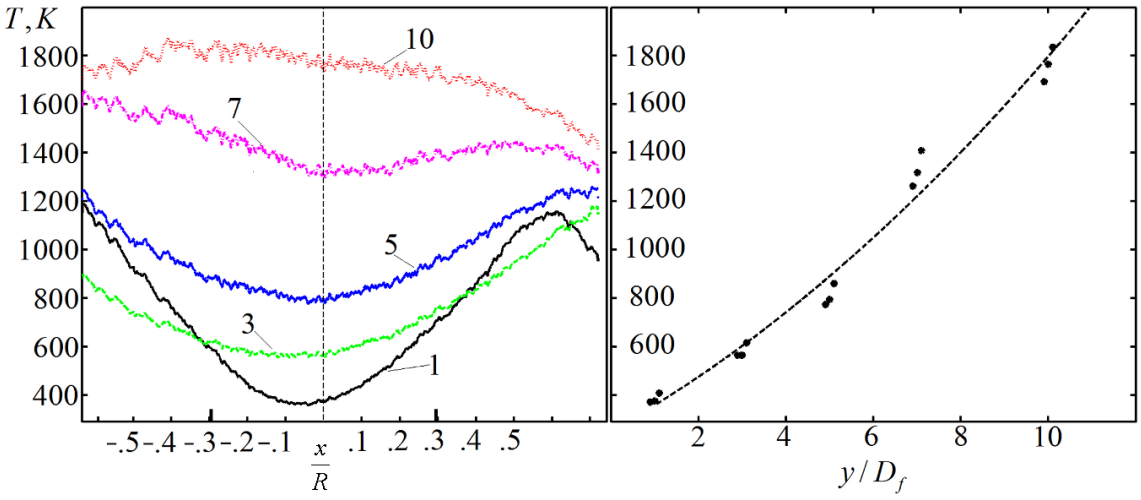

Figure 6.20: Mean temperature radial profiles (left) and the centreline axial temperature (right) for $S = 1.07$ as a function of downstream positions y/D_f.

6.4 Probability density functions of temperature fluctuation

Probability density functions of temperature fluctuations are of increasing interest in combustion modelling and in turbulence in general. Dopazo (1975) formulated the problem of the evolution of the probability density function of temperature fluctuations and presented a close scheme to obtain explicit results for an antisymmetric heated jet. A relatively simple heated jet configuration allowed investigating the probability density functions of temperature fluctuations and promoted similar measurements in other flows, e.g. Sreenivasan (1981). The interest in probability density functions of temperature fluctuations provided a motivation for the measurements in swirling flows.

Therefore, the measurements of the probability density function of temperature fluctuations at several downstream positions and all swirl numbers are presented here. Data for each probability function of temperature fluctuations was compiled by considering a local window of axial length of 1.27(mm) and radial length of 1.55(mm) containing 2976 data points and over 1000 images resulting in ≈3e6 data points for each spatial location. The dimensions of the local windows were chosen on the basis of sufficient number of samples. Five spatial locations were investigated and are shown in Figure 6.21. All probability density functions of the temperature of the mixture fraction are presented here in terms of $P_T(C)$, where P_T denotes probability density function and C is defined as follows:

$$C = \frac{T - \bar{T}}{\sigma_T} \tag{6.1}$$

The p.d.fs. of the temperature fluctuations were computed from the instantaneous temperature minus the mean and normalizing by the standard deviation of the temperature. The range of the C values was divided in a number of equal bins (50 bins were typically used) and the number of occurrences in each bin was counted. The p.d.f. was computed as N/LW, where N is the count of values in each bin or frequency, W is the width of the bin and L is the total number of samples (cardinality of a dataset). The width of the bin was assessed through a set of trial and error procedures and it was found that the convergence of the p.d.f. was almost independent on the number of bins. This procedure is exactly equivalent to that used in non−reacting measurements.

Figures 6.22−6.28 show the probability density functions of the measured temperature fluctuations obtained from several downstream positions y/D_f and spatial locations in the flow. It should be mentioned that only three windows are discussed here, i.e. centreline ($x/R = 0$), at $x/R = -0.3$ and $x/R = -0.4$, because other windows demonstrate similar trend. Figure 6.22 presents the p.d.f. of the temperature fluctuations from centreline window at $y/D_f = 1$ for two swirl numbers 0.3 and 0.58. In addition, the Gaussian p.d.f. is also plotted for comparison. Centreline p.d.f. from the centreline window is with positive kurtosis and in good agreement with the Gaussian p.d.f. The narrow distribution indicates that most of the fluctuations are around the mean, indicating that the temperature distribution is rather homogeneous, which is also demonstrated by the standard deviation (Figures 6.15−6.16). Larger swirl numbers increase turbulent mixing thus rising the centreline mean temperature. Higher turbulence levels pump 'low' temperature fluid towards the centreline thus giving rise in the probability density at some negative value of $\left(T - \bar{T}\right)/\sigma_T$ (≈3 standard deviations), which is also consistent with Sreenivasan (1981).

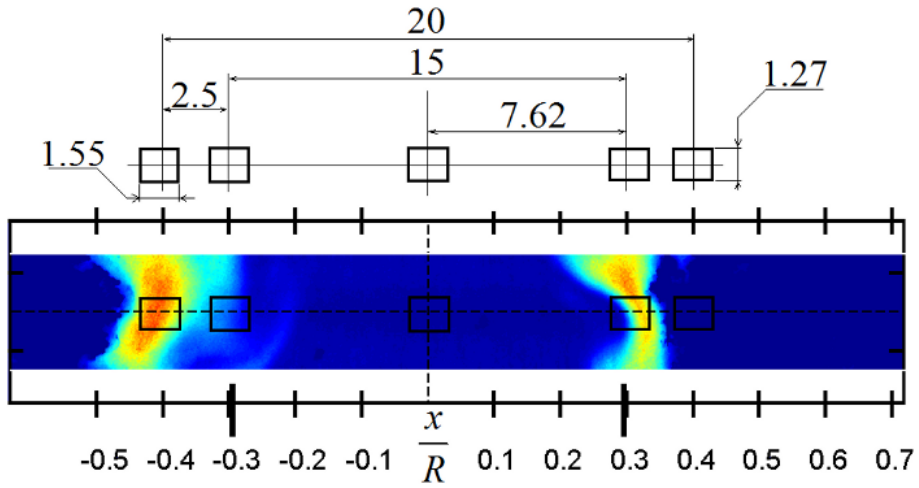

Figure 6.21: Window positions where temperature statistics were evaluated. An instantaneous image of temperature at $y/D_f = 1$ for $S = 0.3$ is also shown. Locations of the windows were chosen within shear layer $\pm$ 0.3 x/R and on the burner centreline axis. In addition, two windows at $\pm$ 0.4 x/R were also chosen. Dimensions are given in mm. Only p.d.fs. computed from windows at -0.4,-0.3 x/R and the centreline window are reported here.

On the other hand, the p.d.f. from shear layer, i.e. -0.3 x/R, shown in Figure 6.25 computed at $y/D_f = 1$ for $S = 0.3$ and 0.58 demonstrates positively skewed distribution for both low and intermediate swirl numbers. The Gaussian p.d.f shows quite significant departure in both cases, i.e. $S = 0.3$ and 0.58, from the experimentally measured p.d.f. This departure can be related to the turbulence intensity levels, even though the relationship is not yet clear.

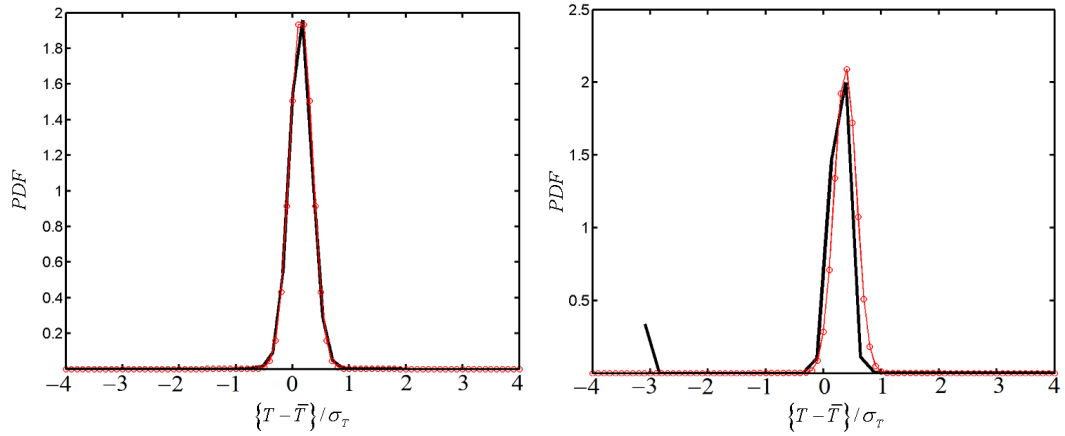

Figure 6.22: P.d.f. of temperature fluctuations computed from centreline window at $y/D_f = 1$ for $S = 0.3$ (left) and 0.58 (right). Gaussian p.d.fs. μ =0.15, σ =0.2 (left) and μ =0.38, σ =0.19 (right) are also shown for comparison as red circle line. A peak in probability at -3 on the left image is perhaps due to intermittency.

Figure 6.24 shows the probability density function of temperature fluctuations computed from centreline window at the same downstream position $y/D_f = 10$ for two swirl numbers $S = 0.58$ and 1.07. It can be seen that quite similar probabilities are observed even though

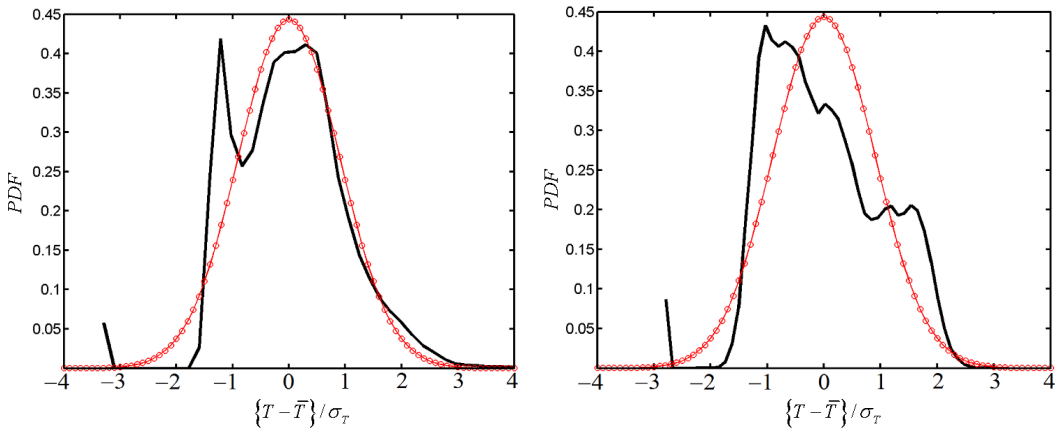

Figure 6.23: P.d.f. of temperature fluctuations computed from centreline window at $y/D_f = 3$ (left) and $y/D_f = 7$ (right) for $S = 1.07$. Gaussian p.d.fs. μ =0, σ =0.9, both left and right, are also shown for comparison as red circle line.

with different skewness. The p.d.f. is positively skewed for intermediate swirl number of 0.58 and negatively skewed for the highest swirl number of 1.07. However, the skewness is small with quite large kurtosis thus indicating that the temperature fluctuates with relatively small fluctuations. It is interesting to note a bimodal p.d.f. distribution as for example in Figure 6.26. On the left hand side of Figure 6.26, the p.d.f. of temperature fluctuations computed from window at -0.3 x/R at $y/D_f = 1$ for $S = 1.07$ is presented with distinct visible unequal bimodal distribution[13]. Since a single Gaussian function cannot represent such bimodal distribution a sum of two Gaussian distributions with different mean and standard deviations, can for example, be used. On Figure 6.26, the sum of two Gaussian distributions with μ_1 =-1.0, σ_1 =0.3 and μ_2 =0.25, σ_2 =0.65 is also shown. The same sum was also normalized to decrease discrepancy between the actual measured p.d.f and the sum of two Gaussian distributions. The lack of experimental data in similar swirling flows does not allow commenting on the generality of the results, especially on that whether the bimodal distribution can be represented as the normalized sum of two Gaussian curves or not.

Figures 6.27 shows p.d.fs. of temperature fluctuations computed from window at $x/R = -0.3$, y/D_f =10 for $S = 0.58$ and $S = 1.07$. Gaussian probability density functions are also shown for comparison. The p.d.fs. exhibit bimodal features with unequal modes and deviation from Gaussian distribution is clearly observed. Figure 6.28 shows p.d.fs. of temperature fluctuations computed from window at $x/R = -0.4$, $y/D_f = 1, 5$ for $S = 0.58$. The deviation from Gaussian distribution is also seen at y/D_f =1. However, for the same operating conditions at y/D_f =5 the deviation is small and primarily due to long tails.

Similar bimodal temperature distribution were also observed by, e.g. Mantzaras & Van Der Meer (1997) for temperature fluctuations in a turbulent, natural gas−fuelled, piloted jet diffusion flame were measured by using Coherent Anto−Stokes Raman Spectroscopy.

[13] A bimodal distribution is a distribution with two different modes. If the two modes are unequal, the larger mode is known as the major mode, while the other smaller as the minor mode. The least frequent p.d.f. value between the modes are known as the antimode. The difference between the major and the minor mode is known as the amplitude.

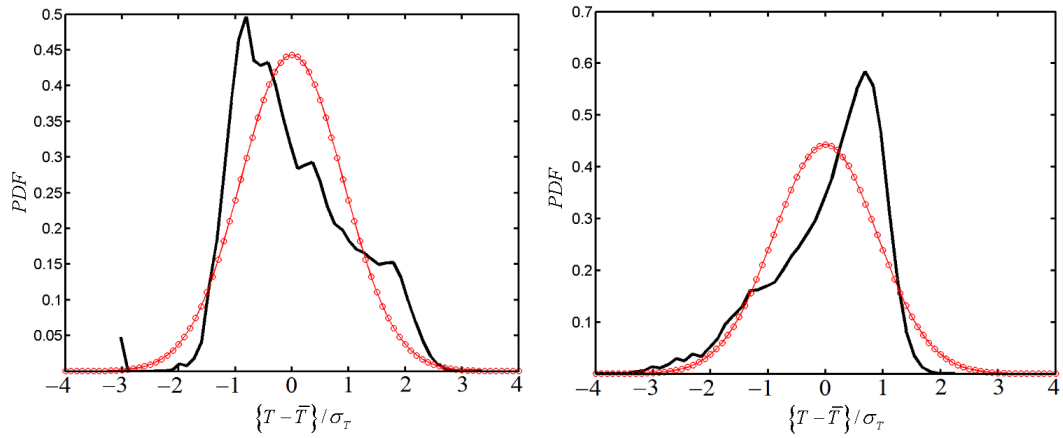

Figure 6.24: P.d.f. of temperature fluctuations computed from centreline window at $y/D_f = 10$ for $S = 0.58$ (left) and 1.07 (right). Gaussian p.d.fs. μ =0, σ =0.9, both left and right, are also shown for comparison as red circle line.

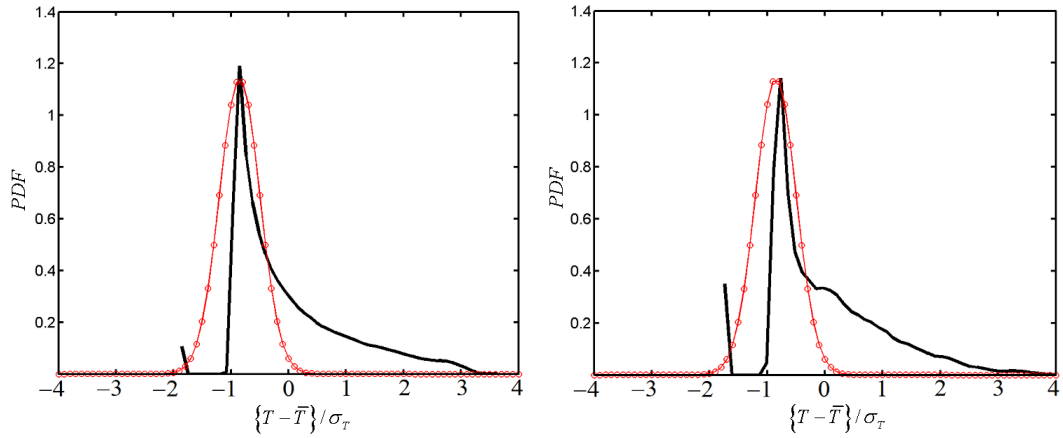

Figure 6.25: P.d.f. of temperature fluctuations computed from window at $x/R = -0.3$ at $y/D_f = 1$ for $S = 0.3$ (left) and 0.58 (right). Gaussian p.d.fs. μ =-0.85, σ =0.35, both left and right, are also shown for comparison as red circle line.

Mantzaras & Van Der Meer pointed out that the bimodal p.d.fs. were observed at the spatial locations that were close to the average reaction zone. It can also be said that the bimodal distribution occurs when the output from two processes, each one from the Gaussian distribution with different mean, are mixed. In the case of the temperature fluctuations it can be thought as the two streams of hot and cold fluid, which are locally mixed within the window of interest. This mixing can be due to flow precession as a result of swirling motion. Figure 6.23 on the left shows the p.d.f. of the temperature fluctuations computed from the centreline window for $S = 1.07$ at $y/D_f = 3$ and also demonstrates the bimodal distribution. However, due to complicated nature of the swirling flows, the probability distribution of temperature fluctuations may significantly deviate from Gaussian distributions. At the 'cold' centreline zones, close to the burner exit, the measured p.d.fs. for low swirl number of $S = 0.3$ and intermediate 0.58 at $y/D_f = 1$ are nearly triangular, which is also consistent with Mantzaras & Van Der Meer (1997).

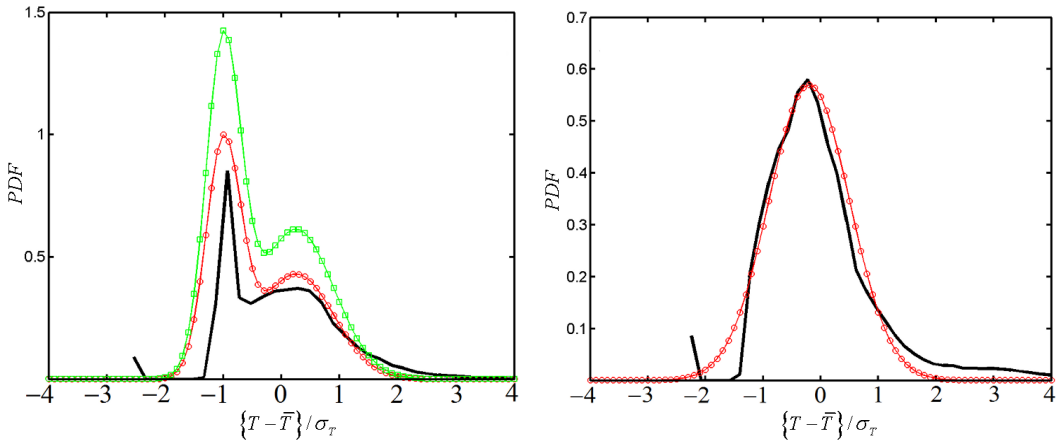

Figure 6.26: P.d.f. of temperature fluctuations computed from window at $x/R = -0.3$ at $y/D_f = 1$ for $S = 1.07$ (left) and $y/D_f = 5$ for $S = 0.58$ (right). On the right, Gaussian p.d.f. with μ =-0.2, σ =0.7 is also shown for comparison as red circle line. On the left, a sum of two Gaussian p.d.f. with μ_1 =-1.0, σ_1 =0.3 and μ_2 =0.25, σ_2 =0.65 is shown as green squares along with same normalized sum shown as red circle line on the same plot.

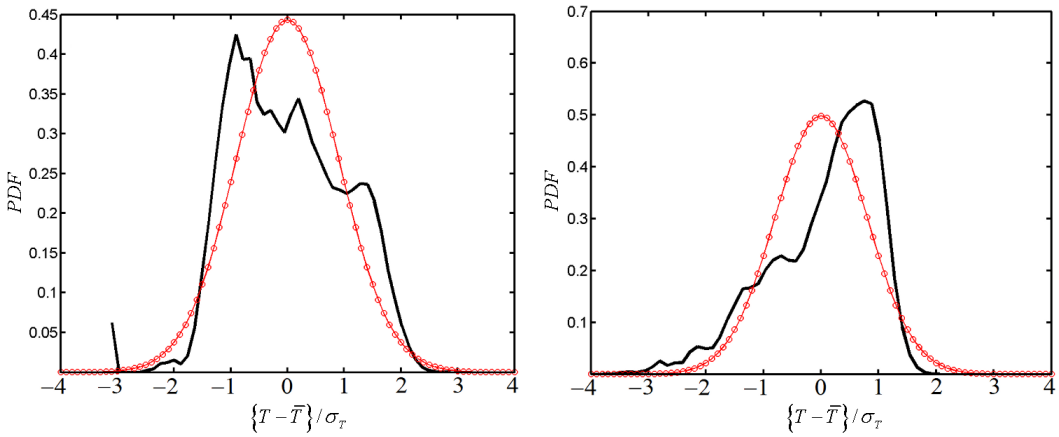

Figure 6.27: P.d.f. of temperature fluctuations computed from window at $x/R = -0.3$ at $y/D_f = 10$ for $S = 0.58$ (left) and $S = 1.07$ (right). Gaussian p.d.fs. μ =0, σ =0.9 (left) and μ =0, σ =0.8 (right), are also shown as red circle line.

Measured probability density function of temperature fluctuations at various downstream positions y/D_f and spatial location in the flow exhibit a wide range of shapes. The wide range of shapes consists of unimodal and bimodal both equal and unequal distributions. Zones with the low temperature fluctuations typically demonstrate unimodal distribution with high kurtosis, while zones with high temperature fluctuations can demonstrate bimodal distribution. At higher downstream locations and higher swirl numbers the p.d.fs. are typically unimodal even though not entirely symmetrical. It is impossible to relate the measured p.d.f. to the specific locations in the flow or to operating conditions due to complicated flow field. It seems to be plausible to assume the Gaussian distribution for the temperature fluctuations in most of the cases.

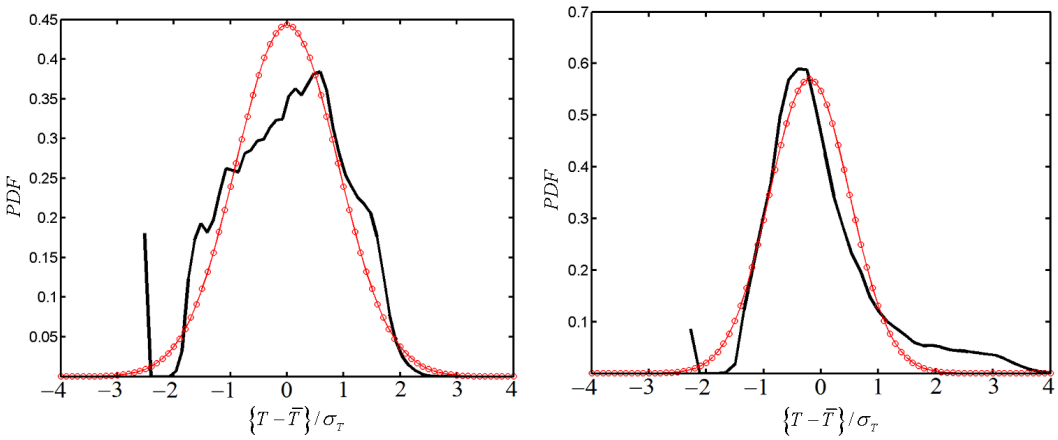

Figure 6.28: P.d.f. of temperature fluctuations computed from window at $-x/R0.4$ at $y/D_f = 1$ (left) and $y/D_f = 5$ (right) for $S = 0.58$. Gaussian p.d.fs. μ =-0.2, σ =0.7 (left) and μ =-0.2, σ =0.5 (right), are also shown for comparison as red circle line.

6.5 Power spectra of temperature fluctuations

Power spectral density (PSD) of temperature fluctuations was determined as the average from 1000 instantaneous images and computed via Fast Fourier Transform by following the same procedure as in non−reacting measurements[14].

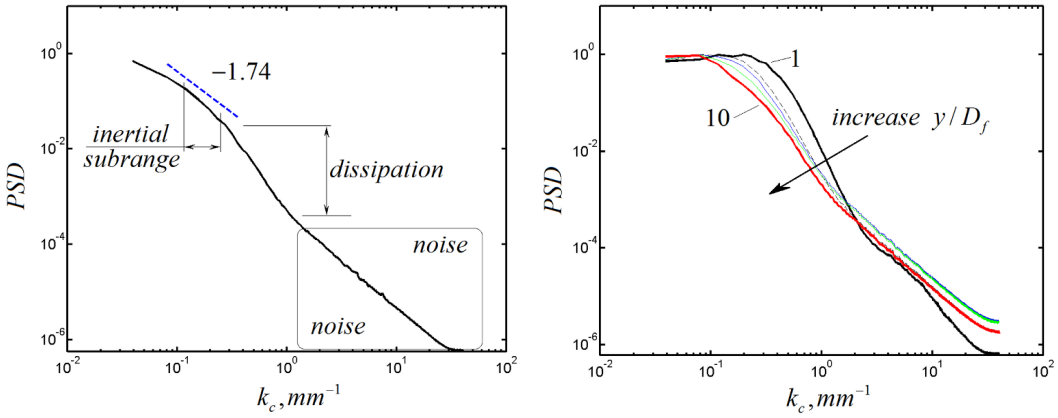

Figure 6.29: A horizontal cut of the 2D fluctuating normalized temperature power spectra at $y/D_f = 10$ for $S = 1.07$ (left) and at $y/D_f = 1 - 10$ for $S = 0.3$. The spectra were computed from the whole image and original image was zero padded to increase frequency resolution. The inertial subrange with -1.74 power law, which is close to Kolmogorov's famous $-5/3$ (-1.66) law, a dissipation range and a noise area are also shown. The spectrum was normalized by its corresponding maximum.

[14]Spectra were computed from 1000 instantaneous images as the average of the square of the magnitude of the 2D Fast Fourier Transform of the temperature fluctuations (mean temperature image was subtracted from each instantaneous temperature image). The wavenumber was computed as $k = \frac{i}{\Delta_x N}$, where N is the number of FFT values, Δ_x is the nominal spatial resolution, which was equal to 0.025(mm) and i is the wavenumber index that goes from 1 to N.

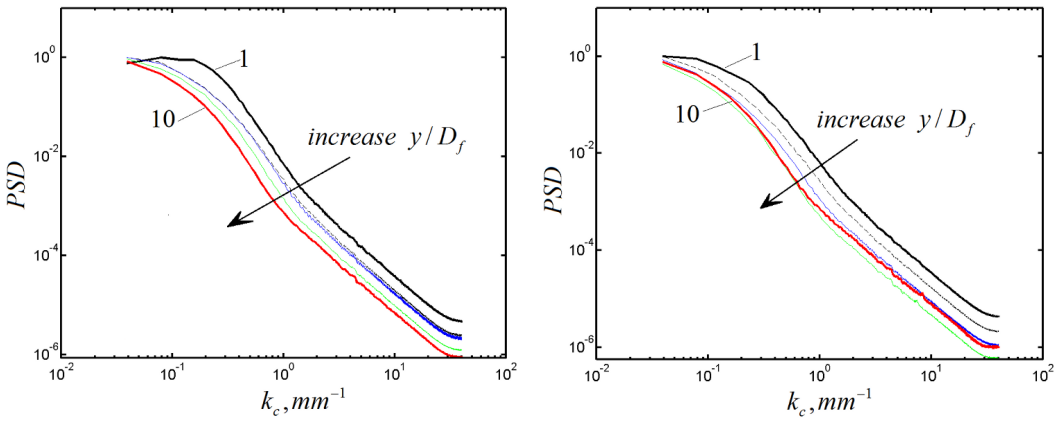

Figure 6.30: A horizontal cut of the 2D normalized fluctuating temperature power spectra at $y/D_f = 1 - 10$ for $S = 058$ (left) and $S = 1.07$ (right). The spectra were computed from the whole image and original image was zero padded to increase frequency resolution. The spectrum was normalized by its corresponding maximum.

Several horizontal cuts of the 2D fluctuating normalized temperature power spectra are shown in Figures 6.29−6.30 as a function of downstream positions y/D_f and swirl numbers S. The power spectrum was normalized by its corresponding maximum for clear visual representation. All of the spectra seem to exhibit a similar appearance, i.e. they are flat at low frequencies, begin to roll off at quite different wavenumbers, decreasing more rapidly in the dissipation range. The temperature spectra shift to lower frequencies with increasing downstream distance, which is clearly seen, e.g. on the right of Figure 6.29. This reduction in frequency can be explained by the increase in dissipative length scales due to higher temperature and perhaps lower velocity. Higher temperature at higher downstream positions leads to higher viscosity and as a result to higher viscosity dumping effects. A small inertial subrange, which can be hardly seen at lower axial distances $y/D_f = 1 - 3$ for $S = 0.3$ is likely, because the turbulence is not fully developed and perhaps due to low local Reynolds number. On the other hand, an extended inertial subrange at higher downstream positions, especially for higher swirl numbers $S = 0.58$ and 1.07 is the sign of fully developed turbulence. Figure 6.30 also shows temperature fluctuations spectra for intermediate and highest swirl number at various downstream positions y/D_f. The spectra are similar for the highest swirl number of 1.07 at $y/D_f = 5, 7$ and 10 indicating developed flow field.

6.6 Thermal dissipation rate

It is typically impossible to measure mixture fraction fields in reacting flows and hence the statistics that are related to the scalar dissipation rate and the mixture fraction in general cannot be obtained. One of the approaches that can be adopted is to investigate the scalar and the thermal dissipation rates separately at the same axial locations and spatial positions in the flow. In fact, this type of measurements cannot be fully exchangeable and can be seen as qualitative measurements rather than quantitative ones. In theory it is possible to obtain the mixture fraction field from the temperature field if assumption

of infinite chemistry is used and one of the major species is measured. This will indicate the 'local regime' of combustion i.e. lean or rich. Nevertheless, in this work the thermal dissipation measurements will be presented as is, without any assumptions. The thermal dissipation rate, considered in this work, is written as squared gradient of the temperature field ∇T multiplied with the thermal diffusivity α.

$$\chi_T = 2\alpha \left(\nabla T\right)^2 = 2\alpha \left[\left(\frac{\partial T}{\partial x}\right)^2 + \left(\frac{\partial T}{\partial y}\right)^2\right] \tag{6.2}$$

$$\alpha = 2 \times 10^{-5} \left(T/300\right)^{1.8} \tag{6.3}$$

The gradient was computed as in case of non−reacting measurements by using the second−order accurate central difference formula. However, it is recommended to use a higher order formula as for example an implicit fourth−order compact finite difference scheme Lele (1992). The same implicit fourth−order compact finite difference scheme was used in Wang (2007). This high order stencil actually acts like a digital bandbass filter that reduces the noise effects in the high wavenumber region.

6.6.1 Dissipation spectra and cutoff length scale

One of the most important questions on laser diagnostic techniques is the issue of spatial resolution and high wavenumber cutoff in turbulent fluctuations. It is well known that the cutoff scale in the kinetic energy dissipation spectrum corresponds to 2% of dissipation spectrum Pope (2000). The scales that are smaller than the wavenumber at 2% of dissipation spectrum contribute little to the total mean dissipation. In this work, the dissipation spectrum or more precisely the power spectral density of fluctuations of radial and axial gradients of temperature are computed as averaged squared Fast Fourier Transform

$$D_x\left(k\right) = \left|\Im\left(\frac{\partial T}{\partial x} - \overline{\frac{\partial T}{\partial x}}\right)\right|^2 \tag{6.4}$$

$$D_y\left(k\right) = \left|\Im\left(\frac{\partial T}{\partial y} - \overline{\frac{\partial T}{\partial y}}\right)\right|^2 \tag{6.5}$$

Figure 6.31 illustrates the windows where spectra of the temperature fluctuations and the thermal dissipation rate spectra are assessed. The dissipation (as well as the temperature fluctuations) spectra were computed from the whole image, which is seen as a rectangle at different downstream positions $y/D_f = 1 - 10$. Spreading of the jet with S is also shown along with the jet spread angles. The half−angle of spreading was defined as the angle between the line joining the maximum mean temperature at various y/D_f and the centreline of the burner.

Figures 6.32−6.34 show a horizontal cut of the 2D normalized spectrum (uncorrected) of the fluctuations of the axial and radial gradients of the temperature for three swirl numbers and various downstream positions $y/D_f = 1 - 10$. The dissipation spectrum was normalized with its corresponding maximum. The horizontal line indicates the 2% level Pope (2000). The dissipation spectrum should decay exponentially after passing the peak value and this is referred as the roll−off region in the current study. If the peak was not

observed, as for example in the axial gradient spectra, the highest value in the measured dissipation spectrum was taken as the reference.

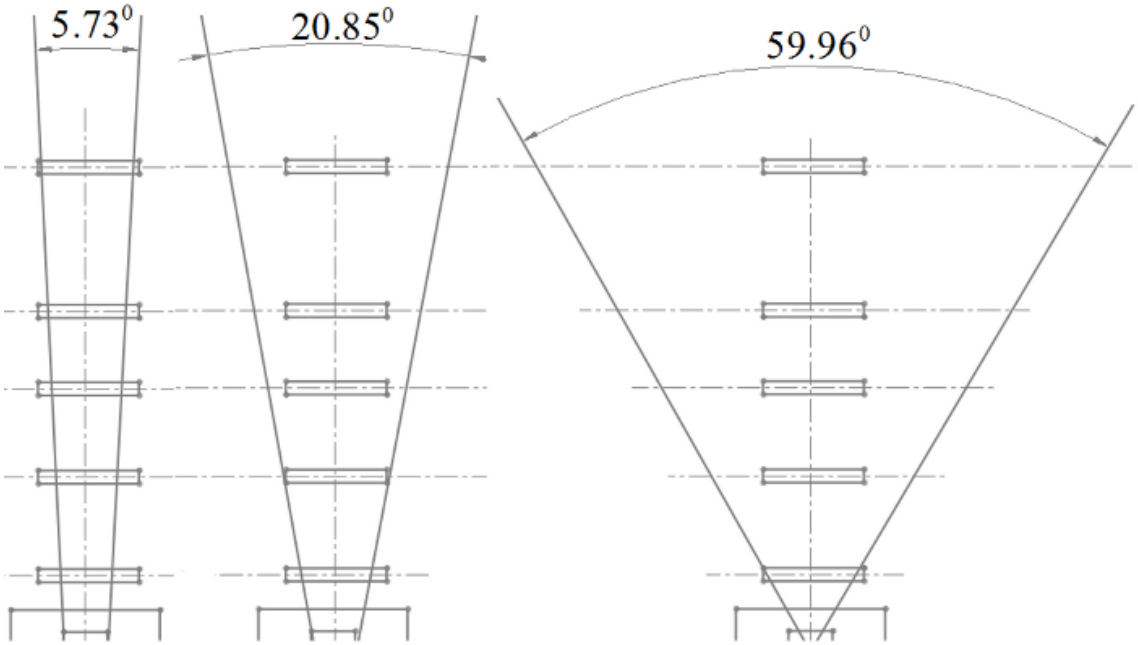

Figure 6.31: Windows where spectra of the temperature fluctuations and the thermal dissipation spectra are assessed. The windows are shown relative to the mean jet structure (temperature) for three swirl numbers of 0.3, 0.58 and 1.07 (from left to right). The spectra were computed from the whole image, which is seen as a rectangle at different downstream positions $y/D_f = 1 - 10$. Spreading of the jet with S is clearly shown along with jet spread angles. The half−angle of spreading was defined as the angle between the line joining the maximum mean temperature at various y/D_f and the centreline of the burner.

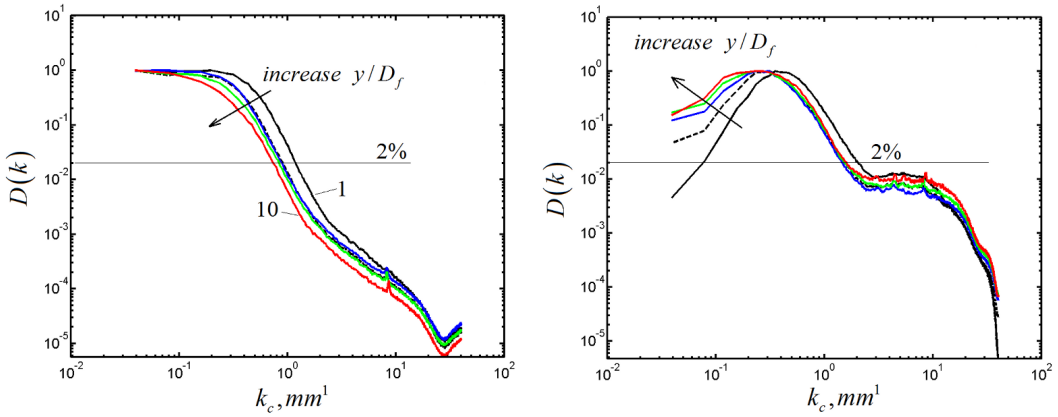

Figure 6.32: A horizontal cut of the 2D normalized spectrum of the fluctuation of axial (left) and radial (right) gradients of temperature $D_(k)$ at $y/D_f = 1 - 10$ for $S = 0.3$. The spectrum was normalized by its corresponding maximum and computed from raw temperature images. The horizontal solid line indicates the 2% level.

A quick observation of the figures above reveal that the dissipation rate spectra computed from radial gradients have a peak, unlike the spectra from the axial gradients. In

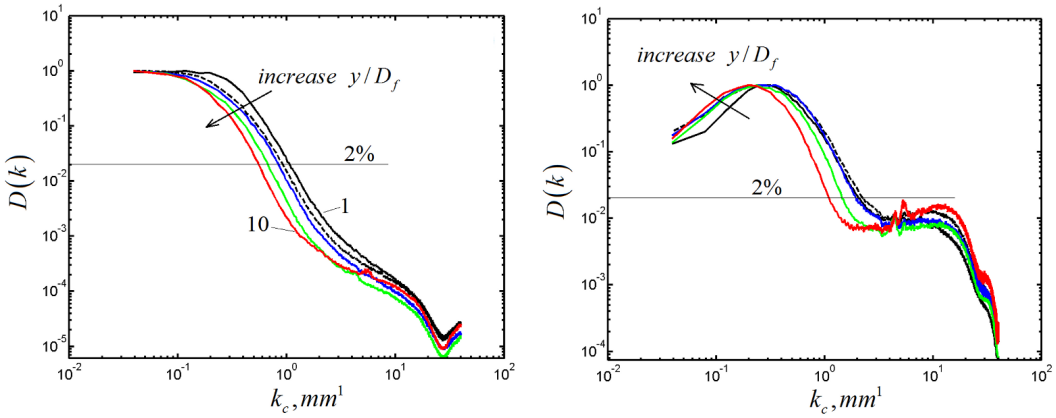

Figure 6.33: A horizontal cut of the 2D normalized spectrum of the fluctuation of axial (left) and radial (right) gradients of temperature $D_(k)$ at $y/D_f = 1 - 10$ for $S = 0.58$. The spectrum was normalized by its corresponding maximum and computed from raw temperature images. The horizontal solid line indicates the 2% level.

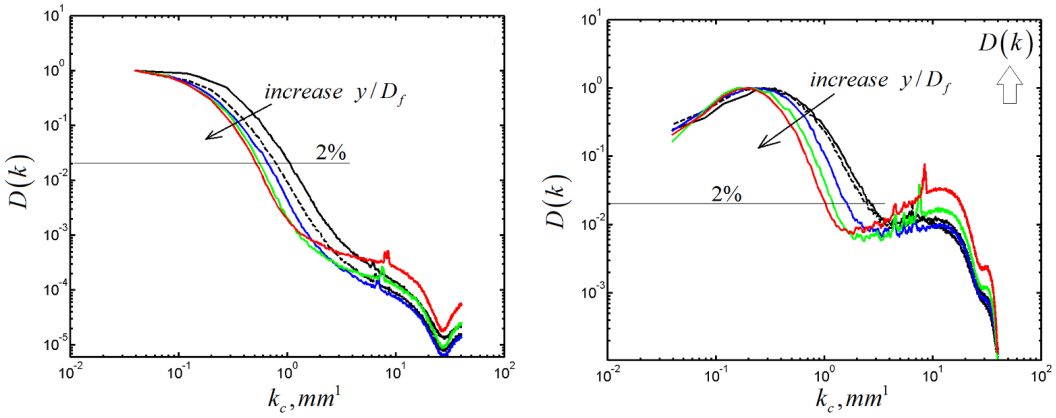

Figure 6.34: A horizontal cut of the 2D normalized spectrum of the fluctuation of axial (left) and radial (right) gradients of temperature $D_(k)$ at $y/D_f = 1 - 10$ for $S = 1.07$. The spectrum was normalized by its corresponding maximum and computed from raw temperature images. The horizontal solid line indicates the 2% level.

both axial and radial cases, the dissipation spectra extend beyond the cut−off scale, so that the noise spectra can be determined. Measurements clearly indicate the noise spectrum at higher wavenumbers, which is also dependent on the swirl number and downstream positions. It is supposed that the noise spectrum is actually related to the temperature and at higher downstream distances and higher swirl numbers (leading to higher temperature) the noise levels are expected to be higher due to lower Rayleigh signal. Since the temperature is inversely proportional to the temperature and the higher temperature leads to lower signal, while the level of the noise typically remains constant, the dissipation spectrum for enhanced mixing will demonstrate larger noise levels, which is clearly seen, e.g. in Figure 6.34.

The dissipation spectra follow the same trend as the power spectra of the temperature fluctuations. The dissipation spectra shift to lower wavenumbers with y/D_f increase for

Table 6.1: Experimentally determined axial (AX) and radial (RA) cut−off length scales (mm^{-1}) measured for $S = 0.3$, 0.58, 1.07 at $y/D_f = 1 - 10$

y/D_f	AX@0.3	RA@0.3	AX@0.58	RA@0.58	AX@1.07	RA@1.07
1	0.85	0.49	0.95	0.45	0.95	0.38
3	1.12	0.62	1.12	0.49	1.28	0.41
5	1.18	0.64	1.22	0.52	1.51	0.62
7	1.2	0.64	1.51	0.69	1.85	0.85
10	1.35	0.67	1.83	0.91	2	0.98

all swirl numbers. Furthermore, the distribution of the thermal dissipation i.e. the shape and extent is quite similar when compared with non−reacting measurements for both axial and radial components (Figure 2.7 on page 62 in Chapter 2). This observation indicates that turbulence structure at the dissipation scales in swirling jet flames is similar to that in non−reacting swirling flows, which is also consistent with Wang *et al.* (2007).

Table 6.1 shows experimentally determined axial and radial cut−off length scales measured in the DLR fuelled swirling flame for three swirl numbers at various downstream positions. The cut−off scales computed from the axial gradients are higher than that computed from radial gradients. The cut−off scales are also dependent on downstream positions and decrease with increase in y/D_f. The turbulence at higher swirl number is expected to be higher and hence a higher cut−off scale is expected, which is also confirmed by the observations. In addition, it was also demonstrated by Wang (2007) that the inverse Rayleigh spectra may be used to determine local cut−off scales for thermal dissipation rate. If the dissipation rate roll−off is assumed, then the cut−off scale may be estimated in any flame where the peak of the dissipation spectrum can be resolved, which is actually equivalent to the Wiener filtering procedure. However, more measurements and additional analyses are clearly needed to clarify these issues.

6.6.2 Temperature dissipation rate

The thermal dissipation structures are investigated in this section at various downstream positions. The thermal dissipation presented here was obtained by using wavelet−based Wiener filtering technique, as described in Chapter . Sample instantaneous images of the thermal dissipation structures (filtered and unfiltered) are shown in Figure 6.35. This figure shows filtered and unfiltered instantaneous images of a gradient squared term of the temperature fluctuations $|\nabla T^{'}|^2$, where the temperature fluctuations were defined as $T^{'} = T - \langle T \rangle$. The raw thermal dissipation rate image appears to be very noisy. In contrast, the filtered thermal dissipation rate is much less noisy. In addition, the results of the dissipative structures from Frank & Kaiser (2006) are also shown[15].

The dissipation rate structures resemble that of scalar dissipation in non−reacting jets and is consistent with Frank & Kaiser (2006). A combined effect of flow shear between the centreline fuel jet and the coflow as well as the flow laminarization due to heat release result in larger dissipation in the radial direction for the lowest swirl number of 0.3. Higher swirl numbers demonstrate 'smeared' and more distributed thermal dissipation fields unlike low

[15]Frank & Kaiser (2006) used high−resolution Rayleigh imaging to measure the detailed structure of the thermal dissipation filed in a turbulent non−premixed $CH_4/H_2/N_2$ jet flame with a jet exit Reynolds number of 152000.

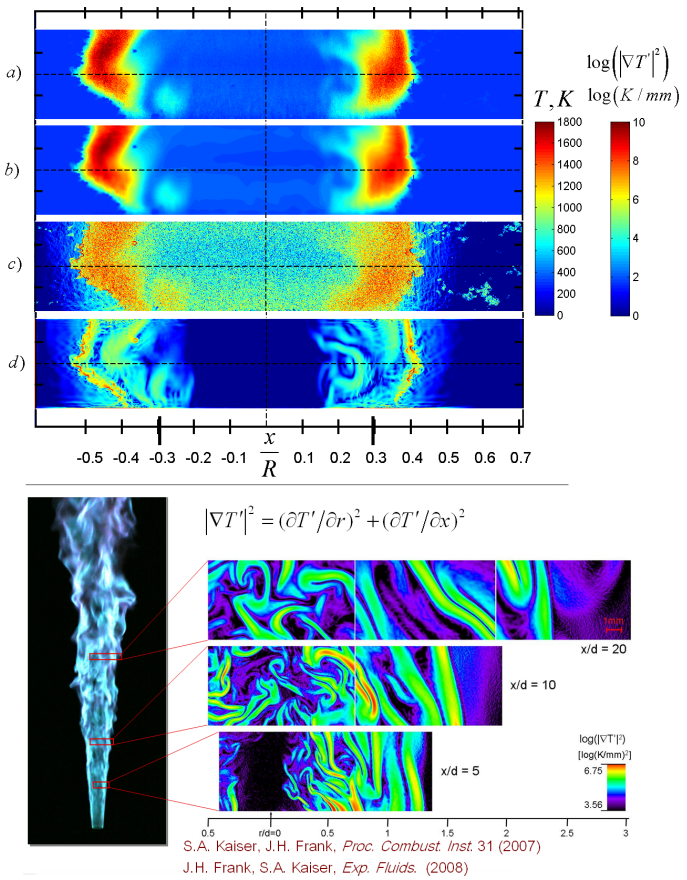

Figure 6.35: Results of the application of the wavelet−based Wiener filter to raw images of temperature. a) Raw temperature obtained from the measurements without filtering; b) Filtered temperature; c) Raw thermal dissipation computed as a gradient squared term of the temperature fluctuations; d) Filtered thermal dissipation. The results on the dissipative structures from Frank & Kaiser (2006) are also shown.

swirl numbers, where the most of the thermal dissipation layers lay within fuel jet shear layer.

Figure 6.36 shows probability density functions $P(C)$ of a gradient squared term of the temperature fluctuation as a function of downstream distance computed from the window located at the jet centreline and from the shear layer, where C was defined as.

$$C = [\ln\left(\left|\nabla T'\right|^2\right) - \overline{\ln\left(\left|\nabla T'\right|^2\right)}]/\sigma_{\ln\left(\left|\nabla T'\right|^2\right)} \tag{6.6}$$

Centreline as well as shear−layer p.d.fs. exhibit features of log−normal distribution with exponential scaling[16] of the tails on the negative side of the dissipation. The high−dissipation positive side of the distribution is apparently log−normally distributed unlike low−dissipation values for all locations in the flow. The 2D dissipation rate exhibits a slope of approximately 2 in the low dissipation portion of the corresponding p.d.f. Similar observations were made by Wang *et al.* (2005) with an explanation that the power−law dependence of the low−dissipation portion of the p.d.f. was a result of the 1D gradient

[16]Exponential scaling appears as a straight line in the semi−log plot. Semi−log plot is an appropriate way of visualising data that are changing with an exponential relationship.

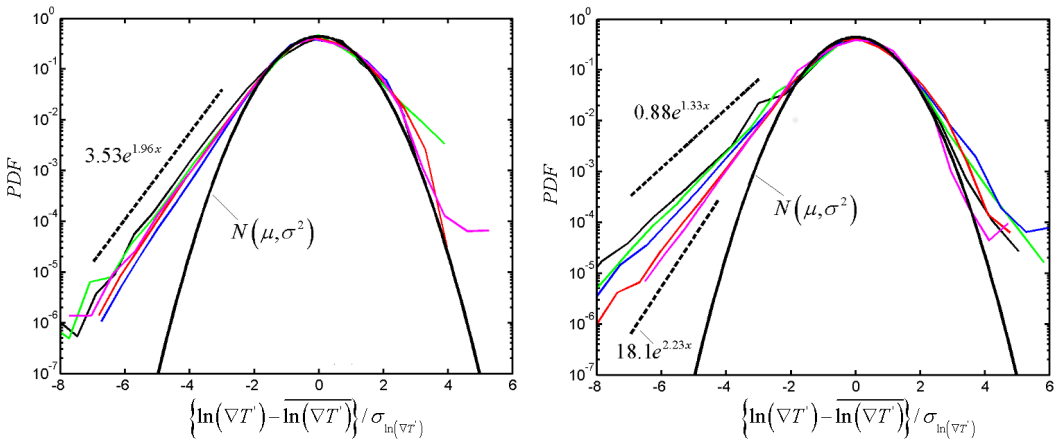

Figure 6.36: Probability density functions (semi−log plot) of a gradient squared term of the temperature fluctuations as a function of downstream distance computed from the window located at the jet centreline (left) and from the shear layer $-0.3x/R$ for $S = 0.3$. Window position is shown in Figure 6.21. Gaussian p.d.f. with $\mu = 0$ and $\sigma = 0.9$ is also shown for comparison.

overestimating the total gradient vector magnitude. These observations are also consistent with the scalar dissipation measurements in non−reacting swirling jets presented earlier.

In non−reacting measurements, the p.d.fs. of the logarithm of the scalar dissipation rate were close to log−normal distributions and the deviation from Gaussian distributions was primarily associated with long tails. It was also demonstrated by quantile plots (q−q plots) of the fluctuations of the logarithm of the scalar dissipation rate. The exponential scaling has been also well documented in non−reacting flows and was reported to be a result of the intermittent nature of the scalar dissipation fluctuations Wang *et al.* (2005), Gurvich & Yaglom (1967). It should be mentioned that several authors indicate substantial deviation from log−normal distribution and even bimodal distribution e.g. Wang *et al.* (2005). Wang reported a bimodal 'double−hump' structure of the dissipation p.d.f. and pointed out that the structure resulted from the intermittent edge of the jet (flapping effects).

6.7 Summary

This chapter presented the characteristics of the temperature field produced by the swirl stabilized burner. Temperature, power spectral density of temperature fluctuations, probability density functions of the temperature fluctuations and thermal dissipation rate measurements in a non−premixed turbulent swirling jet flame were reported. Rayleigh scattering measurement technique was used to obtain the temperature fields as inverse of the Rayleigh signal that was recorded by the CCD camera. The measurements were carried out in swirling reacting DLR fuelled jets as a function of downstream locations as well as a function of the degree of mixing that was quantified by the swirl number. Three swirl numbers were covered, i.e 0.3, 0.58 and 1.07. The measurements were reported within non−dimensional radial and axial coordinates. The temperature measurements were carried out in the region extending up to 10 fuel nozzle diameters at 1, 3, 5, 7 and 10 correspondingly. Temperature measurements were verified by a calibration procedure, which was based on the McKenna burner.

The swirl number highly affected both the temperature distribution and its fluctuations. It was generally observed that the temperature distribution tends to be more uniform with the distance from the burner exit. The centreline temperature increased from nearly ambient temperature (close to the burner exit) to higher values at far away distances from the burner exit and this trend was similar for all swirl numbers even though with different behaviour.

The dissipation rate structures resembled that of scalar dissipation in non−reacting jets and were consistent with Frank & Kaiser (2006). Dissipation rate spectra were computed and dissipation cut−off scales were determined. The cut−off scales increased with downstream distance for each swirl number. At the highest swirl number and at $y/D_f = 1$ the cut−off scale was the smallest, which suggested that the resolution requirements would be the most stringent in the near burner exit regions. In addition, it may be worth to consider, e.g. the 'flame' spectra from small regions within flame zones. However, the discussion of the local thermal dissipation spectra from several windows within 'hot' and 'cold' regions is beyond the scope of the present work.

Probability density functions of a gradient squared term of the temperature fluctuation were computed for different locations and operating conditions. The high−dissipation positive side of the p.d.f. was apparently log−normally distributed unlike low−dissipation values for all locations in the flow. This was also consistent with non−reacting measurements, presented earlier.

7 Flow velocity in swirl-stabilised burner

This last chapter evaluates the occurrence of the recirculation zone by measuring the flow velocity in the swirl−stabilized burner. The recirculation zone and precessing vortex core (PVC) always exist in swirling flows and might be a key parameter in flame dynamics. The formation of the PVC and flame stabilisation is quite well documented in most practical applications, e.g. by Milosavljevic (1990), Abdeli & Masri (2010), Syred & Beer (1973), Syred (2006), Gupta *et al.* (1984), Cassidy & Falvey (1970), Chanaud, (1965). The flame is stabilised in regions of relative low velocity, formed by the recirculation zone. In this work, the velocity measurements in the swirl−stabilized burner were obtained by particle image velocimetry (PIV).

7.1 Mean velocity

In this work, both isothermal and reacting flows were examined as follows: The first case (a) was isothermal flow without central jet, i.e. only swirling coflowing air, the second case (b) was the central fuel jet+swirling coflow and finally the reacting flow (combustion of DLR fuel) was considered. Safety reasons dictated that the investigations under non−reacting conditions were performed by using air instead of 'fuel jet' of $N_2/CH_4/H_2$ mixture. The momentum ratio between the central fuel jet and the swirling coflow was conserved. Under reacting conditions, the investigations were performed by using the same fuel (DLR) as in Rayleigh thermometry with global equivalence ratio of 0.9. The flow statistics are discussed here in terms of the mean absolute velocity, the vorticity and the standard deviation of velocity fluctuations, which were computed as follows (u,v denote axial and radial velocity components):

$$V = \sqrt{u^2 + v^2} \tag{7.1}$$

$$\sigma_V = \sqrt{\frac{1}{N}\sum_{i=1}^{1000}\left(V - \overline{V}\right)^2} \tag{7.2}$$

Figure 7.1 shows mean velocity vectors for the lowest swirl number of 0.3 under isothermal and reacting conditions. As it can be seen from the Figure , the flow exhibits a jet−like structure, which is expected under such low swirl number conditions. Under isothermal conditions without central jet, the flow field is not uniform at the distances close to the burner exit $y/D \approx 2$ and almost uniform further downstream. A low velocity zone on the right hand side at the burner exit in case a) is perhaps due to the central fuel jet pipe acting as a bluff body and generating low velocity region along y−axis. Once the central jet is added, the low velocity region disappears.

Under isothermal conditions with central jet, the flow field is similar to that found without central jet, except that the velocity along the centreline jet remains nearly constant at all downstream locations. The flow asymmetry persists up to $y/D \approx 2.56$ and disappears further downstream. During combustion conditions, the flow field is generally symmetric with well−defined inverted cone shape, unlike higher swirl numbers, which result in tulip shape and as expected, no central recirculation zone is found for $S = 0.3$. The central jet velocity remains nearly constant (≈ 6 (m/s)) within ≈ 50 (mm) distance from the burner exit and decays rapidly to low velocity values further downstream. This decay may be explained by the rapid mixing and subsequent combustion of the fuel jet.

Figure 7.2 shows mean velocity vectors for intermediate swirl number of 0.58 under isothermal and reacting conditions. The swirling motion created a quite large but weak internal recirculation zone under isothermal without central jet conditions. However, under isothermal condition with central jet, no developed recirculation zone is observable. This may be due to the fact that the weak recirculation zone due to rotating swirling coflow cannot overcome momentum of the central axial jet. Under the weak recirculation zone is understood the magnitude of the velocity only within the recirculation zone, and not the extent or velocity directions. However, when no central fuel jet is present, the weak recirculation zone is able to establish itself.

On the other hand, the presence of the recirculation zone, even though it is weak, decreases the velocity of the central fuel jet and leads to a rapid velocity decay, when compared to the lowest swirl number of 0.3. The recirculation zone also acts as an aerodynamic blockage, which creates low velocity stagnation zones between the central fuel jet and the rotating coflow at $\approx \pm 0.39$ x/R; where R is the inner radius of the air coflow annulus. It is, therefore, suggested that the extent of the recirculation zone is dependent on the swirl number, which is known from the theory, as well as on the momentum ratio between the central and coflowing jets. In addition, a clearly visible tulip shape distribution is observed under both isothermal and reacting conditions, regardless of the presence of the fuel centreline jet.

Under combustion conditions, a fully developed recirculation zone is still not clearly visible. However, the velocity of the central fuel jet decreases very rapidly and reaches zero at a certain distance above the burner. This distance is called a forward stagnation point. The forward stagnation point is clearly seen at $\approx$ 65(mm) or 1.28 y/D burner diameters. Therefore, a partial recirculation zone is formed and is not symmetric. This may be due to inherent asymmetry in swirling with axial fuel central jet injection. The asymmetry of the temperature and mixture fraction was also reported in LIF and Rayleigh thermometry experiments and would be discussed in more details later in this chapter.

Figure 7.3 shows mean velocity vectors for the highest swirl number of 1.07 under isothermal and reacting conditions. Unlike intermediate swirl number of 0.58, the recirculation zone is fully developed and seen under all conditions. During isothermal condition without centreline jet, the recirculation zone has the maximum velocity magnitude of circa 6 (m/s) and the extent of this zone is up to ≈ 2.5 burner diameters. The presence of the central jet does not modify the extent of the recirculation zone. However, the velocity magnitude is lower due to the central jet momentum. Strong internal recirculation zone collides with the central fuel jet and since the momentum of the reverse flow is higher than

the central jet, a well defined recirculation zone is formed Gupta (1984). The velocity field has also a well defined tulip shape for both isothermal and reacting conditions.

7.2 Velocity fluctuations

Figure 7.4 shows standard deviation of velocity fluctuations computed from both isothermal and reacting conditions for $S = 0.3$. Under isothermal conditions without central jet, the velocity fluctuations are high close to the burner exit. However, a qualitative picture is quite different. Under isothermal without central jet, the highest velocity fluctuations are within 50 (mm) distance from the burner exit and rapidly decrease further downstream. Under isothermal conditions with central jet, the velocity fluctuations persist at all downstream locations, which may be related to the jet intermittency due to PVC. The central jet exhibits low fluctuations at the jet exit as expected. During combustion, the standard deviation of velocity fluctuations for $S = 0.3$ is different from that found in isothermal jets. The velocity fluctuations along the central jet remain approximately constant, while the highest fluctuations are observed within $0 < y/D < 1$.

Figure 7.5 shows standard deviation of velocity fluctuations for both isothermal and reacting conditions for $S = 0.58$. Under all conditions, the velocity fluctuations within the confines of the recirculation zone are quite low and equal approximately to $2-3$ (m/s). Higher velocity fluctuations are always observed at the interface between the central fuel jet and the swirling coflow and reach ≈ 5 (m/s) under isothermal conditions and $\approx 6-7$ (m/s) under reacting conditions. During the combustion process, the velocity fluctuations are higher than those under isothermal conditions and persist up to ≈ 2 burner diameters. Under isothermal conditions, the highest velocity fluctuations are observed close to the burner exit, up to one burner diameter at the radial distances that correspond to the shear layer between the central jet and the coflow and rapidly decrease further downstream. However, high velocity fluctuations still persist along central jet under isothermal conditions even when no central jet is present. This is somehow surprising and may be perhaps related to the intermittency in the centreline region. At present, the understanding of the intermittency is still limited and no further conclusions are possible except that higher turbulent fluctuations are observed along the centreline. In addition, it can also be suggested that the fluctuations along the centreline are not associated with the axial fuel jet, because an identical picture is seen in both cases, with and without centreline jet. During combustion, the centreline velocity fluctuations seem to be the same for all downstream distances.

Figure 7.6 shows standard deviation of velocity fluctuations for both isothermal and reacting conditions for $S = 1.07$. The same trend as for $S = 0.58$ is clearly observed i.e. higher velocity fluctuations during combustion at the interface between the central fuel jet and the swirling coflow. However, the magnitude of fluctuations is higher and reach ≈ 9 (m/s). The distribution of the velocity fluctuations is more pronounced and high velocity fluctuation zones persist up to 4 burner diameters. The distribution of velocity fluctuations is symmetric unlike under low swirl operating conditions.

7.3 Vorticity

Vorticity has been regarded as an important characteristic of turbulence and hence is presented here. The vorticity is instantaneous rigid body−like vortex of fluid particles rotating at given angular rates without shear deformation, i.e. without relative velocity between adjacent fluid particles. The vorticity can be interpreted as twice the instantaneous rigid body rotation rate of the fluid particles (Panton,1984) and is defined as the curl of the velocity field $V(x, y, z, t)$ as follows:

$$\omega\left(x, y, z, t\right) = \nabla \times V\left(x, y, z, t\right) \tag{7.3}$$

In this work, the vorticity was computed from the velocity gradients of axial and radial velocity components as follows:

$$\omega = \frac{\partial u}{\partial y} - \frac{\partial v}{\partial x} \tag{7.4}$$

Figures 7.7−7.9 show measured mean velocity vorticity for $S = 0.3 - 1.07$ at different downstream positions for a) isothermal coflow only (no central axial jet), b) isothermal coflow+central axial jet and c) combustion (axial jet of DLR fuel+coflow). Mean vorticity was computed from mean images shown in Figures 7.1−7.3. It is clearly seen that for low swirl number of 0.3 and isothermal flow without central jet (a) in Fig. 7.7), the flow is generally irrotational, which is indicated by very low vorticity. However, for the same swirl number but for reacting conditions, the combustion process increases the vorticity significantly. In case a), the maximum vorticity was circa $300(s^{-1})$, while in case c) the vorticity reached approximately $800(s^{-1})$. It is interesting to note that the decay rate at which vorticity progressively decreases is considerably large. This is shown as c) in Figure 7.7 where red colour indicates high level of vorticity. The vorticity magnitude close to the central fuel pipe is very small in cases a) and b) and becomes larger with increasing distance from the burner centreline, which is clearly seen in Figure 7.7.

Figure 7.8 shows measured mean vorticity distribution for $S = 0.58$. Similar trend as for $S = 0.3$ is clearly observed. However, the vorticity magnitude is higher as expected due to stronger swirl and hence, higher pressure gradients along the burner centreline and the surrounding. This creates a large zone of back−flow, which is termed as recirculation zone. Positive and negative vorticity indicate flow rotation in opposite directions, as expected in swirling flows. Next critical observation is that the vorticity field is highly influenced by the flow regime, i.e. combustion or isothermal than the velocity.

Figure 7.9 shows measured mean vorticity distribution for the highest swirl number of 1.07. The vorticity field has similar characteristics as for $S = 0.58$ and is characterized by higher vorticity magnitude during combustion. The positive effect of higher vorticity magnitude during combustion is the improved mixing and subsequent combustion. This higher vorticity magnitude during combustion can be explained by non−uniform spatial temperature distribution, which results in density gradients. Therefore, the effects of the combustion process on the vorticity and the effect of vorticity on the combustion process are mutual.

7.4 Formation of the recirculation zone

The present PIV measurements confirm that the flow shape was symmetrical for $S = 0.3$, and slightly asymmetrical for $0.58-1.07$ as for the LIF and Rayleigh measurements. Most analysis of swirling flows are based on the assumption of axisymmetric flow shape. However, asymmetries are found in practice, which was demonstrated by three independent measurement techniques. Kito (1984) pointed out that small deviation of velocity distribution from symmetry in the inlet section can cause non−negligible asymmetry at downstream sections of the flow. It has been therefore concluded that this particular swirl−stabilized burner had small asymmetries in the flow development section, which resulted in deviation of velocity distribution at donwstream locations that in turn resulted in asymmetry of scalar distribution as well as the temperature. On the top of that, Kito also suggested that the direction of precession of the vortex core was always in the same direction as the swirl for low swirl numbers in the range of $0 < S < 0.4$.

This somehow contradicts with Dellenback *et al.* (1988). Dellenback pointed out that for $0 < S < 0.15$ the direction of precession of the vortex core was opposite to the swirl and for higher swirl number, the direction of precession was in the same direction as the swirl. The asymmetry of the flow field produced by the burner was also reported by Milosavljevich (1994), where the effect of asymmetry was even more pronounced due to the presence of a quarl. The presence of the quarl also resulted in larger recirculation zones, which was reported by Milosavljevich. The recirculation zone seemed to increase considerably due to the quarl opening angle and length. This is also consistent with Dixon (1982). The amount of recirculated mass flow increases with swirl number. On the other hand, the rate of increase of the recirculated mass flow rate decreases when swirl number becomes greater than one Weber & Dugue (1992).

In addition, no external recirculation zone for low and high swirl jets was found, which could be linked to the absence of confinement. However, ambient air entrainment is clearly observed close to the burner exit. The entrainment is larger for higher swirl number indicating essentially the mixing with the ambient air. Regarding flame stabilization, it can be suggested that the flame is stabilized by both the burnt products, which are recycled into fresh reactants by the outflowing coflow, as well as by lower axial velocity. Since low and even intermediate swirl number cannot create well−defined recirculation zone, there must be an alternative mechanism of flame stabilization, which can be linked to the presence of low velocity stagnation zones[1]. These zones are formed due to the difference in velocity between the fuel jet and the coflow. The flame stabilization can also be linked to the lower axial velocity that may match the laminar burning velocity, even though this statement needs to be revised.

It should be noted that in a practical combustion system with confinement, the flow field, the recirculation zone and the flow statistics can be quite different from that presented in this work. The recirculation zone and the flame stabilization as well as velocity fluctuations may be greatly influenced by the flame confinement. It is also suggested that higher velocities near the flame confinement (e.g. along quarl or combustor walls) will result in

[1] There is a number of definitions of a stagnation zone, e.g. is defined as the region where the static pressure exceeds the distant ambient pressure. Charles E. Baukal. *Heat Transfer in Industrial Combustion.* CRC Press LLC, 2000. It is also convenient lo link a stagnation zone to velocity distribution.

higher velocity fluctuations.

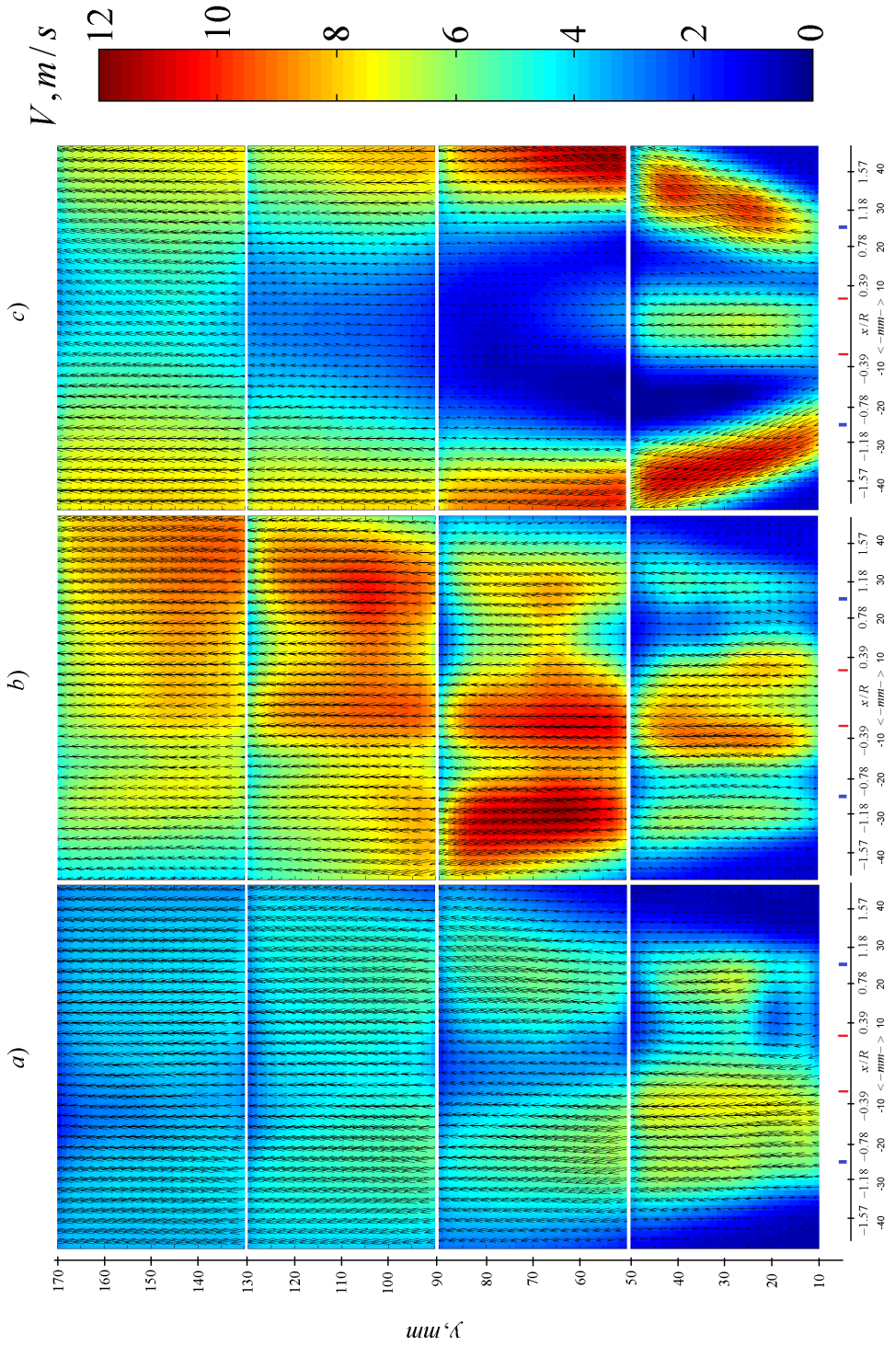

Figure 7.1: Measured mean velocity vectors for $S = 0.3$ at different downstream positions. a) Isothermal coflow only (no central axial jet), b) Isothermal coflow+central axial jet c) Combustion (axial jet of DLR fuel+coflow). Colours represent absolute mean velocity computed from 1000 instantaneous images at 2.5(Hz). The radial coordinate was normalized with the inner radius R of the air coflow annulus.

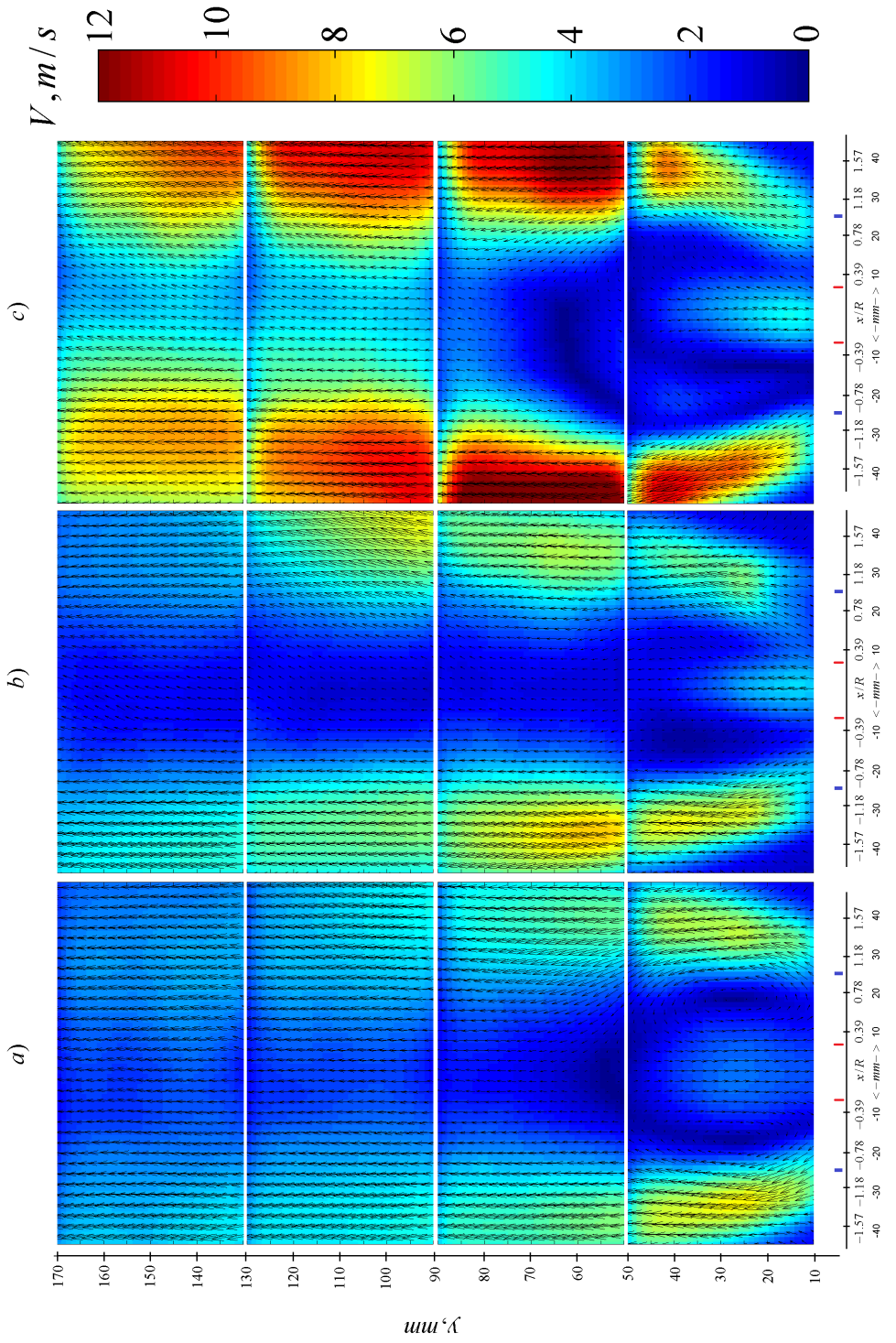

Figure 7.2: Measured mean velocity vectors for $S = 0.58$ at different downstream positions. a) Isothermal coflow only (no central axial jet), b) Isothermal coflow+central axial jet c) Combustion (axial jet of DLR fuel+coflow). Colours represent absolute mean velocity computed from 1000 instantaneous images at 2.5(Hz). The radial coordinate was normalized with the inner radius R of the air coflow annulus.

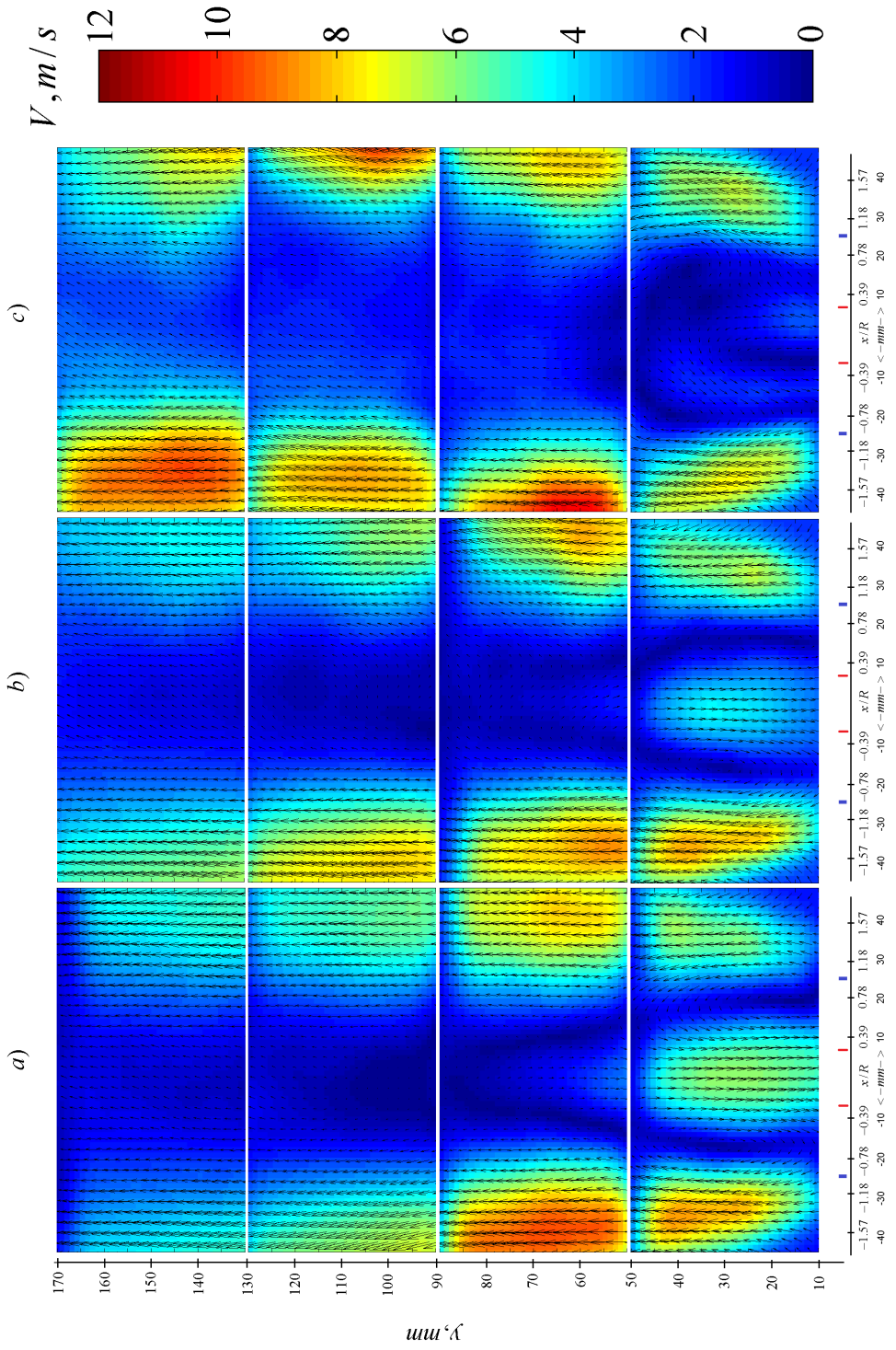

Figure 7.3: Measured mean velocity vectors for $S = 1.07$ at different downstream positions. a) Isothermal coflow only (no central axial jet), b) Isothermal coflow+central axial jet c) Combustion (axial jet of DLR fuel+coflow). Colours represent absolute mean velocity computed from 1000 instantaneous images at 2.5(Hz). The radial coordinate was normalized with the inner radius R of the air coflow annulus.

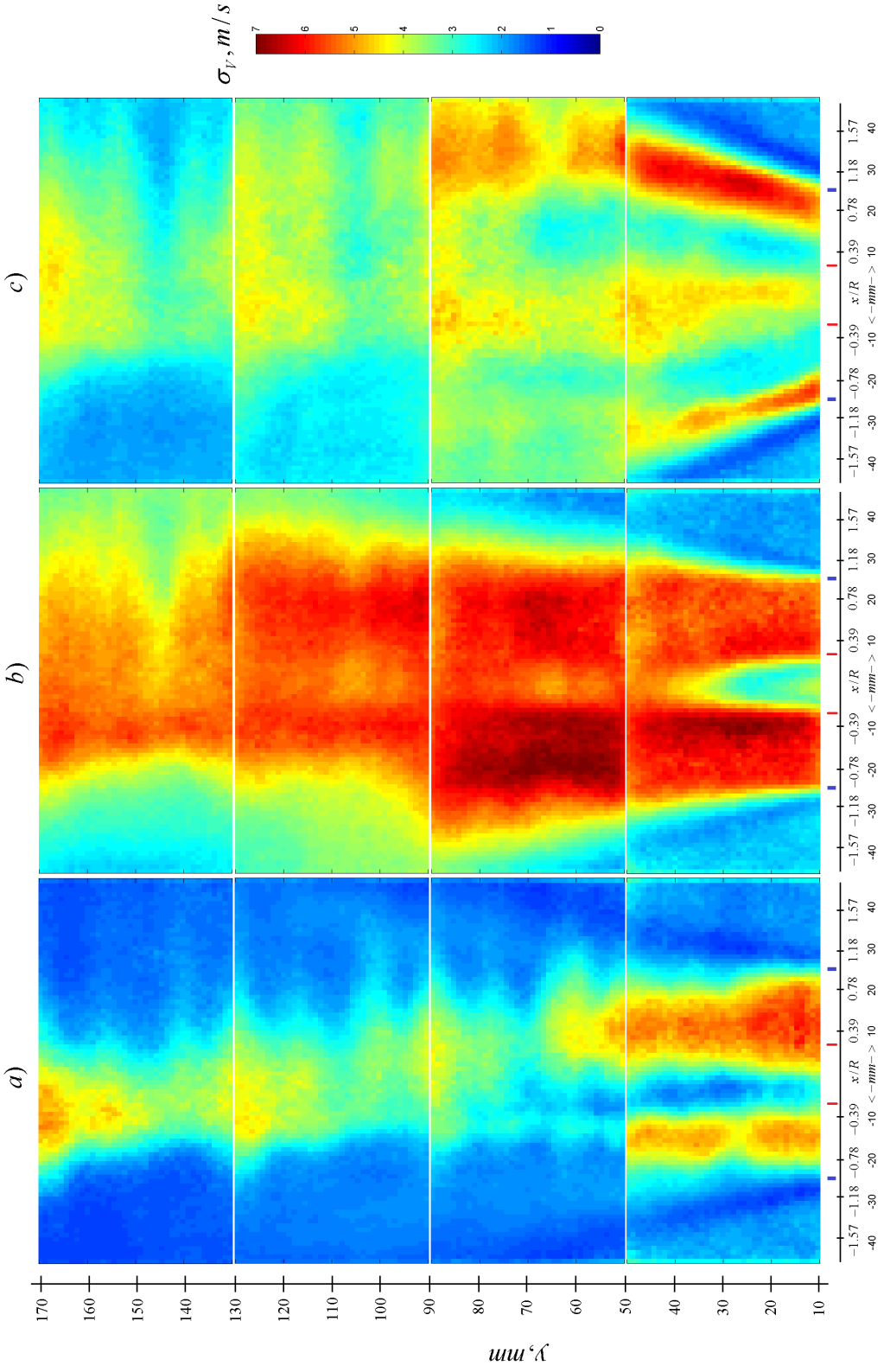

Figure 7.4: Measured standard deviation of velocity fluctuations for $S = 0.3$ at different downstream positions. a) Isothermal coflow only (no central axial jet), b) Isothermal coflow+central axial jet c) Combustion (axial jet of DLR fuel+coflow). Standard deviation was computed from 1000 instantaneous images at 2.5(Hz). The radial coordinate was normalized with the inner radius R of the air coflow annulus.

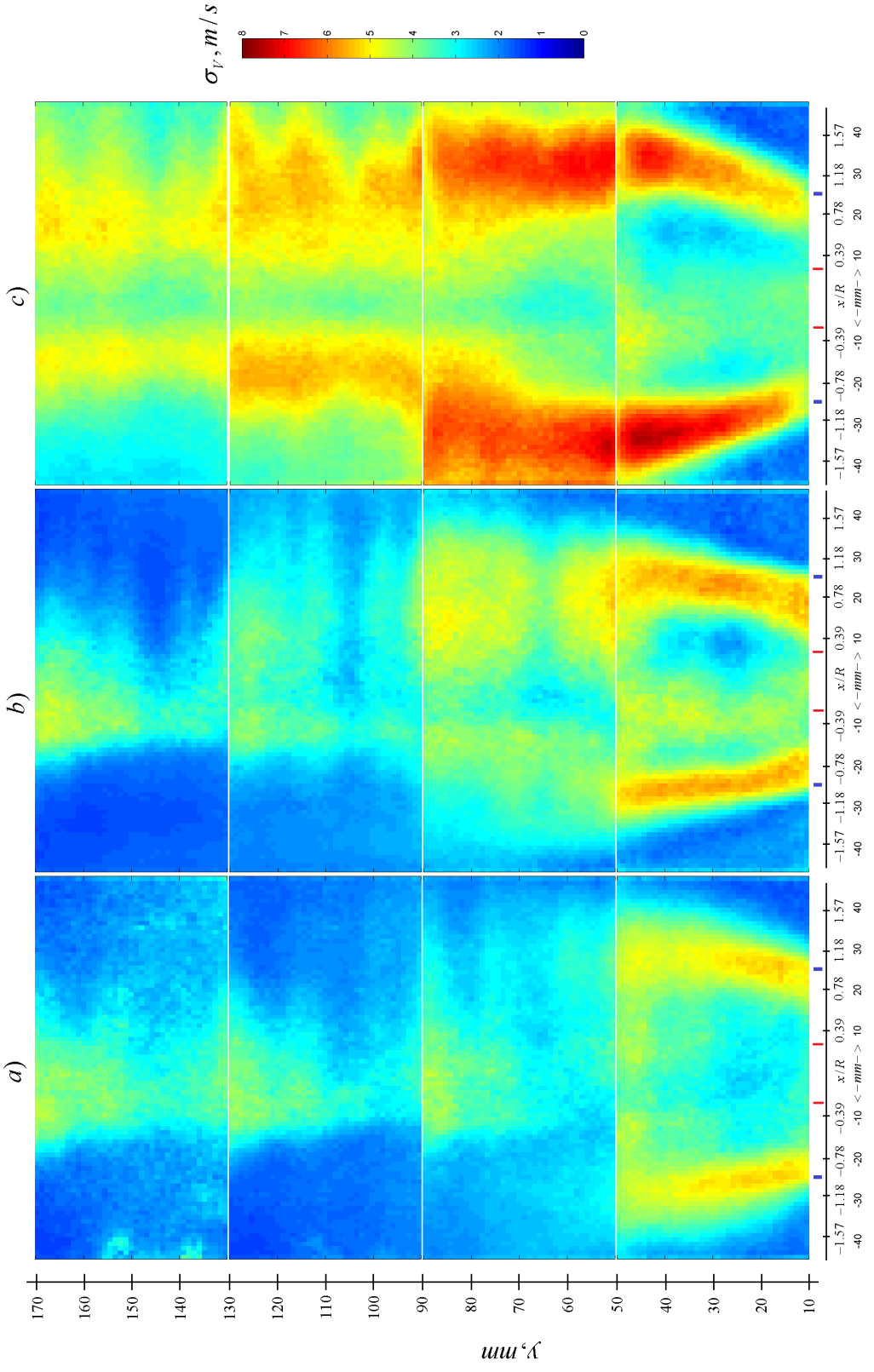

Figure 7.5: Measured standard deviation of velocity fluctuations for $S = 0.58$ at different downstream positions. a) Isothermal coflow only (no central axial jet), b) Isothermal coflow+central axial jet c) Combustion (axial jet of DLR fuel+coflow). Standard deviation was computed from 1000 instantaneous images at 2.5(Hz). The radial coordinate was normalized with the inner radius R of the air coflow annulus.

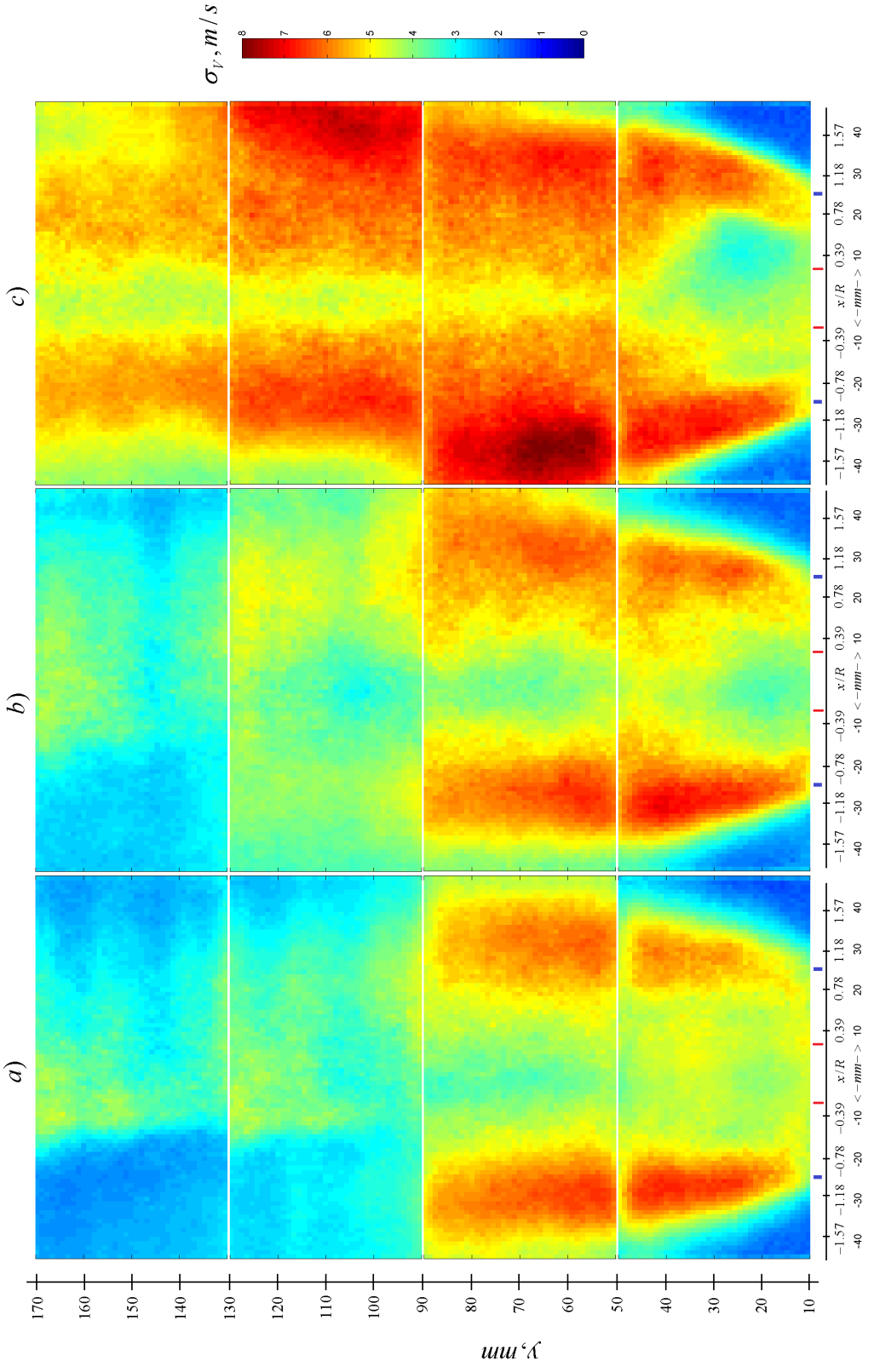

Figure 7.6: Measured standard deviation of velocity fluctuations for $S = 1.07$ at different downstream positions. a) Isothermal coflow only (no central axial jet), b) Isothermal coflow+central axial jet c) Combustion (axial jet of DLR fuel+coflow). Standard deviation was computed from 1000 instantaneous images at 2.5(Hz). The radial coordinate was normalized with the inner radius R of the air coflow annulus.

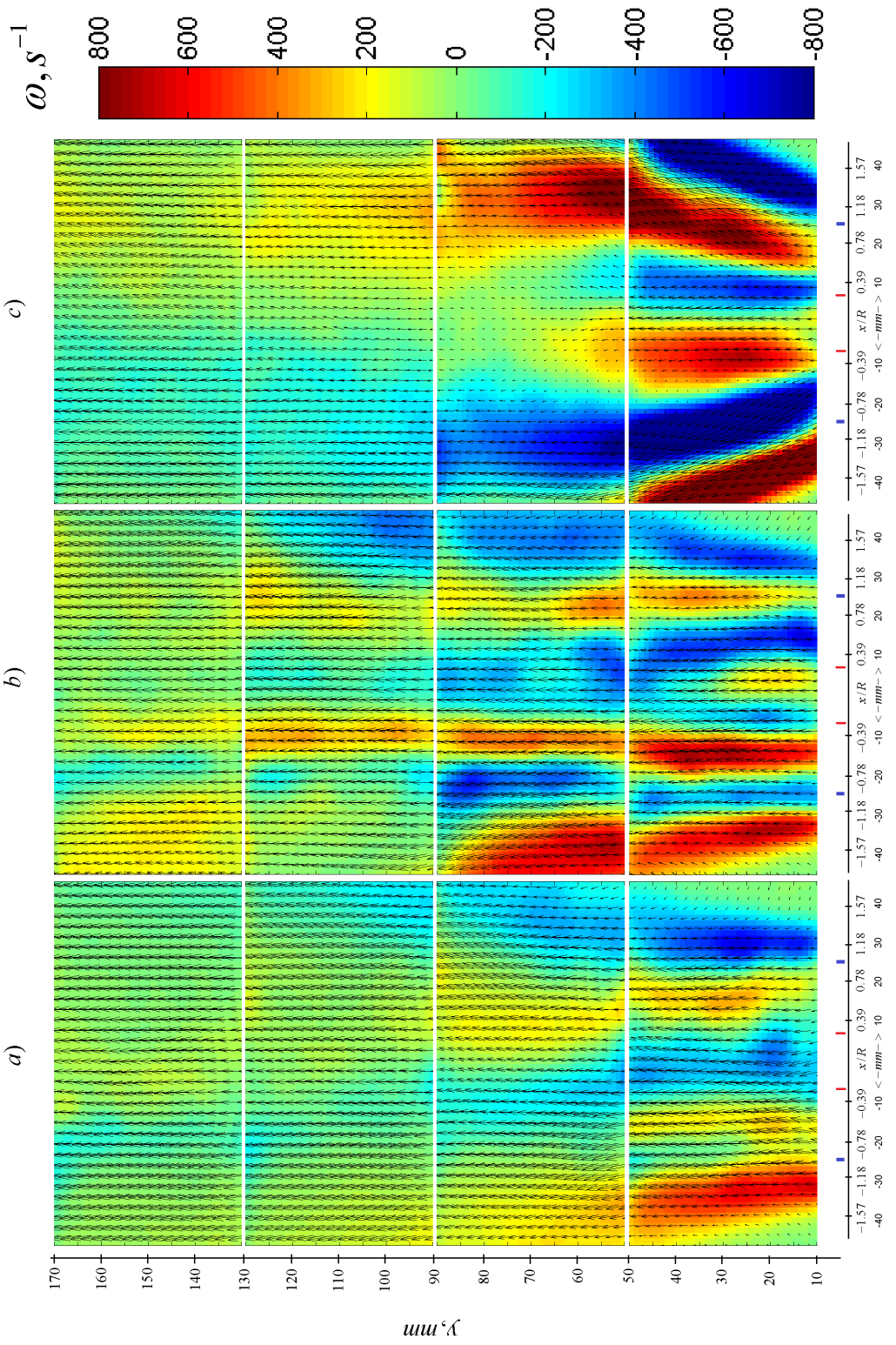

Figure 7.7: Measured mean velocity vorticity for $S = 0.3$ at different downstream positions. a) Isothermal coflow only (no central axial jet), b) Isothermal coflow+central axial jet c) Combustion (axial jet of DLR fuel+coflow). Vorticity was computed from mean image shown in Figure 7.1. The radial coordinate was normalized with the inner radius R of the air coflow annulus. Velocity vectors are also shown on the top of this Figure for convenience.

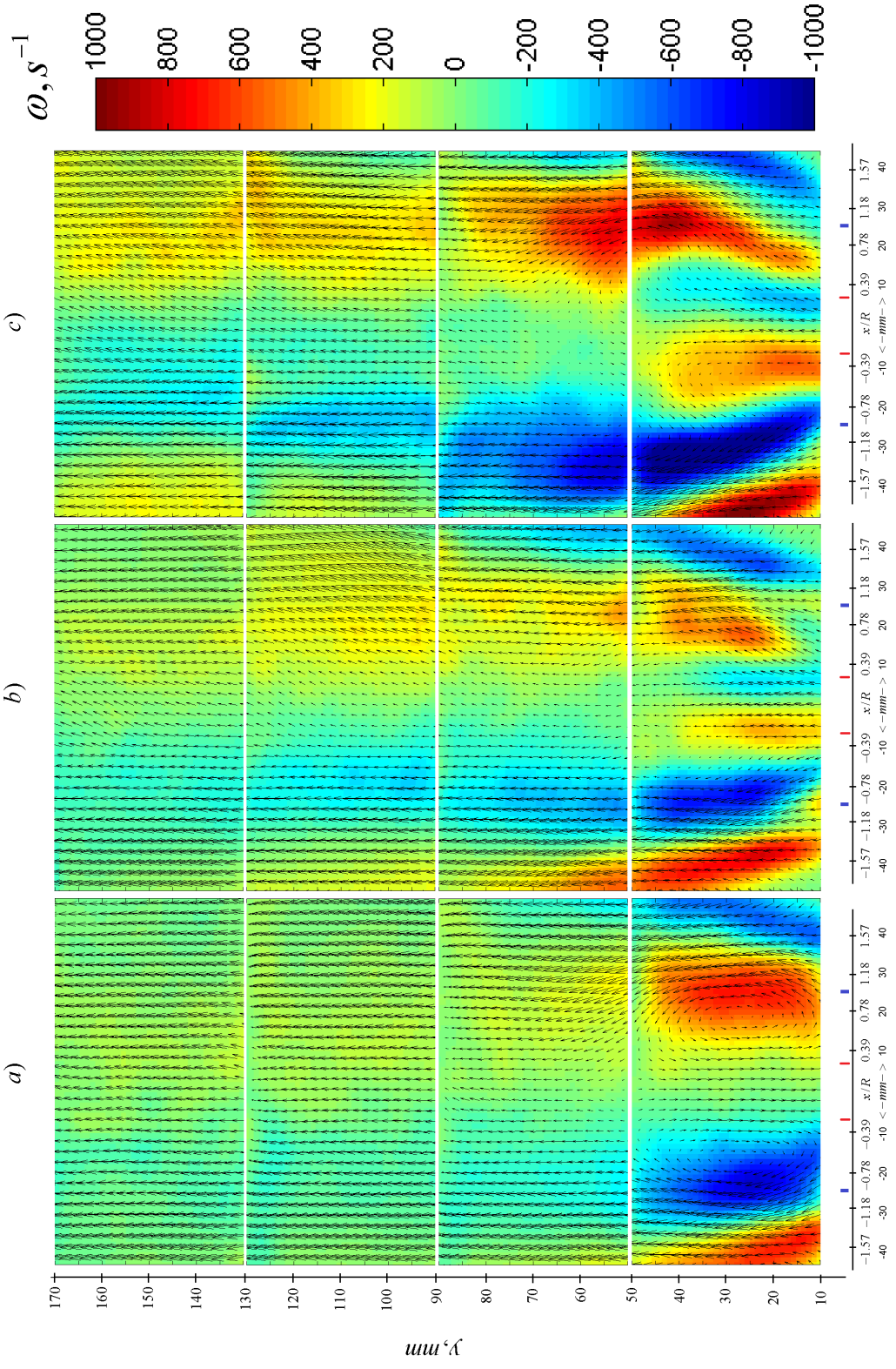

Figure 7.8: Measured mean velocity vorticity for $S = 0.58$ at different downstream positions. a) Isothermal coflow only (no central axial jet), b) Isothermal coflow+central axial jet c) Combustion (axial jet of DLR fuel+coflow). Vorticity was computed from mean image shown in Figure 7.2. The radial coordinate was normalized with the inner radius R of the air coflow annulus. Velocity vectors are also shown on the top of this Figure for convenience.

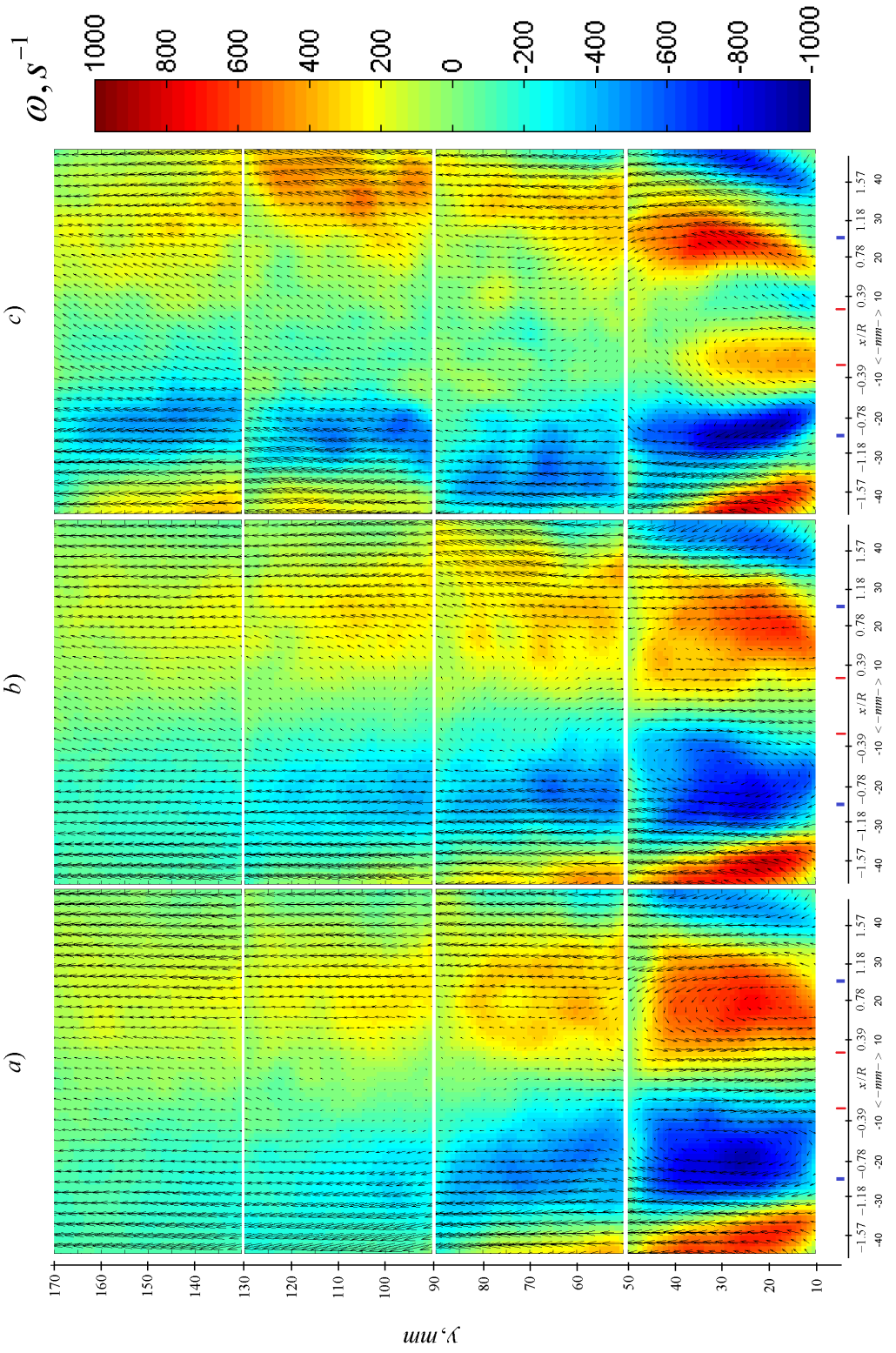

Figure 7.9: Measured mean velocity vorticity for $S = 1.07$ at different downstream positions. a) Isothermal coflow only (no central axial jet), b) Isothermal coflow+central axial jet c) Combustion (axial jet of DLR fuel+coflow). Vorticity was computed from mean image shown in Figure 7.3. The radial coordinate was normalized with the inner radius R of the air coflow annulus. Velocity vectors are also shown on the top of this Figure for convenience.

7.5 Flow structures

Turbulent flow consists of different structures with different length scales (Tennekes & Lumley, 1972). In the context of swirling flow it is interesting to investigate the so−called dominant flow structures or large scale structures. These large scale structures can be associated with flow recirculation, flow vortexes and the PVC. It is expected that the fundamental large scale structures will be different for different swirl numbers. The large scale structures are responsible for flow dynamics and their superposition and interactions cannot be readily evaluated from the mean or standard deviation of velocity fluctuations images. Proper Orthogonal Decomposition (POD), which was proposed by Lumley (1967) to study structure of inhomogeneous turbulent flows, is used in this work.

The proper orthogonal decomposition[2] is a powerful generalised Fourier expansion of a random process using a sum of orthogonal basis functions, which is aimed at obtaining low−dimensional approximation of a high−dimensional process. The POD basis functions $\phi(x)$ are the functions that maximize the following expression Soulopoulos (2009).

$$\frac{\left\langle [\phi(x)\, u(x,t)]^2 \right\rangle}{[\phi(x)\, \phi(x)]} \tag{7.5}$$

where [] is the scalar product and $\langle \cdots \rangle$ is an ensemble averaging procedure over the realizations of $u(x,t)$.

The basis functions are orthogonal to each other so that $[\phi_i(x)\, \phi_j(x)] = \delta_{ij}$, where δ_{ij} is Kronecker delta. The maximisation of expression 7.5 takes place when.

$$\int R\left(x, x'\right) \phi\left(x'\right) dx' = \lambda \phi(x) \tag{7.6}$$

$$R\left(x, x'\right) = \left\langle u(x)\, u^T\left(x'\right) \right\rangle \tag{7.7}$$

where $R\left(x, x'\right)$ denotes the cross correlation matrix of the measurements (superscript T denotes the transpose) and λ denotes eigenvalues.

With the above decomposition the original velocity field $u(x,t)$ can be decomposed into a sum of product of basis functions (eigen functions) $\phi_n(x)$ and the POD coefficients a_i as follows:

$$u(x) = \sum_{i=1}^{\infty} a_i \phi_i(x) \tag{7.8}$$

where i represents the number of eigen functions and a_i are POD coefficients.

The POD coefficients are connected to the eigen values λ of the maximisation problem 7.5 ($\langle a_i a_j \rangle = \delta_{ij} \lambda_i$) and are determined as follows:

$$a_i = [u(x)\, \phi_i(x)] \tag{7.9}$$

The solution of equation 7.5 is found by using the snapshot method, which was intro-

[2]Different names also exist e.g. Principal Component Analysis (PCA), Singular Value Decomposition (SVD), Empirical Eigenfunction Decomposition, Karhunen-Loeve procedure and more.

duced by Sirovich (1987) due to its simplicity and low time complexity[3]. In this method, the correlation matrix R is approximated from a set of N measurements (snapshots[4].), which are uncorrelated with each other. The detailed description of the method of snapshot can be found e.g. in work of Sirovich (1991, 1987). A detailed mathematical description of POD methods can be found, e.g. in the work of Holmes *et al.* (1996) and Berkooz *et al.* (1993).

In this work, the POD method is implemented according to Shim *et al.* (2013) and programmed by using MATLAB (Appendix C) as follows. The mean velocity field from the PIV data is subtracted from instantaneous 2D PIV images so that only velocity fluctuating parts are used $u^{'}(X,t) = (u_m^n - \bar{u}, v_m^n - \bar{v})$, where u_m^n and v_m^n are axial and radial components of velocity correspondingly. Index n runs through the N number of instantaneous 2D PIV images and index m runs through the M points of velocity vectors in a given instantaneous image. All fluctuating velocity components from N instantaneous 2D PIV images are assembled into a single matrix U. The matrix U has the dimensions of $N \times 2 \times n_x \times n_y$, where n_x and n_y are a number of pixels along $x-$axis and $y-$axis in instantaneous 2D PIV images. In this work, each instantaneous image has 86×65 pixels over 1000 instantaneous images, resulting in the matrix U of 1000×11180 values. In the matrix U, each row is composed from a ranked series of stream−wise velocity components u followed by a series of lateral velocity v components from one instantaneous image. Therefore, each row of the matrix U corresponds to one instantaneous two−dimensional velocity field and subsequent square cross correlation matrix R is computed as follows (superscript T denotes the transpose):

$$U(X,t) = \begin{pmatrix} u_{11} & u_{21} & \cdots & \cdots & u_{M1} & v_{11} & v_{21} & \cdots & \cdots & v_{M1} \\ u_{12} & u_{22} & \cdots & \cdots & u_{M2} & v_{12} & v_{22} & \cdots & \cdots & v_{M2} \\ \vdots & \vdots & & & \vdots & \vdots & \vdots & & & \vdots \\ u_{1N} & u_{2N} & \cdots & \cdots & u_{MN} & v_N & v_{2N} & \cdots & \cdots & v_{MN} \end{pmatrix} \tag{7.10}$$

$$R(X,X^{'}) = U \cdot U^T \tag{7.11}$$

The resulting square matrix, R consists of the multiple correlations between u and u, u and v and v and v (Shim *et al.*, 2013). The base functions (eigenfunctions) $\phi^{(m)}(X)$ and eigenvalues $\lambda^{(m)}$ are computed by considering the following eigenvalue problem.

$$R\phi = \lambda\phi \tag{7.12}$$

Eigenfunctions are arranged by their eigenvalues as $\phi\left(sort\left(\lambda^1 > \lambda^2 .... > \cdots \lambda^n\right)\right)$ and POD mods can be computed as follows:

$$a^{(m)}(t) = U\phi \tag{7.13}$$

The POD mods form a matrix in which each matrix row represents a single mod, starting from the first row (first mod) and down to $N-$mod. The first mods are the most energetic

[3]The time complexity quantifies the amount of time taken by an algorithm to run (Sipser, 2006).
[4]Snapshot refers to the velocity two−dimensional data set.

ones and represents the dominant flow structure $\phi^1 = \left(\phi_1^1 \cdots \phi_1^n\right)$.

$$\Phi = \begin{pmatrix} \phi_1^1 & \phi_1^2 & \phi_1^n \\ \phi_2^1 & \phi_2^2 & \phi_2^n \\ \phi_N^n & \phi_N^n & \phi_N^n \end{pmatrix} \tag{7.14}$$

In order to assess the individual percentage contribution of each eigen mode towards the total turbulent flow energy $\sum_{i=1}^{N} \lambda^i$ the relative energy of the POD modes (E^i) and the cumulative energy ratio (ε_j) can be computed. For the case when U represents instantaneous velocity fluctuations, the eigenvalues λ correspond to the turbulent kinetic energy of the respective modes. The turbulent kinetic energy of the respective modes was computed as follows[5]:

$$E^i = \frac{(\lambda^i)^2}{\sum_{i=1}^{N} (\lambda^i)^2}, \quad i = 1, 2, 3...N \tag{7.15}$$

$$\varepsilon_j = \frac{\sum_{i=1}^{j} (\lambda^i)^2}{\sum_{i=1}^{N} (\lambda^i)^2}, \quad i = 1, 2, 3...N \tag{7.16}$$

Finally, the fluctuating velocity fields are reconstructed to check whether the original velocity fields are recovered correctly.

$$u^{'}(X, t) = a\phi^T \tag{7.17}$$

Since non−recirculating zones are not important, the POD analysis was limited to within recirculation zone only. The POD analysis was performed on the field of view spanning along burner centreline $10(mm) \leq y \leq 50(mm)$ and along radial coordinate -1.57$\leq x/R \leq$1.57. The cumulative energy ratio of the eignevalues for different swirl numbers for isothermal coflow+central axial jet and combustion of DRL fuel is shown in Figure 7.10. It is interesting to note that the cumulative energy ratio is similar for all swirl numbers for isothermal jets. It is needed about 40 modes to capture 50% of the energy and about 200 modes to capture 90% of the energy for non−reacting isothermal jets. The cumulative energy ratio of the eignevalues demonstrates non−linear behaviour with steeper increase in the first 50 (isothermal) and 25(reacting) modes. Thus, those modes represent the dominant flow structure. In addition, the effect of swirl number on the flow structure is seen on the right hand side of Figure 7.10. During combustion of DLR fuel and for $S = 0.3$ the flow structure (70% kinetic energy) is well−defined within the first 25 modes. However, during DLR combustion with the highest swirl number of 1.07, 70% kinetic energy can be captured by using ≈70 modes. Therefore, during combustion, a number of nodes, which is needed to capture the same kinetic energy is 2.8 times higher for $S = 1.07$ than for $S = 0.3$. This means that small−scale structures, which are represented by the higher modes tend to play more important role in the overall jet dynamics. It can

[5]Note that the relative energy is computed after sorting the eigenvalues in descending order $\lambda^1 > \lambda^2 .... > \cdots \lambda^n$.

also be attributed to random and noisy effect, from the higher modes (Shim *et al.*, 2013).

Figure 7.11 shows flow structures associated with the first, 2nd and 3rd POD modes for isothermal jets (case 'b' in Figures 7.1−7.9), $S = 0.58$ computed for recirculation zone region near the burner exit. The first mode, which contains the highest energy in an average sense shows several vortex−like structures at the coflow jet as well as at recirculation zone boundaries. In side the recirculation zone, the flow does not contain vortex−like structures and shows flow filed pointing downwards, which is a clear sing of the recirculation zone. Vortex−like structures are found in all modes and may come from three−dimensional structure of the PVC. Therefore, the flow field consists of vortex−like structures superimposed on each other and are dependant on swirl number. Therefore, it can be suggested that there is no single flow dominant structure and flow is composed of many vortical structures that are superimposed on each other.

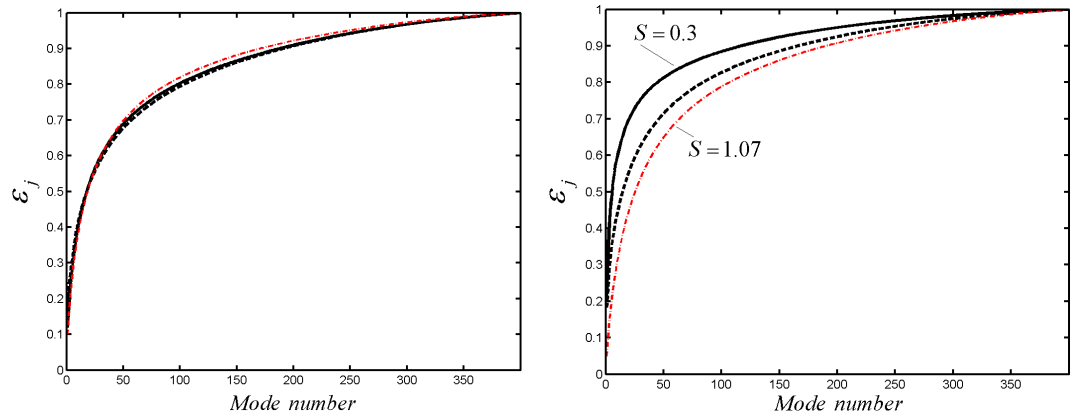

Figure 7.10: The cumulative energy ratio of the eigenvalues for different swirl numbers S computed for near burner exit ($-40 \leq x \leq 40$(mm); $10 \leq y \leq 50$(mm)) region. Left hand side corresponds to case 'b' in Figures 7.1−7.9, i.e. isothermal coflow+central axial jet. Right hand side corresponds to case 'c' in the same figures, i.e. combustion of DLR fuel. Note that the cumulative energy ratio is similar for all swirl numbers for non−reacting jets.

Figure 7.12 shows flow structures associated with the first, 2nd and 3rd POD modes for isothermal jets (case 'b' in Figures 7.1−7.9), $S = 1.07$ computed for recirculation zone region near the burner exit. Similar to Figure 7.11 vortical structures are observed for the first three modes (as well as for other higher modes) without any dominant ones.

Figure 7.13 shows flow structures for the first three modes for reacting flow (axial jet of DLR fuel+coflow) for $S = 0.58$, which corresponds to case 'c' in Figures 7.1−7.9. The flow field has no single dominant mode and consists of a number of vortical structures as in non−reacting case. The cumulative energy ratio of the eigenvalues also suggests that the flow field will not have single dominant mode. This is also consistent with Reichert *et al.* (1994)., where POD method was to extract empirical eigenfunctions from an incompressible turbulent flow in a square duct. Similarly, Figure 7.14 shows flow structures for the first three modes for reacting flow (axial jet of DLR fuel+coflow) for $S = 1.07$. All modes show the presence of the vortical structures the whole measurement area, which encompasses the recirculation zone. The vortical structures may be due to rapid decrease of the instantaneous axial velocity of the axial fuel jet, due to flow reversal.

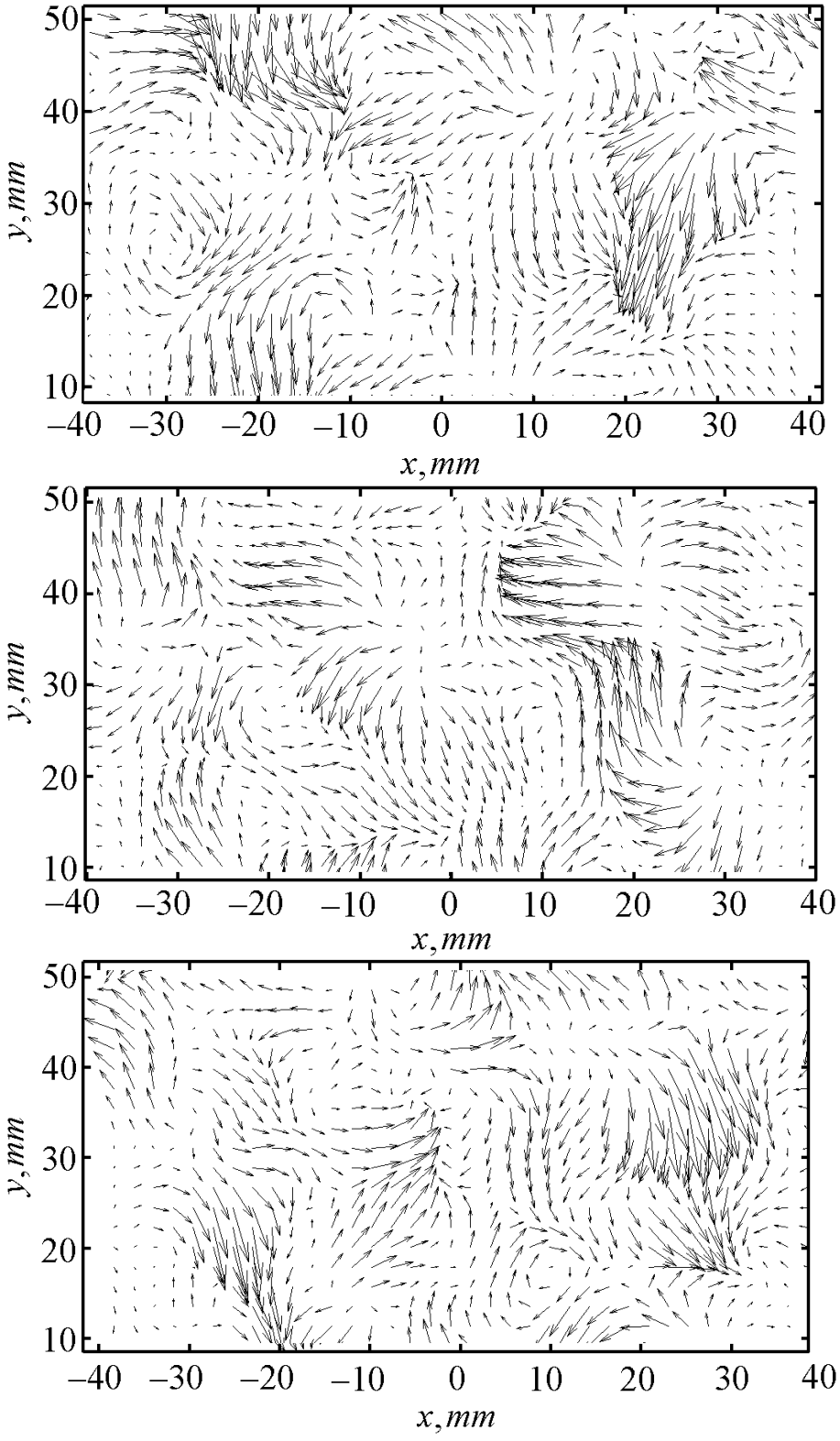

Figure 7.11: Flow structures associated with the first, 2nd and 3rd POD modes for $S = 0.58$ computed for recirculation zone region near the burner exit. Flow structures are shown for isothermal coflow+central axial jet. Note that the flow field does not have single dominant mode and consists of a number of vortical structures. The vortical structures may be due to rapid decrease of the instantaneous axial velocity of the axial fuel jet, due to flow reversal.

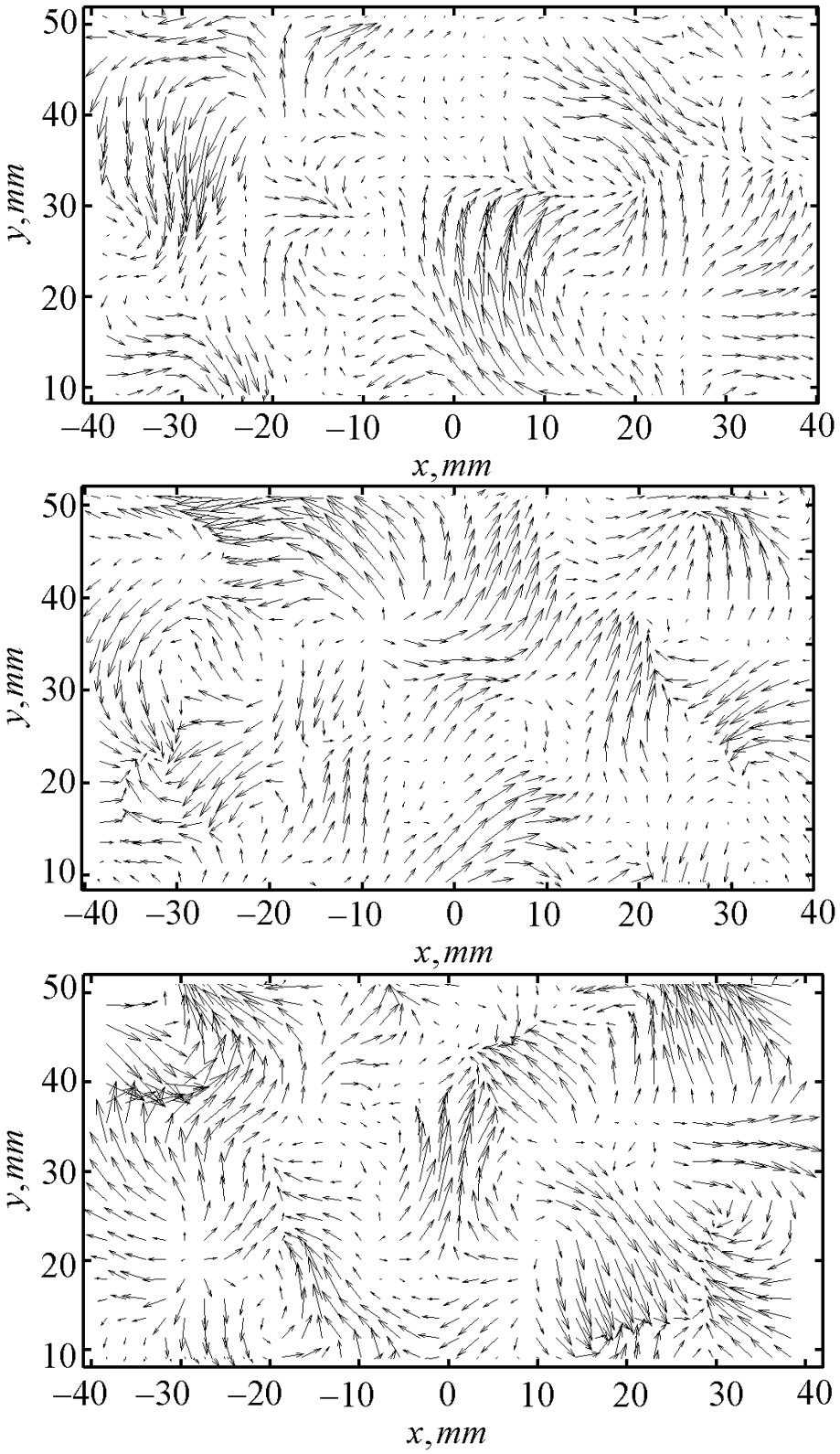

Figure 7.12: Flow structures associated with the first, 2nd and 3rd POD modes for $S = 1.07$ computed for recirculation zone region near the burner exit. Flow structures are shown for isothermal coflow+central axial jet. Note that the flow field does not have single dominant mode and consists of a number of vortical structures. The vortical structures may be due to rapid decrease of the instantaneous axial velocity of the axial fuel jet, due to flow reversal.

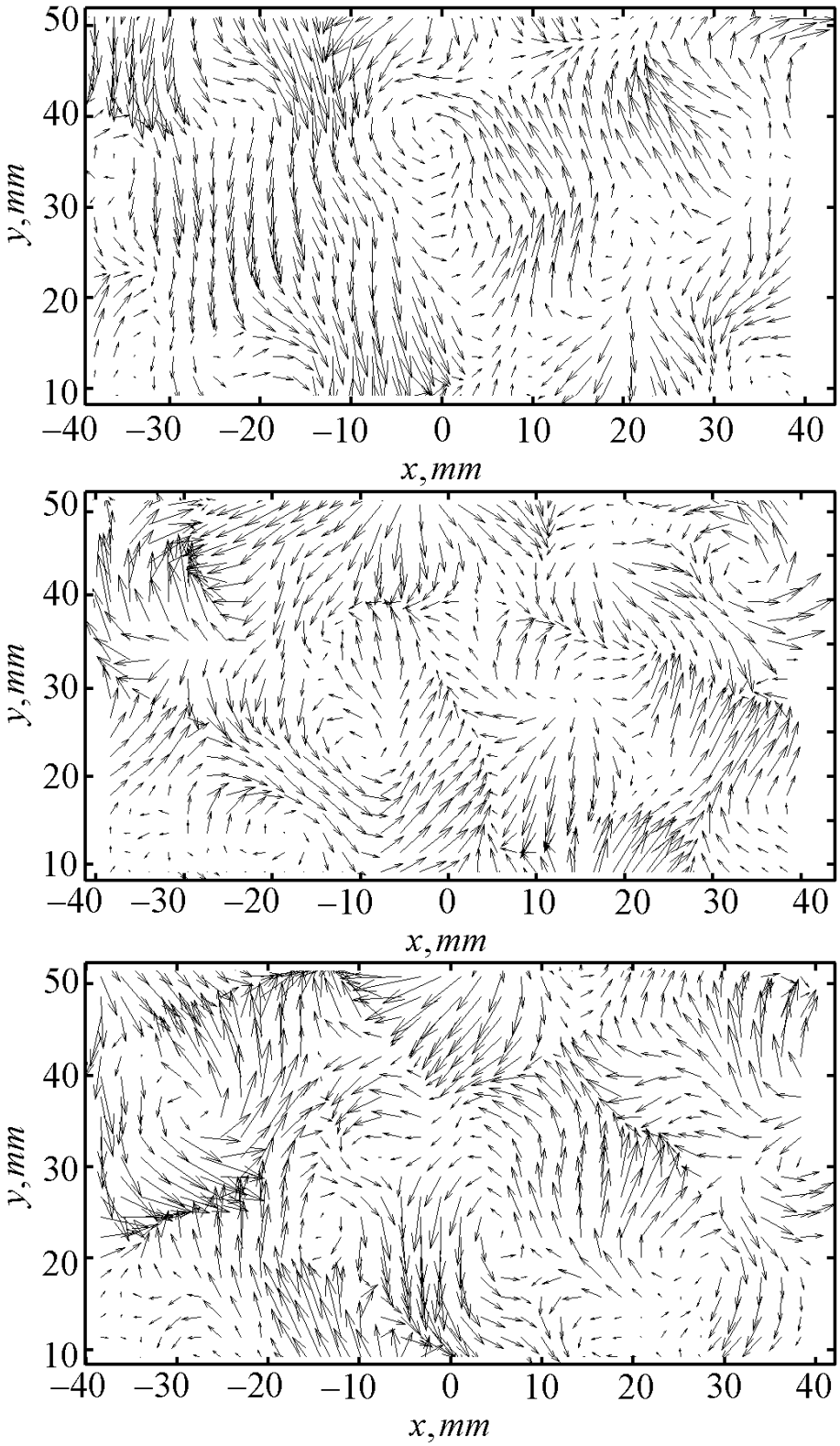

Figure 7.13: Flow structures associated with the first, 2nd and 3rd POD modes for $S = 0.58$ computed for recirculation zone region near the burner exit. Flow structures are shown for reacting jet, i.e. axial jet of DLR fuel+coflow. Note that the flow field does not have single dominant mode and consists of a number of vortical structures. The vortical structures may be due to rapid decrease of the instantaneous axial velocity of the axial fuel jet, due to flow reversal.

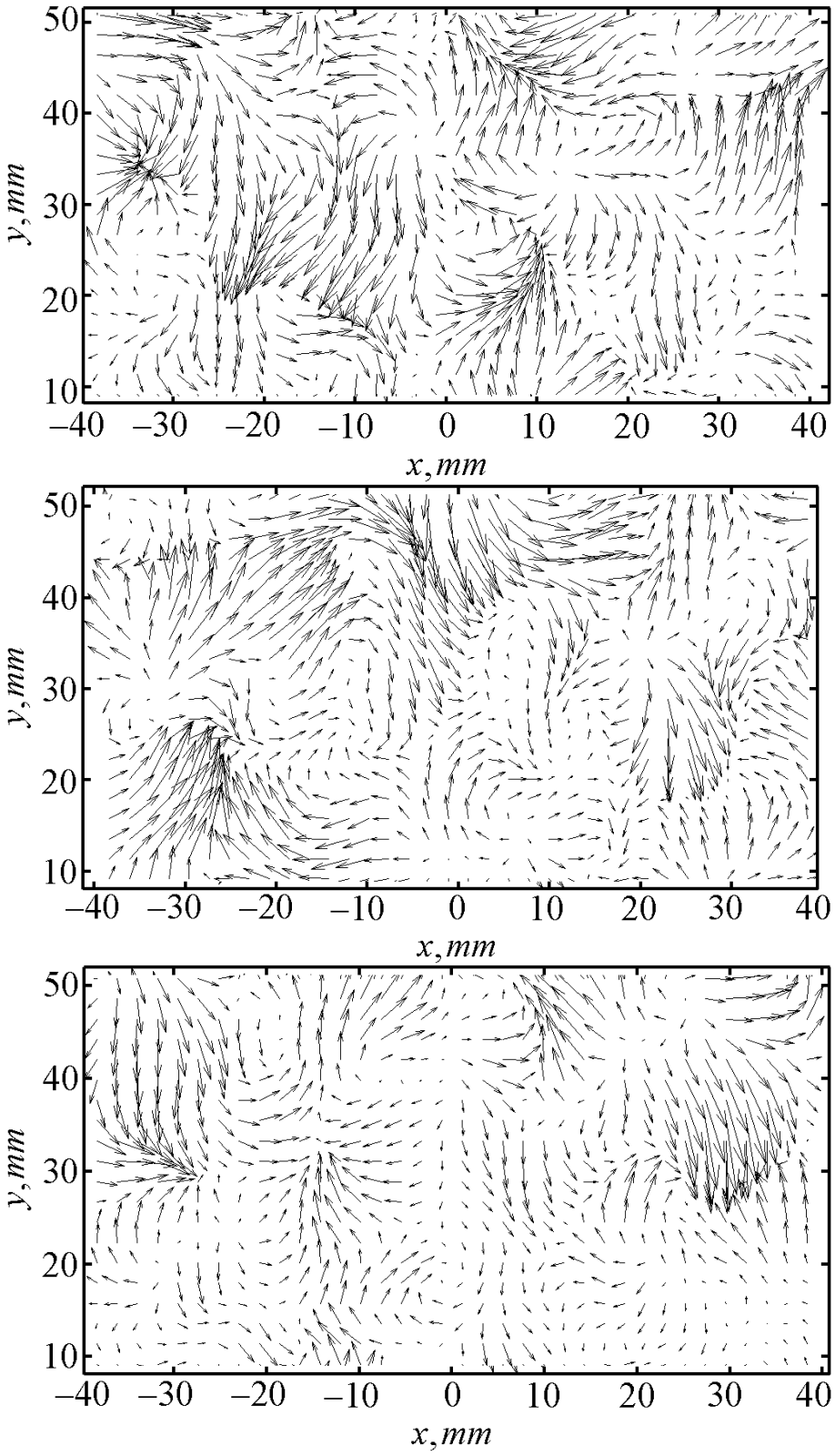

Figure 7.14: Flow structures associated with the first, 2nd and 3rd POD modes for $S = 1.07$ computed for recirculation zone region near the burner exit. Flow structures are shown for reacting jet, i.e. axial jet of DLR fuel+coflow. Note that the flow field does not have single dominant mode and consists of a number of vortical structures. The vortical structures may be due to rapid decrease of the instantaneous axial velocity of the axial fuel jet, due to flow reversal.

7.6 Summary

This chapter continued the discussion on the influence of swirl number (degree of swirl) on turbulent swirling jets dynamics. The flow structures as well as flow statistics were investigated by using particle image velocimetry along with proper orthogonal decomposition (POD). The POD techniques was used to study the so−called dominant modes at different locations for different swirl numbers. It was shown that the flow field consisted of a number of vortical structures without single dominant modes. It has been suggested that those vortical structures may be due to rapid decrease of the instantaneous axial velocity of the axial fuel jet, due to flow reversal (recirculation zone).

Mean velocity, standard deviation of velocity fluctuations and vorticity were presented and discussed. As it was expected, the lowest swirl number did not show that the flame was stabilised by the recirculation zone. On the other hand, higher swirl number ($S = 0.58 - 1.07$) demonstrated that the flame was clearly stabilised by the recirculation zone. As it was suggested by Gupa *et al.* (1984), the reverse flow zone could be identified as approximate position of the precessing vortex core.

Vorticity fields were highly influenced by combustion than velocity fields. It was found that vorticity increased during combustion. In addition, higher velocity fluctuations during combustion at the interface between the central fuel jet and the swirling coflow were observed.

8 Conclusions

The mixing, flow velocity and combustion in a swirl−stabilised burner were studied in this work. The scalar and thermal dissipation rate, mixture fraction distribution, flame temperatures and velocity profiles were measured in a swirling coaxial jet discharged from a swirl−stabilized burner with central axial injection of gas flow (fuel). The burner with outer diameter of $D = 50.8$(mm) and inner nozzle diameter of $D_f = 15$(mm) was used. The measurements were reported up to 2 outer (burner) nozzle diameters or 7 inner fuel nozzle diameters downstream of the burner exit at a Reynolds number of 29000. The velocity distributions were reported up to ≈4 burner diameters. Three swirl numbers were considered, namely 0.3, 0.58 and 1.07. The main conclusions are as follows:

8.1 Isothermal jets

- The mean flow shape was symmetrical for swirl number of 0.3 and slightly asymmetrical for swirl numbers of 0.58 and 1.07 perhaps due to slight asymmetry in flow development section. The mixing levels were affected by swirl level and the mixing improved as the swirl number increased.
- The maximum of instantaneous scalar dissipation rate was found to be up to 35 (s^{-1}) depending on realizations, laser sheet axial position (along vertical $y-$ axis) and swirl numbers. The scalar dissipation rate increased with the increase in swirl number for axial positions $y/D_f = 1 - 5$ due to highly inhomogeneous scalar distribution, which suggests high spatial fluctuations of dissipation rate. At higher positions and high swirl numbers, i.e. $y/D_f = 7$ and $S = 1.07$ the scalar dissipation rate decreased to small values due to highly homogeneous mixture indicating well−mixed regime, in which mixture fraction gradients were small.
- The values of the mean scalar dissipation rate were much smaller than the values found in instantaneous images. The values of up to 35(s^{-1}), assuming diffusivity value of 12.4(mm^2/s), were found in instantaneous realizations while mean values were circa 3(s^{-1}) or less. The higher scalar dissipation rate values in the mean images corresponded to lower axial positions, where the mixture fraction gradients were the largest. As result, the mixture fraction varied greatly within short distances, which increased the scalar dissipation rate values. Most of the scalar dissipation rate was concentrated at the fuel jet periphery, i.e. at ±0.3 x/R for $y/D_f = 1$ and $y/D_f = 3$ and could be even seen in instantaneous images. However, at higher axial distances, far away from the jet origin no distinct scalar dissipation rate regions could be observed.
- The probability density functions of the logarithm of the scalar dissipation rate fluctuations were found to be slightly negatively skewed at low swirl number ($S = 0.3$)

and almost symmetrical when swirl number increased up to 0.58−1.07.

- The joint p.d.f. between the scalar fluctuations and the logarithm of the scalar dissipation rates were compared with the product of the individual p.d.f. At all five chosen window locations the contours of the product of the individual p.d.f. appeared close to circular, even though not entirely symmetric. The joint p.d.f. had a little oval shape and seemed skewed towards both negative and positive dissipation fluctuations.
- The centre of the joint p.d.f. and the product of individual p.d.f. seemed to have the same origin. The assumption of statistical independence was therefore in better agreement with the experimental data under assumptions of homogeneous flow field or well−mixed regime. It was showed that, the flow field at high axial location and large swirl number was nearly homogeneous with small scalar fluctuations. However the deviations from the assumption of statistical independence were clearly observed, where the flow was not homogeneous with large scalar fluctuations.
- The conditional mean of the scalar dissipation rate, the standard deviation of the scalar dissipation rate, the weighted probability of occurrence of the mean conditional scalar dissipation rate and the conditional probability were also reported. General observation of the conditional mean revealed that the mean increased with the mixture fraction, reaching a maximum value, then gradually decreased and reached zero. With increasing swirl number the conditional mean decreased and its maximum values shifted to lower mixture fraction values and this trend was similar for all axial positions $y/D_f = 1 - 7$. For lower swirl numbers the conditional mean had clearly visible smooth shape.
- The standard deviation of the scalar dissipation rate fluctuations conditioned on the mixture fraction demonstrated similar trends as the conditional mean with similar bell−shaped curve. Even though the peak of the standard deviation was approximately constant irrespective of swirl number or the degree of mixing, the distribution was dependant on the swirl numbers.
- The weighted probability of occurrence had bell−shaped positively skewed curve and generally followed the conditional mean. The maximum values of the weighted probability were similar to those in the conditional mean for small and moderate swirl numbers. The actual location of the weighted probability peak was dependant on swirl numbers and axial position in the flow.
- Mean absolute velocity and standard deviation of velocity fluctuations were also measured by using a PIV technique. No recirculation zone for low swirl number of 0.3 was found. Intermediate swirl number of 0.58 demonstrated weak recirculation zone when swirling coflow was only used. For the same number, no recirculation zone was found when central jet was central fuel axial jet+coflow were used. The highest swirl number of 1.07 resulted in strong and well−defined recirculation zone. The velocity fluctuations were high along the centreline for $S = 0.3$ and low for $S = 0.58, 1.07$. The highest standard deviation was found to be at the axial positions close to the burner exit.

8.2 Reacting jets

- The flame was stably attached to the fuel nozzle for all three swirl numbers. The configuration of the flame at low swirl number $S = 0.3$ was slightly asymmetrical and the flame behaved more like a jet flame, which was also confirmed by the direct flame photography. The flame at higher swirl numbers, i.e. at $S = 0.58$ and $S = 1.07$ was different from that for $S = 0.3$. The difference was primary in the heigh and the shape of the flame, i.e. the heigh was smaller and the edge of the flame was wider.
- The instantaneous images of temperature distribution were reported here for different swirl numbers at several downstream locations $y/D_f = 1 - 10$. The temperature was affected by the swirl number at all downstream positions. At higher downstream positions, the temperature distribution tended to be more uniform, which was seen even in instantaneous images. At the lowest swirl number and at $y/D_f = 1$, high temperature zones concentrated within the shear layer, i.e. between the fuel and air coflows $\pm 0.3x/R$, while at the moderate swirl number no distinct visible high temperature zones were observable at the same downstream position.
- The centreline temperature increased from nearly ambient temperature (close to the burner exit) to higher values at far away distances from the burner exit, i.e. at different y/D_f and this trend was similar for all swirl numbers.
- The mean temperature for $S = 0.58$ was found to be higher than for $S = 0.3$ and equalled to $\approx$1800K at $y/D_f = 1$. The development of the combustion field for $S = 0.58$ followed the same trend as for $S = 0.3$.
- At low swirl number the standard deviation of temperature fluctuations was highly non−uniform, especially at lower downstream positions, which indicated highly non-uniform temperature distribution. In contrast, for intermediate and the highest swirl numbers, the standard deviation became smaller and more distributed. A low standard deviation indicated that most of the temperature was close to the average. A high standard deviation indicated high temperature fluctuations.
- Measured probability density function of temperature fluctuations at various downstream positions y/D_f and spatial location in the flow exhibited a wide range of shapes. The wide range of shapes consisted of unimodal and bimodal both equal and unequal distributions. Zones with the low temperature fluctuations typically demonstrated unimodal distribution with high kurtosis, while zones with high temperature fluctuation could demonstrate the bimodal distribution. At higher downstream locations and higher swirl numbers the p.d.fs. were typically unimodal even though not entirely symmetrical. It seems to be plausible to assume the Gaussian distribution for the temperature fluctuations in most of the cases.
- The temperature spectra seemed to exhibit a similar appearance, i.e. they were flat at low frequencies, began to roll off at quite different wave numbers, decreasing more rapidly in the dissipation rate range. The dissipation rate spectra shifted to lower frequencies with increasing downstream distance. This reduction in frequency can be explained by the increase in dissipative length scales due to higher temperature and perhaps lower velocity. Higher temperature at higher downstream positions leads to higher viscosity and as a result to higher viscosity dumping effects. A small inertial

subrange, which can be hardly seen at lower axial distances $y/D_f = 1-3$ for $S = 0.3$ was likely because the turbulence was not fully developed and perhaps due to low local Reynolds number. On the other hand, an extended inertial subrange at higher downstream positions, especially for higher swirl numbers $S = 0.58$ and 1.07 was the sign of fully developed turbulence.

- A combined effect of flow shear between the centreline fuel jet and the coflow as well as the flow laminarization due to heat release resulted in larger temperature dissipation rate in the radial direction for the lowest swirl number of 0.3. Higher swirl numbers demonstrated 'smeared' temperature dissipation rate fields.
- Centreline as well as shear−layer p.d.fs. of the thermal dissipation rate exhibited features of log−normal distribution with exponential scaling of the tails on the negative side of the dissipation rate. The high−dissipation rate positive side of the distribution was apparently log−normally distributed unlike low−dissipation rate values for all locations in the flow.
- During combustion conditions, the velocity flow field was generally symmetric with well−defined inverted cone shape for $S = 0.3$, unlike for $S = 0.58, 1.07$. Higher swirl numbers resulted in tulip shape. The central jet velocity remained nearly constant ($\approx$6 (m/s)) within $\approx$50 (mm) distance from the burner exit ($S = 0.3$) and decayed rapidly to low velocity values further downstream. This decay may be explained by the rapid mixing and subsequent combustion of the fuel jet.
- The highest swirl number 1.07 resulted in fully developed recirculation zone, while moderate swirl number 0.58 demonstrated asymmetric and not well−developed recirculation zone.

8.3 Recommendations for future work

Most published research on combustion dynamics is generally limited to atmospheric conditions, i.e. atmospheric pressure and temperature. However, real combustion systems operate at elevated pressure and temperature. High pressure experiments in swirling flows should be carried out and expanded to higher degrees of swirl. Experiments on practical combustors and full scale combustion chambers should also be performed even though in some cases can be complicated. In addition, the climate change and the shortage in fuel supply create a basis for future measurements in combustion of alternative fuels. It is quite obvious that such full scale experiments and studies at elevated pressure and temperature require a robust combustion chamber with optical access, which is able to withstand high thermal stress.

More work can be carried on to study scalar and thermal dissipation rate with improved spatial and temporal resolution. In addition, higher power pulsed laser can be employed in order to increase the signal−to−noise ratios, especially in Rayleigh thermometry. Ideally, full 3D scalar dissipation rate measurements should be performed, especially in swirling flows. The scalar or thermal dissipation rate is computed as the radial and axial derivatives of scalar or temperature fields. In this work, the scalar and thermal dissipation rate were computed by using the second-order accurate central difference formula. On the other hand, a higher order scheme is recommended, e.g. fourth−order compact finite

difference scheme Lele (1992). Conducting further experiments will help to relate existing combustion models with the experimental data, contribute to the fundamental study of combustion phenomena and provide data source of validation for numerical simulations.

In terms of flame diagnostics, Particle Image Velocimetry (PIV) can be combined with Rayleigh thermometry for simultaneously measurements of velocity fields and temperature. In sooting flames or in dusty environment, the filtered Rayleigh scattering can also be used with relatively simple implementation. The PIV can also be combined with the present PLIF technique, which can provide simultaneous maps of velocity and mixture fraction. The measurements of turbulent fluxes and the budget of the scalar variance can help to validate the accuracy of the scalar dissipation rate measurements. A further development of advanced diagnostic techniques can help to study advanced combustion phenomena, including high temperature air combustion (flameless oxidation) and pulsed detonation mode of combustion within rockets and scram jet engines.

It is also interesting to investigate the influence of scalar dissipation rate on combustion dynamics. A specially designed burner (Figure 8.1), which is able to produce swirling flows with different swirling characteristics simultaneously, can be used in advanced measurements. The burner can consist of, e.g. two swirlers, which can create swirling flows with high and low swirling intensity. High scalar dissipation rate, which results from high swirling flow (firs swirler) should delay combustion. The lower swirling flow should decrease scalar dissipation rate, which will allow the combustion process to proceed. This process is similar to premixed combustion without an actual premixer.

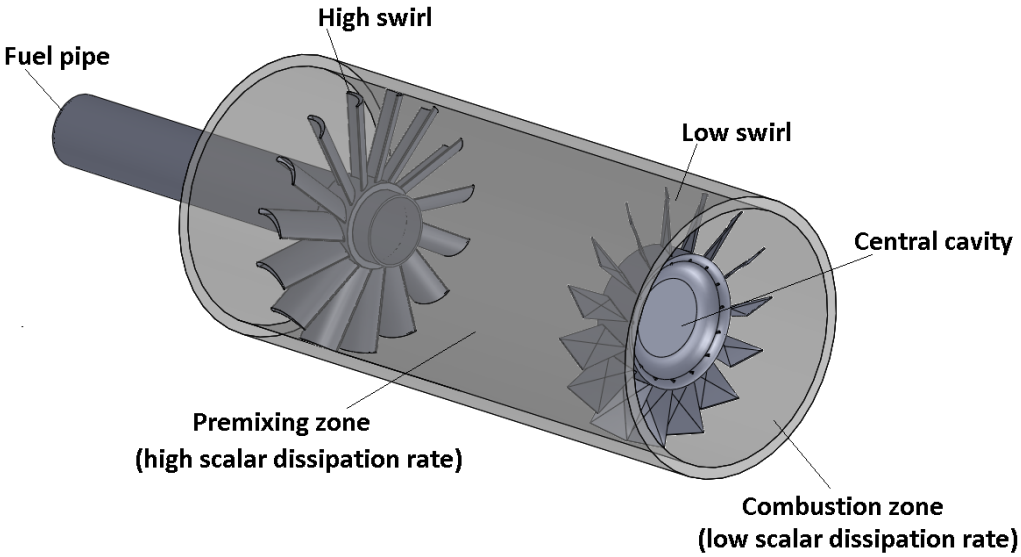

Figure 8.1: Proposed burner, which can be used for advanced measurements. Premixing zone is used to create homogeneous ar/fuel mixture and suppress combustion due to high scalar dissipation rate. Central cavity is used to enhance the recirculation zone and acts as a sudden expansion.

Bibliography

[1] D.J. Anderson, C.A. Greated, J.D.C. Jones, G. Nimmo and S. Wiseall. *Fibre optic PIV studies in an industrial combustor.* Proc. 8th Int. Symp. on Applications of Laser Techniques to Fluid Mechanics, Lisbon, 1996.

[2] F. Anselmet and R. A. Antonia. *Joint statistics between temperature and its dissipation.*Phys. Fluids 28, 1048, 1985.

[3] R.A. Antonia and L. B. Brown. *The destruction of temperature fluctuation in a turbulent plane jet.* J. Fluid Mechanics, 134, pp.67−83, 1983.

[4] R.A. Antonia, L. B. Brown, D. Britz and A. J. Chambers. *A comparison of properties of temporal and spatial temperature increments in a turbulent plane jet.* Phys. Fluids 27, pp.87−93, 1984.

[5] R.A. Antonia and J. Mi. *Temperature dissipation in a turbulent round jet.* J. of Fluid Mechanics, 250, pp.531−551, 1993.

[6] P. Arfi. *Reduction of NO_x emissions from gas turbines using internal exhaust gas recirculation.* PhD Thesis, Technion−Israel Institute of Technology, 2002.

[7] M. Aigner, A. Mayer, P. Schiessel. and W. Strittmatter. *Second generation Low-emission combustors for ABB gas turbines: Test under full engine conditions.* ASME 90−GT−308, 1990.

[8] Samer F. Ahmed. *Scalar dissipation rate statistics in turbulent flows using planar laser induced fluorescence measurements.* Int. Heat Fluid Flow 33, pp.220−231, 2012.

[9] Y.M. Al-Abdeli and A.R. Masri. *Precession and recirculation in turbulent swirling isothermal jets.* Combustion Science and Technology, 176:5-6, pp.645−665, 2010.

[10] R.S. Barlow, J.H. Frank, A.N. Karpetis and J.−Y. Chen. *Piloted methane/air jet flames: Transport effects and aspects of scalar structure.* Combustion and Flame 143, pp.433−449, 2005.

[11] R. Bazile, D. Stepowski. *Measurements of the vaporization dynamics in the development zone of a burning spray by planar laser induced fluorescence and Raman scattering.* Exp. Fluids 16, pp.171−180, 1994.

[12] R.A. Betta, J.C. Schlatter, S.G. Nickolas, M.B. Cutrone, K.W. Beebe, Y. Furuse and T. Tsuchiya. *Development of a catalytic combustor for heavy−duty utility gas turbine.* Journal of Engineering for Gas Turbines and Power. Vol.119, p.844, 1997.

[13] J.M. Beller and N.A. Chigier. *Combustion Aerodynamics.* Robert E. Krieger Publishing Company Inc., 1983.

[14] G. Berkooz, P. Holmes, and J.L. Lumley. *The proper orthogonal decomposition in the analysis of turbulent flows.* Annual Review of Fluid Mechanics, 25(1),pp.539−575, 1993.

[15] R.W. Bilger. *Some aspects of scalar dissipation.* Flow, turbulence and combustion, Vol. 72, pp.93−104, 2004.

[16] R.W. Bilger, S.B. Pope, K.N.C. Bray, and J.F. Driscoll. *Paradigms in turbulent combustion research.* In Proceedings of the Combustion Institute, volu. 30, pp.21−42, 2005.

[17] R.W. Bilger. *Future progress in energy combustion research.* Progress in Energy and Combustion Science, 26, pp.367−380, 2000.

[18] R.W. Bilger. *Some aspects of scalar dissipation.* Flow, Turbulence and Combustion,72, pp.93−104, 2004.

[19] R.W. Bilger. *Turbulent diffusion flames.* Annual Review of Fluid Mechanics, 21, pp.101−135, 1989.

[20] R.W. Bilger. *Conditional moment closure for turbulent reacting flow.* Phys. Fluids 5(2), 436−444, 1993.

[21] R.W. Bilger. *The structure of diffusion flames.* Combustion Science and Technology, 13, pp.155−170, 1976a.

[22] R.W. Bilger. *Turbulent jet diffusion flames.* Progress in Energy and Combustion Science, 1, pp.87−109, 1976b.

[23] W.S. Blazowski. *Future Jet Fuel: Combustion problems and requirements.* Progress in Energy and Combustion Sciences, Vol.4, pp.177−199, 1978.

[24] G. Blanquart, H. Pitsch. *Modelling autoignition in non−premixed turbulent combustion using a stochastic flamelet approach.* Proc. Combust. Inst. 30, pp.2745−2753, 2005.

[25] R.A. Bryant, J. M. Donbar and J. F. Driscoll. *Acetone laser induced fluorescence for low pressure/low temperature flow visualization.* Exp. Fluids 28, pp. 471−476, 2000.

[26] R. Borghi and P. Moreau. *Turbulent combustion in a premixed flow.* Acta astronaut 4, pp.321−341, 1977.

[27] M. Bruchhausen, F. Guillard, F. Lemoine. *Instantaneous measurement of two-dimensional temperature distributions by means of two-color planar laser induced fluorescence (PLIF).* Exp. Fluids 38, pp123−131, 2005.

[28] T. Burden. *The length, time and velocity scales of turbulence.* Lecture Notes, Spring 2008.

[29] G. Bulat. *Large eddy simulations of reacting swirling flows in an industrial burner.* (PhD Thesis), University of London, Faculty of Engineering, 2012.

[30] W. K. Bushea and H. Steiner. *Conditional moment closure for large eddy simulation of non−premixed turbulent reacting flows.* Phys. Fluids 11(7), 7 July 1999.

[31] R. Cabra, J.Y. Chen, R.W. Dibble, A.N. Karpetis, and R.S. Barlow. *Lifted methane−air flames in a vitiated coflow.* Combustion and flame 143, pp.491−506, 2005.

[32] J. Cai, D. Wang, C. Tong, R.S. Barlow, and A.N. Karpetis. *Investigation of subgrid−scale mixing of mixture fraction and temperature in turbulent partially premixed flames.* Proc. of the Combustion Institute No. 32, pp.1517−1525, 2009.

[33] D. Carati and E.V. Eijnden. *On the self−similarity assumption on dynamic models for large eddy simulation.* Phys. Fluids 9, pp.2165−2167, 1997.

[34] J.J. Cassidy and H.T. Falvey. *Observation of unsteady flow arising after vortex breakdown.* J. Fluid Mech., 41, pp.727−736, 1970.

[35] R. Connell and D. Kulasiri. *Modelling velocity structures in turbulent floods using proper orthogonal decomposition.* Centre for Advanced Computational Solutions (C-fACS), Lincoln University.

[36] R.H. Chan, C.W. Ho and M. Nikolova. *Salt-and-pepper noise removal by median-type noise detectors and detail-preserving regularization.* IEEE Transactions on Image Processing 18 (10), pp.1479−1485, 2005.

[37] C.M. Cha and P. Trouillet. *Filtered density-function modeling for large-eddy simulations of turbulent reacting flows.* Center for Turbulent Research Annual Research Briefs 2002.

[38] R.C. Chanaud. *Observations of oscillatory motion in certain swirling flows.* J. Fluid Mech., 21(1), pp.111−127, 1965.

[39] Q. Chen and C. Tong. *Investigation of the subgrid-scale stress and its production rate in a convective atmospheric boundary layer using measurement data.* J. Fluid Mech., Vol. 547, pp.65−104, 2006.

[40] Y.−C. Chen. *Measurements of the inner layer temperature in highly streatched turbulent Bunsen flames.* Rheinish Westfalische Technische Hochschule Aachen, Fakultat fur Maschinenwesen, 1994.

[41] S.G. Chumakov. *Subgrid models for large eddy simulation: Scalar flux, scalar dissipation and energy dissipation.* PhD thesis, University of Wisconsin-Madison, 2005.

[42] A.W. Cook and J.J. Riley. *A subgrid model for equilibrium chemistry in turbulent flows.* Phys. Fluids 6, p.2868, 1994.

[43] S.M. Correa. *Lean premixed combustion from gas turbine: Review and Required Research.* Fossil Fuel Combustion. ASME PD, Vol. 33, 1991.

[44] S.M. Correa. *A review of NOx formation under gas-turbine combustion conditions.* Combustion Science and Technology, Vol.87, pp.329−362, 1992.

[45] S.M. Correa. *Power generation and aero-propulsion gas turbines from combustion science to combustion technology.* 27th Symposium (International) on Combustion. The Combustion Institute Pittsburgh, 1998.

[46] P.J. Colucci, F.A. Jaberi, P. Givi and S.B. Pope *Filtered density function for large eddy simulation of turbulent reacting flows.* Phys. Fluids 10(2), February 1998.

[47] J.P. Crimaldi. *Planar laser induced fluorescence in aqueous flows.* Exp. Fluids 44, pp.851−863, 2008.

[48] P.J. Crutzen. *The role of NO and NO2 in the chemistry of the troposphere and the stratosphere.* Annual Rev. Earth Planet Sciences. Vol.7, pp.443−472, 1979.

[49] N.A. Chigier. *Energy, Combustion and Environment.* Chapter: Nitrogen oxides. McGraw Hill, England, pp.326-337, 1981.

[50] A.J. Chandy, D.J. Glaze and S.H. Frankel. *A hybrid large eddy simulation/filtered mass density function for the calculation of strongly radiating turbulent flames.* J. Heat Trans. 131, 2009.

[51] R.K. Cheng, D. Littlejohn, N. Nazeer and K.O. Smith. *Laboratory studies of the flow field characteristics of low-swirl injectors for adaption to fuel-flexible turbines.* ASME Turbo Expo, GT2006-90878, 2006.

[52] DaVis Software. *LaVision Inc.* Anna−Vandenhoeck−Ring 19 301 W. Michigan Ave., Suite 403, www.lavisioninc.com.

[53] W.J.A. Dahm and K.A. Buch. *Lognormality of the scalar dissipation PDF in turbulent flows.* Phys. Fluids 1(7), pp.1290−1293, 1989.

[54] W. Danhong. *Experimental investigation of filtered density functions in turbulent jets and turbulent partially premixed flames.* PhD thesis, Clemson University, 2005.

[55] P. Dellenback, D.E. Metzger and G.P. Neitzel. *Measurements in turbulent swirling flow through an abrupt axisymmetric expansion.* AIAA Journal, 26 (6), pp.669−681, 1988.

[56] R.W. Dibble and M.B. Long. *Investigation of differential diffusion in turbulent jet flows using planar laser Rayleigh scattering.* Combustion and Flame 143, pp.644−649, 2005.

[57] R.W. Dibble, W. Kollmann and R.W. Schefer. *Measurements and predictions of scalar dissipation in turbulent jet flames.* Twentieth Symposium (International) on Combustion/The Combustion Institute, pp. 345−352, 1984.

[58] D.L. Donoho. *De-Noising by soft-thresholding.* IEEE Transactions in information theory, Vol. 41, No. 3, May 1995.

[59] T.F. Dixon, J. S. Truelove and T. F. Wall. *Aerodynamic studies on swirled coaxial jets from nozzles with divergent quarls.* J. of Fluids Eng., Vol 105, pp.197−203, 1983.

[60] P. Domingo, L. Vervisch and D. Veynante. *Large eddy simulation of a lifted jet flame in a vitiated coflow.* Combustion and Flame 152, pp. 415−432, 2008.

[61] C. Dopazo. *Probability density function approach for a turbulent axisymmetric heated jet. Centerline evolution.* Phys. Fluids 18(4), April 1975.

[62] S.E. Elgobashi and B.E. Launder. *Turbulent time scales and the dissipation rate of temperature variance in the thermal mixing layer.* Phys. Fluids 26 (9), pp.2415−2419, 1983.

[63] J.W. Elsner, and L. Kurzak. *Semi-preserving development of a slightly heated free swirling jet.* J. Fluid Mech. 199, pp.237−255, 1989.

[64] J.W. Elsner and L. Kurzak. *Characteristics of turbulent flow in slightly heated free swirling jets.* J. Fluid Mech. 180, pp.147−160, 1987.

[65] E. Effelsberg and N. Peters. *Scalar dissipation rates in turbulent jets and jet diffusion flames.* 22nd Intl. Symp. On Combustion by the Combustion Institute, pp.693−700, 1988.

[66] M. Estribeau, P.Magnan. *Fast MTF measurement of CMOS imagers using ISO 12233 slanted edge methodology.* Proc. of SPIE Vol. 5251− Detectors and associated signal processing.

[67] C. Espey, J.E. Dec, T.A. Litzinger and D.A. Santavicca. *Planar laser Rayleigh scattering for quantitative vapor-fuel imaging in a diesel jet.* Combustion and Flame 109, pp.65−86 (1997).

[68] E. Effelsberg and N. Peters. *Scalar dissipation rates in turbulent jets and jet diffusion flames.* Twenty-Second Symposium (International) on Combustion/the Combustion Institute, pp.693−700, 1988.

[69] A. Evlampiev. *Numerical combustion modeling for complex reaction systems.* (PhD thesis), Eindhoven University of Technology, Netherlands, 2007.

[70] D.A. Everest, J.F. Driscoll, W.J.A. Dahm, and D.A. Feikema. *Images of two dimensional field and temperature gradients to quantify mixing rates within a nonpremixed turbulent jet flame.* Combustion and Flame 101,pp.58−68, 1995.

[71] L. Facciolo. *A study on axially rotating pipe and swirling jet flows.* PhD thesis, KTH Mechanics, Stockholm, Sweden, TRITA-MEK Tech. Rep. 2006:02, 2006.

[72] S. Farokhi, R. Taghavi and E.J. Rice. *Effect of initial swirl distribution on the evolution of a turbulent jet.* AIAA J. 27, pp.700−706, 1989.

[73] P. Ferrao, F. Caldas, M.V. Heitor and M. Matos. *On the analysis of turbulent scalar mixing in coaxial jet flows.* 9th int. symposium on application of laser techniques to fluid mechanics, 1998.

[74] P. Ferrao and M.V. Heitor. *Probe and optical diagnostics for scalar measurements in premixed flames.* Exp. Fluids 24, pp.389−398, 1998.

[75] J. Fielding, J.H. Frank, S.A. Kaiser, M.D. Smooke and M.B. Long. *Polarized/depolarized Rayleigh scattering for determining fuel concentrations in flames.* Proceedings of the Combustion Institute, Vol. 29, pp.2703−2709, 2002.

[76] M.S. Feyedelem and T. Sarpkaya. *Free and near free surface swirling turbulent jets.* AIAA J. 36, pp.359−364, 1998.

[77] J.H. Frank, S.A. Kaiser and J.C. Oefelein. *Analysis of scalar mixing dynamics in LES using high-resolution imaging of laser Rayleigh scattering in turbulent non-reacting jets and non−premixed jet flames.* Proc. Combust. Inst., 2010.

[78] T.C. Frank and Omer L. Gulder. *Premixed turbulent flame front structure investigation by Rayleigh scattering in the thin reaction zone regime.* Proceedings of the Combustion Institute 32, pp.1747−1754, 2009.

[79] J.H. Frank and S.A. Kaiser. *High-resolution Rayleigh imaging of dissipative structures in a turbulent jet flame.* Paper 1249, 13th Int. Symp. on Applications of Laser Techniques to Fluid Mechanics, Lisbon, Portugal, 26−29 June, 2006.

[80] J. Floyd, A.M. Kempf, A. Kronenburg and R.H. Ram. *A simple model for the filtered density function for passive scalar combustion LES.* Combustion Theory and Modelling, 13:4, pp.559−588, 2009.

[81] F. Gao and E.F. O'Brien. *A large−eddy simulation scheme for turbulent reacting flows.* Phys. Fluids A 5, p.1282, 1993.

[82] M. Germano, U. Piomelli, P. Moin and W. Cabot. *A dynamic subgrid-scale eddy viscosity model.* Phys. Fluids A3 (7): pp.1760−1765, 1991.

[83] S.P. Ghael, A.M. Sayeed and R.G. Baraniuk. *Improved wavelet denoising via empirical Wiener filtering.* Proceedings of SPIE, Mathematical Imaging, San Diego, July, 1997.

[84] R.L. Gordon, A.R. Masri, S.B. Pope, and G.M. Goldin. *Transport budgets in turbulent lifted flames of methane autoigniting in a vitiated co-flow.* Combustion and Flame 151, pp.495−511, 2007.

[85] F.C. Gouldin and R.N. Halthore. *Rayleigh scattering for density measurements in premixed flames.* Exp. Fluids 4, pp.269−278, 1986.

[86] J.W. Goodman. *Introduction to Fourier Optics.* McGraw-Hill, 1996.

[87] A. Gupta, R.S. Mehta, A. Wang, D.C. Haworth and M.F. Modest. *A LES/FDF/PMC model for luminous turbulent flames.* In: Proceedings of the sixth joint meeting of the U.S. sections of the combust. institute, Ann Arbor, MI 17−20 May, 2009.

[88] A.K. Gupta. *Gas turbine combustion: Prospects and challenges.* Israel Annual Conference on Space Sciences. pp.A2−A8, 1995.

[89] A.K. Gupta, D.G. Lilley, and N. Syred. *Swirl flows.* ABACUS Press, Cambridge, USA, 1985.

[90] A.S. Gurvich and A.M. Yaglom *Breakdown of eddies and probability distributions for small scale turbulence.* Phys. Fluids 10, pp.59−65, 1967.

[91] I. Glassman. *Soot formation in combustion processes. 22nd Symposium (International) on combustion.* The combustion institute Pittsburgh, pp.295−311, 1988.

[92] R. T. Gilchrist and J. W. Naughton. *An experimental study of incompressible jets with different initial swirl profiles: Mean results.* AIAA J. 43, pp.741−751, 2005.

[93] P. Givi. *Model−free simulations of turbulent reactive flows.* Prog. Energy Combust. Sci. 15,pp.1−107, 1989.

[94] I. Grant, G.H. Smith, D. Infield, X. Wang, Y. Zhao and S. Fu. *Measurements of the flow around wind turbine rotors by particle image velocimetry.* Proc. 7th Int. Symp. on Applications of Laser Techniques to Fluid Mechanics, Lisbon, 1994.

[95] M.A. Gregor and A. Dreizler. *A quasi−adiabatic laminar flat flame burner for high temperature calibration.* Meas. Sci. Technol. 20, 2009.

[96] J. Haumann and A. Leipertz. *Low power laser Rayleigh probe for flow mixing studies.* Exp. Fluids 5, pp.230−234, 1987.

[97] D.C. Haworth. *Progress in probability density function methods for turbulent reacting flows.* Prog. in Energy and Combust. Sci. 36, pp.168−259, 2010.

[98] C. Heye, H. Koo and V. Raman. *Probability Density Function Approach for Large Eddy Simulation of Turbulent Spray Combustion.* 7th US National Technical Meeting of the Combustion Institute Hosted by the Georgia Institute of Technology, Atlanta, GA March 20−23, 2011.

[99] Boshu He, Meiqian Chen, Shumin Liu, Lijuan Fan, Jinyuan Xu and Wei-Ping Pan. *Measured vorticity distributions in a model of tangentially fired furnace.* Experimental Thermal and Fluid Science 29, pp.537−554, 2005.

[100] Y. Huang. *Combustion dynamics of swirl-stabilized lean premixed flames in an acoustically-driven environment (PhD diss).* University of Iowa, 2008.

[101] P. Holmes, J. Lumley, and G. Berkooz. *Turbulence, coherent structures, dynamical systems and symmetry.* Cambridge University Press, 1996.

[102] M.L. Jakobsen, D.R. McCluskey, W.J. Easson, D.H. Glass and C.A. Greated . *Pneumatic particle conveyance in pipe bend: simultaneous two-phase PIV measurements of the slip velocity between the air and the particle phases.* Proc. 7th Int. Symp. on Applications of Laser Techniques to Fluid Mechanics, Lisbon, 1994.

[103] S. James, J. Zhu and M.S. Anand. *Large-eddy simulations as a design tool for gas turbine combustion systems.* AIAA J., 44, p.674, 2006.

[104] S. James, J. Zhu and M.S. Anand. *LES/FDF of turbulent flames using complex chemical kinetics.* AIAA Paper No. 2006−4746, 2006.

[105] S. James, J. Zhu and M.S. Anand. *Large eddy simulations of turbulent flames using the filtered density function model.* Proc. Combust. Inst. 31, p.1737, 2007.

[106] Jayesh and Z. Warhaft. *Probability distribution, conditional dissipation and transport of passive temperature fluctuations in grid generated turbulence.* Phys. Fluids A 4, 2292, 1992.

[107] C. Jimenez, F. Ducros, B. Cuenot, and B. Bedat. *Subgrid scale variance and dissipation of a scalar field in large eddy simulations.* Phys. Fluids 13(6), 6 June 2001.

[108] P. Kailasnath, K.R. Sreenivasan and J. R. Saylor. *Conditional scalar dissipation rates in turbulent wakes, jets and boundary layers.* Phys. Fluids A 5, 3207, 1993.

[109] S. Kampmann, A. Leipertz, K. Dobbeling, J. Haumann, and Th. Sattelmayer. *Two-dimensional temperature measurements in a technical combustor with laser Rayleigh scattering.* Applied optics, Vol. 32, No. 30, 20 October 1993.

[110] C.M. Kaul, V. Raman, G. Balarac, and H. Pitsch. *Numerical errors in the computation of subflter scalar variance in large eddy simulations.* Phys. Fluids 21, pp.55−102, 2009.

[111] A.N. Kolmogorov. *A refinement of previous hypothesis concerning the local structure of turbulence in a viscous incompressible fluid at high Reynolds number.* J. Fluid. Mech. 13, 82, 1962.

[112] D.A. Kerr. *Determining MTF with a Slant Edge Target.* The Pumkin- a library of selected writings of Douglas A. Kerr.

[113] K. A. Kemenov, H. Wang and S. B. Pope. *Modeling effects of subgrid-scale mixture fraction variance in LES of a piloted diffusion flame.* Combustion Theory and Modelling, September 2010, pp.1-19.

[114] I. Keeheon Ye. *Investigation of the scalar variance and scalar dissipation rate in URANS and LES.* PhD thesis, Waterloo, Ontario, Canada, 2011.

[115] A. Kempf , W. Malalasekera, K. K. J. Ranga-Dinesh and O. Stein. *Large eddy simulations of swirling non-premixed flames with flamelet models: A comparison of numerical methods.* Flow Turbulence Combust, 2008.

[116] O. Kito. *Axi−asymmetric character of turbulent swirling flow in a straight circular pipe.* JSME, Bulletin, vol. 27, April 1984, pp.683−690.

[117] W. Kollman and J. Janicka. *The probability density function of a passive scalar in turbulent shear flows.* Phys. Fluids 25(10), pp.1755−1769, 1982.

[118] D.C. Kyritsis, V. S. Santoro and A. Gomez. *Quantitative scalar dissipation rate measurements in vortex-perturbed counterflow diffusion flames.* Proceedings of the combustion institute, Vol. 29, pp.1679−1685, 2002.

[119] F.J. Krawczynski, B. Renou, L. Danaila, and F.X. Demoulin. *Small−scale measurements in a partially stirred reactor.* Exp. Fluids 40(5), pp.667−682, 2002.

[120] A. Krothapalli, D.P. Wishart and L.M. Lourenco. *Near field structure of a supersonic jet: 'on-line' PIV study.* Proc. 7th Int. Symp. on Applications of Laser Techniques to Fluid Mechanics, Lisbon, 1994.

[121] Tae-Woo Lee, N. Hegde. *Laser-induced breakdown spectroscopy for in situ diagnostics of combustion parameters including temperature.* Combustion and Flame 142, pp.314−316, 2005.

[122] C.J. Lawn. *Principles of Combustion Engineering for Boilers.* Academic press, London, UK, 1987.

[123] T. Landenfeld, A. Kremer, E.P. Hassel, J. Janicka, T. Scha, J. Kazenwadel, C. Schulz, and J. Wolfrum. *Laser diagnostic and numerical studies of strongly swirling natural gas flames.* Proc. of the Combustion Institute, 27, 1998.

[124] Y. Levy and R. Gordon. *Investigation of a combustion chamber (in Hebrew).* Technion report. Haifa, Israel, 1999.

[125] Y. Levy. *Principle and Practice of the low NOx FLOXCOM gas turbine combustor.* Lund University June 19−21, Lund, Sweden, 2005.

[126] E. Levy, D. Peles, M. Opher-Lipson, and S. G. Lipson. *Modulation transfer function of a lens measured with a random target method.* Applied optics, Vol. 38, No.4, 1.02.99.

[127] A.H. Lefebvre. *The role of fuel preparation in low-emissions combustion.* Journal of Engineering for Gas Turbines and Power. Vol.117, pp.617−655, 1995.

[128] A.H. Lefebvre. *Gas turbine combustors. Chapter: Emissions.* MacGraw Hill Series in Energy Combustion and Environment. pp.463−514, 1982.

[129] A.H. Lefebvre. *Fuel effects on gas turbine combustion, liner temperature pattern factor, and pollutant emissions.* AIAA Journal of Aircraft. Vol.21, No. 11, pp.887−898, 1984.

[130] A.H. Lefebvre. *Fuel effects on gas turbine combustion-ignition, stability and combustion efficiency.* Journal of Engineering for Gas Turbines and Power. Vol.107, pp.24−37, 1985.

[131] S.K. Lele. *Compact finite-difference schemes with spectral-like resolution.* Journal of Computational Physics, Vol. 103, pp.16−42, 1992.

[132] S. Liu, C. Meneveau, and J. Katz. *On the properties of similarity subgrid-scale models as deduced from measurements in a turbulent jet.* Journal of Fluid Mechanics, 275, pp.83−119, 1994.

[133] D.G. Lilley. *Swirl flows in combustion: a review.* AIAA journal, 15(8), 1977.

[134] J. Lumley. *The structure of inhomogeneous turbulent flows.* In Proceedings of International Colloquium on the Fine Scale Structure of the Atmosphere and its Influence on Radio Wave Propagation, 1967.

[135] M. Loffler, S. Pfadler, F. Beyrau, A. Leipertz, F. Dinkelacker, Y. Huai and A. Sadiki. *Experimental determination of the sub-grid scale scalar flux in a non-reacting jet-flow.* Flow Turbulence Combust. 81, pp.205−219, 2008.

[136] A.E. Lutz, R.J. Kee, J.F. Grcar, F. M. Rupley. *OPPDIF: A Fortran program for computing opposed-flow diffusion flames.* Thermal & Plasma Processes Department Sandia National Laboratories, Livermore, CA 94551-0969, 1997.

[137] J. Mantzaras and T.H. Van Der Meer. *Coherent Anti-Stokes Raman Spectroscopy Measurements of Temperature Fluctuations in Turbulent Natural Gas-Fueled Piloted Jet Diffusion Flames.* Combustion and Flame 110, pp.39−53, 1997.

[138] S.D. Mason, J. H. Chen and H. G. Im. *Effects of unsteady scalar dissipation rate on ignition of non-premixed hydrogen/air mixtures in counter flow.* Proceedings of the combustion institute, Vol. 29, pp.1629−1636, 2002.

[139] E. Mastorakos, A.M.K.P. Taylor and J. H. Whitelaw. *Scalar dissipation rate at the extinction of turbulent counterflow non−premixed flames.* Combustion and flame 91, pp.55−64, 1992.

[140] E. Mastorakos, T. A. Baritaud, and T. J. Poinsot. *Numerical simulations of autoignition in turbulent mixing flows.* Combustion and Flame 109(1-2), pp.198−223, 1997.

[141] E. Mastorakos, A. Pires da Cruz, T. A. Baritaud, T.J. Poinsot. *A model for the effects of mixing on the autoignition of turbulent flows.* Combust. Sci. Technol.109, pp.243−282, 1997b.

[142] C.N. Markides and E. Mastorakos. *Measurements of scalar dissipation in a turbulent plume with planar laser-induced fluorescence of acetone.* Chemical Engineering Science 61, pp.2835−2842, 2006.

[143] B. Merci, D. Roekaerts, B. Naud, S. B. Pope. *Comparative study of micromixing models in transported scalar PDF simulations of turbulent nonpremixed bluff body flames.* Combustion and Flame 146, pp.109−130, 2006.

[144] R.D. Mehta, D. H. Wood and P.D. Clausen. *Some effects of swirl on turbulent mixing layer development.* Phys. Fluids 3, pp.2716−2724, 1991.

[145] J. Meyers et al. (eds). *Quality and Reliability of Large-Eddy Simulations.* Springer Science+Business Media B.V. 2008. p.93.

[146] A. Melling. *Tracer particles and seeding for particle image velocimetry.* Meas. Sci. Technol. pp.1406−1416, 1997.

[147] V.D. Milosavljevic. *Natural gas, kerosene and pulverized fuel fired swirl burners.* PhD thesis, Imperial College of Science Technology and Medicine. Department of Mechanical Engineering. July 1993.

[148] V.D. Milosavljevic, A.M.K.P. Taylor and J.H. Whitelaw. *Influence of burner geometry and flow rates on the stability and symmetry of swirl-stabilized nonpremixed flames.* Combustion and Flame 80, pp.196−208, 1990.

[149] R.B. Miles, and D. M. Nosenchuck. *Quantitative flow visualization in sodium vapour-seeded hypersonic helium. Lecture notes in engineering.* Hrsg: Gad-el-Hak, M. Vol. 45, Springer: Berlin, 1989.

[150] J. Mi and G.J. Nathan. *The influence of probe resolution on the measurement of a passive scalar and its derivatives.* Exp. Fluids 34, pp.687−696, 2003.

[151] K. McGrattan, J. Floyd and Simo Hostikka. *A mixture fraction combustion model for large scale fire simulation.* 2001 ASME International Mechanical Engineering Congress and Expedition, Volume 1. CD-ROM Proceedings. November, New York, pp.11−16, 2001.

[152] R.B Miles, W.R Lempert and J.N Forkey. *Laser Rayleigh scattering.* Meas. Sci. Technol. 12, R33−R51, 2001.

[153] A.F. Moene. *Swirling pipe flow with axial strain experiment and large eddy simulation.* Technische Universiteit Eindhoven, 2003.

[154] L. Muniz, Martinez and M.G. Mungal. *Applications of PIV to turbulent reacting flows.* Proc. 8th Int. Symp. on Applications of Laser Techniques to Fluid Mechanics, Lisbon, 1996.

[155] I. Namer and R.W. Schefer. *Error estimates for Rayleigh scattering density and temperature measurements in premixed flames.* Exp. Fluids 3, pp.1−9,1985.

[156] M. Namazian, R.W Scheffer and J. Kelly. *Scalar dissipation measurements in the developing region of a jet.* Combustion and Flame 74, pp.147−160, 1988.

[157] M.V. Otiigen and I. Namer. *Rayleigh scattering temperature measurements in a plane turbulent air jet at moderate Reynolds numbers.* Exp. Fluids 6, pp.461−466 , 1988.

[158] M. Oberlack, R. Arlitt, N. Peters. *On stochastic Damkohler number variations in a homogeneous flow reactor.* Combust. Theor. Model. 4, pp.495−509, 2000.

[159] R. Orlu. *Experimental study of passive scalar mixing in swirling jet flows.* Technical Reports from Royal Institute of Technology KTH Mechanics, Stockholm, Sweden, September 2006.

[160] M. Oljaca, X. Gu, A. Glezer, M. Baffico and F. Lund. *Ultrasound scattering by a swirling jet.* Phys. Fluids 10, pp.886−898, 1998.

[161] A. Olivani, G. Solero, F. Cozzi and A. Cogh. *Near field flow structure of isothermal swirling flows and reacting non-premixed swirling flames.* Experimental Thermal and Fluid Science 31, pp.427−436, 2007.

[162] S.H. Park and H.D. Shin. *Measurements of entrainment characteristics of swirling jets.* Int. J. Heat Mass Transfer 36, pp.4009−4020, 1993.

[163] R.L. Panton. *Vorticity dynamics, in: Incompressible Flow.* John Wiley & Sons, New York, 1984.

[164] N. Paone, G.M. Revel and E. Nino. *Velocity measurement in high turbulent premixed flames by a PIV measurement system.* Proc. 8th Int. Symp. on Applications of Laser Techniques to Fluid Mechanics, Lisbon, 1996.

[165] D. Peter. *Slanted-edge MTF for digital camera and scanner analysis.* Proc. IS&T 2000 PICS Conference, pp.135-138, 2000.

[166] M. Petrou and P.Bosdogianni. *Image Processing: The Fundamentals.* John Wiley & Sons Ltd., 1999.

[167] C. Pera, J. Reveillon, L. Vervisch, P. Domingo. *Modeling subgrid scale mixture fraction variance in LES of evaporating spray.* Combustion and Flame 146, pp.635−648, 2006.

[168] H. Pitsch and H. Steiner. *Scalar mixing and dissipation rate in large-eddy simulations of non-premixed turbulent combustion.* Proc. of the Combustion Institute, Vol. 28, pp.41−49, 2000.

[169] W.M. Pitts, C. D Richards and M. S. Levenson. *Large- and small-scale structures and their interactions in an axisymmetric jet.* NIST internal report NISTIR 6393, National institute of standards and technology, Gaithersburg, MD, 1999.

[170] C. Pierce and P. Moin. *A dynamic model for subgrid-scale variance and dissipation rate of a conserved scalar.* Phys. Fluids, 12, pp.3041−3044, 1998.

[171] F. Picano, F. Battista, G. Troiani and C. M. Casciola. *Dynamics of PIV seeding particles in turbulent premixed flames.* Exp. Fluids 50(1), pp.75−88, 2011.

[172] S.B. Pope. *Self-conditioned fields for large-eddy simulations of turbulent flows.* J. Fluid Mech., Vol. 652, pp.139−169, 2010.

[173] S.B. Pope. *Computations of turbulent combustion: progress and challenges.* Proc. Combust. Inst. 23:pp.591−612, 1990.

[174] S.B. Pope. *Ten questions concerning the large-eddy simulation of turbulent flows.* New Journal of Physics 35, 16 March 2004.

[175] S.B. Pope. *Turbulent flows.* Cambridge University press, 2000.

[176] S.B. Pope. *PDF methods for turbulent reactive flows.* Prog. Energy Combust. Sci. 11(2), pp.119−192, 1985.

[177] S. Prucker, W. Meier and W. Stricker. *A flat flame burner as calibration source for combustion research. Temperatures and species concentrations of premixed H_2/air flames.* Rev. Sci. Instrum. 85(9), September 1994.

[178] V. Raman, H. Pitsch and R.O. Fox. *Hybrid large eddy simulation/Lagrangian filtered density function approach for simulating turbulent combustion.* Combustion and Flame 143, pp.56−78, 2005.

[179] R.S. Reichert, F.F. Hatay, S. Biringen and A. Huse. *Proper orthogonal decomposition applied to turbulent flow in a square duct.* Phys. Fluids 6(9), September 1994.

[180] A. Sahay A, E.E. O'Brien. *Uniform mean scalar gradient in grid turbulence: conditioned dissipation and production.* Phys. Fluids A 5,pp.1076−1078, 1993.

[181] S. Sahu. *Experimental study of isothermal and evaporative sprays.* PhD thesis, Mechanical Engineering Department, Imperial College London, United Kingdom.

[182] K. Sardi, A.M.K.P. Taylor and J. Whitelaw. *Conditional scalar dissipation statistics in a turbulent counterflow.* J. Fluid Mech. vol. 361, pp.1−24, 1998.

[183] E. Sameib and M.J. Flynn. *A method for measuring the presampled MTF of digital radiographic systems using an edge test device.* 102 Med. Phys. 25.1., January 1998.

[184] M. Samet and S. Einav. *Mean value measurements of a turbulent swirling-jet.* AIAA J. 26, pp.619−620, 1988.

[185] M. Sipser. *Introduction to the Theory of Computation.* Course Technology Inc, 2006.

[186] L. Sirovich. *Analysis of turbulent flows by means of the empirical eigenfunctions.* Fluid Dynamics Research, 8:85−100, 1991.

[187] L. Sirovich. *Turbulence and the dynamics of coherent structures, part I, II, III.* Quarterly of Applied Mathematics, 45:pp.560−590, 1987.

[188] Y.M. Shim, R.N. Sharma and P.J. Richards. *Proper orthogonal decomposition analysis of the flow field in a plane jet.* Exp. Therm. Fluid Sci.,2013.

[189] J. Scholz, T. Wiersbinski, P. Ruhnau, D. Kondermann, C.S. Garbe, R. Hain and V. Beushausen. *Double−pulse planar−LIF investigations using fluorescence motion analysis for mixture formation investigation.* Exp. Fluids 45, pp.583593, 2008.

[190] Je.W. Shan, D.B. Lang, P.E. Dimotakis. *Scalar concentration measurements in liquid-phase flows with pulsed lasers.* Exp. Fluids 36, pp.268−273, 2004.

[191] M. Schmidt and F. Loffler. *Experimental investigations on two-phase flow past a sphere using digital particle-image-velocimetry.* Exp. Fluids 14, pp.296−304, 1993.

[192] M. Sneep and W. Ubachs. *Direct measurement of the Rayleigh scattering cross section in various gases.* J. of Quantitative Spectroscopy & Radiative Transfer 92, pp.293−310, 2005.

[193] N. Soulopoulos. *Experimental investigation of scalar mixing in unsteady turbulent jets.* PhD thesis, Imperial College London, Mechanical Engineering Department, April 2009.

[194] K.R. Sreenivasan , R.A. Antonia and H.Q. Dahn. *Temperature dissipation fluctuations in a turbulent boundary layer.* Phys. Fluids 20, pp.1238−1249, 1977.

[195] K.R. Sreenivasan. *Evolution of the centerline probability density function of temperature in a plane turbulent wake.* Phys. Fluids 24(7), July 1981.

[196] D.G. Sloan, P.J Smith and L.D. Smoot. *Modeling of swirl in turbulent flow systems.* Prog. Energy Combust. Sci., Vol. 12, pp.163−250, 1986.

[197] J.A. Sutton and J.F. Driscoll. *Rayleigh scattering cross sections of combustion species at 266, 355, and 532 nm for thermometry applications.* Optics letters, Vol. 29, No. 22, November 15, 2004.

[198] G Sutton, A. Levick, G. Edwards and D. Greenhalgh. A combustion temperature and species standard for the calibration of laser diagnostic techniques. Combustion and Flame 147 (1-2), pp.39−48, 2006.

[199] M.R.H Sheikhi, T.G. Drozda, P. Givi, F.A. Jaberi and S.B. Pope. *Large eddy simulation of a turbulent nonpremixed piloted methane jet flame (Sandia Flame D).* Proc. Combust. Inst. 30, pp.549−56, 2005

[200] W. Steenbergen. *Turbulent pipe flow with swirl (PhD thesis).* Technishe Universiteit Eindhoven, Netherlands, 1995.

[201] J.N. Stewart, Q. Wang, R.P. Moseley, P.W. Bearman and J.K. Harvey. *Measurement of vortical flows in a low speed wind tunnel using particle image velocimetry.* Proc. 8th Int. Symp. on Applications of Laser Techniques to Fluid Mechanics, Lisbon, 1996.

[202] J.A. Sutton and J.F. Driscoll. *Scalar dissipation rate measurements in flames. A method to improve spatial resolution by using nitric oxide PLIF.* Proceedings of the Combustion Institute, Vol. 29, pp.2727−2734, 2002.

[203] G. Sutton, A. Levick, G. Edwards and D. Greenhalgh. *A combustion temperature and species standard for the calibration of laser diagnostic techniques.* Combustion and Flame 147, pp.39−48, 2006.

[204] G. Sutton. *The development of a combustion temperature standard for the calibration of optical diagnostic techniques.* PhD thesis, Cranfield University, 2005.

[205] O.S. Sun and L.K. Su. *Experimental assessment of scalar mixing models for large-eddy simulation.* 34th AIAA Fluid Dynamics Conference and Exhibit, 28 June1 July 2004, Portland, Oregon.

[206] O.S. Sun, L.r K. Su and T.M. *Burton. Joint experimental and numerical studies of subgrid scalar mixing models for LES.* 44th Aerospace Sciences Meeting and Exhibit, pp.9−12 January 2006, Reno, Nevada.

[207] L.K. Su. *Measurements of the three-dimensional scalar dissipation rate in gas-phase planar turbulent jets.* Center for Turbulence Research Annual Research Briefs, 1998.

[208] N. Syred and J.M. Beer. *Effect of combustion upon precessing vortex cores generated by swirl combustors.* 14th Symposium (International) on Combustion, The Combustion Institute, Pittsburgh, PA, pp.537−550, 1973.

[209] N. Syred. *A review of oscillation mechanisms and the role of the precessing vortex core (PVC) in swirl combustion systems.* Progress in Energy and Combustion Science, Vol. 32, Issue 2, pp.93−161, 2006.

[210] Bo Tao, J. Katz and C. Meneveau. *Statistical geometry of subgrid-scale stresses determined from holographic particle image velocimetry measurement.* J. Fluid Mech., Vol. 457, pp. 35−78, 2002.

[211] B. Tatian. *Method for obtaining the transfer function from the edge response function.* Journal of the Optical Society of America. 55(8), pp.1014−1019, 1965.

[212] V. Tangirala, R.H. Chen and J.F. Driscoll. *Effect of heat release and swirl on the recirculation within swirl-stabilized flames.* Combust. Sci.& Tech., vol. 51, pp.75−95, 1984.

[213] A.M.K.P. Taylor (ed). *Instrumentation for flows with combustion.* Academic press limited, 1993.

[214] H. Tennekes and J.L. Lumley. *A first course in turbulence.* The MIT press 1972.

[215] T. Tran, Y. Kochar, J. Seitzman. *Measurements of acetone fluorescence and phosphorescence at high pressures and temperatures.* Published by the American Institute of Aeronautics and Astronautics Inc.

[216] C. Tropea, A. Yarin and J.F. Foss (Eds.). *Springer Handbook of Experimental Fluid Mechanics.* Springer−Verlag Berlin Heidelberg, 2007.

[217] M.C. Thurber. *Acetone laser−induced fluorescence for temperature and multiparameter imaging in gaseous flows.* Topical Report TSD-120, Thermosciences Division, Department of Mechanical Engineering, Stanford University, March 1999.

[218] M.C. Thurber. *Acetone laser−induced fluorescence for temperature and multiparameter imaging in gaseous flows.* PhD. Thesis, Stanford University, 1999.

[219] I.K. Toh, D. Honnery, D. and J. Soria. *Velocity and scalar measurements of a low swirl jet.* In Proc. 4th Australian Conf. Laser Diagnostics Fluid Mech. Comb., pp.129−132. The University of Adelaide, South Australia, Australia, 2005.

[220] C. Tong, J. Wyngaard and J. Brasseurs. *Experimental Study of the Subgrid-Scale Stresses in the Atmospheric Surface Layer.* J. og Atmospheric sciences, Vol. 56. 15 July 1999.

[221] C. Tong, J.C. Wyngaard, S. Khanna and J.G. Brasseur. *Resolvable and subgrid-scale measurement in the atmospheric surface layer: Technique and issues.* Journal of atmospheric science, Vol. 55, 1998.

[222] C. Tong. *Measurements of conserved scalar filtered density function in a turbulent jet.* Phys. Fluids 13(10), October 2001.

[223] C. Tong. *Investigation of scalar filtered density function in turbulent partially premixed flames.* Army Research Office and Air Force Office of Scientific Research Contractors' Meeting in Chemical Propulsion Held in Arlington, Virginia on June 12−14, 2006.

[224] *T−20 USAF 1951.* Chart standard layout, product specifications.

[225] L. Vervisch, P. Domingo, G. Lodato and D. Veynante. *Scalar energy fluctuations in large-eddy simulation of turbulent flames: Statistical budgets and mesh quality criterion.* Combustion and Flame 157, pp.778−789, 2010.

[226] D. Veynante and L. Vervish. *Turbulent combustion modeling.* Lecture series, Von Karman Institute, 1999, 2001, 2003, Belgium.

[227] E. Van Vliet, S.M. Van Bergen, J.J. Derksen, L.M. Portela, H.E.A. Van den Akker. *Time-resolved, 3D, laser-induced fluorescence measurements of fine-structure passive scalar mixing in a tubular reactor.* Exp. Fluids 37, pp.1−21, 2004.

[228] A. Vranos. *Turbulent mixing and NOx formation in gas turbine combustors.* Combustion and flame 22, pp.253−258, 1974.

[229] J. Warnatz, U. Maas, R.W. Dibble. *Combustion. 2nd Edition.* Springer Verlag. Berlin, 1999.

[230] J.A. Wunning. *Flamelelose oidation von brennstoff (German).* PhD thesis, Aachen, Germany, 1991.

[231] D. Wang and C. Tong. *Conditionally filtered scalar dissipation, scalar diffusion, and velocity in a turbulent jet.* Phys. Fluids 14(7), July 2002.

[232] G.H. Wang, N.T. Clemens. *Effects of imaging system blur on measurements of flow scalars and scalar gradients.* Exp. Fluids 37, pp.194−205, 2004.

[233] G.H. Wang, N.T. Clemens and P.L. Varghese. *High-repetition rate measurements of temperature and thermal dissipation in a non-premixed turbulent jet flame.* Proceedings of the combustion Institute Vol. 30, pp.691−699, 2005.

[234] D. Wang, C. Tong, R.S. Barlow, and A.N. Karpetis. *Experimental study of scalar filtered mass density function in turbulent partially premixed flames.* Proc. of the Combustion Institute 31, pp.15331541, 2007.

[235] D. Wang and C. Tong. *Experimental study of velocity-scalar filtered joint density function for LES of turbulent combustion.* Proc. of the Combustion Institute 30, pp.567−574, 2005.

[236] D. Wang, C. Tong and S.B. Pope. *Experimental study of velocity filtered joint density function for large eddy simulation.* Phys. Fluids 16(10), October 2004.

[237] G. Wang, A.N. Karpetis, R.S. Barlow. *Dissipation length scales in turbulent nonpremixed jet flames.* Combustion and Flame 148, pp.62−75, 2007.

[238] R. Weber and J. Dugue. *Combustion accelerated swirling flows in high confinements.* Prog. Energy Combust. Sci., 18, pp.349−367, 1992.

[239] J. Westerweel. *Fundamentals of digital particle image velocimetry.* Meas. Sci. Technol., 8, pp.1379−1392, 1997.

[240] J. Westerweel, R.J. Adrian, J.G.M. Eggels and F.T.M. Nieuwstadt. emphMeasurements with particle image velocimetry on fully developed turbulent pipe flow at low Reynolds number. Laser Techniques and Applications in Fluid Mechanics, Proc. 6th Int. Symp., Lisbon, 1992.

[241] J. Westerweel. *Digital Particle Image Velocimetry - Theory and Application (PhD thesis).* Delft University of Technology, the Netherlands, 1993.

[242] J.A. Wunning. *Flamelelose Oxidation von Brennstoff.* PhD thesis, Aachen, 1991.

[243] M.C. Thurber, F. Grisch, B. J. Kirby, M. Votsmeier, and R.K. Hanson. *Measurements and modeling of acetone laser−induced fluorescence with implications for temperature−imaging diagnostics.* Applied optics, Vol. 37, No. 21, 20 July 1998.

[244] J.C. Wyngaard. *Spatial resolution requirements of a resistance wire temperature sensor.* Phys. Fluids 14, pp.2052−2054, 1971.

[245] L.S. Yuen, J.E. Peters, and R.P. Lucht. *Pressure dependence of laser−induced fluorescence from acetone.* Applied optics, Vol. 36, No. 15, 20 May 1997.

[246] Huang, Yun. *Combustion dynamics of swirl−stabilized lean premixed flames in an acoustically−driven environment.* (PhD thesis), University of Iowa, 2008.

[247] J. Zetterberg, Z. Li, M. Afzelius and M. Alden. *Two−dimensional temperature measurements in flames using filtered Rayleigh scattering at 254 nm.* Applied spectroscopy, Vol. 62, No. 7, 2008.

[248] Y.B. Zeldovitch, P.Y. Sadovnikov. and D.A. Frank Kamenetskii. *Oxidation of nitrogen in combustion.* Academy of sciences. Moscow-Leningrad, USSR, (Russian), 1947.

[249] L.X. Zhou, L.Y. Hu, and F. Wang. *Large−eddy simulation of turbulent combustion using different combustion models.* Fuel, No. 87, pp.3123−3131, 2008.

[250] Yue Min Zhu, V. Kaftandjian, G. Peix, and D. Babot. *Modulation transfer function evaluation of linear solid-state x-ray-sensitive detectors using edge techniques.* Applied optics, 1.08.95, Vol. 34 No.22.

Appendix A

Burner Thermal Power Computation

In all cases, the burner was operated with a mixture of 22.1%CH_4, 33.2%H_2, and 44.7% N_2 and air at atmospheric pressure at a global equivalence ratio of 0.9. The volumetric flow rate for this global equivalence ratio is 65.63(l/min).

- Higher heating value for the fuel was computed as (0.221×55.5) + (0.332×141.79) = 59.28(MJ/kg).
- Fuel molar mass (0.221×16) + (0.332×2) + (0.447×28) = 16.694(g/mol).
- Fuel specific gas constant $R = 8314/16.694 = 498$ (J/kgK).
- Fuel density $\rho = P/(RT) = 101325/(498 \times 300) = 0.68$ (kg/m^3).
- Fuel volumetric flow rate 65×1.66e-5 = 0.00108(m^3/s).
- Fuel mass flow rate 0.00108×0.68 = 0.000734(kg/s).
- Burner thermal power 0.000734×59.28e6× = 43511(J/s) or ≈43(KW).

Appendix B

Charge-Coupled Device Linearity

An important characteristics of a imaging system is the linearity in response to incident light. The signal of a CCD camera should ideally be linearly proportional to the amount of light incident on the CCD sensor. There is the EMVA 1288 standard[1], which defines how the linearity of a camera system can be measured. In this work, a method of constant illumination with variable exposure time was used. The dark current may depend on the camera exposure time, it is required that the dark image is measured and subtracted at every exposure time used. Therefore, the linearity plot can be computed by recording the signal level from the CCD camera as a function of exposure time. The signal is presented as normalised intensity levels as a function of exposure time. Figure B.1 shows a linearity plot of the Imager Intense CCD camera that was used in this work.

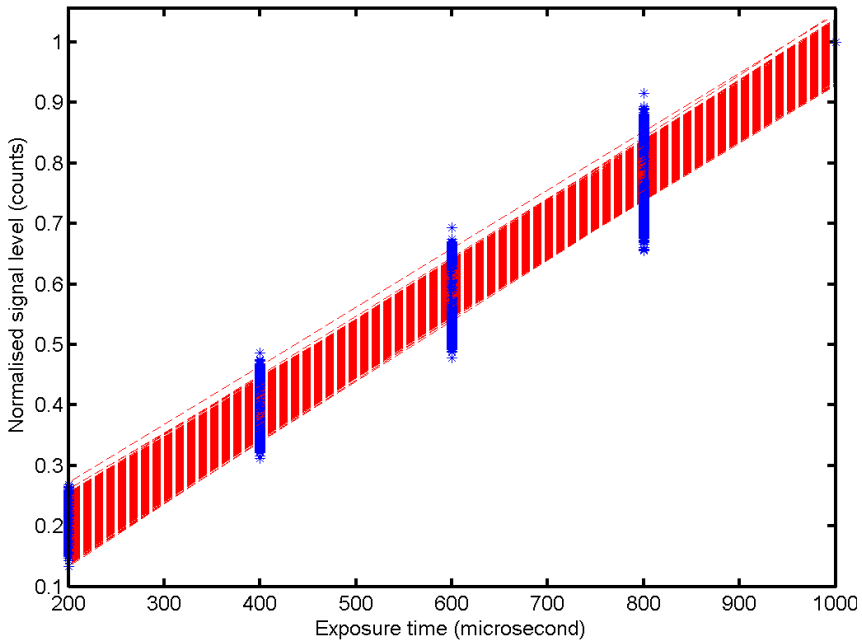

Figure B.1: Values of the linearity measuring sequence (scatter plot) for the camera used in this work and linear regression of these values (red dashed lines). Note that different intensity values come from different parts of the image due to non-uniform illumination.

[1]EMVA Standard 1288, standard for characterisation of image sensors and cameras.Release 3.1, November 12, 2012, Issued by European Machine Vision Association, www.emva.org.

Appendix C

MATLAB script for POD analysis

```
% square cross correlation matrix
% U is input velocity matrix
R = U*U';
% eigenfunctions and eigenvalues
[phi lambda] = eig(R);
% sort eigenvalues
[lambda index] = sort(diag(lambda),'descend');
% sort eigenfunctions according to eigenvalues
phi = phi(:,index);
% POD modes
a = phi * U;

% compute relative energy
Energy = lambda./sum(lambda)*100;
% compute cumulative energy
for i=1:length(Energy);cumEnergy(i) = sum(Energy(1:i))/sum(Energy);end

% reconstruct image
checkImage = 1; % wich image to check
Xpixels = 86; Ypixels = 65;
un = phi' * a;
  Vx_reconstructed = ...
      reshape(un(checkImage,1:Xpixels*Ypixels),Xpixels,Ypixels);
  Vy_reconstructed = ...
      reshape(un(checkImage,(Xpixels*Ypixels)+1:end),Xpixels,Ypixels);
```